

## Abstract

# Fundamental physics and device design using the steady-state *ab initio* laser theory

Alexander Witte Cerjan

2015

In this thesis we generalize and extend the steady-state *ab initio* laser theory (SALT), first developed by Türeci and Stone, and apply it to problems in laser design. SALT as first formulated modeled the gain medium as identical two-level atoms, leading to the well-known Maxwell Bloch laser equations. The result is a set of coupled non-linear wave equations that treats the openness of the cavity exactly and the non-linear modal interactions to infinite order. Most gain media have more than two atomic levels, and in this thesis we generalize the SALT equations to treat realistic and complex gain media, specifically N-level atomic media with a single lasing transition, N-level atomic media with multiple lasing transitions and semiconductor gain media with particle-hole band excitations. The extension to multiple transitions requires fundamentally enlarging the set of SALT equations, by adding a set of population equations that must be solved self-consistently with the non-linear wave equations for the lasing modes in standard SALT. In addition, the population equation can be generalized to treat gain diffusion, an important problem in a number of laser systems, not treated in SALT or in most earlier laser theories. The semiconductor version (Semi-SALT) includes the continuum of particle-hole transitions and the effect of Pauli blocking of transitions, but is only developed and applied in the free-carrier approximation. The resulting theory is termed complex SALT (C-SALT). We also demonstrate how to incorporate amplification and injected signals naturally within the SALT framework, yielding injection SALT (I-SALT). The generalization to I-SALT leads to a larger set of self-consistent coupled non-linear wave equations, a set for the lasing modes and a set for the injected and amplified fields, coupled through cross gain saturation. It clearly distinguishes the lasing modes, which correspond to poles of the scattering matrix, from the injected fields, which do not; in this limit the locking of a lasing mode corresponds to the injected signal forcing

the lasing pole off the real axis, reducing its amplitude to zero. I-SALT is shown to reduce to a version of the standard Adler theory of injection-locked lasing in a certain limit (the single pole approximation).

We apply SALT to design a highly multimode cavity for use as a spatially incoherent light source for applications to imaging and microscopy. Laser illumination typically leads to coherent artifacts that degrade optical images; this can be alleviated by having a very large number of modes ( $\sim 500$ ) which are spatially independent and average out such artifacts. We used SALT to model a D-shaped laser cavity with chaotic ray dynamics and showed that a certain shape greatly increases the number of lasing modes for the same cavity size and pump strength, due to a flat distribution of Q-values and reduced mode competition. An on-chip electrically-pumped semiconductor laser was realized using this cavity design and showed negligible coherent artifacts in imaging, as well as much better efficiency and power per mode than traditional incoherent light sources such as LEDs.

The thesis also goes beyond semiclassical laser theory to treat quantum noise and the laser linewidth in a SALT-based approach. We demonstrate that SALT solutions can be used in conjunction with a temporal coupled mode theory (TCMT) to derive an analytic formula for the quantum limited laser linewidth in terms of integrals over SALT solutions. This linewidth formula is a substantial generalization of the well-known Schawlow-Townes result and includes all previously known corrections: the Petermann factor, Henry alpha factor, incomplete inversion factor and the “bad cavity factor”. However, unlike previous theories these corrections are not simply multiplicative and are not separable in general. The predictions of TCMT linewidth theory are tested quantitatively by means of an FDTD algorithm that includes the Langevin noise as a source term.

Fundamental physics and device design using the  
steady-state *ab initio* laser theory

A Dissertation  
Presented to the Faculty of the Graduate School  
of  
Yale University  
in Candidacy for the Degree of  
Doctor of Philosophy

by  
Alexander Witte Cerjan

Dissertation Director: A. Douglas Stone

May, 2015

Copyright © 2015 by Alexander Witte Cerjan  
All rights reserved.

# Contents

<b>Acknowledgments</b>	<b>xxii</b>
<b>1 Introduction</b>	<b>1</b>
1.1 Basic laser properties . . . . .	5
1.2 Modern laser cavities . . . . .	8
1.3 Types of gain media . . . . .	12
1.4 Derivation of the Maxwell-Bloch equations . . . . .	14
1.4.1 Standard approximations . . . . .	18
1.4.2 Finite difference time domain simulations . . . . .	20
1.5 Overview of this thesis . . . . .	21
<b>2 The steady-state <i>ab initio</i> laser theory</b>	<b>24</b>
2.1 Derivation of SALT . . . . .	25
2.1.1 Numerical solution . . . . .	27
2.2 Region of validity . . . . .	28
2.3 TCF states . . . . .	31
2.3.1 TCF lasing map Jacobian . . . . .	33
2.4 Partially reflecting mirror TCF states . . . . .	35
2.4.1 Analytic solution . . . . .	36
2.4.2 Implementation in the TCF equations . . . . .	38
2.4.3 Partially reflecting mirrors in FDTD . . . . .	39
2.5 Summary . . . . .	40

<b>3</b>	<b>Complex gain media</b>	<b>42</b>
3.1	Derivation of the atomic rate equations . . . . .	44
3.2	Renormalization of a single transition, N-level medium . . . . .	47
3.2.1	Physical limits of interest . . . . .	49
3.2.2	Numerical comparison . . . . .	51
3.2.3	Numerical efficiency . . . . .	57
3.3	Multiple lasing transitions . . . . .	60
3.3.1	Comparison with FDTD . . . . .	62
3.4	Gain diffusion . . . . .	64
3.4.1	Simulations of diffusive gain media . . . . .	66
3.5	Discussion of the stationary population approximation . . . . .	70
3.6	Free-carrier semiconductors in SALT . . . . .	71
3.6.1	Performing the Semi-SALT calculation . . . . .	74
3.6.2	Semi-SALT results . . . . .	75
3.7	Summary . . . . .	76
<b>4</b>	<b>Injected Signals</b>	<b>78</b>
4.1	Derivation of I-SALT . . . . .	81
4.2	From I-SALT to Adler's Model . . . . .	87
4.3	Injection simulations . . . . .	90
4.3.1	Injected signals in FDTD . . . . .	91
4.3.2	Locking transition . . . . .	92
4.3.3	partially locked states . . . . .	98
4.3.4	I-SALT and Adler I-SALT below threshold . . . . .	98
4.3.5	Injected Quadrupole Resonators . . . . .	100
<b>5</b>	<b>Designing an incoherent light source</b>	<b>103</b>
5.1	D-shaped cavity design with SALT . . . . .	106
5.2	Using the single pole approximation . . . . .	109
5.3	Experimental results . . . . .	113

<b>6</b>	<b>The TCMT linewidth formula: a quantitative test</b>	<b>115</b>
6.1	Temporal coupled mode theory . . . . .	118
6.2	Microscopic and macroscopic noise equivalence . . . . .	123
6.3	Noisy FDTD equations . . . . .	126
6.4	Numerical linewidth analysis . . . . .	130
6.4.1	frequency domain analysis . . . . .	130
6.4.2	time domain confirmation . . . . .	132
6.5	Linewidth comparison results . . . . .	134
6.5.1	linewidth scaling relations . . . . .	138
<b>7</b>	<b>Conclusion</b>	<b>141</b>
<b>A</b>	<b>FDTD simulation algorithm</b>	<b>145</b>
<b>B</b>	<b>Derivation of the TCF lasing map Jacobian</b>	<b>149</b>
<b>C</b>	<b>N-level FDTD simulation constants</b>	<b>153</b>
<b>D</b>	<b>Matrix definitions</b>	<b>155</b>
<b>E</b>	<b>Treatment of beating populations</b>	<b>156</b>
<b>F</b>	<b>Stability Analysis</b>	<b>159</b>

# List of Figures

1.1	(a) Schematic of a simple laser cavity formed by a perfectly reflecting mirror on the left and a partially reflecting mirror on the right. The electric field is shown as red arrows, forming a standing wave between the two mirrors. The gain medium fills the space between the two mirrors and is being pumped from an external source, shown in orange. (b) Schematic of a simple four-level gain medium, where electrons are pumped from the ground state to the top state, then non-radiatively decay to the metastable upper lasing level, before finally undergoing stimulated emission and dropping to the lower lasing level. The energy difference between the two lasing states is labeled as the atomic transition frequency, $\omega_a$ . . . . .	7
1.2	(a) A cleaved facet of a dry-etched Quantum Cascade ridge waveguide made of alternating layers of $\text{In}_{0.52}\text{Al}_{0.48}\text{As}$ and $\text{In}_{0.53}\text{Ga}_{0.47}\text{As}$ [51], which has an effective index of refraction of $n \approx 3.25$ [52], constructed on $\text{SiO}_2$ , $8\mu\text{m}$ in width, in which the gain medium is made of quantum cascade layers. (b) Numerical simulations of the transverse direction of such a ridge waveguide performed using COMSOL [53]. . . . .	9

1.3	(a) Toroidal microresonator with an intrinsic $Q = 1.00 \times 10^8$ [39]. (b) Plot of the electric field profile of a two-dimensional slice of a defect photonic crystal. Regions with a different dielectric constant are denoted with black lines [41]. (c) Diagram of a random laser indicating localized scatterers embedded in a gain medium with negligible index of refraction. Arrows inside of the gain region show one possible path for coherent scattering of light leading to a lasing mode. . . . .	10
1.4	Schematic of the energy levels and decay channels for a helium-neon laser [73].	13
2.1	(a) Comparison between SALT and FDTD simulation results for an $n = 1.5$ dielectric slab cavity with $k_a = 40$ , $\gamma_{\perp} = 4$ , $\gamma_{\parallel} = 0.001$ , and thus $\Delta = 2$ . Different colors show the modal intensities as a function of the pump strength. Excellent quantitative agreement is seen between the two methods as the SIA is well satisfied. (b) Comparison between SALT and FDTD simulation results for the same dielectric slab cavity, but with $\gamma_{\parallel} = 0.2$ . No agreement between FDTD and SALT is seen as the SIA is not satisfied. Rates are given in units of $c/L$ , and modal intensities and pump strengths are given in dimensionless SALT units. . . . .	29
2.2	FDTD simulation of a dielectric cavity with $k_a = 40$ , $n = 1.5$ , $\gamma_{\perp} = 4$ , $\gamma_{\parallel} = 0.001$ . Blue curve shows the inversion at a single pixel at the end of the cavity as calculated by the FDTD algorithm. The red curve shows the calculated inversion if the inversion could be adiabatically eliminated using Eq. (2.10). Units are given in values of $c/L$ . . . . .	30
2.3	Plot of the modal intensity as a function of pump strength for a partially reflecting cavity with $L = 1$ , $\varepsilon_c = 1$ , $k_a = 40$ , $\gamma_{\perp} = 4$ , and $\Lambda k_a = 2$ . Triangles show FDTD results, while lines give the SALT results. Rates and frequencies are given in units of $c/L$ , while modal intensities and pump strengths are given in terms of dimensionless SALT units. . . . .	40
3.1	Schematic of a four-level gain medium. . . . .	50

3.2	<p>Modal intensities as functions of the normalized equilibrium inversion <math>d'_0/d_c</math> (effective pump) in a 1D microcavity edge emitting laser (schematic inset). The cavity is bounded on one side by a perfect mirror and on the other side by air, and has uniform refractive index <math>n = 1.5</math>. Solid lines are results obtained by the time-independent SALT method; open circles are results of FDTD simulations with a coherently pumped four-level medium (Fig. 3.1); solid triangles are results of FDTD simulations with a coherently pumped six-level medium with a lasing transition between <math> \varphi_3\rangle</math> and <math> \varphi_1\rangle</math>. Full simulation parameters are given in Appendix C. Both the four-level and six-level media are chosen to satisfy the stationary population approximation. The dephasing rate is <math>\gamma_{\perp} = 4</math>. The four-level system is in the linear regime described by Eqs. (3.27)-(3.28), while the six-level system is in the non-linear regime described by Eqs. (3.29)-(3.30). The spectra at <math>d_0/d_c = 0.488</math>, and the gain curve, are shown in the upper left inset. . . . .</p>	53
3.3	<p>(a) Unscaled modal intensity of the six-level simulations from Fig. 3.2 as a function of the pump. A cross sectional area of <math>1\text{m}^2</math> is assumed to calculate the power. (b) Inversion as a function of the pump at the cavity boundary. Dashed lines in plots a and b correspond to the pump values shown in plot c. (c) Inversion as a function of position within the cavity for three different pump values, cyan corresponds with <math>\mathcal{P} = 3.75 \times 10^8 \text{s}^{-1}</math>, magenta with <math>\mathcal{P} = 1.65 \times 10^9 \text{s}^{-1}</math>, and orange with <math>\mathcal{P} = 4.85 \times 10^9 \text{s}^{-1}</math> to show the evolution of the inversion within the cavity as a function of the pump strength. As can be seen, the inversion at the end of the cavity stays relatively constant as the pump strength is increased. . . . .</p>	55

- 3.4 Breakdown of the equivalence between SALT and FDTD when the stationary population approximation is not valid is shown here in two different ways. Here, modal intensities as a function of the normalized equilibrium inversion  $d'_0/d_c$  (effective pump) are shown for a 1D microcavity edge emitting laser with  $\gamma_\perp = 4$  and  $n = 1.5$ . Solid lines again represent results obtained from SALT, while open circles represent FDTD simulations of a simple four-level system with  $\gamma'_\parallel = 0.1$ . Triangles represent FDTD simulations of a six-level system in the non-linear parameter regime in which  $\gamma'_\parallel \sim 0.001$  for  $d'_0 \leq 0.1$ , and thus satisfying the stationary population approximation, but  $\gamma'_\parallel \sim 0.01$  for  $d'_0 \geq 0.45$ , and consequently no longer satisfying the stationary population approximation. . . . . 56
- 3.5 SALT and FDTD results for a one-dimensional random laser. Modal intensities are plotted against the normalized equilibrium inversion  $d'_0/d_c$  (effective pump). Solid lines represent SALT results, and circles represent FDTD simulations for a four-level system with  $\gamma'_\parallel = 0.001$ . The refractive index distribution of the edge emitting random laser is described in the text. The gain medium has  $\gamma_\perp = 4$  and is in the regime described by Eqs. (3.27)-(3.28). Left inset: log-log plot of the indicated region where three modes turn on in close proximity. Right inset: schematic of the cavity structure. . . . . 57
- 3.6 Comparison of SALT and FDTD run-times. Modal intensities are shown as a function of the run-time for SALT (squares) and four-level FDTD simulations (circles), using the parameters of Fig. 3.2. FDTD simulations that have not begun to lase are marked as crosses. Plot (a) shows data for  $d_0/d_c = 0.071$ , just above the first lasing threshold. SALT determined the steady-state single modal intensity in under three minutes, while the FDTD required  $\sim 5000$  minutes to reach steady state. Plot (b) shows data for  $d_0/d_c = 0.486$ , well above the third lasing threshold. SALT calculated all data up to and including this pump value in under 90 minutes, whereas FDTD required  $> 500$  minutes for the first two modes to reach steady-state, with the third mode intensity (green circles) still fluctuating after 5000 minutes (not shown). 58

- 3.7 Plot of modal intensities as a function of pump strength for a cavity with  $n = 1.5$  and a gain medium consisting of atoms with two different atomic transitions,  $\omega_{a,1} = 40$ ,  $\gamma_{\perp,1} = 4$ ,  $\theta_1 = .1$ ,  $\omega_{a,2} = 38$ ,  $\gamma_{\perp,2} = 3$ ,  $\theta_2 = .1$ , and 6 atomic levels in total, with decay rates as indicated in the schematic. Results from C-SALT using the stationary population approximation are shown as straight lines, results from FDTD simulations are shown as triangles. The different colors indicate different lasing modes. Inset shows the modal frequencies and their intensities at  $P = .0035$ . All values are reported in units of  $c/L$ . . . . . 63
- 3.8 (Left panel) Plot of the modal intensities calculated using C-SALT as a function of pump strength for a dielectric slab cavity,  $n = 1.5$ , and a two level, single transition atomic gain medium, with  $\omega_a = 40$  and  $\gamma_{\perp} = 4$ , values again in units of  $c/L$ . Simulations for three different diffusion strengths are shown in solid, dashed, and dot-dashed lines. Different colors correspond to different lasing modes within each simulation. (Right panel) Plot of the inversion in the cavity as a function of position in the cavity at a pump strength of  $d_0 = 0.345$ . Darker colors indicate increasing values of the diffusion coefficient. Schematic shows a one-sided dielectric slab cavity containing a two level atomic medium subject to uniform pumping. . . . . 66
- 3.9 (Left panel) Plot of the modal intensities calculated using SALT as a function of pump strength for a partially pumped dielectric slab cavity,  $n = 1.5$ , containing a four level, single transition atomic gain medium. Simulations of four different values of diffusion are shown as solid, dotted, dot-dashed, and dashed lines. The first lasing mode to turn on in all of the simulations is shown in red, and the second lasing mode, which only turns on in two of the simulations, in blue. (Right panel) Plot of the inversion in the cavity as a function of position in the cavity at a pump strength of  $d_0 = 0.37$ . Darker colors indicate increasing values of the diffusion coefficient. Schematic shows a partially pumped one-sided dielectric slab cavity containing a four level atomic medium with a single lasing transition. . . . . 68

3.10	Plot of the non-interacting modal thresholds as a function of the diffusion coefficient in a quadrupole cavity with $\epsilon = 0.16$ , $r_0 = 3.45\mu m$ , $k_a = 6.27\mu m^{-1}$ , $\gamma_{\perp} = .19\mu m^{-1}$ , $n = 3 + .004i$ . Only the three modes that become the threshold lasing mode for different values of the diffusion are plotted. Left schematic within the plot shows the boundary of the simulated region, black circle, boundary of the cavity, blue quadrupole, and applied pump profile, red circle. The right schematic within the plot depicts the four level gain medium that fills the entire quadrupole cavity. Markers in the plot correspond to the threshold lasing mode and corresponding inversion profile accounting for the effects of diffusion at their locations. The inversion profile is shown in a false color plot, with red corresponding to large inversion, and blue corresponding to small inversion. The white boundary in the plots denotes the cavity boundary. . . . .	69
3.11	(Left panel) Plot of the lasing thresholds for each of the non-interacting modes in the cavity as a function of the applied electric potential, $\phi$ , for a single sided, slab semiconductor laser. The energy gap at $q = 0$ has been set to $E_g = 40$ , and the chemical potential set at half that, $\mu = 20$ . The non-interacting thresholds of the two modes studied in the right panel are given the same colors as appear in the right panel. (Right panel) Plot of the frequencies of the two lasing modes as a function of the applied electric potential. The frequency for the second lasing mode (red) is only shown after it reaches threshold. . . . .	76
4.1	Schematic depicting the total field and scattering field regions for a FDTD algorithm. Field quantities in the total field region are a combination of fields from the source and any scattering events which might be taking place to the left of the diagram. Fields measured in the scattered field region are only those originally from leftward moving waves from the source that subsequently scattered off any interfaces. . . . .	91

4.2 (Top) Simulations of single-mode injection locking in a one-sided dielectric slab cavity with  $n = 1.5$  (schematic) with a perfect mirror at one end and an index step to vacuum at the other. First, the pump is increased above the threshold for lasing at  $\omega_{1,free} = 40.714$ ,  $d_0 = 0.0603$  to  $d_0 = 0.08$ , and then held at a fixed value (vertical black line) while the input signal amplitude is ramped from  $B_{in} = 0$  until the free-running signal is quenched and the system “locks” (vertical orange line) to the injected frequency,  $\omega_{in} = 40.4$  at  $B_{in} = 0.176$ . Finally, the simulation is continued in the locked regime to  $B_{in} = 0.4$ . Solid lines are output intensities calculated from I-SALT; blue is lasing output, red is amplified output at signal frequency, dot-dashed black is total output. Triangles are the same quantities from FDTD for the same dielectric slab laser with  $\omega_a = 40$ , the width of the gain curve,  $\gamma_{\perp} = 4$ , and  $\gamma_{\parallel} = 0.001$ . The green curve in the locked regime is the prediction of our generalized Adler equations, (4.35) and (4.36). The top inset shows gain curve and  $\omega_{in}$  (red),  $\omega_1$  (blue). (Bottom) Frequency variation of the first lasing mode. Blue line is from I-SALT and blue triangles from FDTD. The green line shows the prediction of the Adler theory. The red line is the injected signal frequency. Again, the orange dashed line shows the locking threshold from I-SALT; frequencies beyond this point are taken as the real part of the location of the pole of the scattering matrix. Blue dashed lines showing negligible frequency shift are I-SALT calculation with uniform gain saturation and no spatial hole burning. The inset shows a plot of the phase shift between input and output signals of an injection-locked dielectric slab cavity at a fixed input intensity. I-SALT (red curve) and FDTD simulations (red triangles) are seen to have a better quantitative and qualitative agreement than the Adler prediction (green curve). For comparison with the Adler theory, the horizontal axis is plotted in terms of the free-running lasing frequency in the absence of an injected signal at threshold,  $\omega_{1,free}$ . Frequencies and rates are given in units of  $c/L$ , while the atomic inversion and modal intensities are given in SALT units of  $E_c$  and  $d_c$ . . . . .

- 4.3 (a) Motion of the pole as described in the text corresponding to the free-running lasing mode in the locking scenario of Fig. 4.2. As the pump is increased below threshold the pole of the scattering matrix is pulled upwards towards the real axis and “in” towards  $\omega_a = 40$  (blue dashed line, recall there is no signal yet at  $\omega_{in} = 40.4$ ). Free-running lasing occurs when the pole reaches the real axis at  $\omega_{1,free} = 40.714$  and continues as the pump is increased further above threshold with negligible further frequency shift. Then the pump is fixed and the input signal is ramped, causing the pole (solid blue line) to move to higher frequency, away from the input frequency, and eventually off the real axis as the effects of gain saturation cause the lasing mode to go below threshold. The inset shows a magnification on the motion of the pole of the lasing mode inside the dotted box. (b) Frequency spectrum from FDTD simulations across the locking transition, showing no additional lines appearing, indicating that the effect is purely due to gain cross saturation. Frequencies and rates are given in units of  $c/L$ , while the atomic inversion and modal intensities are given in SALT units of  $E_c$  and  $d_c$ . 95
- 4.4 Partial locking transition as described in the text for a laser with two free-running modes and an injected signal (schematic) using a similar pumping and input ramping scheme as Fig. 4.2, starting at the first lasing threshold  $d_0 = 0.101$  and pumping until  $d_0 = 0.13$ , then increasing the input signal from  $B_{in} = 0$  to  $B_{in} = 0.4$ . Solid lines are output intensities calculated from I-SALT; blue and cyan lines are lasing output, the red line is amplified output at signal frequency,  $\omega_{in} = 20.3$ , the dot-dashed black line is total output. Triangles are the same quantities from FDTD for a similar dielectric slab laser with  $n = 3$ ,  $\omega_a = 20.5$ ,  $\gamma_{\perp} = 3$ ,  $\gamma_{\parallel} = 0.001$ . The inset shows the relationship of the three frequencies. As expected, the lasing mode nearest to the injected signal locks to the injected signal (orange line), then the more distant lasing mode locks (purple line). Frequencies and rates are given in units of  $c/L$ , while the atomic inversion and modal intensities are given in SALT units of  $E_c$  and  $d_c$ . . . . . 97

4.5 Comparison of the predictions of I-SALT (blue line), the SPA of I-SALT, given by Eqs. (4.26) and (4.27) (green line), the Adler model, as given by Eqs. (4.35) and (4.36) (red line), and FDTD (blue triangles) for both the output intensity (top) and the phase offset (bottom). The input intensity is negligible ( $|B_{in}|^2 = 10^{-4}$  in normalized SALT units) compared to the output, while the pump (gain) is increased from  $d_0 = 0$  to  $d_0 = 0.067$ , thus placing the simulations in the regime of validity for the Adler approximations. The vertical orange dashed line denotes the first lasing threshold in the absence of an incident signal, whereas the vertical purple dashed line shows where I-SALT predicts the unlocking transition to occur. Simulations are shown for a single-sided dielectric slab cavity with  $n = 1.5$ ,  $\omega_a = 40$ ,  $\omega_{in} = 40.7$ ,  $\omega_{1,free} = 40.714$ ,  $\gamma_{\perp} = 4$ , and  $\gamma_{\parallel} = 0.001$ . Frequencies and rates are given in units of  $c/L$ , while the atomic inversion and modal intensities are given in SALT units of  $E_c$  and  $d_c$ . . . . . 99

4.6	<p>Simulations of a uniform index quadrupole cavity laser amplifier with <math>n = 1.5</math> (boundary indicated in white). The parameters chosen are <math>R_0 = 1.72\mu m</math>, <math>\lambda_a = 1\mu m</math>, <math>\gamma_{\perp} = 0.03\mu m</math>, and <math>\epsilon = 0.16</math>. The injected wavelength for all three simulations is the same as the that for the first free-running mode, <math>\lambda_{in} = \lambda_1 = 0.989\mu m</math>. The pump value was increased from <math>D_0 = 0</math> to the first free-running lasing threshold, <math>d_0 = 0.065</math>, vertical orange dashed line. The three solid curves show the amplifier output for three different injection conditions: blue, injection with the TCF corresponding to the first lasing mode; green, injection with the TCF corresponding to the second lasing mode; red, injection with the TCF corresponding to the third lasing mode. Lower plots show in color scale the normalized mode amplitude profiles: (a) The first free-running lasing mode at threshold. (b) The amplified mode with the first lasing mode's incoming TCF as input. (c) The amplified mode with the second lasing mode's incoming TCF as input. (d) The amplified mode with the third lasing mode's incoming TCF as input. The full disk shown in blue is the simulation region used; only TM modes were simulated. The atomic inversion and modal intensities are given in SALT units of <math>E_c</math> and <math>d_c</math>.</p>	101
5.1	<p>Schematic of a D-shaped cavity. . . . .</p>	105

5.2	<p>(Left panel) Semilog plot of the <math>Q</math>-factors for the first twenty modes for circular and D-shaped cavities with <math>R = 5\mu m</math>, <math>n = 3.5</math>, <math>k_a = 1\mu m^{-1}</math>, and <math>\gamma_{\perp} = 0.03\mu m^{-1}</math> in order of their modal thresholds as predicted by SALT. The circular cavity displays a few very high <math>Q</math> modes corresponding to whispering gallery modes, while the <math>Q</math> distributions for the D-shaped cavities are seen to be much more uniform, with no strongly preferred modes. (Right panel) Semilog plot of the threshold pump values, <math>d_0</math>, for the same set of circular and D-shaped cavities. Dashed lines show the non-interacting modal thresholds, while the solid lines show the thresholds calculated with five lasing modes active in the cavity. Thus, the first five values for the solid lines are exact, while the remaining values should be viewed as a lower bound, due to the increased gain saturation as the pump is further increased to reach subsequent modal thresholds. . . . .</p>	107
5.3	<p>Spatial profile of the amplitude for the first four lasing modes at threshold for <math>r_0 = .3R</math>, <math>r_0 = .5R</math>, and <math>r_0 = .7R</math>, shown in the first, second, and third columns respectively. . . . .</p>	108
5.4	<p>Plot of the normalized modal thresholds as predicted by SALT for circular and D-shaped cavities with <math>R = 5\mu m</math>, <math>n = 3.5</math>, <math>k_a = 1\mu m^{-1}</math>, and <math>\gamma_{\perp} = 0.03\mu m^{-1}</math>. Each curve has been normalized by the first lasing threshold for that laser cavity. Dashed lines denote non-interacting normalized modal thresholds while solid lines denote interacting modal thresholds when each system has five active lasing modes. Again, the solid lines are thus exact for the first five modes, while the remaining values represent a lower bound as increased competition will drive them higher as the pump is increased. . .</p>	109

- 5.5 (Left panel) Comparison between SPA-SALT (solid lines) and full SALT (dashed lines) calculations for the D-shaped and circular cavities with  $R = 5\mu\text{m}$ ,  $n = 3.5$ ,  $k_a = 1\mu\text{m}^{-1}$ , and  $\gamma_{\perp} = 0.03\mu\text{m}^{-1}$ . Excellent agreement is seen between these two calculations, especially for the  $r_0 = .5R$  case, where the two curves are nearly indistinguishable. (Right panel) Solid lines again indicate the same SPA-SALT calculations shown in the left panel, and are plotted alongside SPA-SALT simulations performed using mode profiles calculated with COMSOL Multiphysics. Semi-quantitative agreement is seen, indicating that COMSOL Multiphysics can be easily expanded to give good above threshold predictions of lasers in the multimode regime. . . . . 111
- 5.6 (a,b) Optical images of the speckle pattern at the end of a  $1\text{m}$  long multimode fiber by emission from a Fabry-Pérot laser (a) and D-shaped cavity laser (b). The Fabry-Pérot laser emission produced high contrast speckle ( $C = 0.58$ ), indicating that lasing was limited to  $\sim 3$  transverse modes, whereas the D cavity laser produced low contrast speckle ( $C = 0.03$ ), implying independent lasing in  $\sim 1000$  modes. (c,d) The emission from the end of the multimode fiber was used to illuminate an Air Force resolution test chart in transmission mode through an immobile ground glass diffuser. The high spatial coherence of the Fabry-Pérot laser produced a speckled image (c) whereas the low spatial coherence of the D laser emission gave a high quality image with low speckle contrast (d) [122]. . . . . 114

- 6.1 (a) Intensity spectrum of the output electric field of an  $n = 3$  dielectric slab cavity. The simulation parameters for the cavity are  $\gamma_{\perp} = .5$ ,  $\omega_a = 42.4$ ,  $\gamma_{\parallel} = .01$ ,  $\theta = 2 \times 10^{-9}$ ,  $N_A = 10^{10}$ , and the cavity is uniformly pumped at  $D_0 = 0.275$  which is close to 5 times the threshold lasing pump of  $D_{0,thr} = 0.0488$ . The rates quoted here are given in units of  $c/L$ , while the intensity is given in SALT units of  $4\theta^2/(\hbar^2\gamma_{\perp}\gamma_{\parallel})$ , and the number and inversion of gain atoms are given in the SALT units of  $4\pi\theta^2/(\hbar\gamma_{\perp})$ . (b) Plot of the fitted Lorentz error function (red line) and numerically integrated FDTD data (blue dots) of the simulation shown in (a). The spectral resolution for the simulated data in (a) and (b) is  $d\omega = 1.96 \times 10^{-5}$ . The analytic curve fit parameters are found using MATLAB's curve fitting algorithms. . . . . 131
- 6.2 Plot of the autocorrelation of the electric field simulated numerically for the same parameter used in Fig. 6.1 (blue line) and the analytic prediction for the envelope of the autocorrelation given in the second factor in Eq. (6.72) (green line). The fast oscillations in the numerically simulated electric field are at the lasing frequency  $\omega_0$ , which is much faster than the other time scales in the problem, and leads to the densely packed curve shown in blue. Quantities are normalized, and plotted in units of  $\delta\omega\delta t$ . . . . . 133

6.3 (Left panel) Plot showing the linewidth predictions given by the TCMT given in Eq. (6.2) (green), corrected Schawlow-Townes theory given in Eq. (6.73) (blue), corrected Schawlow-Townes theory calculated using the spatially averaged output power in Eq. (6.78) (cyan), integral form of the Chong-Stone linewidth formula given in Eq. (6.74) (orange), and FDTD simulations (magenta) for a uniformly pumped, dielectric slab cavity with  $n = 3$ ,  $\omega_a = 42.4$ ,  $\gamma_{\perp} = .5$ ,  $\gamma_{\parallel} = .01$ ,  $\theta = 2 \times 10^{-9}$ , and  $N_A = 10^{10}$ . Except where noted, all of the linewidth formulas are evaluated using the spatially dependent integral definition of the power given by Eq. (6.77). (Right panel) Plot of the same data shown on a log-log scale. The rates and frequency are given in units of  $c/L$ , the number of atoms in the cavity is given in terms of the SALT units of  $4\pi\theta^2/(\hbar\gamma_{\perp})$ , and the output power is given in the SALT units of  $4\theta^2/(\hbar^2\gamma_{\perp}\gamma_{\parallel})$ . . . . . 135

6.4 (Left panel) Plot of the steady-state inversion,  $D(x)$ , as a function of the location in the cavity for three different values of the output power,  $P = 0.524$  (blue),  $P = 1.252$  (green), and  $P = 3.116$  (red). These values correspond to the first, sixth, and eighteenth data points shown in Fig. 6.3. Strong spatial hole-burning is seen in the inversion due to the lasing mode. (Right panel) Plot of the normalized spatial profile of the lasing mode,  $|\psi_0(x)|$ , as a function of position in the cavity for the same three values of the output power shown in the left panel. The output power is given in dimensionless SALT units of  $4\theta^2/(\hbar^2\gamma_{\perp}\gamma_{\parallel})$ . . . . . 136

6.5 (Left panel) Plot showing the linewidth predictions given by the TCMT (green line), corrected Schawlow-Townes theory (blue line), and FDTD simulations (red diamonds and magenta triangles) for a uniformly pumped, dielectric slab cavity with  $n = 3$ ,  $\omega_a = 42.4$ ,  $\gamma_{\perp} = .5$ ,  $\gamma_{\parallel} = .04$ ,  $\theta = 4 \times 10^{-9}$ , and  $N_A = 10^{10}$ . The results of the new FDTD simulations are shown as red triangles, and are plotted alongside the FDTD results from Fig. 6.3, shown as magenta triangles. (Right panel) Plot showing the linewidth predictions given by the TCMT (green line), rescaled TCMT prediction from Fig. 6.3 (magenta dashed line), corrected Schawlow-Townes theory (blue line), and FDTD simulations (cyan squares) for a uniformly pumped, dielectric slab cavity with  $n = 3$ ,  $\omega_a = 42.4$ ,  $\gamma_{\perp} = .25$ ,  $\gamma_{\parallel} = .02$ ,  $\theta = 2 \times 10^{-9}$ , and  $N_A = 10^{10}$ . The rates and frequency are given in units of  $c/L$ , the number of atoms in the cavity is given in terms of the SALT units of  $4\pi\theta^2/(\hbar\gamma_{\perp})$ , and the output power is given in the SALT units of  $4\theta^2/(\hbar^2\gamma_{\perp}\gamma_{\parallel})$ . . . . . 139

# List of Tables

F.1	Stability eigenvalues for the cavity shown in Fig. 4.2 at two different locations of pump and injection strength. The first column shows the eigenvalues right before the injected mode is turned on, with only a single lasing mode active in the cavity. The second column shows the eigenvalues when both the lasing mode and amplified mode are present in the cavity and have nearly the same output intensity. In both cases, the I-SALT solution is found to be stable, though in the second case, an extra marginal eigenvalue is found. . . . .	162
-----	--	-----

# Acknowledgments

There are many friends and colleagues who have been an indispensable source of insight and camaraderie during my time at Yale. I would first like to express my deepest appreciation for my thesis advisor, A. Douglas Stone, whose guidance and motivation were essential to the completion of this thesis. I have benefited enormously from the breadth and depth of your knowledge in both physics and philosophy, and look forward to collaborating with you, both on science and soccer, for many years to come. A warm thanks must be extended to the other members of my thesis committee. I greatly appreciated the chance to work with Hui Cao on the incoherent source project, and to take excellent classes from both Leonid Glazman and Peter Rakich.

I owe a debt of gratitude to the other denizens of the Stone group office with whom I have had the pleasure working beside. Arthur Goetschy provided a constant source of inspiration, through his tireless dedication to research, and friendship, especially when the quest science had to be postponed for the quest for beer. Yidong Chong tolerated me while I was still getting my bearings in the group and taught me how to read scientific papers with a critical eye. Ananda Roy provided companionship through our scientific discussions, but more importantly through commiseration on the banalities constituting the daily life of research. I would like to thank Li Ge for many compelling discussions about SALT and the inner workings of the two-dimensional radial solution method. Finally William Sweeney whom, despite our short overlap thus far, I have already learned much from and look forward to many engaging conversations in the future.

I would like to thank Brandon Redding for providing the best possible interaction a theorist could ever desire: “Hey Alex, we’re going to build this device, but it would be

awesome if you could simulate it too.” Thank you for helping me maintain the perspective that theory is only as useful as the experiments it is able to aid. I only hope that all of my future dealings with experimentalists (or just the experiments themselves) will be so straightforward.

My collaborators at the Massachusetts Institute of Technology deserve recognition for all of the work we have done together. Adi Pick, it has been fantastic discussing science and mathematics with you over the last year and change. David Liu, it was a pleasure assisting you in the direct-solver project. Finally Steven Johnson, I greatly appreciate all of the help and advice you gave me over the course of the noisy-FDTD project. Thank you for agreeing to be the outside reader for this dissertation.

I’d like to recognize those members of my cohort who have provided camaraderie over the years both in classes and the lab, Faustin Carter, Chris McKitterick, Eric Holland, and Brian Vlastakis. I wish you nothing but the best as we enter the next stage in our careers. To Bradley Hayes and Henny Admoni, I am extraordinarily grateful that our paths crossed. I have greatly enjoyed the late nights over a board game, climbing, Brazilian jiu-jitsu, and the conversation that wove throughout. Valerie Morley, thank you for keeping me sane, your curiosity and sense of humor are marvelous. Finally, to my family, I couldn’t have done this without your love and support. Thank you.

# Chapter 1

## Introduction

Since their invention in 1960, lasers have become an indispensable part of the modern world. Lasers can be found in most homes inside of CD drives on computers and used with optical fibers to connect those homes to the telecommunications network. This same technology has found its way into numerous and diverse commercial applications; for example, carbon dioxide lasers are used in both welding and surgery. The primary reason for the proliferation of lasers in modern life is the extremely broad range of capabilities of lasers; battery powered semiconductor laser diodes are used at every conference in the world inside hand-held devices, while the neodymium-doped phosphate glass lasers at Lawrence Livermore National Laboratory are able to deliver 500 terawatts within a few picoseconds to a capsule, forcing its contents close enough together to undergo fusion [1]. The range of capabilities of lasers covers a large area in a two-dimensional parameter space, providing coherent, monochromatic light for a wide range of frequencies, and a large range of output powers [2,3]. (In addition to coherence and monochromaticity, the final signature of a laser is the Poisson statistics of the emitted photons [4,5].) In recognition of lasers as one of the most important scientific discoveries of the 20<sup>th</sup> century, the Nobel Prize Committee has awarded a significant number prizes for the research leading to the discovery and subsequent development of the theoretical and experimental methods integral to the study of lasers.

The word laser is an acronym that was originally coined by Gordon Gould in his 1959 conference paper titled “The LASER, Light Amplification by Stimulated Emission of Radiation” [6], but is one of the unfortunate misnomers in physics, as lasers do not amplify, instead

they undergo self-oscillation. Amplification requires an initial signal, whereas lasers are remarkable in their ability to spontaneously organize themselves to both produce and amplify their own signals, a process usually termed self-oscillation. This process of self-organization in lasers is mathematically similar to the phenomenon seen in magnetic materials in which the unpaired electron spins throughout the material spontaneously align themselves at low temperatures to produce a net magnetic field, and both phenomena can be described by the Ginzburg-Landau theory of second-order phase transitions [7–10]. However, this analogy should not be pushed too far, as magnetic systems are in a state of equilibrium, while lasers are subject to both pumping and dissipation (as light leaves the cavity), inherently a non-equilibrium state.

The concepts of stimulated emission and spontaneous emission originate from Albert Einstein in 1917 with his derivation of the  $A$  and  $B$  coefficients for emission and absorption of radiation [11]. The first experimental demonstration of a device undergoing self-oscillation and stimulated emission was performed using microwave radiation by Charles Townes and James Gordon [12], coined a maser (microwave amplification by stimulated emission of radiation), but the device was unable to operate continuously as it depleted the gain medium too quickly. The solution to this problem, using a three level gain medium, was suggested by Nikolay Basov and Aleksandr Prokhorov [13], which eventually led to Townes, Basov, and Prokhorov sharing the Nobel Prize in 1964. The first laser operating in the optical regime was built by Theodore Maiman in 1960, using a flashlamp to pump a synthetic ruby crystal [14], and this touched off a strange set of affairs wherein the first working laser was not built by the person who wrote the first paper on lasers, Gould, and neither of them hold the patent for the laser, which is instead held by Townes and Arthur Schawlow under the heading of ‘optical maser.’ For the sake of completeness, it should be mentioned that Gould fought for thirty years through the federal court system with the U.S. Patent Office and was eventually issued patents for many integral components and technologies relating to operating most types of lasers. Finally, the first laser able to generate a continuous wave output, rather than the pulsed output seen in Maiman’s ruby laser, was built later in 1960 by Ali Javan, William R. Bennett, and Donald Herriott, using helium and neon to provide the amplification [15].

The initial state of a laser is devoid of light in the cavity, and with the atoms comprising the two-level gain medium in their ground state. In this state the laser acts as an absorber, as incident light at frequencies close to the atomic transition frequency will excite the atoms, decreasing the field amplitude. As the pump on the gain medium is increased, the steady-state of the system is changed, as gain atoms begin to occupy the excited energy level, decreasing the absorption of the system, until the pump is strong enough that the transparency point is reached where an equal number of atoms reside in both the excited and ground states, resulting in no net absorption or gain in the cavity. As the pump is increased further, the cavity operates as an amplifier, incident light at frequencies close to the atomic transition frequency will be amplified, and in the absence of incident light the cavity will produce amplified spontaneous emission (ASE). Finally, upon reaching a critical value of the pump where the gain balances the losses at the cavity boundary, the first steady-state lasing mode will arise out of the ASE noise background, producing a continuous emission of coherent, monochromatic light. The rate of stimulated emission is dependent upon the local strength of the electric field, thus in the presence of a steady-state lasing signal the stimulated emission rate is spatially non-uniform, following the contours of the intensity of the lasing mode. The treatment of this spatially non-uniform rate of stimulated emission resides at the crux of one of the major difficulties of providing a full treatment of the spatial degrees of freedom of lasers.

All of the properties of a laser, except for those due to the quantum fluctuations, can be described semiclassically, through quantizing the energy levels of the atomic gain medium while treating the electromagnetic field classically. For a two-level atomic gain medium this process results in three non-linearly coupled partial differential equations in space and time, the Maxwell-Bloch equations, comprised of the Bloch equations for the evolution of the atomic polarization and inversion, and Maxwell's wave equation for the electromagnetic field. It is straightforward to generalize these equations to an arbitrary number of atomic levels and lasing transitions. There is universal agreement that these equations contain all of the relevant physics [2, 3, 5, 16], however, given their structure as non-linearly coupled three-dimensional vectorial equations, the direct solution of the Maxwell-Bloch equations is nearly impossible for all but the simplest of systems. The standard approximations used

to analyze these equations begin by removing the spatial degrees of freedom through approximating the lasing modes as the closed cavity modes, and will be discussed further in Sec. 1.4. However, the 1980s saw the development of lasers constructed using semiconductor technology, such as Fabry-Pérot lasers simply using the cleaved facet ends for optical confinement. The reflectivity of these facets due to Fresnel reflection is much lower than the mirrors used in earlier lasers, and this increased open-ness led to the discovery of the Petermann factor which accounts for the increased noise due to the open nature of laser cavities [17]. Furthermore, semiconductor gain media cannot be treated as a two-level gain media, which yields an increased noise spectrum and resulted in the discovery of the Henry  $\alpha$ -factor [18,19]. Subsequently, distributed feedback (DFB) lasers were constructed, which use diffraction gratings at the ends of the cavity that are designed to reflect only a limited part of the spectrum, unlike the broadband mirrors used by Fabry-Pérot cavities, and thus require a more sophisticated treatment of their spatial degrees of freedom [20].

Another decade of development in semiconductor fabrication techniques led to a proliferation in the different types of laser resonators available, such as disks, toroids, and spheres. For these systems, the highly approximate treatment of the spatial degrees of freedom used in the original analytic analyses of the Maxwell-Bloch equations falls apart. The most extreme examples of this are provided by random lasers, which do not have a cavity and have no isolated resonances, yet are still able to lase. This exemplifies the second major obstacle in providing a proper treatment of the spatial degrees of freedom, correctly accounting for the losses across the boundary of the cavity. Additionally, many of these cavities were being constructed on the few- and sub-millimeter scale, which exist in a new, previously unstudied parameter regime where stable multimode laser output is possible. These new devices stimulated theoretical developments in how to model these systems analytically, such as the steady-state *ab initio* laser theory (SALT), originally developed in 2006 by Türeci, Stone, *et al.* as a scattering theory to treat arbitrarily shaped cavities and is able to solve the spatial degrees of freedom of the Maxwell-Bloch equations nearly exactly [21–25].

In this thesis we will be demonstrating how the steady-state *ab initio* laser theory can be used both to gain new fundamental insights into laser physics as well as an efficient tool for the rapid development of novel experimental devices. We will first derive the appropriate

equations to treat realistic and complex gain media with multiple atomic levels, transitions, and gain diffusion within SALT. Next, we will demonstrate how to simultaneously treat injected signals naturally within the SALT framework, showing that the injection-locking transition is caused by gain competition, rather than synchronization as previous theories predicted. SALT is then used to design and optimize a chaotic cavity laser for use as an incoherent light source. Finally, we show how to obtain the quantum limited laser linewidth through considering perturbations of the SALT solution and demonstrate quantitative agreement between this prediction and finite difference time domain simulations of the Maxwell-Bloch equations coupled to Langevin noise sources.

For the sake of completeness, it should be noted that lasers can be operated either in a pulsed or continuous wave (CW) regime. Pulsed operation can be beneficial for many reasons, such as giving sufficient time for heat dissipation from the gain media. However, one important type of pulsed operation is called mode locked lasing, wherein individual Gaussian wave packets of electric field are circulated through the gain medium, and the resulting output has a range of frequencies present depending on the duration of the pulse [2, 26, 27]. This technique is capable of delivering large amounts of energy over extremely short periods of time [1], and is also useful for imaging techniques such as angle-resolved photoemission spectroscopy [28–30]. In contrast, continuous wave lasers emit continuously, allowing the signal to be monochromatic, up to the quantum limited Schawlow-Townes linewidth [31]. In this thesis only continuous wave lasers will be considered.

## 1.1 Basic laser properties

Most lasers are comprised of two main elements, a cavity which serves to confine the light to provide optical feedback, and a gain medium which supplies the amplification using energy drawn from an external pump. An example of this can be seen in Fig. 1.1(a), which shows a simple Fabry-Pérot cavity formed by two parallel mirrors surrounding a gain medium, one of which is partially transmissive, that provide the necessary optical confinement to build up the required electric field for the device to undergo lasing action. The decay rate of the photons in the resonator due to the losses at the boundary can be calculated using

the reflectivity of the partially transmissive mirror,  $R$ , as

$$\gamma_c = \frac{-c}{2nL} \ln(R), \quad (1.1)$$

where  $n$  is the index of refraction of the passive cavity between the two mirrors, assumed here to be a constant,  $L$  is the length of the cavity, and the factor of 2 accounts for the increased effective length of the cavity due to the perfect mirror on one edge [3]. As the cavity is open, the frequencies of the modes of the passive cavity are necessarily complex, and can be written as  $\omega_n - i\gamma_c/2$ , where  $\omega_n$  is the real part of the frequency of the  $n$ th mode. This is used to define the free spectral range of the one-dimensional cavity,  $\Delta$ , which is the distance between the real part of the frequency of two neighboring passive cavity modes, which can also be expressed as

$$\Delta = \frac{\pi c}{nL}. \quad (1.2)$$

The figure of merit for the finesse of a cavity is the Quality ( $Q$ ) factor,

$$Q = \frac{\omega_0}{\gamma_c}, \quad (1.3)$$

which measures how much energy is lost per cycle, with large values corresponding to greater confinement of the light. In general, the greater the  $Q$ -factor of the cavity, the less pump power is required to achieve lasing, but the less output emission is produced [2].

For a particular atom, molecule, artificial atom, or other structure to act as a gain medium, it must be able to build up a population inversion between two energy levels, which for convenience are termed the upper,  $|\varphi_u\rangle$ , and lower,  $|\varphi_l\rangle$ , energy levels [3, 16]. Building a population inversion usually requires the upper state to be long-lived, while electrons in the lower state decay rapidly, so that as the gain medium is pumped more electrons accumulate in the upper state than the lower state. Quantum mechanically, the inversion for a single atom is defined as the difference in the probabilities of the electron occupying the upper state and the lower state,

$$d = \rho_{uu} - \rho_{ll}, \quad (1.4)$$

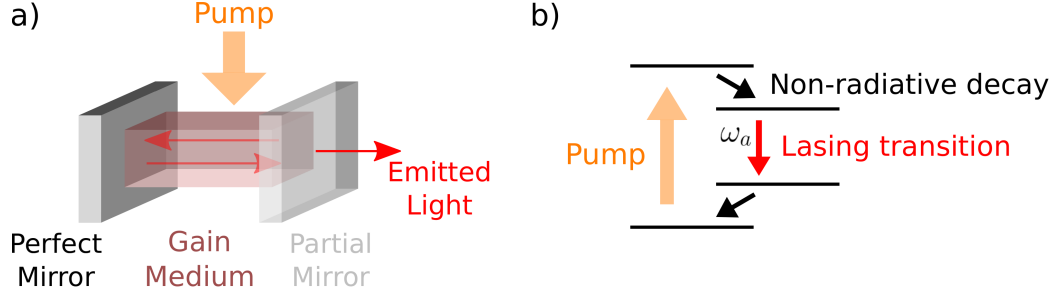


Figure 1.1: (a) Schematic of a simple laser cavity formed by a perfectly reflecting mirror on the left and a partially reflecting mirror on the right. The electric field is shown as red arrows, forming a standing wave between the two mirrors. The gain medium fills the space between the two mirrors and is being pumped from an external source, shown in orange. (b) Schematic of a simple four-level gain medium, where electrons are pumped from the ground state to the top state, then non-radiatively decay to the metastable upper lasing level, before finally undergoing stimulated emission and dropping to the lower lasing level. The energy difference between the two lasing states is labeled as the atomic transition frequency,  $\omega_a$ .

where  $\rho_{ii}$  diagonal element of the density matrix, which is the probability of the electron being in state  $|\varphi_i\rangle$ . The total inversion as a function of position is the classical average of all of the quantum mechanical inversions of each of the atoms at that location,

$$D(x) = \sum_{\alpha} \langle d^{(\alpha)} \rangle \delta(x - x^{(\alpha)}), \quad (1.5)$$

where  $d^{(\alpha)}$  is the inversion of atom  $\alpha$  at location  $x^{(\alpha)}$ , and the summation runs over all of the atoms in the cavity [3]. The dipole moment of the gain atom is defined as,

$$\boldsymbol{\theta}^{(\alpha)} = q \langle \varphi_l | \hat{\mathbf{x}}^{(\alpha)} | \varphi_u \rangle, \quad (1.6)$$

where  $q$  is the charge of the gain carrier, typically an electron, and  $\hat{\mathbf{x}}$  is the quantum mechanical position operator in the direction of the electric field. The collective action of the dipole moments of the gain atoms at a specific location is termed the polarization,  $P_g(x)$  [2]. In this thesis, unless otherwise specified, we will refer to the energy levels and other properties of gain media as atomic levels, or atomic properties, as the exact chemical structure of the gain medium is not relevant for the discussion here. The major exception to this will be semiconductor gain media, which unlike atomic gain media have a continuum of energy states available both in the conduction and valence electron bands, resulting in

phenomena that are not easily seen in atomic or molecular gain media such as the Henry  $\alpha$ -factor [18, 19].

The gain medium filling the cavity in Fig. 1.1(a) is depicted in Fig. 1.1(b), and has four atomic levels, a top state which rapidly decays non-radiatively to the metastable upper lasing state, and the lower lasing level which quickly decays to the ground state. Thus by pumping on the electrons in the ground state, a long-lived population inversion can be achieved between the two lasing states, which are separated in energy by  $\hbar\omega_a$ , and thus can spontaneously emit a photon, or undergo stimulated emission in the presence of an electric field.

## 1.2 Modern laser cavities

As noted above, the proliferation of the shapes and sizes of laser cavities stimulated theoretical developments in how to model these systems analytically, such as SALT. The Fabry-Pérot laser shown in Fig. 1.1 is representative of the earliest lasers developed; however, the advances in materials science and developments in semiconductor fabrication techniques have allowed for a much greater array of cavity shapes to be explored. Important types of modern laser cavities are vertical cavity surface emitting lasers (VCSELs), which can be readily made on a semiconductor wafer and are extremely useful for optical communications [32–34], microdisk and microsphere lasers, which can have extremely large  $Q$  factors [35–39], distributed feedback (DFB) and photonic crystal lasers, which use a Bragg mirror to provide optical confinement [20, 40–47], and random lasers, for which there is no cavity in the usual sense [48–50].

In semiconductor based devices such as VCSELs and microdisk lasers, as well as microsphere lasers, optical confinement is provided by the index of refraction mismatch across the boundaries of the cavity. For cavities with a rectangular geometry, this is termed Fresnel reflection and requires a change in the refractive index at the longitudinal edges of the cavity, along the axis of propagation of the light as seen in Fig. 1.1(a), as well as in the transverse direction, perpendicular to the direction of the light’s travel. Confinement in the transverse direction can be seen in Fig. 1.2(a) which shows the cleaved facet of a dry-

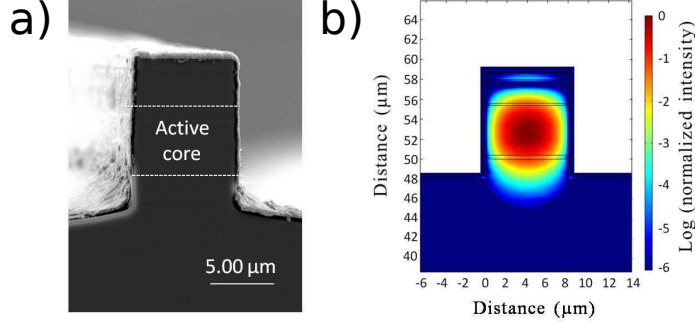


Figure 1.2: (a) A cleaved facet of a dry-etched Quantum Cascade ridge waveguide made of alternating layers of  $\text{In}_{0.52}\text{Al}_{0.48}\text{As}$  and  $\text{In}_{0.53}\text{Ga}_{0.47}\text{As}$  [51], which has an effective index of refraction of  $n \approx 3.25$  [52], constructed on  $\text{SiO}_2$ ,  $8\mu\text{m}$  in width, in which the gain medium is made of quantum cascade layers. (b) Numerical simulations of the transverse direction of such a ridge waveguide performed using COMSOL [53].

etched Quantum Cascade ridge waveguide made of alternating layers of  $\text{In}_{0.52}\text{Al}_{0.48}\text{As}$  and  $\text{In}_{0.53}\text{Ga}_{0.47}\text{As}$  [51], which has an effective index of refraction of  $n \approx 3.25$  [52], constructed on an insulating layer of  $\text{SiO}_2$ , which has a refractive index of  $n = 1.82$ , and is  $8\mu\text{m}$  in width [53]. The optical confinement is demonstrated in Fig. 1.2(b) which shows a numerical simulation using COMSOL of the transverse field profile for such a ridge waveguide. While many transverse field profiles are possible in such structures, usually only the lowest order transverse mode is seen as it best utilizes the gain medium. This is what is referred to when discussing one-dimensional cavities, the field is confined to a single mode in the transverse direction, thus the only degree of freedom available to it is in the longitudinal direction.

Optical confinement for microdisk, shown in Fig. 1.3(a), and microsphere lasers is greatly enhanced beyond what is possible with Fresnel reflection, resulting in very little radiated light [35–37]. The modes that take the greatest advantage of this phenomena are termed ‘whispering gallery’ modes, after a similar phenomena which occurs with acoustic waves traveling along the edge of a circular room [54]. Using this principle, such devices are able to support these high- $Q$  modes even at small cavity sizes only a few microns in diameter, greatly reducing the necessary input power to make such devices lase. Due to the spherical symmetry of microdisk and microsphere lasers, all of the modes supported by these devices are circulating modes, with no variation in the azimuthal direction. An important

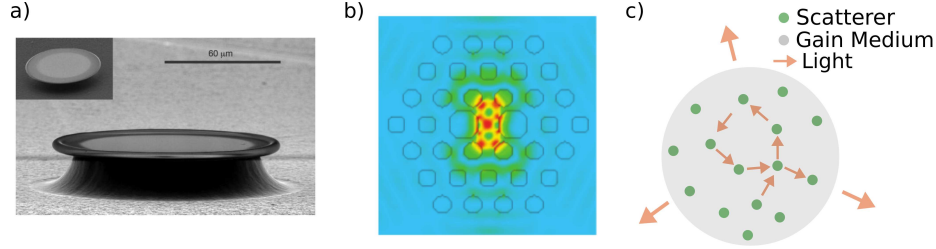


Figure 1.3: (a) Toroidal microresonator with an intrinsic  $Q = 1.00 \times 10^8$  [39]. (b) Plot of the electric field profile of a two-dimensional slice of a defect photonic crystal. Regions with a different dielectric constant are denoted with black lines [41]. (c) Diagram of a random laser indicating localized scatterers embedded in a gain medium with negligible index of refraction. Arrows inside of the gain region show one possible path for coherent scattering of light leading to a lasing mode.

consequence of this is that the emissions from these devices are also azimuthally symmetric, with a radially decreasing intensity characteristic of all such waves in multiple dimensions. Thus, in experiments, these cavities are typically coupled to a nearby waveguide or fiber optic to extract light [55–58]. Another consequence of having high- $Q$  circulating modes is that it is very difficult to achieve multimode lasing due to their increased spatial overlap when compared with standing modes [59]. Breaking the cylindrical symmetry of a cavity removes both of these features. Small breaking of the cavity symmetry forces the formation of standing wave rather than running modes, thus increasing the likelihood of multimode operation, and possibly resulting in directional emission, depending on the strength of the symmetry breaking. However, larger amounts of symmetry breaking lead to an entirely new regime where the ray dynamics of the closed cavity are chaotic and the modes must be solved for directly and cannot be calculated using other analytic methods such as perturbation theory [60–64]. We refer to such resonators as chaotic cavities, but note that these cavities are no more or less likely to exhibit chaotic dynamics in their temporal behavior, as despite their similar sounding names these two effects are completely unrelated. We will discuss an application of such chaotic cavities in Ch. 5.

DFB lasers are unique among the laser cavities discussed so far in that the Bragg mirrors used to provide optical confinement are not broadband, and instead operate only over a small range of frequencies [20]. This provides a mechanism for controlling the frequency of the laser emission. Photonic crystals take this concept one step further, embedding a cavity

in a two- or three-dimensional lattice of materials with differing dielectric constants [40]. This results in a stratification of the allowed frequencies within the photonic crystal nearly identical to the band structure present in the allowed energy levels of electrons in crystal lattices. The most common way to construct a laser using photonic crystals is to create a defect within the photonic crystal lattice, which results in a localized mode, shown in Fig. 1.3(b). Due to the lack of available states in bulk photonic crystal, the light is trapped at the defect location, resulting in high finesse cavities [41–47].

In stark contrast to the excellent optical confinement provided by microdisk resonators are random lasers, which do not have a cavity in the conventional sense, and are constructed of scatterers which either provide gain or are embedded in a gain medium as depicted in Fig. 1.3(c). Nevertheless, disordered systems made of a variety of different materials have all been found to exhibit lasing, demonstrating the universality of the random lasing phenomenon [65–71]. Disordered systems such as random lasers are characterized by their transport mean free path,  $l_{tr}$ , which is the average distance that light travels before its propagation direction is randomized [50, 72]. The transport mean free path for the dielectric scatterers with radius less than the wavelength of the lasing light,  $R_s < \lambda$ , we are considering is equal to the scattering mean free path,  $l_{tr} = l_s$ , the average distance light travels between two consecutive scattering events. This leads to three qualitatively distinct types of random lasers depending on the system size  $L$ , the ballistic regime,  $L \leq l_{tr}$ , the diffusive regime,  $L \gg l_{tr} \gg \lambda$ , and the localized regime,  $kl_{tr} \simeq 1$ , where  $k$  is the wave vector of the laser light. The division between these regimes can also be characterized in terms of the Thouless number,

$$\delta = \frac{\langle \gamma_c \rangle}{\Delta}, \quad (1.7)$$

where  $\langle \gamma_c \rangle$  is the average decay rate, or width, of the passive cavity modes of the random laser, and  $\Delta$  is the free spectral range. In the diffusive regime modes overlap,  $\delta > 1$ , whereas in the localized regime modes are well separated,  $\delta < 1$ .

### 1.3 Types of gain media

The gain medium shown in Fig. 1.1(b) is only representative of the general structure of the relevant atomic levels to a laser. The actual structure for a real gain medium is usually more complex, as can be seen in Fig. 1.4 for a helium-neon laser, in which electrons ejected from a cathode collide with ground state helium atoms, exciting them. These excited helium atoms then impart their energy to the neon atoms by colliding with them, where finally the excited neon atoms are able to undergo a variety of lasing transitions to return to the ground state [73]. The atomic level diagrams are similarly complicated for ruby [74], neodymium-doped yttrium aluminum garnet  $\text{Nd:Y}_3\text{Al}_5\text{O}_{12}$  (Nd:YAG) [20], carbon dioxide [75], and organic dye molecules, the most common of which are now Rhodamine 6G and Rhodamine B [76–84]. The situation is no different for gain media constructed out of artificial atoms. Quantum well lasers are semiconductor diode lasers in which the active region is engineered to be thin enough that quantum confinement in one dimension occurs, stratifying the continuum of available energy states [20, 85, 86]. Quantum dot lasers are constructed to force quantum confinement to occur in all three dimensions, creating an artificial atom with discrete energy levels [87–90]. Finally, quantum cascade lasers are made of a periodic structure of thin layers with varying material composition, forming a superlattice, which introduces a varying electric potential across the device, similar to a quantum well laser. However, unlike quantum well lasers, upon undergoing a lasing transition the electron does not recombine with a hole, and instead non-radiatively decays to the next metastable layer to undergo lasing action again. Thus, for each electron injected into the device, multiple photons can be produced [91–93].

Most of the complexity of these diagrams stems from atomic levels which quickly decay non-radiatively, while there is only a single pair of levels capable of undergoing lasing action. If the decay rates between atomic levels,  $\gamma_{ij}$  (decay from level  $|\varphi_j\rangle$  to level  $|\varphi_i\rangle$ ), are much faster than the decay rate between the upper lasing level and the lower lasing level,  $\gamma_{ij} \gg \gamma_{lu}$ , and much faster than the dephasing rate of the lasing transition,  $\gamma_{ij} \gg \gamma_{\perp}$ , then dynamics associated with the atomic level can be adiabatically eliminated, and the effects of having such a level can be renormalized into the remainder of the rates of the

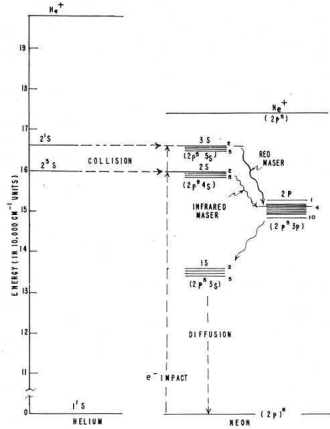


Figure 1.4: Schematic of the energy levels and decay channels for a helium-neon laser [73].

system [94–98]. Based on the relative magnitudes of these decay rates, as well as the cavity decay rate  $\gamma_c$ , lasers can be categorized into one of three types [99–101]. Class A lasers are those for which both the polarization and the inversion decay much faster than the cavity,  $\gamma_c \ll \gamma_{\parallel} \ll \gamma_{\perp}$ , where  $\gamma_{\parallel}$  is the renormalized decay rate of the inversion. In class A lasers the dynamics of both the polarization and the inversion can be adiabatically eliminated and the system has only a single independent field, the electric field. In class B lasers, the polarization still decays quickly, but the inversion and cavity decay rates are of similar magnitude,  $\gamma_c \sim \gamma_{\parallel} \ll \gamma_{\perp}$ , and as such only the polarization can be eliminated, resulting in two relevant fields. Finally, for class C lasers, all of the time scales are of similar order,  $\gamma_c \sim \gamma_{\parallel} \sim \gamma_{\perp}$ , and the dynamics of all three fields must be considered. Most lasers are either class A, such as atomic gas lasers (helium-neon, argon, krypton) and dye lasers, or class B, such as ruby, neodymium, carbon dioxide, and most solid state devices [99, 101]. Thus, even though the actual structure of the atomic energy levels can be quite complicated for most of these gain media, one is usually able to renormalize all of this complexity into just a pair of energy levels for the upper and lower lasing states [98].

Semiconductor gain media are quite different from the other gain media discussed so far though, as the upper lasing state is effectively smeared out over the entire conduction band, as is the lower lasing state over the valence band, as in both bands there is a continuum of energy levels available to the electrons and holes rather than the discrete energy levels of atomic gain media [90, 101–104]. This also means that there is not a single central atomic

transition frequency, but instead that the gain curve is asymmetric, with more gain existing above the band gap edge than below it. The asymmetric gain curve also enhances the noise properties of the resulting laser [18, 19]. Lasers made using a semiconductor gain medium were first constructed in 1962, and have represented a huge advancement for the field of laser physics as fabrication techniques improved, and could make use of technology being developed for consumer electronics [105–107]. These experimental methods have allowed for the development of quantum well, quantum dot, and quantum cascade lasers already discussed, as well as many novel cavity designs discussed in the previous section.

## 1.4 Derivation of the Maxwell-Bloch equations

The goal of a laser theory is to give a complete description of the photons, gain material, and the interactions between them, as well as a treatment of the loss of light through the edges of the cavity. Within the cavity, the interaction between the gain medium and the electromagnetic field is well understood as it conserves the total energy of the system and can be expressed as a simple Hamiltonian [4]. However, without providing a full treatment of the world outside of the laser cavity, the loss of energy through the boundary of the cavity is inherently non-Hermitian, making the theoretical analysis of this effect more difficult [108–111]. As such, it is useful to begin by understanding the light-matter interactions, where we will treat the electromagnetic field semiclassically, removing the difficulties associated with the quantization of the electromagnetic field in an open cavity. In doing so, we neglect the quantum fluctuations inherent to the electromagnetic field, preventing the study of the noise properties of the field. The equation of motion for the electromagnetic field is given by Maxwell’s wave equation [112],

$$\left[ \nabla \times \nabla \times - \frac{\varepsilon_c(\mathbf{x})}{c^2} \partial_t^2 \right] \mathbf{E}(\mathbf{x}, t) = \frac{4\pi}{c^2} \partial_t^2 \mathbf{P}_g(\mathbf{x}, t), \quad (1.8)$$

where the effect of the passive cavity is described by the linear cavity dielectric function,  $\varepsilon_c(\mathbf{x})$ , which in general can vary in space and frequency, and is a tensor quantity. However, the frequency response of the passive medium usually varies only weakly over the frequency

range of interest for lasing action and can thus be neglected. Furthermore, anisotropic dielectric materials are rare, and of these media, the dielectric tensor is usually still diagonal, as is the case for birefringent and uniaxial materials. The amplifying response of the gain medium is described by the non-linear gain polarization,  $\mathbf{P}_g$ , which acts as a source for this equation and includes contributions from all of the lasing transitions of every gain atom in the cavity.

The non-interacting Hamiltonian for a single electron of a gain atom  $\alpha$  can be written as

$$H_0^{(\alpha)} = \frac{\hat{\mathbf{p}}^{(\alpha)2}}{2m} + V^{(\alpha)}(\hat{\mathbf{x}}^{(\alpha)}), \quad (1.9)$$

$$H_0^{(\alpha)}|\varphi_n^{(\alpha)}\rangle = E_n^{(\alpha)}|\varphi_n^{(\alpha)}\rangle, \quad (1.10)$$

where  $\hat{\mathbf{p}}^{(\alpha)}$  is the momentum operator for the electron,  $m$  is the mass of the electron,  $V^{(\alpha)}$  is the potential energy of the electron as a function of its position  $\hat{\mathbf{x}}^{(\alpha)}$ , and  $|\varphi_j^{(\alpha)}\rangle$  is the wave function of the electron in the  $j$ th atomic energy level with corresponding energy  $E_j^{(\alpha)}$ . However, for a charged particle in an external electromagnetic field, the single particle Hamiltonian must be altered to include the effects of the field,

$$H^{(\alpha)} = \frac{(\hat{\mathbf{p}}^{(\alpha)} - \frac{e}{c}\mathbf{A})^2}{2m} + q^{(\alpha)}\phi + V^{(\alpha)}(\hat{\mathbf{x}}^{(\alpha)}), \quad (1.11)$$

where  $\mathbf{A}$  is the vector potential and  $\phi$  is the electric potential. For a traveling wave with frequency  $\omega$  inside of a laser cavity,  $\phi = 0$ . Thus the full single particle Hamiltonian can be decomposed into interacting and non-interacting components,

$$H^{(\alpha)} = H_0^{(\alpha)} - \frac{e}{mc}\hat{\mathbf{p}}^{(\alpha)} \cdot \mathbf{A} + \frac{e^2}{2mc^2}\mathbf{A}^2, \quad (1.12)$$

where  $\mathbf{A} \cdot \hat{\mathbf{p}} = \hat{\mathbf{p}} \cdot \mathbf{A}$  as we have chosen the Coulomb gauge,  $\nabla \cdot \mathbf{A} = 0$ . In general, terms proportional to  $\mathbf{A}^2$  correspond to photons interacting with other photons directly, a phenomenon which is quite weak [4], and as such, we will neglect this term. The interaction term can be further simplified by noting that the expectation value of the electron's mo-

mentum can be related to its position and the energy difference between the two states,

$$\begin{aligned}\langle \varphi_u^{(\alpha)} | \hat{\mathbf{p}}^{(\alpha)} | \varphi_l^{(\alpha)} \rangle &= \frac{im}{\hbar} \langle \varphi_u^{(\alpha)} | [H_0, \hat{\mathbf{x}}^{(\alpha)}] | \varphi_l^{(\alpha)} \rangle \\ &= \frac{im}{\hbar} (E_u - E_l) \langle \varphi_u^{(\alpha)} | \hat{\mathbf{x}}^{(\alpha)} | \varphi_l^{(\alpha)} \rangle,\end{aligned}\quad (1.13)$$

where the indices  $u$  and  $l$  refer to the upper and lower atomic energy levels of the lasing transition,  $\hbar\omega_a = E_u - E_l$ . While the time dependence in Eq. (1.13) has been suppressed, this term oscillates as  $e^{i\omega_a t}$ , and thus only strongly couples to the positive frequency portion of the vector potential,  $\mathbf{A}^+$  [113]. This is the commonly made rotating wave approximation (RWA), and corresponds to neglecting processes that undergo fast oscillations. Furthermore, the oscillation frequency can be combined with the vector potential to re-express the interacting Hamiltonian in terms of the electric field,

$$\mathbf{E}^+ = -\frac{1}{c} \partial_t \mathbf{A}^+ = \frac{i\omega_a}{c} \mathbf{A}^+, \quad (1.14)$$

resulting in

$$H_I = e \hat{\mathbf{x}} \cdot \mathbf{E}. \quad (1.15)$$

The effect of the gain atoms upon the electric field is contained in the source term in Eq. (1.8), which can now be defined as

$$\mathbf{P}_g(\mathbf{x}, t) = - \sum_{\alpha} \delta(\mathbf{x} - \mathbf{x}^{(\alpha)}) \text{Tr}[\hat{\rho}^{(\alpha)} e \hat{\mathbf{x}}^{(\alpha)}], \quad (1.16)$$

where the  $M \times M$  density matrix of atom  $\alpha$  is denoted by  $\hat{\rho}^{(\alpha)}$ , where  $M$  is the number of atomic levels involved in the lasing process. Among the  $M$  levels a subset of them will contribute to lasing and support lasing transitions; the others will simply be part of the downward cascade of electronic excitations involved in the pumping and emission in steady-state. These pairs have a dipole moment,

$$\boldsymbol{\theta}_{nm}^{(\alpha)} = e \langle \varphi_n | \hat{\mathbf{x}}^{(\alpha)} | \varphi_m \rangle. \quad (1.17)$$

The dipole moment is always zero for  $n = m$  due to spatial symmetry. By assuming that the full polarization can be expressed in term of the density matrix for individual atoms, we are ignoring interatomic coherence effects which are quite small for conventional lasers (but not e.g. for polariton lasers).

To complete the semiclassical lasing equations, one must consider the quantum equations of motion for the average polarization of the gain medium. At this point it will be useful to simplify our analysis to distinguishable but otherwise identical two-level gain atoms with a single lasing transition, so that the evolution of the positive frequency portion of the total polarization of the gain medium,  $\mathbf{P}_g = 2\text{Re}[\mathbf{P}_g^+]$ , can be written as

$$\partial_t \mathbf{P}_g^+(\mathbf{x}, t) = -N(\mathbf{x}) \partial_t (\rho_{21}) \boldsymbol{\theta}_{12}, \quad (1.18)$$

where we initially assume a fixed density of gain atoms  $N(\mathbf{x})$ . The evolution of the off-diagonal density matrix element can be found from the Heisenberg equation of motion,

$$\partial_t \rho_{21} = \frac{-i}{\hbar} \langle \varphi_2 | [H_0 + H_I, \hat{\rho}] | \varphi_1 \rangle \quad (1.19)$$

$$= -(\gamma_{\perp} + i\omega_a) \rho_{21} + \frac{i}{\hbar} (\rho_{22} - \rho_{11}) \boldsymbol{\theta}_{21} \cdot \mathbf{E}(\mathbf{x}, t), \quad (1.20)$$

where we have now added the effect of environmental dephasing on the gain atoms in the standard manner in terms of a transverse relaxation/dephasing rate  $\gamma_{\perp, nm}$  and identified the atomic transition frequency as  $\omega_a = \omega_{21}$ . Note that when deriving Eq. (1.20) the dipole approximation has been used, which states that the electric field does not change much on the length scale of the atom, and thus can be approximated as a constant in

$$\langle \varphi_2 | \hat{\mathbf{x}} \cdot \mathbf{E}(\hat{\mathbf{x}}) | \varphi_1 \rangle \approx \langle \varphi_2 | \hat{\mathbf{x}} | \varphi_1 \rangle \cdot \mathbf{E}(\mathbf{x}), \quad (1.21)$$

where the electric field is now evaluated at the average position of the electron of the atom. This allows for the evolution of the total polarization to be written as

$$\partial_t \mathbf{P}_g^+(\mathbf{x}, t) = -(\gamma_{\perp} + i\omega_a) \mathbf{P}_g^+ - \frac{id}{\hbar} (\boldsymbol{\theta} \cdot \mathbf{E}) \boldsymbol{\theta}^*, \quad (1.22)$$

in which the inversion of the atomic gain medium is defined as  $d = N(x)(\rho_{22} - \rho_{11})$ , and the subscripts on the dipole matrix element have been dropped. Similarly, the equation of motion for the inversion can also be derived from the Heisenberg equation of motion,

$$\partial_t \rho_{22} = -\frac{i}{\hbar} (\boldsymbol{\theta}_{21} \rho_{12} - \rho_{21} \boldsymbol{\theta}_{12}) \cdot \mathbf{E}(\mathbf{x}, t), \quad (1.23)$$

along with an analogous equation for  $\partial_t \rho_{11}$ , resulting in

$$\partial_t d(\mathbf{x}, t) = -\gamma_{\parallel} (d - d_0(\mathbf{x})) - \frac{2}{i\hbar} (\mathbf{P}_g^- - \mathbf{P}_g^+) \cdot \mathbf{E}, \quad (1.24)$$

where we have again included the effects of relaxation due to the ambient environment as  $\gamma_{\parallel}$ , and  $d_0(x)$  is the inversion in the absence of an electric field and plays the role of the pump in this theory.

Thus, the full set of semiclassical lasing equations which represent the fundamental theory and comprise all of the relevant physics for lasers, and which for the two-level gain medium are termed the Maxwell-Bloch equations, are given by Eqs. (1.8), (1.22), and (1.24). These equations represent a coupled set of partial differential equations for the electric field, atomic polarization, and atomic inversion in both space and time. It should be noted that there are many similar derivations that lead to these same equations, with starting points in quantizing both the electromagnetic fields and the atomic levels [4], or starting from a purely classical picture and treating the response of the atom to the electric field as a dipole [16]. One extremely important point about these equations is that the coupling between the electric field and the gain atoms is strong, which prevents the general solution to the fully quantum theory of lasers from being approximated by perturbation theory techniques, and greatly restricts the regime of validity for typical simple approximations of the semiclassical equations [3].

#### 1.4.1 Standard approximations

Within the semiclassical picture of the Maxwell-Bloch equations the usual way of treating the cavity boundary is through the slowly varying envelope approximation (SVEA) [3]. To

use this, one divides the electric field into its spatial profile,  $\mathbf{u}(\mathbf{x})$  which is time-independent, and its time varying amplitude,  $E_0(t)e^{-i\omega t}$ ,

$$\mathbf{E}(\mathbf{x}, t) = E_0(t)\mathbf{u}(\mathbf{x})e^{-i\omega t}, \quad (1.25)$$

in which the spatial derivatives of the spatial profile are known,

$$\nabla \times \nabla \times \mathbf{u}(\mathbf{x}) = \mathbf{k}^2 \mathbf{u}(\mathbf{x}), \quad (1.26)$$

where  $\mathbf{k}^2 = \varepsilon_c \omega^2 / c^2$  is the wave vector, and we are assuming that the dielectric function within the cavity is a constant such that  $\nabla \cdot \mathbf{E} = 0$ . Note that by choosing  $k \in \mathbb{R}$  for  $\varepsilon_c \in \mathbb{R}$ , we are implicitly claiming that  $\mathbf{u}(\mathbf{x})$  is a closed cavity mode and this will force us to account for the losses at the boundary of the cavity elsewhere. Treating the modes of the cavity as closed cavity modes constitutes the standard modal approximation. While this technique is applicable in all dimensions, the SVEA has typically been coupled with the paraxial approximation, yielding Laguerre-Gaussian and Hermite-Gaussian modes [114].

The SVEA claims that the temporal variation of the electric field envelope,  $E_0(t)$  is much slower than the fast oscillations at the lasing frequency, so that  $\partial_t^2 E_0(t) \approx 0$ . This allows for the wave equation, Eq. (1.8), to be rewritten as

$$\left[ -\mathbf{k}^2 E_0 + \frac{\varepsilon_c \omega^2}{c^2} E_0 - \frac{2i\varepsilon_c \omega}{c^2} \partial_t E_0 - \frac{\varepsilon_c}{c^2} \partial_t^2 E_0 \right] \mathbf{u}(\mathbf{x}) e^{-i\omega t} = -\frac{4\pi\omega^2}{c^2} P_0(t) \mathbf{u}(\mathbf{x}) e^{-i\omega t}, \quad (1.27)$$

where a similar approximation has been used on the total atomic polarization which is assumed to have the same spatial profile as the electric field. Rearranging this leads to the envelope evolution equation,

$$\partial_t E_0 = -\kappa E_0 + \frac{2\pi i \omega}{\varepsilon_c} P_0(t), \quad (1.28)$$

where the field decay rate,  $\kappa = \gamma_c/2$ , has been added as a phenomenological term and represents the loss of the electromagnetic field either through intrinsic losses due to the passive cavity medium, or the escape of the field through the edges of the cavity. In some

texts,  $\kappa$  is introduced via relating it to the conductivity of the medium,  $\sigma$ , as this can be a source of loss for the electromagnetic field [3]. While this is technically true, this definition misses the broader point that even for a non-conducting medium,  $\kappa \neq 0$ , as for a laser to emit light, the cavity must have an opening, which leads to losses from the cavity due to imperfect reflection at that boundary.

A substantially more rigorous treatment of the losses at the cavity boundary, while still using the closed cavity modes, was performed by Spencer and Lamb in 1972 [115], which treats the open boundary of the cavity as a  $\delta$ -function and relates the cavity decay rate to its strength. However, studies in treating the inherent open boundary of arbitrarily shaped cavities analytically were not attempted until the development of the steady-state *ab initio* laser theory, which is discussed in Ch. 2.

#### 1.4.2 Finite difference time domain simulations

In lieu of further analytic treatments of the open cavity, many studies have been performed using numerical methods which treat the cavity boundary exactly but prohibit further analytic analysis. The primary algorithm for this is termed the finite difference time domain (FDTD) algorithm, which was originally proposed by Yee in 1966 [116], but was not feasible for use until computer technology advanced another few decades [117]. The purpose of the FDTD algorithm, given explicitly in Appendix A, is to directly integrate, in space and time, the Maxwell-Bloch equations until a steady-state solution is found. This method uses only the rotating wave approximation, which is well understood and ubiquitous in laser physics. Thus, essentially exact steady-state solutions of a laser system, if they exist, can be found using this method. Furthermore, any solutions found using other approximations can be verified through this direct calculation.

There are a few major drawbacks to the FDTD algorithm. First, it is extremely computationally expensive, as it requires directly simulating the electric, magnetic, and atomic field at every pixel within the discretized cavity, for every time step. Second, due to its brute force nature, very little analytic analysis can be performed using this method. Additionally, there is no test to confirm whether convergence of the FDTD algorithm has actually been achieved. In practice, one typically runs the simulation for an order of magnitude or two

longer than the largest time scale in the system,  $T_1 = 1/\gamma_{\parallel}$ , but this is no guarantee of the stability of the final solution. Finally, there is no way to extract information about the modes below threshold, preventing one from determining when subsequent lasing modes will reach threshold. In this thesis we will use the FDTD method to confirm that the SALT solution for a laser system is correct, and that the steady-state approximation used in deriving the SALT solution results in an accurate portrayal of the actual system. In our experience, knowledge of the SALT solution is of great use in determining whether the FDTD simulation has converged, and in debugging the FDTD algorithm.

## 1.5 Overview of this thesis

In this thesis we will be using and expanding upon the steady state *ab initio* laser theory (SALT), originally developed by Türeci, Stone, and Ge [21–25, 97], to study complex laser systems. SALT addresses all of the difficulties discussed above; it is able to treat the open boundary(s) of the laser cavity exactly, yield analytic insight into the underlying physics, and is more computationally efficient than FDTD simulations.

A full introduction to SALT is given in Ch. 2, in which the self-consistent, coupled lasing mode equation is derived for a two-level atomic gain medium. Here the stationary inversion approximation (SIA) will also be introduced, and its regime of validity is determined. We then discuss the expansion of the lasing mode solutions to the SALT equations in terms of both the threshold constant flux (TCF) basis states [25] and the position space basis used in more recent solution techniques [118]. The lasing map for the TCF solution is then derived and its numerical implementation and Jacobian are then given. Finally, a method for using SALT to simulate high- $Q$  cavities is examined through the implementation of a partially reflecting mirror.

The generalization of SALT to treat complex gain media (C-SALT) is given in Ch. 3. First, the renormalization of an arbitrary number of atomic levels with a single lasing transition to a two-level atomic system is derived and agreement between SALT and FDTD simulations is shown [98]. Next, the general solution method for an atomic gain medium with any number of levels and lasing transitions is given, including a treatment of diffusion [119].

Without diffusion, agreement is again shown between C-SALT and FDTD simulations. With diffusion, the transition between multimode lasing (low diffusion) and gain clamped, single-mode lasing is elucidated. Finally, a preliminary treatment of semiconductor lasers is given, including results demonstrating the shift in the lasing frequency due to Pauli blocking.

Ch. 4 demonstrates how to treat injected signals into a laser cavity within the SALT framework (I-SALT) [120]. The Adler theory for injected signals is discussed [115,121], and I-SALT is shown to reduce to the Adler equations in the single pole approximation. The Adler theory's prediction that the frequency of the lasing mode shifts towards that of the injected signal is also examined [2]. This prediction is then compared with both I-SALT and FDTD simulations and found to be incorrect in some cases. The case of partially-locked lasing is also discussed, i.e., when two lasing modes are active and the injected signal suppresses one of the signals, but not the second. Finally, an initial linear stability analysis for SALT is given.

In Ch. 5 we use SALT to optimize a chaotic cavity for producing spatially incoherent light. To generate incoherent light using a laser, the laser must be operating in the deep multimode regime such that there are enough active modes to effectively suppress the speckle that would be seen for just a single lasing mode. Reaching the deep multimode regime is shown to require two different properties, first that the cavity has a relatively uniform distribution of  $Q$ -factors, and second that the effects of gain competition do not prevent many of these modes from reaching threshold. We demonstrate here that a chaotic, D-shaped cavity satisfies both of these criteria, and a laser system using this cavity is subsequently experimentally verified to produce incoherent light [122]. Finally, in this section we also demonstrate the excellent agreement between full SALT simulations, using the single pole approximation of SALT, and the single pole approximation of SALT using spatial mode profiles, modal frequencies, and modal decay rates calculated using COMSOL Multiphysics.

Ch. 6 demonstrates how to use the SALT solutions to calculate the quantum limited laser linewidths due to phase fluctuations [123]. This theory contains the Schawlow-Townes linewidth formula and all known corrections to it, but demonstrates that these effects are

fundamentally intertwined, and can only be separated in certain limits. This macroscopic derivation is then found to be in agreement with a microscopic theory in which each individual gain atom is assumed to be coupled to an independent reservoir. Finally, we perform FDTD simulations coupled to Langevin noise sources for the gain medium using such a microscopic model and demonstrate quantitative agreement with the theoretical prediction [124].

## Chapter 2

# The steady-state *ab initio* laser theory

The steady-state *ab initio* laser theory (SALT) is a recently developed method of overcoming the theoretical challenges raised in Ch. 1 by formulating the semiclassical lasing equations, Eqs. (1.8), (1.22), and (1.24), for arbitrary geometry and assuming that the electric field can be decomposed into countably many constituent frequencies associated with lasing modes. It was developed by Türeci, Stone, and Ge to obtain directly the steady state solutions for complex laser systems without time integration [21–23, 25], and instead operates in the frequency domain, where it is able to solve very accurately for all of the semiclassical properties of a laser, including the modal thresholds, frequencies, and output intensity as a function of the pump. SALT employs only two approximations, the commonly made rotating wave approximation (RWA), and in the multimode regime, the less traditional stationary inversion approximation (SIA), which is only true for multimode lasing in microlasers and will be discussed further in Sec. 2.2. The SALT equations are frequency domain wave equations for the lasing modes, coupled non-linearly through the spatially varying cross gain saturation. These equations can be solved efficiently numerically for the steady-state properties of laser cavities of arbitrary complexity, in any number of dimensions; the numerical methods of solution will be detailed in Sec. 2.1.1. This approach allows a more rigorous understanding of the lasing solutions than is possible with previous theories

for cavities with a complex or random internal structure, and has already led to a number of new discoveries, such as mode frustration in partially pumped cavities [125], control of emission properties of random lasers through selective pumping [126–130], and a more general form of the Schawlow-Townes linewidth formula [131, 132]. For single transition gain media without diffusion, SALT has also been shown to give excellent agreement with FDTD simulations at a substantially reduced computational cost, as will be discussed in Sec. 2.2 [24, 98].

## 2.1 Derivation of SALT

To derive the SALT equations, we begin with the Maxwell-Bloch equations, Eqs. (1.8), (1.22), and (1.24), and make a multimode ansatz, stating that the electric field and polarization can be broken up into  $N_L$  modes with distinct frequencies representing each lasing mode,

$$\mathbf{E}^+(x, t) = \sum_{\mu}^{N_L} \Psi_{\mu}(x) e^{-i\omega_{\mu}t} \quad (2.1)$$

$$\mathbf{P}_g^+(x, t) = \sum_{\mu}^{N_L} \mathbf{p}_{\mu}(x) e^{-i\omega_{\mu}t} \quad (2.2)$$

where the plus superscript denotes the positive frequency component of the field,  $\mathbf{E} = 2\text{Re}[\mathbf{E}^+]$ , and  $\Psi_{\mu}(x)$  and  $\mathbf{p}_{\mu}(x)$  are the spatial profiles of the electric field and corresponding polarization of the lasing mode with frequency  $\omega_{\mu}$ . The multimode ansatz allows us to match frequency components of the electric and polarization fields through Eq. (1.22),

$$\mathbf{p}_{\mu} = \frac{\boldsymbol{\theta}^*}{\hbar} \frac{d}{\omega_{\mu} - \omega_a + i\gamma_{\perp}} (\Psi_{\mu} \cdot \boldsymbol{\theta}). \quad (2.3)$$

We now simplify our analysis by treating slab or two-dimensional geometries for which the electric fields in the transverse magnetic (TM) modes, can be taken to be a scalar,  $\mathbf{E} \rightarrow E$ ), noting that the treatment discussed here is still completely applicable in geometries for which the fields must be treated as vectors [118]. Inserting Eq. (2.3) into Eq. (1.24)

results in,

$$\begin{aligned} \partial_t d = & -\gamma_{\parallel}(d - d_0) - \frac{4|\theta|^2 d}{\hbar^2} \left( \sum_{\mu}^{N_L} \frac{\gamma_{\perp}}{(\omega_{\mu} - \omega_a)^2 + \gamma_{\perp}^2} |\Psi_{\mu}(x)|^2 + \right. \\ & \left. \sum_{\mu > \nu}^{N_L} \operatorname{Re} \left[ \frac{(2\gamma_{\perp} - i(\omega_{\nu} - \omega_{\mu})) \Psi_{\mu}(x) \Psi_{\nu}^*(x)}{(\gamma_{\perp} + i(\omega_{\nu} - \omega_a))(\gamma_{\perp} - i(\omega_{\mu} - \omega_a))} e^{i(\omega_{\nu} - \omega_{\mu})t} \right] \right), \end{aligned} \quad (2.4)$$

where now the motivation for the SIA is clear. In using the SIA,  $\partial_t d = 0$ , the modal beating terms on the right-hand side of the equation are neglected. This assumption requires that the dynamics caused by these beating terms, whose frequency is of the order of the free spectral range,  $\Delta$ , must be fast when compared with the relaxation rate of the inversion, such that the inversion only experiences the time average of these terms, which is zero. This allows us to directly solve for the inversion as a function of the modal intensities,

$$d(x) = \frac{d_0(x)}{1 + \frac{4|\theta|^2}{\hbar^2 \gamma_{\perp} \gamma_{\parallel}} \sum_{\nu}^{N_L} \Gamma_{\nu} |\Psi_{\nu}(x)|^2}, \quad (2.5)$$

where  $\Gamma_{\nu} = \gamma_{\perp}^2 / ((\omega_{\nu} - \omega_a)^2 + \gamma_{\perp}^2)$  is the homogeneously broadened gain curve. This equation suggests a natural scaling for the electric field,  $E_{\text{SALT}} = 2|\theta| / (\hbar \sqrt{\gamma_{\perp} \gamma_{\parallel}}) E$ . Inserting Eqs. (2.5) and (2.3) back into the wave equation, we recover the SALT equations,

$$0 = [\nabla^2 + (\varepsilon_c(x) + 4\pi\chi_g(x, \omega_{\mu})) k_{\mu}^2] \Psi_{\mu}(x), \quad (2.6)$$

$$\chi_g(x, \omega) = \frac{1}{4\pi} \frac{\gamma_{\perp} d_0(x)}{\omega - \omega_a + i\gamma_{\perp}} \left( \frac{1}{1 + \sum_{\nu}^{N_L} \Gamma_{\nu} |\Psi_{\nu}|^2} \right), \quad (2.7)$$

where the atomic inversion has also now been rescaled to its natural units,  $d_{\text{SALT}} = 4\pi|\theta|^2 / (\hbar \gamma_{\perp}) d$ . Together, Eqs. (2.6) and (2.7) represent  $N_L$  wave equations, one for each lasing mode, coupled together through the non-linear spatial hole-burning found in the denominator of the non-linear susceptibility,  $\chi_g$ . The SIA along with the field scaling implies that the lasing equations obey a set of scaling relations. Thus, the solution to these equations is seen to be independent of many of the properties of the gain medium, such as the inversion relaxation time and dipole matrix element.

### 2.1.1 Numerical solution

To solve the SALT equations, Eqs. (2.6) and (2.7), simultaneously, each lasing mode is expanded over a basis,

$$\Psi_\mu(x) = \sum_{n=1}^{N_B} a_n^{(\mu)} f_n(x; \omega_\mu) \quad (2.8)$$

where the  $N_B$  basis functions  $f_n$  are fixed, but possibly dependent upon the lasing frequency  $\omega_\mu$ , and the complex expansion coefficients  $a_n$  are found via a non-linear solution algorithm. It is important to note that lasing modes have an undetermined global phase, which amounts to being able to choose a single expansion coefficient for each lasing mode as real,  $a_0^{(\mu)} \in \mathbb{R}$ . Inserting Eq. (2.8) into Eqs. (2.6) and (2.7) yields  $2N_B$  equations for finding the amplitude and phase of the expansion coefficients,  $a_n$ . This ‘‘gauge freedom’’ allows one to determine self-consistently the lasing frequency,  $\omega_\mu$ . There are at least two useful sets of basis functions for solving the SALT equations. The original work on SALT used a constant flux (CF) basis set, whose members are defined to map to outgoing waves beyond a surface of last scattering, within which the entire laser cavity is contained. Matching the basis functions on this boundary to purely outgoing waves results in non-Hermitian states that satisfy the Sommerfeld radiation condition [133]. The CF basis method is the most developed and is used exclusively in this thesis, and will be discussed further in Sec. 2.3 [21, 25, 97].

Recently it has been shown that one can use a position space basis [118] combined with a perfectly matched layer (PML) boundary to implement the outgoing boundary condition. In this formulation, the basis functions take the form of delta functions,

$$f_n(x) = \delta(x - x_n). \quad (2.9)$$

The benefit to using this basis is removing the need to solve for an entire library of CF basis functions before considering the lasing problem. Numerically, finding these basis functions is the most expensive step. However, this comes at the cost of increasing the difficulty in locating and tracking the below threshold modes as the pump on the gain medium is increased.

## 2.2 Region of validity

We now address the validity of the SIA which will define the regime of validity of multimode SALT and its generalizations. A number of works in early laser theory rely on the SIA, including a seminal paper by Spencer and Lamb [115], which derives a preliminary version of the SALT theory. Most relevant to our work is that of Fu and Haken in 1991 [134], who argued that the SIA was valid and steady-state multimode operation was possible as long as  $\gamma_{\parallel}, \kappa \ll \gamma_{\perp}, \Delta$ , where  $\gamma_{\perp}$  is the relaxation rate of the polarization and  $\Delta$  is the free spectral range of the laser. They then studied a simplified model of a Fabry-Pérot-type laser and showed that the multimode state with the largest number of modes was typically the stable state. They also pointed out that in order for  $\Delta \gg \gamma_{\parallel}$  to hold, one typically would need to look at linear laser cavities of length  $L \leq 100\mu\text{m}$ .

Fu and Haken did not justify the requirement  $\kappa \ll \gamma_{\perp}$  in their work and we find that through comparison with FDTD simulations the SIA and SALT work well even when  $\kappa \geq \gamma_{\perp}$  (“bad cavity” limit). In the latter case the polarization cannot be adiabatically eliminated and does not follow the electric field instantaneously until steady state is reached; but in the steady state the SIA holds and the lasing fields are accurately determined by SALT.  $\kappa$  itself is not a relevant frequency scale for the validity of the SIA in the laser without injection; as long as  $\gamma_{\parallel} \ll \gamma_{\perp}, \Delta$  the SIA, and hence SALT, will describe the steady-state. The relaxation oscillation frequency,  $\omega_r \sim \sqrt{\kappa\gamma_{\parallel}}$ , describing the damped oscillations in returning to steady-state, can be relevant if it coincides with beat frequency of nearby modes, i.e. it is  $\sim \Delta$ . In this case, relaxing fluctuations could be resonantly enhanced and destabilize the multimode state. However, since  $\kappa \leq \Delta, \omega_r \leq \sqrt{\Delta\gamma_{\parallel}} < \Delta, \gamma_{\perp}$  (we assume that in the interesting cases  $\gamma_{\perp} \geq \Delta$ ; otherwise multimode lasing is unlikely, since  $\gamma_{\perp}$  is the width of the gain curve). Thus, for steady-state multimode lasing all that is required for the SALT to work is  $\gamma_{\parallel} \ll \gamma_{\perp}, \Delta$ .

The excellent agreement between SALT and FDTD can be seen in Fig. 2.1(a), where the steady-state SALT solutions are compared against the full FDTD simulation of a gain medium that satisfies the SIA, and excellent agreement is found. As FDTD simulations treat the complete dynamics of the electric field, atomic polarization, and inversion, it serves as

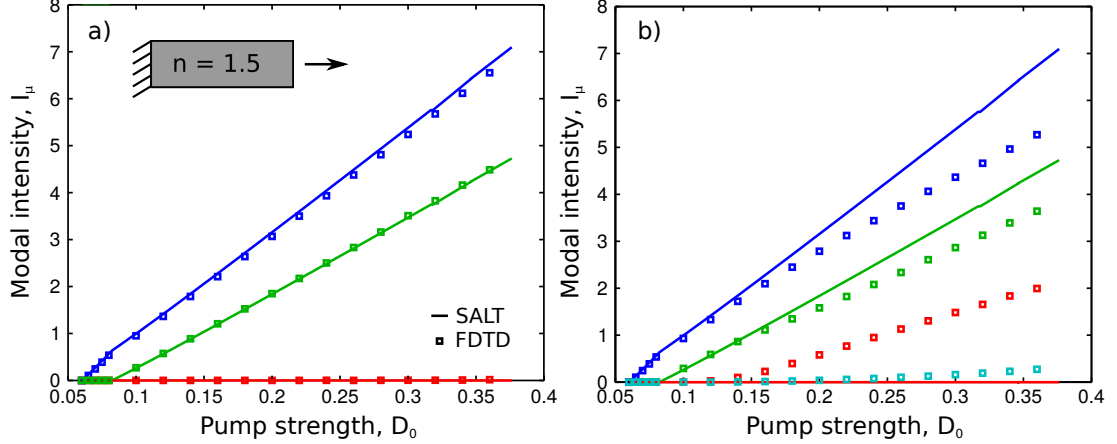


Figure 2.1: (a) Comparison between SALT and FDTD simulation results for an  $n = 1.5$  dielectric slab cavity with  $k_a = 40$ ,  $\gamma_{\perp} = 4$ ,  $\gamma_{\parallel} = 0.001$ , and thus  $\Delta = 2$ . Different colors show the modal intensities as a function of the pump strength. Excellent quantitative agreement is seen between the two methods as the SIA is well satisfied. (b) Comparison between SALT and FDTD simulation results for the same dielectric slab cavity, but with  $\gamma_{\parallel} = 0.2$ . No agreement between FDTD and SALT is seen as the SIA is not satisfied. Rates are given in units of  $c/L$ , and modal intensities and pump strengths are given in dimensionless SALT units.

an independent test of the validity of the SIA. However, as can be seen Fig. 2.1(b), when  $\gamma_{\parallel}$  is increased such that the SIA is no longer satisfied, additional frequencies are seen to appear in the resulting FDTD spectrum. These extra peaks are not lasing modes, but rather the due to the inversion being driven at the beat frequency between the two lasing modes (blue and green), yielding additional frequency components in the electric field.

Adiabatic elimination is another commonly used technique to simplify the lasing equations [99, 100]. In a system with multiple coupled fields with well separated decay rates, adiabatic elimination is possible since the fastest field(s), those with the largest decay rates, will exactly follow the slower fields, and can be solved for in terms of those fields, including dynamics occurring away from the steady-state. Instead, the SALT solution is only correct after the transient field has decayed, and all that remains is the steady-state solution. The necessary feature for adiabatic elimination in general is that the decay time for one of the fields be much faster than the other time scales in the problem. For example, in a Class B laser the decay rates of the electric field and the atomic inversion are both much slower than that of the polarization,  $\kappa \sim \gamma_{\parallel} \ll \gamma_{\perp}$ , and as such the polarization can be defined for all time in terms of the other two fields [99]. From a theoretical perspective, to justify adi-

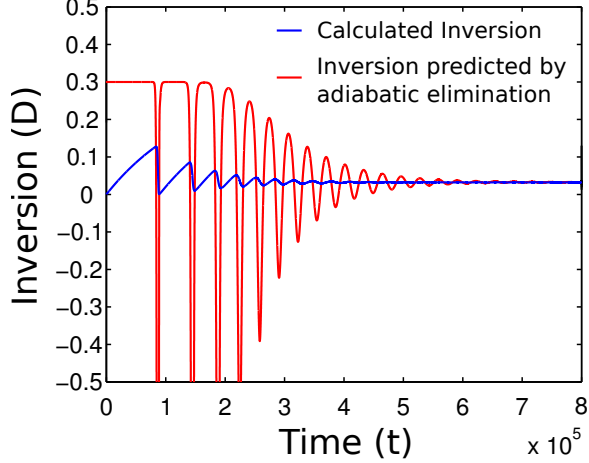


Figure 2.2: FDTD simulation of a dielectric cavity with  $k_a = 40$ ,  $n = 1.5$ ,  $\gamma_{\perp} = 4$ ,  $\gamma_{\parallel} = 0.001$ . Blue curve shows the inversion at a single pixel at the end of the cavity as calculated by the FDTD algorithm. The red curve shows the calculated inversion if the inversion could be adiabatically eliminated using Eq. (2.10). Units are given in values of  $c/L$ .

adiabatic elimination of the inversion alone requires being in an unphysical parameter regime,  $\gamma_{\parallel} \gg \gamma_{\perp}, \kappa$ .

If adiabatic elimination of the inversion were possible, it would be visible in both the steady-state and transient regimes of the laser's operation. We can directly show that this is not the case through the use of FDTD simulations and plotting the transient regime, as seen in Fig. 2.2, in which a single mode laser in a low- $Q$  cavity is shown, with  $n = 1.5$ , which is in the regime of  $\gamma_{\parallel} \ll \gamma_{\perp} \sim \kappa$ . The blue curve in Fig. 2.2 shows the actual inversion as a function of time at a pixel near the end of the cavity. Relaxation oscillations are well defined, and they decay to the steady state value, which can be predicted using SALT. The red curve in Fig. 2.2 instead shows the inversion calculated if we were to assume that the inversion can be completely determined by the polarization and electric field for all time, that is,

$$\partial_t d = 0 = -\gamma_{\parallel}(d - d_0) - 4\pi\gamma_{\parallel}(E^+(P^+)^* - c.c.) \quad (2.10)$$

where the inversion equation has been written in SALT units. As can be seen, the SIA is not the same as adiabatic elimination, as attempting to use adiabatic elimination yields completely incorrect values for the inversion in the transient regime, though agreement is seen in the steady-state regime, as expected. While the FDTD does not directly simulate

$E^+$ , we can calculate it from the Fourier transform of  $E$ . (The FDTD does directly simulate  $P^+$ .)

### 2.3 TCF states

As lasing modes are purely outgoing, it is useful to design a complete set of purely outgoing states to comprise a basis over which the lasing modes can be expanded. Such a set are the threshold constant flux (TCF) states, defined as

$$[-\nabla \times \nabla \times + (\varepsilon_c(\mathbf{x}) + \eta_n F(\mathbf{x})) \mathbf{k}^2] \mathbf{u}_n(\mathbf{x}; \omega) = 0, \quad (2.11)$$

where  $\eta_n$  and  $\mathbf{u}_n(\mathbf{x}; \omega)$  are the eigenvalue and eigenvectors of the TCF equations, and  $d_0(x) = d_0 F(x)$  is the profile of the pump. The TCF states also must satisfy an outgoing boundary condition, such that beyond a surface of last scattering the states are purely outgoing. This condition can be formally represented by the Sommerfeld radiation condition [133],

$$\lim_{|x| \rightarrow \infty} \left( \frac{\partial}{\partial |x|} - i\mathbf{k} \right) \mathbf{u}_n(\mathbf{x}; \omega) = 0, \quad (2.12)$$

and in practice the TCF states can be matched to outgoing waves along the last scattering surface [23, 97]. In one-dimension, the TCF wave equation and boundary condition can be written as

$$[\nabla^2 + (\varepsilon_c(x) + \eta_n F(x)) k^2] u_n(x; \omega) = 0, \quad (2.13)$$

$$\partial_x u_n(x; \omega)|_{x=L} = ik u_n(L; \omega), \quad (2.14)$$

$$u_n(0; \omega) = 0, \quad (2.15)$$

where final equation is written for a perfectly reflecting boundary condition at  $x = 0$ . In the case of a two-sided cavity, this would be replaced by an outgoing boundary condition similar to Eq. (2.14). The eigenvalues  $\eta_n$  represent the electric susceptibility required to “pull up” the  $n$ th pole of the passive cavity to lase at frequency  $\omega$ , specified as an input to these equations [25].

Numerically, the TCF basis can be found by discretizing the cavity, with the operators  $\nabla^2$ ,  $\varepsilon_c(x)$ , and  $F(x)$  becoming matrices, and the basis functions  $u_n(x)$  as eigenvectors that solve the generalized equation expressed in Eq. (2.13). The dielectric and pump profile are functions of a single variable, thus their matrix representations are diagonal, while the derivative operator can be expressed in a finite difference scheme for a one-dimensional cavity as

$$\partial_x^2 \rightarrow \frac{u_n(x_{p+1}) + u_n(x_{p-1}) - 2u_n(x_p)}{\Delta x^2}, \quad (2.16)$$

where  $u_n(x_p)$  is the value of the  $n$ th TCF state at the  $p$ th pixel, and the distance between pixels is  $\Delta x$ . At the boundaries of the cavity, proper implementation of the derivative operator requires knowledge of the value of the TCF basis function outside of the cavity,  $u_n(x_{P+1})$ . This can be expressed in terms of the values inside the cavity by discretizing Eq. (2.14),

$$\frac{u_n(x_{P+1}) - u_n(x_P)}{\Delta x} = ik \frac{u_n(x_{P+1}) + u_n(x_P)}{2}, \quad (2.17)$$

leading to a closed set of equations for the value of the TCF function at the  $L$  pixel locations. In discretizing this equation we have also chosen to place the boundary of the cavity halfway between  $x_P$  and  $x_{P+1}$ , such that the total length of the cavity (assuming a perfect mirror at  $x = 0$ ) is  $L = (P + .5)\Delta x$ . With the TCF equations properly discretized, the basis functions and eigenvalues can be found using generalized eigenvalue solvers common in many numerical software libraries. In multiple dimensions such a discretization scheme is still possible, but additional care must be taken to properly match to the outgoing boundary condition. One method for solving the TCF equations in two-dimensions is to use a radial discretization scheme [23, 97]. This allows for the cavity to be embedded within a circular surface of last scattering on which the TCF state is matched with outgoing Hankel functions. This allows for an analytic expression for the boundary condition but comes at the cost of having a non-uniform density of pixels in the cavity due to the disk discretization scheme, which is computationally expensive.

Once the solutions to the TCF equations are known, this is an efficient basis to solve the SALT equations in due to the similarities between Eqs. (2.13) and (2.6) at, or below, the first lasing threshold when the spatial hole-burning term in the denominator vanishes.

At the first lasing threshold, one of the TCF eigenvalues solves the equation,

$$\eta_0(\omega) = \frac{\gamma_{\perp} d_0}{\omega - \omega_a + i\gamma_{\perp}}, \quad (2.18)$$

allowing for the lasing mode to be represented as a single TCF state.

Above the first lasing threshold, the solution for active lasing modes can be found by inserting the expansion of the lasing modes in terms of the TCF states, Eq. (2.8), into the SALT equations, Eqs. (2.6) and (2.7), and using the definition of the TCF states, Eq. (2.13), to write down the lasing map equation [25],

$$\eta_l a_l^{(\mu)} = \sum_{n=1}^{N_{TCF}} T_{ln}^{(\mu)} a_n^{(\mu)}, \quad (2.19)$$

$$T_{ln}^{(\mu)} = \frac{\gamma_{\perp} d_0}{L(\omega_{\mu} - \omega_a + i\gamma_{\perp})} \int_C dx \frac{F(x) u_l(x; \omega_{\mu}) u_n(x; \omega_{\mu})}{1 + \sum_{\sigma}^{N_L} \Gamma_{\sigma} |\Psi_{\sigma}(x)|^2}. \quad (2.20)$$

These coupled equations represent  $2N_{TCF}N_L$  independent equations to solve, where  $N_{TCF}$  is the number of TCF states chosen in the expansion of the lasing modes in Eq. (2.8), and  $N_L$  is the number of active lasing modes. This problem can be solved efficiently with known non-linear numerical techniques such as Newton's method. For systems with both many active lasing modes and many TCF states required in the lasing mode expansions (conditions that are typical for many multi-dimensional cavities), it is beneficial to also supply the non-linear solver with the Jacobian of the non-linear equations to speedup the non-linear solver.

### 2.3.1 TCF lasing map Jacobian

Before deriving the Jacobian, it is useful to briefly discuss other necessary elements of the numerical solution of the SALT equations. When actually solving the system of lasing map equations numerically, it is best to choose a slightly different set of definitions for the lasing map, Eq. (2.19), to avoid converging to the zero amplitude solution and fix the gauge

condition,

$$\eta_n^{(\mu)} \tilde{a}_n^{(\mu)} = \frac{d_0 \gamma_{\perp}}{\omega_{\mu} - \omega_a + i\gamma_{\perp}} \sum_{m=1}^{N_{TCF}} T_{nm}^{(\mu)} \tilde{a}_m^{(\mu)}, \quad (2.21)$$

$$\Psi_{\mu}(x) = Z_{\mu} \left( \tilde{a}_1^{(\mu)} u_1^{(\mu)} + \sum_{n=2}^{N_{TCF}} \tilde{a}_n^{(\mu)} u_n^{(\mu)} \right) = \sum_n a_n^{(\mu)} u_n^{(\mu)}, \quad (2.22)$$

where  $Z_{\mu}$  and  $\tilde{a}_1$  are chosen as

$$Z_{\mu} = \text{Re}[\text{Max}\{\{a_n^{(\mu)}\}\}], \quad (2.23)$$

$$\tilde{a}_1 = 1. \quad (2.24)$$

Thus, as previously discussed [21, 23, 97], for  $N_{TCF}$  eigenvectors comprising a single lasing mode, there are  $2(N_{TCF} - 1)$  unknowns for the complex valued  $\tilde{a}_n^{(\mu)}$ , along with the overall scale  $Z_{\mu}$ , and frequency  $\omega_{\mu}$ .

When the non-linear solver is invoked to solve the lasing map problem, it attempts to minimize

$$y_n^{(\mu)} = \frac{\omega_{\mu} - \omega_a + i\gamma_{\perp}}{d_0 \gamma_{\perp}} \eta_n^{(\mu)} \tilde{a}_n^{(\mu)} - \sum_{m=1}^{N_{TCF}} T_{nm}^{(\mu)} \tilde{a}_m^{(\mu)}. \quad (2.25)$$

However, this is still a complex valued object, which we must reduce to a pair of real-valued equations for input into traditional non-linear solver schemes. In the remainder of this section we will use the superscripts  $R$  and  $I$  to denote real and imaginary parts of objects. Decomposing Eq. (2.25) into its real and imaginary components,

$$y_n^{R,\mu} = C_n^{R,\mu} \tilde{a}_n^{R,\mu} - C_n^{I,\mu} \tilde{a}_n^{I,\mu} - \sum_m T_{nm}^{R,\mu} \tilde{a}_m^{R,\mu} + \sum_m T_{nm}^{I,\mu} \tilde{a}_m^{I,\mu}, \quad (2.26)$$

$$y_n^{I,\mu} = C_n^{I,\mu} \tilde{a}_n^{R,\mu} + C_n^{R,\mu} \tilde{a}_n^{I,\mu} - \sum_m T_{nm}^{R,\mu} \tilde{a}_m^{I,\mu} - \sum_m T_{nm}^{I,\mu} \tilde{a}_m^{R,\mu}, \quad (2.27)$$

$$C_n^{\mu} = \frac{\omega_{\mu} - \omega_a + i\gamma_{\perp}}{d_0 \gamma_{\perp}} \eta_l^{(\mu)}, \quad (2.28)$$

we can now identify all of the requisite terms that we will need to calculate to construct the Jacobian. In this notation, the  $2N_{TCF}$  unknown variables for each lasing mode that we

need to solve for are

$$\vec{e} = [Z_\mu, \omega_\mu, \tilde{a}_2^R, \tilde{a}_2^I, \tilde{a}_3^R, \tilde{a}_3^I, \dots, \tilde{a}_N^R, \tilde{a}_N^I]. \quad (2.29)$$

Non-linear numerical solvers usually use a multi-dimensional extension of Newton's method, which necessitates knowing the first derivative of the function with respect to the input variables. Thus, when invoked to solve the problem  $\vec{y} = 0$ , if the Jacobian is not supplied, the non-linear equation solver begins to calculate the Jacobian numerically, which requires  $2N_{TCF}N_L$  calls of the function. This cost is not noticed in small, one-dimensional SALT calculations because the system size is small enough to make both the calculation of the lasing map and the steps of accessing the TCF libraries stored on the hard drive negligible (reading and writing to the disk is expensive). However, in multi-dimensional systems, or even large one-dimensional systems, these steps are not negligible, and as additional lasing modes turn on above threshold the calculation slows down precipitously. Thus, it is advantageous to provide the information on how to calculate the Jacobian to the non-linear solver, allowing for its construction in a single call to the function. This is not without some additional overhead, as constructing the Jacobian for Eq. (2.25) is non-trivial, but overall the computational effort can be seen to be substantially less for the analytic form of the Jacobian derived here over the numerically calculated version that would otherwise be generated. Thus, it is in our interest to calculate the Jacobian analytically and provide these formula to the non-linear solver,

$$J_{i,j} = \frac{\partial y_i}{\partial e_j}. \quad (2.30)$$

The derivation of the Jacobian for the modified lasing map equation, (2.21), is a lengthy but straightforward excersize in bookkeeping, and is performed in Appendix B

## 2.4 Partially reflecting mirror TCF states

The TCF states introduced in Sec. 2.3 are limited in their ability to efficiently simulate high- $Q$  cavities due to the requirement that any feature within the cavity must be represented by a passive cavity dielectric of finite width. This has allowed for SALT using the TCF states

to simulate many important features of the microcavity lasers it was originally designed for, which are usually constructed of semiconductors, and have a passive cavity dielectric of  $n \sim 3.5$  (for GaAs). However, in a one-dimensional system, this is a very lossy system, with the reflectivity coefficient defined by Fresnel reflection,

$$R = \frac{(n - 1)^2}{(n + 1)^2}, \quad (2.31)$$

which leads to  $R \sim .30$  for semiconductor structures. This can be overcome by including a photonic crystal mirror, increasing the reflectivity of those frequencies near the lasing frequency. However, this requires additional features in the simulation, increasing the number of required pixels for accurate simulation. While this is not a prohibitive cost for SALT, it can be for FDTD, and especially the noisy-FDTD discussed in Ch. 6. Here, we detail how to implement a partially reflecting mirror via a delta function added to the passive cavity dielectric, facilitating the simulation of high- $Q$  cavities, and present quantitative agreement between SALT and FDTD for such a system.

### 2.4.1 Analytic solution

The usual boundary conditions for an electric field oriented parallel to the direction of propagation require continuity of the field and the derivative,

$$E_{out}^{\parallel} - E_{in}^{\parallel} = 0, \quad (2.32)$$

$$\partial_x E_{out}^{\parallel} - \partial_x E_{in}^{\parallel} = 0. \quad (2.33)$$

However, in the presence of a delta-function in the dielectric, the usual arguments used for demonstrating continuity of the derivative must be altered, as can be seen by integrating the wave equation across a small region near the interface, extending  $\epsilon$  in both directions from the interface,

$$0 = [\partial_x^2 + k^2 \epsilon_c + k^2 \Lambda \delta(x - L)] E, \quad (2.34)$$

$$\int_{L-\epsilon}^{L+\epsilon} \partial_x^2 E dx = -k^2 \left[ \int_{L-\epsilon}^{L+\epsilon} \epsilon_c E dx + \Lambda \int_{L-\epsilon}^{L+\epsilon} \delta(x - L) E dx \right]. \quad (2.35)$$

As  $\epsilon \rightarrow 0$ , the first integral on the right-hand side vanishes (as usual), but the second does not,

$$\partial_x E_{out}^{\parallel}|_{x=L} - \partial_x E_{in}^{\parallel}|_{x=L} = -k^2 \Lambda E(L), \quad (2.36)$$

in which it is now obvious that the derivative of the electric field will be discontinuous across such a boundary. In these equations, we have defined  $\Lambda$  as the strength of the partially reflecting mirror.

These two equations, Eqs. (2.32) and (2.36) can be used to solve for the reflection and transmission coefficients, by defining the incoming and outgoing fields as

$$E_{in}^{\parallel} = e^{ikx} + r e^{-ikx}, \quad (2.37)$$

$$E_{out}^{\parallel} = t e^{ikx}, \quad (2.38)$$

which after some simple algebra reveals that

$$r = \left( \frac{\frac{ik\Lambda}{2}}{1 - \frac{ik\Lambda}{2}} \right) e^{2ikL}, \quad (2.39)$$

$$t = \left( \frac{1}{1 - \frac{ik\Lambda}{2}} \right), \quad (2.40)$$

or written as as the transmission and reflection coefficients for the field intensity,

$$R = |r|^2 = \frac{\left(\frac{k\Lambda}{2}\right)^2}{1 + \left(\frac{k\Lambda}{2}\right)^2}, \quad (2.41)$$

$$T = |t|^2 = \frac{1}{1 + \left(\frac{k\Lambda}{2}\right)^2}, \quad (2.42)$$

which demonstrates that even though we did not make the strength of the delta function frequency dependent (dispersive), the overall transmission and reflection coefficients are still dependent on the product  $k\Lambda$ , as shorter wavelengths will be closer in length to the delta-function width, and thus undergo stronger scattering.

### 2.4.2 Implementation in the TCF equations

There are (at least) two different ways to implement this delta-function in the TCF equations, corresponding to exactly where one decides to place the delta-function mirror. Recall that for the numerical solution of the TCF states,  $u(x)$ , the actual boundary between the cavity and the outside lies  $\Delta x/2$  away from the final grid point,  $u(x_P)$ . The delta function can either be incorporated at this halfway point by altering the derivative condition defining the TCF states, or incorporated at the final location inside the cavity, by including it in the definition of the dielectric. Both methods produce very similar results for reasonable values of  $\Delta x \leq \lambda_a/30$ . Furthermore, even though the addition of this delta function technically makes the cavity non-uniform, the TCF eigenvalues can still be used to find the passive cavity resonances as is possible for uniform cavities [25],

$$\eta(\omega) = \varepsilon_c \left( \frac{\left(\omega_0 - \frac{i\gamma_c}{2}\right)^2 - \omega^2}{\omega^2} \right), \quad (2.43)$$

where here  $\varepsilon_c$  is the uniform passive cavity dielectric, excluding the partially reflecting mirror. The values generated for the passive cavity decay rates  $\gamma_c$  here match up to within a few percent of those generated with the traditional definition of the cavity decay rate, Eq. (1.1).

#### Altering the boundary condition

To incorporate the delta-function into the derivative condition, we first note that the outgoing boundary condition has been changed, and we instead have the equations,

$$ikAe^{ikL} - \partial_x u(x)|_{x=L} = -k^2 \Lambda u(L), \quad (2.44)$$

$$Ae^{ikL} = u(L), \quad (2.45)$$

which result in the partially outgoing boundary condition,

$$\partial_x u(x)|_{x=L} = (ik + k^2 \Lambda)u(L). \quad (2.46)$$

This can be readily discretized in the usual way,  $\partial_x u(x) = (1/\Delta x)(u(x_{p+1}) - u(x_p))$ , and  $u(x) = (1/2)(u(x_{p+1}) + u(x_p))$ , which allows us to define the grid point outside of the cavity,  $u(x_{P+1})$ , in terms of the grid point just inside the cavity,  $u(x_P)$ , such that the Laplacian operator is fully defined,

$$u(x_{P+1}) = \left( \frac{2 + \Delta x k^2 \Lambda + ik \Delta x}{2 - \Delta x k^2 \Lambda - ik \Delta x} \right) u(x_P). \quad (2.47)$$

Just as before, the discretized set of TCF equations can now be solved as a generalized eigenvalue problem.

### Altering the cavity dielectric

Alternatively, the partially reflecting mirror can be incorporated into the passive cavity dielectric,

$$\varepsilon_{c,total}(x) = \varepsilon_c(x) + \Lambda \delta(x - L), \quad (2.48)$$

and discretized as

$$\varepsilon_{c,total}(x_n) = \varepsilon_c(x_n) + \frac{\Lambda}{\Delta x} \delta_{x_n, x_P}, \quad (2.49)$$

where  $\delta_{ij}$  is the Kronecker delta. While the previous method results in a change to the Laplacian operator, this method instead alters the cavity dielectric operator, however, both yield very similar results numerically. Note, that using the traditional TCF scheme,  $x_P$  is actually  $\Delta x/2$  away from the edge of the cavity, so these two methods are not exactly identical.

### 2.4.3 Partially reflecting mirrors in FDTD

Implementing the partially reflecting mirror in FDTD is identical to the alteration of the passive cavity dielectric discussed above,

$$\varepsilon_{c,total}(x_n) = \varepsilon_c(x_n) + \frac{\Lambda}{\Delta x} \delta_{x_n, x_P}. \quad (2.50)$$

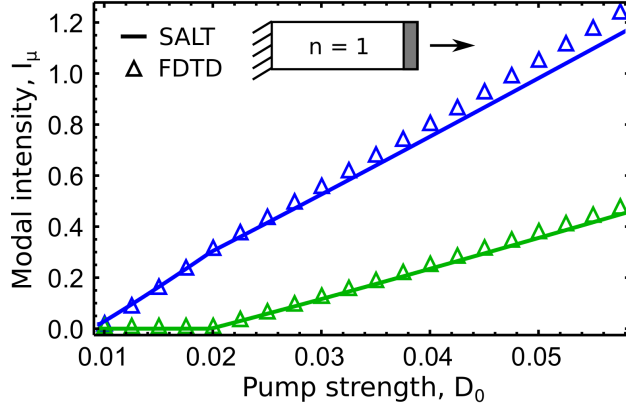


Figure 2.3: Plot of the modal intensity as a function of pump strength for a partially reflecting cavity with  $L = 1$ ,  $\varepsilon_c = 1$ ,  $k_a = 40$ ,  $\gamma_\perp = 4$ , and  $\Lambda k_a = 2$ . Triangles show FDTD results, while lines give the SALT results. Rates and frequencies are given in units of  $c/L$ , while modal intensities and pump strengths are given in terms of dimensionless SALT units.

However, there is a slight difference because in FDTD the boundary of the cavity also coincides with a grid point (unlike the TCF definition). Thus, here,  $x_P$  represents the location of the actual edge of the cavity. This leads to the field update equation,

$$E(x_P, t_{m+1}) = E(x_P, t_m) + \frac{\Delta t}{\Delta x} \left( \frac{1}{\varepsilon_c(x_P) + \frac{\Lambda}{\Delta x}} \right) \left( H(x_{P+\frac{1}{2}}, t_{m+\frac{1}{2}}) - H(x_{P-\frac{1}{2}}, t_{m+\frac{1}{2}}) \right), \quad (2.51)$$

where the effects of gain media and absorption (through a conductivity  $\sigma$ ) can be incorporated with ease.

This allows for direct numerical comparison between SALT and FDTD simulations of a partially reflecting cavity with a perfect mirror on one end. Good quantitative agreement between these two methods can be seen in Fig. 2.3, where SALT simulations were performed using the alteration to the derivative condition.

## 2.5 Summary

In this chapter we have reviewed the standard SALT theory developed by Türeci and Stone alongside the TCF basis developed by Ge *et al.* used to facilitate its solution [21–23, 25, 97]. As part of my work for this thesis, I implemented my own versions of the TCF and SALT equations, customized to the questions addressed in this thesis. This involved developing

the Jacobian speedup to analyze the chaotic cavity lasers discussed in Ch. 5 as well as simulations of multimode random lasers for work performed with Arthur Goetschy [135]. I derived and implemented the partially reflecting mirror TCF states in one-dimension. Finally, I developed my own finite difference time domain (FDTD) simulation code for use in verifying the SALT solutions. In the following chapters I discuss the generalization of SALT to complex gain media (C-SALT) and lasers subjected to an injected signal (I-SALT).

## Chapter 3

# Complex gain media

The past two decades have seen an explosion in the types and configurations of laser systems. This development has been fueled by advances in microfabrication techniques and motivated by applications to integrated on-chip optics, for more efficient optical communications and sensing, as well as basic scientific interest. Many of these advances involve lasers with complex gain media, such as semiconductor lasers [90,103], quantum cascade lasers [92,136], and rotationally excited gases [137], for which the two level atomic system approximation is poorly suited. For example, though the band structure of the semiconductor gain medium can be approximated as a series of two level atomic transitions, multiple transitions are required to represent the effects of Pauli blocking [138–140]. Cascaded-transition quantum cascade lasers are designed with two lasing transitions to operate at longer wavelengths [141,142]. Additionally, for both rotationally excited gases and semiconductor media the carriers are allowed to diffuse through the cavity, an effect that is not addressed in the Maxwell-Bloch equations [137].

Many analytic treatments of complex gain media have also been developed, using multiple atomic rate equations for each atomic level to model the dynamics of the gain media [94,95]. The effects of gain diffusion along the longitudinal axis have also been added to these models, treating the atomic inversion as having two components, a spatially uniform term and a grating at  $2k_a$ , where  $k_a$  is the central atomic transition frequency, caused by spatial hole-burning [136,143–145]. However, these treatments have focused on scalar electromagnetic fields appropriate for the one-dimensional structures being studied, either

Fabry-Pérot or ring lasers. Furthermore, these treatments also take for granted knowledge of the lasing mode structure in their assumptions about the resulting grating imposed on the atomic inversion by spatial hole-burning, which is not generalizable to arbitrary multi-dimensional laser cavities, or even short, low- $Q$  one-dimensional cavities where the gain saturation varies greatly close to the mirror, but is nearly uniform close to the boundary. A numerical method for simulating lasers with diffusion in a laser cavity with an arbitrary shape has been developed using the FDTD algorithm, but it is too computationally demanding to study a large parameter space necessary for device design [146, 147].

For SALT to be a useful modeling tool in describing these types of laser systems, it is imperative that it is able to operate with gain media that are more complicated than two-level systems. To do so, we need to make the stationary population approximation, which is the multi-level generalization of the SIA. To avoid confusion with the single pole approximation (discussed later), no abbreviations will be used for either approximation. The simplest case, that of a single transition the gain susceptibility for N-level lasers, can be explicitly calculated in terms of the stationary inversion profile and the lasing fields and inserted into the wave equation so as to require only a single set of coupled electric field equations [98]. We first treat this case and show that the N-level model can be reduced to the two-level Maxwell-Bloch model with renormalized relaxation and pump parameters [98].

Such a simplification is not possible with multiple lasing transitions, but, as we will show, the stationary population approximation leads instead to coupled sets of field and population equations that can be solved iteratively almost as efficiently as the SALT equations. The full requirements of the stationary population approximation are discussed in Sec. 3.5. The generalized theory, which we call complex-SALT (C-SALT) [119], allows us to treat steady-state lasing with (i) an arbitrary number of atomic levels and lasing transitions, and (ii) gain diffusion. As already noted, direct integration in space and time of the lasing equations with diffusing gain centers [139, 140, 146, 147] is very challenging. C-SALT can obtain the same steady-state solution with relative ease, allowing one to use the method for exploration of basic laser physics, and, potentially, for device design.

In Sec. 3.3, we solve the C-SALT equations for multimode lasing with multiple transitions but without gain diffusion and demonstrate excellent agreement with FDTD sim-

ulations. Including gain diffusion in the C-SALT equations and studying both one- and two-dimensional lasers cavities, we identify two distinct physical situations in which carrier diffusion can have a substantial effect. The first is when the carrier diffusion competes with spatial hole-burning in a uniformly pumped cavity, leading to a transition between multi-mode lasing to a gain-clamping regime in which only a single lasing mode reaches threshold (as one finds when spatial hole-burning is absent [3]). The second situation is when carrier diffusion competes with non-uniform pumping so as to mitigate the spatial selection effects which occur in the absence of diffusion. We are not aware of prior quantitative theoretical studies of these effects.

### 3.1 Derivation of the atomic rate equations

To derive the equations of motion for the atomic degrees of freedom, it is useful to return to the quantum mechanical picture introduced in Sec. 1.4, with the total atomic polarization,  $\mathbf{P}_g$ , given by Eq. (1.16), and the definition for the atomic dipole matrix element,  $\boldsymbol{\theta}$ , Eq. (1.17). However, instead of assuming that our medium is only a two-level medium, reducing the size of the density matrix  $\rho$ , we will continue to assume that it is an  $M \times M$  matrix, with an arbitrary number of levels. Among the  $M$  levels a subset of them will contribute to lasing and support lasing transitions; the others will simply be part of the downward cascade of electronic excitations involved in the pumping and emission in steady-state. Lasing transitions will arise from pairs of level which have sufficiently large polarization due to their population inversion to contribute substantially to a lasing line at a nearby frequency.

To complete the semiclassical lasing equations, one must consider the quantum equations of motion for the average polarization of the gain medium,

$$\partial_t \mathbf{P}_g(\mathbf{x}, t) = -N(\mathbf{x}) \sum_n^M \sum_m^M \partial_t(\rho_{nm}) \boldsymbol{\theta}_{mn}, \quad (3.1)$$

where we have again assumed identical “atoms” and written the density matrix elements as  $\rho_{nm} = \langle n | \hat{\rho} | m \rangle$ , and we initially assume a fixed density of gain atoms  $N(\mathbf{x})$ . Again,

the equation of motion for the density matrix can still be calculated from the Heisenberg equation of motion Eq. (1.19), and upon evaluating the commutator and simplifying, this can be re-written as

$$\partial_t \rho_{nm} = -i\omega_{nm}\rho_{nm} - \frac{i}{\hbar} \sum_k^M (\boldsymbol{\theta}_{nk}\rho_{km} - \rho_{nk}\boldsymbol{\theta}_{km}) \cdot \mathbf{E}(\mathbf{x}, t), \quad (3.2)$$

where  $\omega_{nm} = (1/\hbar)(E_n - E_m)$  is the transition frequency.

From this equation, we can see that off-diagonal density matrix elements, which determine the gain polarization, can couple to one another within manifolds of atomic transitions. If we include all terms in the equation of motion, then the time evolution of a specific off-diagonal element,  $\rho_{nm}$ , will depend not only on the level populations ( $\rho_{nn}, \rho_{mm}$ ), but also on other off-diagonal elements, i.e. on the polarization of other transitions. If this is the case one cannot arrive at lasing equations of the standard form and one cannot define the polarization associated with a specific transition. However, physically these off-diagonal terms correspond to coherent multiple excitation, leading to effects such as electrically induced transparency, and inversion-less lasing. Conventional lasers do not typically operate in this regime. To reach this regime, the non-radiative relaxation rates between non-lasing transitions must be of similar order to those between lasing levels, which makes it difficult for the gain medium to build up the necessary inversion to lase [94]. As such, we will assume that we are in the weakly coupled polarization regime and thus that off-diagonal density matrix elements depend only on the level populations of that specific pair of levels. The equation of motion for the off-diagonal elements for such a pair is

$$\partial_t \rho_{nm} = -(\gamma_{\perp, nm} + i\omega_{nm}) \rho_{nm} + \frac{i}{\hbar} (\rho_{nn} - \rho_{mm}) \boldsymbol{\theta}_{nm} \cdot \mathbf{E}(\mathbf{x}, t), \quad (m \neq n) \quad (3.3)$$

where we have now added the effect of environmental dephasing on the gain atoms in the standard manner in terms of a transverse relaxation/dephasing rate  $\gamma_{\perp, nm}$ .

With the above assumption, the total gain polarization can now be broken up into  $N_T$

constituent polarizations of each lasing transition,

$$\mathbf{P}_g(\mathbf{x}, t) = \sum_j^{N_T} \mathbf{p}_j(\mathbf{x}, t) \quad (3.4)$$

$$\mathbf{p}_j^+(\mathbf{x}, t) = -N(\mathbf{x})\rho_{nm}\theta_{mn} \quad (3.5)$$

where each transition, previously labeled by the pair of levels,  $n, m$ , has been relabeled with a transition index  $j$ , where  $\mathbf{p}_j^+$  is the positive frequency part of  $\mathbf{p}_j = \mathbf{p}_j^+ + \mathbf{p}_j^-$ , and by definition  $\omega_{nm} > 0$ .

From the form of the gain polarization as a transition sum, Eq. (3.4), it is clear that every constituent polarization in the gain medium contributes to the total source term in the wave equation, Eq. (1.8). Strictly speaking, it is thus impossible to say that one portion of the electric field is driven by only a single transition if multiple transitions are present in the gain medium, though practically there are many cases where these transitions are so well separated in frequency that this is effectively the case. Each constituent polarization, from Eq. (3.3), obeys its own equation of motion,

$$\partial_t \mathbf{p}_j^+(\mathbf{x}, t) = -(\gamma_{\perp,j} + i\omega_{a,j}) \mathbf{p}_j^+ - \frac{id_j}{\hbar} (\boldsymbol{\theta}_j \cdot \mathbf{E}) \boldsymbol{\theta}_j^*, \quad (3.6)$$

in which the properties of the  $j$ th constituent polarization are given in terms of the dephasing rate,  $\gamma_{\perp,j}$ , the atomic transition frequency,  $\omega_{a,j}$ , the constituent inversion,  $d_j = N(\mathbf{x})(\rho_{nn}^{(j)} - \rho_{mm}^{(j)})$ , and the dipole matrix element,  $\boldsymbol{\theta}_j$ .

The equation of motion for the density matrix, Eq. (1.19), also determines the evolution of the populations in each atomic level, given by the diagonal elements of the density matrix,

$$\partial_t \rho_{nn} = -\frac{i}{\hbar} \sum_k^M (\boldsymbol{\theta}_{nk} \rho_{kn} - \rho_{nk} \boldsymbol{\theta}_{kn}) \cdot \mathbf{E}(\mathbf{x}, t). \quad (3.7)$$

As can be seen here, atomic level populations couple only to the constituent polarizations with which they share a transition, and atomic levels which are not a part of any lasing transition do not appear at this stage on the right hand side of the equation for the populations. However typically all levels are coupled non-radiatively through other degrees

of freedom (“the bath”) and these effects need to be included phenomenologically in the standard manner, leading to

$$\partial_t \rho_n = \sum_{m \neq n}^M \gamma_{nm} \rho_m - \sum_{m \neq n}^M \gamma_{mn} \rho_n - \frac{1}{i\hbar} \sum_j^{N_T} \xi_{n,j} (\mathbf{p}_j^- - \mathbf{p}_j^+) \cdot \mathbf{E}. \quad (3.8)$$

Here  $\gamma_{nm}$  represents either the non-radiative decay rate between a higher level  $m$  and a lower level  $n$  or pumping rate from lower level  $m$  to higher level  $n$ ,  $\rho_n \equiv N(\mathbf{x})\rho_{nn}$  is the total number of electrons in level  $n$  of atoms at location  $\mathbf{x}$ .  $\xi_{n,j}$  represents the relationship between the population of level,  $n$  and a given lasing transition,  $j$ ;  $\xi_{n,j} = 1$  if  $n$  is the upper level of the transition,  $\xi_{n,j} = -1$  if  $n$  is the lower level of the transition, and  $\xi_{n,j} = 0$  if  $n$  is not involved in that lasing transition.

Thus the full set of semiclassical lasing equations are Eqs. (1.8), (3.4), (3.6), and (3.8), which define the wave equation for the electric field, the total polarization in terms of the constituent polarizations, the equation of motion for each constituent polarization, and the equation of motion for the populations in each atomic level respectively. Since now the time evolution of the off-diagonal elements of the density matrix are contained in the polarization equations, we will henceforth represent the populations (diagonal elements) in terms of a density *vector* with components  $\rho_n(x)$ .

## 3.2 Renormalization of a single transition, N-level medium

A gain medium with an arbitrary number of atomic levels but only a single lasing transition can be renormalized to an effective two-level gain medium when using the stationary population approximation. To demonstrate this, it is most effective to separate the two lasing populations from the density vector  $\rho_n$ , defining  $\tilde{\rho}_n$ , the density vector with  $M - 2$  elements, omitting the lasing levels,  $\rho_u$  and  $\rho_l$ , which are the populations of the upper and lower lasing levels respectively. Following Eq. (3.8), the rate equation for an arbitrary *non-lasing* level in the system can be written as

$$\dot{\tilde{\rho}}_i = \sum_j^{M-2} \gamma_{ij} \tilde{\rho}_j - \sum_j^{M-2} \gamma_{ji} \tilde{\rho}_i + \gamma_{iu} \rho_u + \gamma_{il} \rho_l - (\gamma_{ui} + \gamma_{li}) \tilde{\rho}_i, \quad (3.9)$$

where the summations are taken over all non-lasing levels. Here we do not distinguish between decay rates and pumping rates;  $\gamma_{ij}$  is simply interpreted as the rate at which level  $|\varphi_j\rangle$  transitions into level  $|\varphi_i\rangle$ , regardless of the energies of those states. If the populations of all the non-lasing transitions are stationary, i.e.  $\dot{\tilde{\rho}}_i = 0$ , then we can rewrite Eq. (3.9) as

$$\sum_j^{M-2} G_{ij} \tilde{\rho}_j = \gamma_{iu} \tilde{\rho}_u + \gamma_{il} \tilde{\rho}_l, \quad (3.10)$$

$$G_{ij} = (s_i + \gamma_{ui} + \gamma_{li}) \delta_{ij} - \gamma_{ij}. \quad (3.11)$$

Here,  $s_i \equiv \sum_j^{M-2} \gamma_{ji}$  and  $\delta_{ij}$  is the Kronecker delta. Inverting Eq. (3.10) gives

$$\tilde{\rho}_i = \sum_j^{M-2} [G^{-1}]_{ij} (\gamma_{ju} \rho_u + \gamma_{jl} \rho_l). \quad (3.12)$$

Hence, we can express the total number density of gain atoms as

$$N(x) = \sum_i^{M-2} \tilde{\rho}_i + \rho_u + \rho_l \quad (3.13)$$

$$= T_u \rho_u + T_l \rho_l \quad (3.14)$$

where

$$T_u = 1 + \sum_i^{M-2} \sum_j^{M-2} [G^{-1}]_{ij} \gamma_{ju}, \quad (3.15)$$

$$T_l = 1 + \sum_i^{M-2} \sum_j^{M-2} [G^{-1}]_{ij} \gamma_{jl}. \quad (3.16)$$

Noting that  $d = \rho_u - \rho_l$ , we can write the populations of the lasing states as

$$\rho_u = \frac{N + T_l d}{T_l + T_u}, \quad (3.17)$$

$$\rho_l = \frac{N - T_u d}{T_l + T_u}. \quad (3.18)$$

From the equations of motion for the lasing levels Eq. (3.8), we can solve for the inversion

equation

$$\dot{d} = \dot{\rho}_u - \dot{\rho}_l = \sum_i (\gamma_{ui} - \gamma_{li}) \rho_i - s_u \rho_u + s_l \rho_l - \frac{2}{i\hbar} \mathbf{E}^+ \cdot ((\mathbf{P}^+)^* - \mathbf{P}^+), \quad (3.19)$$

where  $s_u = \sum_j^{M-2} \gamma_{ju} + \gamma_{lu}$  and  $s_l$  is defined similarly. Inserting Eq. (3.12) into this equation gives

$$\dot{d} = B_u \rho_u + B_l \rho_l - \frac{2}{i\hbar} \mathbf{E}^+ \cdot ((\mathbf{P}^+)^* - \mathbf{P}^+), \quad (3.20)$$

in which,

$$B_u = -s_u + \sum_i^{M-2} \sum_j^{M-2} (\gamma_{ui} - \gamma_{li}) [G^{-1}]_{ij} \gamma_{ju}, \quad (3.21)$$

$$B_l = s_l + \sum_i^{M-2} \sum_j^{M-2} (\gamma_{ui} - \gamma_{li}) [G^{-1}]_{ij} \gamma_{jl}. \quad (3.22)$$

Plugging in Eqs. (3.17) and (3.18) now yields the inversion equation in the same form as Eq. (1.24), with the renormalized inversion relaxation rate and equilibrium inversion,

$$\gamma'_{\parallel} = \frac{B_l T_u - B_u T_l}{T_u + T_l}, \quad (3.23)$$

$$d'_0(x) = \frac{B_u + B_l}{B_l T_u - B_u T_l} N(x), \quad (3.24)$$

proving that such a renormalization of an N-level atomic gain medium, with only a single lasing transition is possible under the stationary population approximation.

### 3.2.1 Physical limits of interest

The most immediately useful system to study, due to its relative simplicity while still retaining some of the critical features lacking in the two-level model, is a four-level atomic gain medium with a single lasing transition in which non-radiative transitions are only allowed between neighboring atomic levels, as illustrated in (Fig. 3.1), where the four levels are labelled from 0 – 3 in order of increasing energy. The parameters  $d'_0$  and  $\gamma'_{\parallel}$  for such a

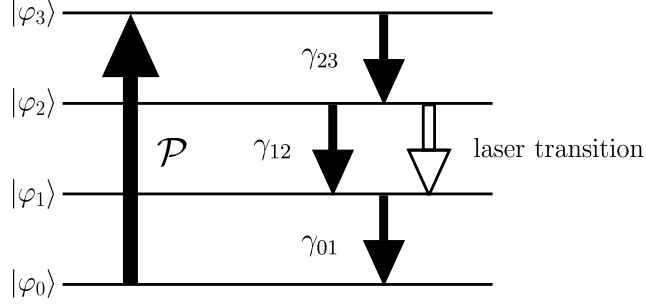


Figure 3.1: Schematic of a four-level gain medium.

system can be solved for using Eqs. (3.23) and (3.24) as [97],

$$\gamma'_{\parallel} = 2\gamma_{12} \left( 1 + \frac{S}{2 + \frac{\gamma_{01}}{\mathcal{P}} + \frac{\gamma_{01}}{\gamma_{23}}} \right) \quad (3.25)$$

$$D'_0 = \frac{S\mathcal{P}n}{\gamma_{01} + \left( S + 2 + \frac{\gamma_{01}}{\gamma_{23}} \right) \mathcal{P}}, \quad (3.26)$$

where  $S = (\gamma_{01} - \gamma_{12})/\gamma_{12}$ , and the pumping rate has been relabelled,  $\mathcal{P} = \gamma_{30}$ . Equation (3.26) for the inversion in the absence of laser emission (which here acts as the effective pump parameter) has been discussed by Siegman [2], while Eq. (3.25) for the effective relaxation rate has been derived for a special case by Khanin [96]. These expressions have not been used previously (to our knowledge) to solve the four-level lasing equations in terms of the two-level solutions. Here, we are modelling the pump as incoherent, such that the pump does not cause any additional non-radiative relaxations from the top state,  $|\varphi_3\rangle$ , to the bottom state,  $|\varphi_0\rangle$ . If this system were being excited by a coherent pump, such as another laser, this results in an additional decay rate,  $\gamma_{03} = \mathcal{P}$ , and alters the above results by adding a factor of 2 in front of the terms  $\gamma_{01}/\gamma_{23}$  in the denominators of Eqs. (3.25) and (3.26).

There are two important physical regimes for the four-level atomic gain medium. First, the linear regime, is when  $\gamma_{23} \sim \gamma_{01} \gg \gamma_{12} \gg \mathcal{P}$ , for which one recovers the expected behavior that the equilibrium inversion increases linearly with the pump and that  $\gamma'_{\parallel}$  is a

constant:

$$\gamma'_{\parallel} \approx 2\gamma_{12}, \quad (3.27)$$

$$d'_0(x) \approx \frac{\mathcal{P}}{\gamma_{12}} N(x). \quad (3.28)$$

In this case, varying the equilibrium inversion and the pump strength are essentially equivalent.

The second regime of interest, the non-linear regime, is when  $\gamma_{23} \sim \gamma_{01} \gg \gamma_{12} \sim \mathcal{P}$ , i.e. when the slow decay rate between the lasing levels is on the same order as the pump rate. In this regime,  $\gamma'_{\parallel}$  increases with increasing pump and  $d'_0$  saturates with increasing pump:

$$\gamma'_{\parallel} \approx 2(\gamma_{12} + \mathcal{P}), \quad (3.29)$$

$$d'_0(x) \approx \frac{1}{1 + \frac{\mathcal{P}}{\gamma_{12}}} \left( \frac{\mathcal{P}}{\gamma_{12}} \right) N(x). \quad (3.30)$$

This regime is also interesting from the viewpoint of SALT. As  $\gamma'_{\parallel}$  increases with  $\mathcal{P}$ , a laser could satisfy the inequality  $\gamma'_{\parallel} \ll \gamma_{\perp}$  near threshold, leading to stationary inversion and an accurate solution via SALT, but fail to satisfy the inequality as the pump becomes stronger, leading to a decrease in the accuracy of SALT. For a system with an arbitrary number of levels, the first regime always occurs at sufficiently small pump values; the second regime is obtainable if electrons in the upper lasing level are relatively long-lived compared to electrons in other levels.

### 3.2.2 Numerical comparison

To perform a well-controlled comparison between the renormalized SALT equations for an N-level gain medium and direct integration of the rate equations through the use of FDTD, we studied 1D microcavity lasers for which the FDTD calculations are tractable and fast enough to generate extensive steady-state data. We first consider the same simple edge emitting uniform-index laser treated in Refs. [21, 22, 24], with a perfect mirror at the origin, active region of length  $L$  terminating abruptly in air (see schematic, Fig. 3.2). The simulations were carried out using standard FDTD for the electromagnetic field, and



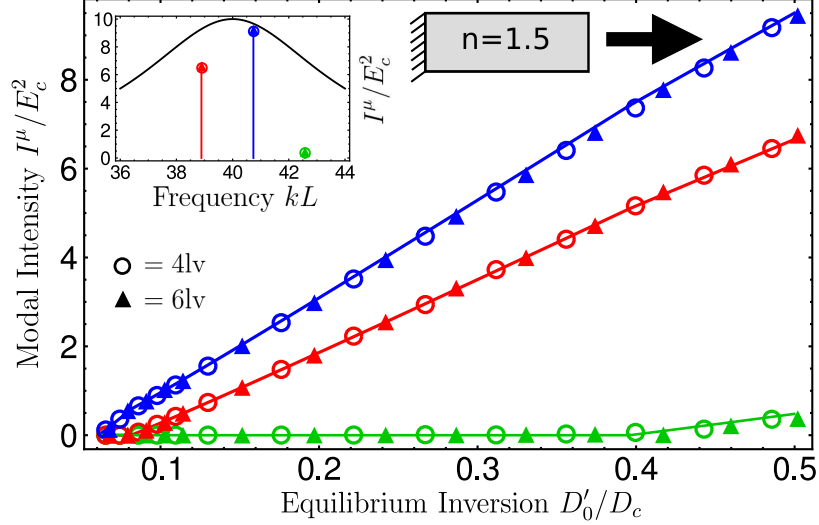


Figure 3.2: Modal intensities as functions of the normalized equilibrium inversion  $d'_0/d_c$  (effective pump) in a 1D microcavity edge emitting laser (schematic inset). The cavity is bounded on one side by a perfect mirror and on the other side by air, and has uniform refractive index  $n = 1.5$ . Solid lines are results obtained by the time-independent SALT method; open circles are results of FDTD simulations with a coherently pumped four-level medium (Fig. 3.1); solid triangles are results of FDTD simulations with a coherently pumped six-level medium with a lasing transition between  $|\varphi_3\rangle$  and  $|\varphi_1\rangle$ . Full simulation parameters are given in Appendix C. Both the four-level and six-level media are chosen to satisfy the stationary population approximation. The dephasing rate is  $\gamma_{\perp} = 4$ . The four-level system is in the linear regime described by Eqs. (3.27)-(3.28), while the six-level system is in the non-linear regime described by Eqs. (3.29)-(3.30). The spectra at  $d_0/d_c = 0.488$ , and the gain curve, are shown in the upper left inset.

presented here which does discretize space. It is worth emphasizing that SALT treats the non-linearity to infinite order; in the earlier work on the Maxwell-Bloch model [24] it was shown that for this same cavity the common cubic approximation for the non-linearity fails both quantitatively and qualitatively.

These results demonstrate that so long as the system satisfies the stationary population approximation, the mapping between systems with an arbitrary number of levels to an effective two-level system is nearly exact, and SALT is able to very accurately determine the steady state properties of the cavity. If two cavities, each with an arbitrary number of levels, have the same effective parameters  $d'_0$  and  $\gamma'_{\parallel}$ , and otherwise have the same polarization relaxation rate and atomic transition frequency, the cavities are equivalent from the electromagnetic point of view, and will have identical lasing properties.

The six-level simulations shown in Fig. 3.2 occupy the non-linear parameter regime of

Eqs. (3.29)-(3.30), i.e.  $\gamma'_{\parallel}$  is a linear function and  $d'_0$  a non-linear function of  $\mathcal{P}$ . However, the unscaled intensity of each mode at the edge of the cavity is, to leading order, linear in  $\mathcal{P}$ . The reason for this can be seen by rearranging Eq. (2.7), inserting the expressions for  $\gamma'_{\parallel}$  and  $d'_0$ , and noting that at the end of the cavity the inversion is roughly independent of the pump strength as seen in Fig. 3.3(c), as,

$$\frac{4g^2}{\hbar^2\gamma_{\perp}} \sum_{\nu=1}^{N_L} \Gamma_{\nu} |\Psi_{\nu}(x)|^2 = \gamma'_{\parallel} \left( \frac{d'_0}{d(x)} - 1 \right). \quad (3.32)$$

Substituting in Eqs. (3.29) and (3.30), which are valid for this simulation, gives

$$\frac{2g^2}{\hbar^2\gamma_{\perp}} \sum_{\nu=1}^{N_L} \Gamma_{\nu} |\Psi_{\nu}(x)|^2 = \mathcal{P} \left( \frac{N}{D(x)} - 1 \right) - \gamma_{12}. \quad (3.33)$$

The inversion  $d$  is a function of both position and the pump, and can be seen in Fig. 3.3(c) to have large spatial variations. Close to the mirror (left side of the cavity), the inversion is only strongly depleted at the maxima of the field intensity as the field intensity minima are nearly zero. This situation is unique to microlasers, whose resonators are only a few tens of wavelengths long. However, at the cavity edge,  $d$  should be mostly independent of the pump, as at this location every mode is at its maximum intensity and the effect of spatial hole-burning is most pronounced. The FDTD simulation results, shown in Fig. 3.3, demonstrate that  $d$  indeed varies very weakly with  $\mathcal{P}$  at the cavity edge. Since the left hand side of Eq. (3.33) evaluated at  $x = L$  is proportional to the total output intensity, the pump-independence of  $d(x)$  implies a linear behavior of the total unscaled output intensity as a function of the pump. Furthermore, in the absence of an unlikely conspiracy among the active lasing modes, each mode should independently be linearly dependent upon the pump strength, which is the behavior observed in Fig. 3.3(a).

The mapping between the  $N$ -level laser and two-level SALT breaks down at large pump strengths, when the condition  $\gamma'_{\parallel} \ll \gamma_{\perp}, \Delta$  is violated due to the increase of  $\gamma'_{\parallel}$  with  $\mathcal{P}$ . In Ref. [24], following an argument by Haken [134], it was demonstrated that violating this condition causes the SIA for the two-level model to break down. This effect can be seen in the four-level laser data in Fig. 3.4, where  $\gamma'_{\parallel} = 0.1, \gamma_{\perp} = 4.0$  and accuracy is already

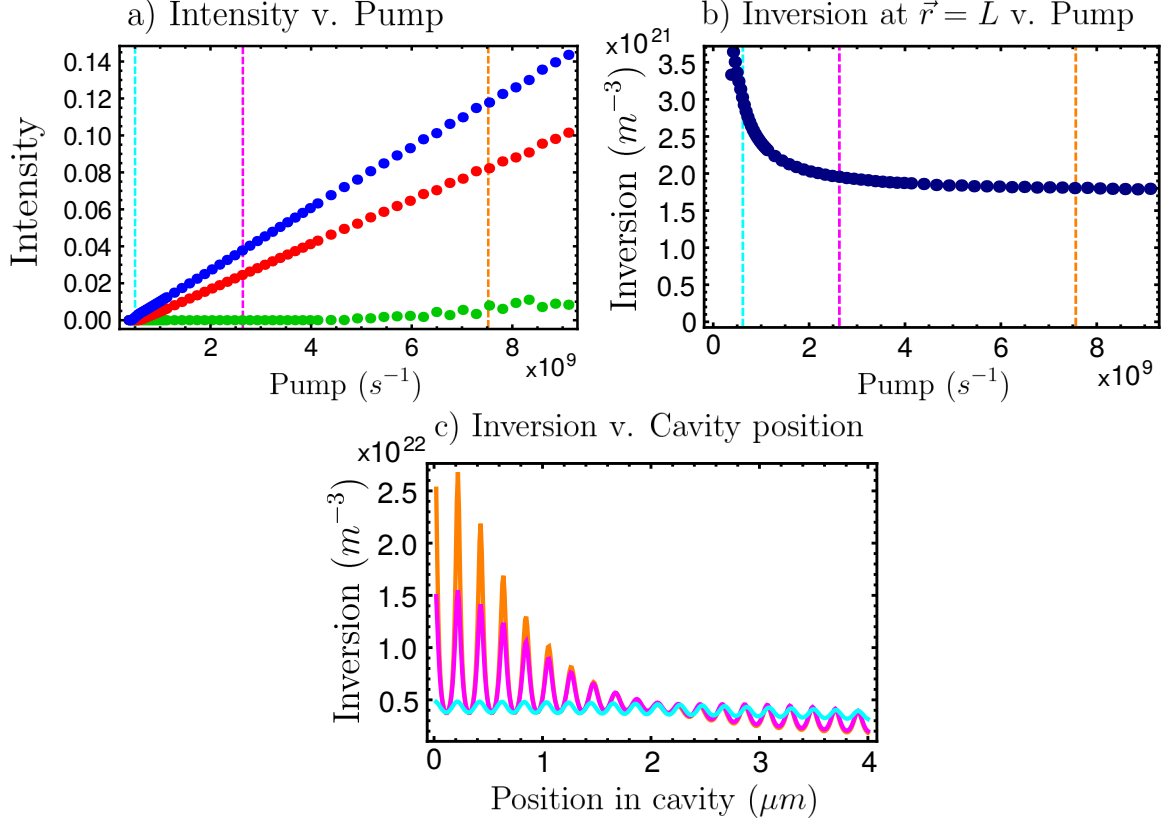


Figure 3.3: (a) Unscaled modal intensity of the six-level simulations from Fig. 3.2 as a function of the pump. A cross sectional area of  $1m^2$  is assumed to calculate the power. (b) Inversion as a function of the pump at the cavity boundary. Dashed lines in plots a and b correspond to the pump values shown in plot c. (c) Inversion as a function of position within the cavity for three different pump values, cyan corresponds with  $\mathcal{P} = 3.75 \times 10^8 s^{-1}$ , magenta with  $\mathcal{P} = 1.65 \times 10^9 s^{-1}$ , and orange with  $\mathcal{P} = 4.85 \times 10^9 s^{-1}$  to show the evolution of the inversion within the cavity as a function of the pump strength. As can be seen, the inversion at the end of the cavity stays relatively constant as the pump strength is increased.

lost for the third lasing mode. For the six-level data of Fig. 3.4, which is in the non-linear parameter regime, the stationary population approximation is satisfied and SALT agrees with the FDTD simulations for small values of the normalized equilibrium inversion; for larger values of  $d'_0$ , the SALT and FDTD results begin to diverge as  $\gamma'_{\parallel}$  becomes similar to  $\gamma_{\perp}, \Delta$ .

Finally, to demonstrate that the mapping to an effective two-level model works equally well for a complex laser cavity, Fig. 3.5 shows a comparison between SALT and FDTD simulations for a four-level gain medium in a one-dimensional random dielectric structure. A number of studies have been published on random lasers using such simulations [149,150];

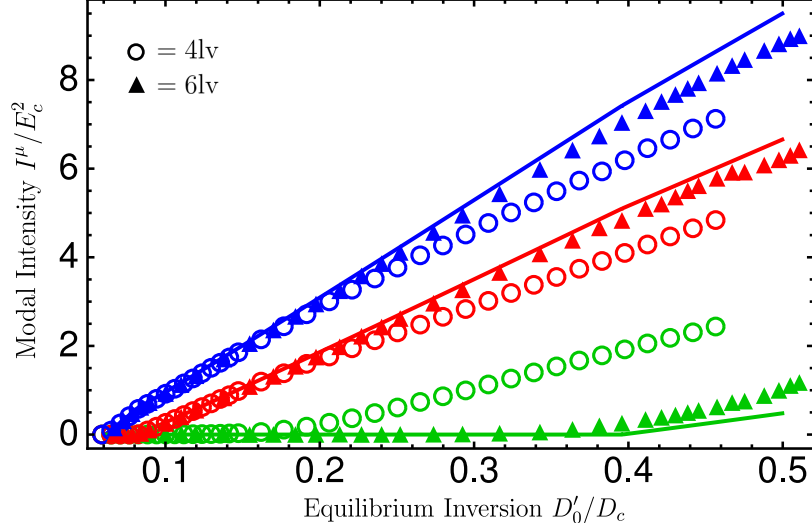


Figure 3.4: Breakdown of the equivalence between SALT and FDTD when the stationary population approximation is not valid is shown here in two different ways. Here, modal intensities as a function of the normalized equilibrium inversion  $d'_0/d_c$  (effective pump) are shown for a 1D microcavity edge emitting laser with  $\gamma_{\perp} = 4$  and  $n = 1.5$ . Solid lines again represent results obtained from SALT, while open circles represent FDTD simulations of a simple four-level system with  $\gamma'_{\parallel} = 0.1$ . Triangles represent FDTD simulations of a six-level system in the non-linear parameter regime in which  $\gamma'_{\parallel} \sim 0.001$  for  $d'_0 \leq 0.1$ , and thus satisfying the stationary population approximation, but  $\gamma'_{\parallel} \sim 0.01$  for  $d'_0 \geq 0.45$ , and consequently no longer satisfying the stationary population approximation.

SALT provides a much more efficient method for such studies, which often require generating a statistical ensemble of lasers. Here, the passive cavity dielectric function contains  $\sim 31$  layers, alternating randomly between regions with refractive indices  $n_1 = 1.25$  and  $n_2 = 1$ . Each random layer was generated according to the formula  $l_{1,2} = \langle l_{1,2} \rangle (1 + \eta \zeta)$  where  $\langle l_1 \rangle = (1/3)(L/30)$  and  $\langle l_2 \rangle = (2/3)(L/30)$  are the average thicknesses of the layers,  $\eta = 0.9$  represents the degree of randomness of the cavity, and  $\zeta \in [-1, 1]$  is a randomly generated number. The gain medium was added uniformly to the entire cavity, and the coherent pump was likewise uniform. The transition frequency was chosen such that  $n_1 k_a L = 120$ , corresponding to roughly 20 wavelengths inside of the cavity. We find only small discrepancies between the SALT and FDTD results, with  $\sim 1.1\%$  difference in the modal intensities. These differences did not vary significantly between different realizations of the random laser.

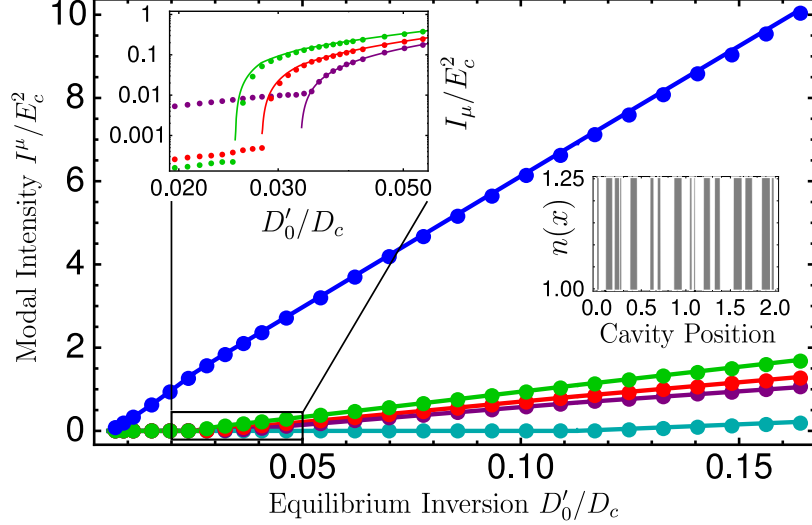


Figure 3.5: SALT and FDTD results for a one-dimensional random laser. Modal intensities are plotted against the normalized equilibrium inversion  $d'_0/d_c$  (effective pump). Solid lines represent SALT results, and circles represent FDTD simulations for a four-level system with  $\gamma'_{\parallel} = 0.001$ . The refractive index distribution of the edge emitting random laser is described in the text. The gain medium has  $\gamma_{\perp} = 4$  and is in the regime described by Eqs. (3.27)-(3.28). Left inset: log-log plot of the indicated region where three modes turn on in close proximity. Right inset: schematic of the cavity structure.

### 3.2.3 Numerical efficiency

In this section we present a set of benchmarks comparing the computational efficiency of SALT to FDTD. SALT calculations enjoy three main advantages over FDTD simulations of the semiclassical laser equations. First and foremost, SALT directly finds the steady-state solutions, so no time integration is involved, which substantially decreases computational effort. Second, SALT unambiguously determines how many modes are lasing at a given pump, whereas it can be difficult to determine, especially for multimode lasing, when an FDTD simulation has reached the steady-state with all modes that will lase “on.” Third, within SALT, with minimal additional computational effort, it is possible to monitor modes which are *below* threshold via a modified threshold matrix [23], and hence to ascertain if more modes are likely to turn on in some interval of pump.

Structurally SALT has one disadvantage with respect to FDTD. The convergence time in FDTD is determined by the longest time scale in the problem, which is the greater of beating period between consecutive modes and the relaxation oscillation time. These time

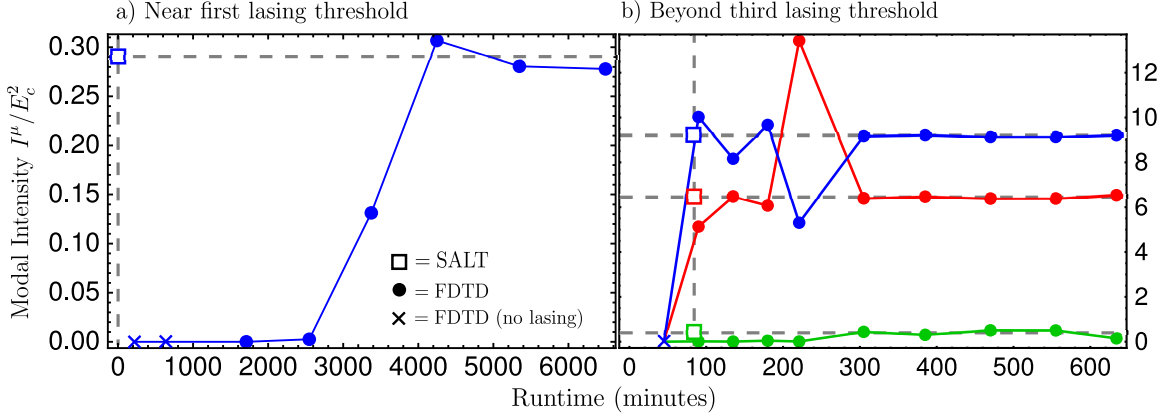


Figure 3.6: Comparison of SALT and FDTD run-times. Modal intensities are shown as a function of the run-time for SALT (squares) and four-level FDTD simulations (circles), using the parameters of Fig. 3.2. FDTD simulations that have not begun to lase are marked as crosses. Plot (a) shows data for  $d_0/d_c = 0.071$ , just above the first lasing threshold. SALT determined the steady-state single modal intensity in under three minutes, while the FDTD required  $\sim 5000$  minutes to reach steady state. Plot (b) shows data for  $d_0/d_c = 0.486$ , well above the third lasing threshold. SALT calculated all data up to and including this pump value in under 90 minutes, whereas FDTD required  $> 500$  minutes for the first two modes to reach steady-state, with the third mode intensity (green circles) still fluctuating after 500 minutes (not shown).

scales are usually independent of the number of modes lasing in the cavity, so the efficiency is largely independent of the pump in the multimode regime. This is not the case for SALT, as the computational time increases as  $N_L^2$  where  $N_L$  is the number of lasing modes. As SALT was implemented in this and previous works, it automatically calculates the entire lasing fields and spectrum up to a specific pump level, using the results from the lower pump values iteratively to expedite convergence. Thus this implementation of SALT is not optimized to produce numerical data at a single given pump level, well above threshold, as one can do easily with FDTD. However studies of the convergence of SALT with an initial guess far away from the final solution have shown that SALT is rather robust and flows to the correct stable solution [97], and codes optimized for this different type of calculation should be possible. As we see in Fig. 3.6, even a sub-optimal implementation of SALT is substantially more efficient than FDTD even when calculating the steady state of a single pump value.

Calculating full modal intensity/frequency curves as a function of the pump strength, such as in Fig. 3.2, is generally much more efficient using SALT. For example, in order to

generate the curves seen in Fig. 3.2, SALT ran for a little under 2 processor hours. To generate all of the FDTD data for the four level simulations took 267 processor days. If one is attempting to explore a large parameter space of designs or system parameters, SALT may make studies feasible which are simply impractical using FDTD, particularly in more realistic multi-dimensional structures.

As mentioned before, the bulk of the computational effort required for the SALT algorithm, especially in higher dimensions, is in solving for the TCF states. The TCF generalized eigenvalue problem is essentially identical in computational complexity to solving for a portion of the linear resonance spectrum of a cavity, something which is challenging in higher dimensional complex structures but feasible, particularly if one can use the scalar wave equation, as is the case for TM two-dimensional modes. In practice the number of TCF states needed is often  $\sim 10 - 20$  and should not exceed  $\sim 100$  in most cases of interest. It should be noted that the TCF basis library needs to be generated at a few dozen  $k$  values, which does increase the full computation compared to a single resonance calculation. Once one has a TCF basis library, using the SALT algorithm to iterate above threshold does not directly scale with the dimensionality of the system. However, more recent developments in solving the SALT equations are moving away from the use of the TCF equations, allowing for the use of finite element method algorithms, vastly decreasing the solution time for the Helmholtz equation in multi-dimensional cavities [118].

The runtime comparison shown in Fig. 3.6 is specific to the case of an FDTD implementation of a general atomic system without a specified number of modes. The most computationally expensive part of this calculation is in the left multiplication of the matrix determining the evolution of the atomic degrees of freedom. This can be greatly sped up by directly hard-coding the matrix inversion step, but this then forces a rewrite of the code for treating atomic gain media with different numbers of energy levels. Thus, for the simulations shown here, the matrix inversion is performed with a call to a generic inversion algorithm, which is computationally expensive. For performing FDTD simulations of the Maxwell-Bloch equations, where only three atomic fields are necessary (the inversion, and the real and imaginary parts of the polarization), the increase in efficiency of using SALT is not nearly so dramatic.

### 3.3 Multiple lasing transitions

When multiple lasing transitions are present, the multimode ansatz used in the derivation of SALT, Eq. (2.2) must be expanded to include constituent polarizations, Eq. (3.5),

$$p_j^+(x, t) = \sum_{\mu}^{N_L} p_{j,\mu}(x) e^{-i\omega_{\mu}t} \quad (3.34)$$

which still allows one to match frequency components for each constituent polarization using Eq. (3.4) to find

$$p_{j,\mu} = \frac{|\theta_j|^2}{\hbar} \frac{d_j}{\omega_{\mu} - \omega_{a,j} + i\gamma_{\perp,j}} \Psi_{\mu}. \quad (3.35)$$

To derive the C-SALT equations, this solution for the constituent polarization is inserted into the equation of motion for the atomic levels, Eq. (3.8), and the RWA is again made, resulting in

$$\partial_t \rho_n = \sum_{m \neq n}^M \gamma_{nm} \rho_m - \sum_{m \neq n}^M \gamma_{mn} \rho_n - \sum_j^{N_T} \frac{2|\theta_j|^2 \xi_{n,j} d_j}{\hbar^2 \gamma_{\perp,j}} \left( \sum_{\nu, \mu} \Gamma_{\nu,j} \Psi_{\nu}^* \Psi_{\mu} e^{-i(\omega_{\mu} - \omega_{\nu})t} \right). \quad (3.36)$$

To proceed, we first rewrite this equation in terms of a  $M$  element population density vector at each position in the cavity,  $\boldsymbol{\rho}(x)$ , whose components are the atomic level populations  $\rho_n(x)$ . Additionally, we make the stationary population approximation, which states that the beating between different lasing modes does not lead to significant time-dependence in the level populations, so  $\partial_t \boldsymbol{\rho} \approx 0$ . While a more detailed discussion of SPA will be given in Sec. 3.5, it is worth noting here that it is valid for most laser systems of interest, i.e. those with fast decays into and out of the lasing levels, while the upper lasing level of each transition is metastable and thus long lived. These fast relaxation rates need not be small compared to  $\Delta$  and  $\gamma_{\perp}$ , only the relaxation rates of the metastable upper lasing transitions need be slow in this sense, a condition which is numerically tested and confirmed by the FDTD simulations.

Thus, the above equation can be rewritten as

$$\mathbf{0} = R\boldsymbol{\rho} + \sum_j^{N_T} \frac{2|\theta_j|^2}{\hbar^2 \gamma_{\perp,j}} \left( \sum_{\nu} \Gamma_{\nu,j} |\Psi_{\nu}|^2 \right) \Xi_j \boldsymbol{\rho}, \quad (3.37)$$

where  $R$  is a matrix containing information about the pump and decay rates, and  $\Xi_j$  is a matrix containing information about which level populations are coupled to the partial polarizations and constitute the  $j$ th lasing transition. The full forms of these matrices are given in Appendix D.

Equation (3.37) is a homogeneous equation satisfied by the “vector” of atomic populations at each point in space. It requires knowledge of the lasing modes to be solved and hence will need to be solved simultaneously with the electric field equations. In addition, in the absence of gain diffusion, the total number of gain atoms at each point in space,  $N(x)$ , is externally fixed, and is a given of the problem. Hence the homogeneous Eq. (3.37) is to be solved subject to the normalization condition

$$\sum_n^M \rho_n(x) = N(x), \quad (3.38)$$

which uniquely determines the level population vector.

It is convenient to incorporate this normalization condition directly into Eq. (3.37) by defining a matrix  $B$  and an  $M$ -component total number vector  $\mathbf{N}(x)$  such that

$$B\boldsymbol{\rho} = \mathbf{N}(x), \quad (3.39)$$

where neither the matrix  $B$ , nor the vector  $\mathbf{N}(x)$  are uniquely defined, but must be chosen to represent Eq. (3.38). The normalization can then be inserted into Eq. (3.37), resulting in

$$\boldsymbol{\rho} = \left[ R + B + \sum_j^{N_T} \frac{2|\theta_j|^2}{\hbar^2\gamma_{\perp,j}} \left( \sum_{\nu}^{N_L} \Gamma_{\nu,j} |\Psi_{\nu}|^2 \right) \Xi_j \right]^{-1} \mathbf{N}(x). \quad (3.40)$$

To incorporate multiple lasing transitions into the SALT formalism to recover the C-SALT equations, all that must be altered is the equation for the electric susceptibility, Eq. (2.7), not the wave equation itself. Using Eq. (3.35), the electric susceptibility can be written as

$$\chi_g(x, \omega) = \frac{1}{\hbar} \sum_j^{N_T} \frac{|\theta_j|^2 d_j}{\omega - \omega_{a,j} + i\gamma_{\perp,j}}, \quad (3.41)$$

where  $d_j \equiv \rho_n^{(j)} - \rho_m^{(j)}$  is determined from Eq. (3.40). The main difference here is now the

atomic population densities cannot be directly inserted into the wave equation through the use of a scalar inversion equation. Instead we must simultaneously solve the wave equation, Eq. (2.6), and the population equation, Eq. (3.40). Using a non-linear iteration algorithm to solve the problem numerically, one inserts an initial guess for the field profiles,  $\{\Psi_\mu(x)\}$ , and uses these to solve for the full spatial profile of the atomic population densities. This result for the population densities generates a guess for the susceptibility, which can be inserted into the wave equation and iterated back and forth to self-consistency.

There is one other important difference between Eqs (2.7) and (3.41) in the case of a “partially pumped” laser, in which pumping is applied to only a subset of the regions containing gain media [126–130]. One needs to distinguish physically between two situations: 1) Having a (given) spatial density of gain atoms, which can be non-uniform, and hence will lead to non-uniform but always positive gain under conditions of uniform spatial pumping. This is taken into account from the specification of  $N(x)$  under the assumed conditions of spatially uniform pumping. 2) Spatial non-uniform pumping (“partial pumping”) in which there is a uniform distribution of gain atoms, which are not equally pumped. This would appear in our formalism as a variation with spatial position of the pumping rate parameters in the  $R$  matrix of Eq. (3.40). In this case non-pumped regions would act as absorbers for laser light, which would automatically be taken into account in terms of a spatial variation in the susceptibility function,  $\chi_g(x)$ , which would now have an absorbing form in those unpumped regions.

### 3.3.1 Comparison with FDTD

To perform a well controlled test of the stationary population approximation in C-SALT, for the case of multiple transitions, we studied 1D microcavity lasers for which FDTD simulations are tractable. We used a FDTD scheme similar to the one proposed by Bidégaray [148], altered to include multiple lasing transitions and additional atomic populations. These additional lasing transitions can be included into the FDTD simulations by extending both the atomic population and polarization vector  $\mathbf{u}$ , Eq. (A.10), and coupling matrix  $M$ , Eq. (3.31), to include an arbitrary number of real and imaginary atomic polarization terms that all couple to the electric field, and the evolution equation for the electric field Eq. (A.8)

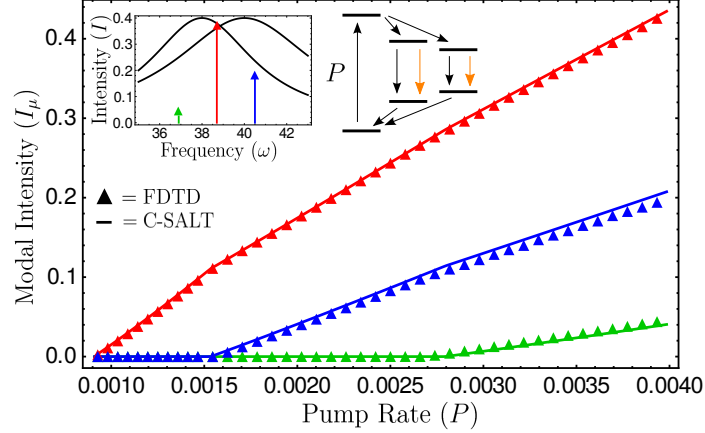


Figure 3.7: Plot of modal intensities as a function of pump strength for a cavity with  $n = 1.5$  and a gain medium consisting of atoms with two different atomic transitions,  $\omega_{a,1} = 40$ ,  $\gamma_{\perp,1} = 4$ ,  $\theta_1 = .1$ ,  $\omega_{a,2} = 38$ ,  $\gamma_{\perp,2} = 3$ ,  $\theta_2 = .1$ , and 6 atomic levels in total, with decay rates as indicated in the schematic. Results from C-SALT using the stationary population approximation are shown as straight lines, results from FDTD simulations are shown as triangles. The different colors indicate different lasing modes. Inset shows the modal frequencies and their intensities at  $P = .0035$ . All values are reported in units of  $c/L$ .

is extended to include contributions from these transitions as well. The simulations were run for a total duration at least  $40(1/\gamma_{\parallel})$ , the longest time scale in the model, to ensure a steady state was reached. The simulated laser cavity consists of a dielectric slab of background refractive index  $n = 1.5$ , with a perfectly-reflecting mirror on one side and an interface with air on the other. Distributed uniformly within the slab is a six-level gain medium, with two atomic transitions of slightly different frequencies and widths. The gain linewidths of the transitions overlap, as shown in the inset of Fig. 3.7, so each lasing mode receives significant gain contributions from both transitions. As shown in Fig. 3.7, excellent agreement is seen between C-SALT and FDTD simulations, both in predictions of modal intensity and frequency, thus quantitatively verifying the use of the stationary population approximation. In these simulations, only the relaxation rates of the metastable upper lasing levels are small compared to  $\Delta$  and  $\gamma_{\perp,j}$ ; the relaxation rates of other atomic levels are of the same order. This provides evidence for our earlier claim that the only rates which must be small when compared to  $\Delta$  and  $\gamma_{\perp,j}$  are those of the metastable upper lasing state.

### 3.4 Gain diffusion

The formalism developed in Sec. 3.3 can be extended to include gain diffusion, a phenomenon found in many types of gain media. A term representing this effect can be added to Eq. (3.36), resulting in

$$\partial_t \rho_n = \sum_{m \neq n}^M \gamma_{nm} \rho_m - \sum_{m \neq n}^M \gamma_{mn} \rho_n + D_n \nabla^2 \rho_n - \sum_j^{N_T} \frac{2|\theta_j|^2 \xi_{n,j} d_j}{\hbar^2 \gamma_{\perp,j}} \left( \sum_{\nu, \mu} \Gamma_{\nu,j} \Psi_{\nu}^* \Psi_{\mu} e^{-i(\omega_{\mu} - \omega_{\nu})t} \right), \quad (3.42)$$

where  $D_n$  is the longitudinal diffusion coefficient for the atomic level  $|n\rangle$ . Despite the similarities of Eqs. (3.36) and (3.42), there is one important difference, namely that the atomic populations at each spatial location are now coupled together. Thus, when diffusion is present, the population density vector  $\boldsymbol{\rho}$  is an  $M \times P$  dimensional vector whose components are atomic populations at each of  $P$  discretized spatial locations. The stationary population approximation can still be made, resulting in a generalized homogeneous equation for the population density vector,

$$\mathbf{0} = (R + D \nabla^2) \boldsymbol{\rho} + \sum_j^{N_T} \frac{2|\theta_j|^2}{\hbar^2 \gamma_{\perp,j}} \left( \sum_{\nu} \Gamma_{\nu,j} |\Psi_{\nu}|^2 \right) \Xi_j \boldsymbol{\rho}, \quad (3.43)$$

where  $D$  is the matrix of longitudinal diffusion coefficients at each spatial location, and the other two matrices  $R$ , and  $\Xi$  have also now been similarly expanded over the position basis as well. To correctly normalize Eq. (3.43), we note that one consequence of the stationary population approximation is  $\partial_t \sum_n \rho_n = 0$ , and when performing this sum on Eq. (3.42), one finds that the total population density is homogeneous in the steady state in the presence of diffusion,

$$0 = \nabla^2 \left( \sum_n^M D_n \rho_n \right). \quad (3.44)$$

Furthermore, the walls of the cavity prevent any flux of gain atoms across its borders, which is represented by the Neumann boundary condition

$$\partial_x \rho_n |_{x=0,L} = 0. \quad (3.45)$$

This, together with Eq. (3.44), yields the normalization

$$\sum_n^M \rho_n(x) = N. \quad (3.46)$$

This is a simple restatement of the fact that a diffusive gain medium in a passive cavity will be evenly distributed in the steady state, unlike a non-diffusive gain medium where the density of gain atoms can fluctuate depending on their distribution.

Note however, that while the diffusion condition implies that the number of “atoms” will be uniform in space, their excitation distribution will not be. Spatial hole-burning due to the spatial variation of the lasing modes above threshold will lead to a non-uniform gain even in the presence of uniform pumping and diffusion, and this effect is still captured by the theory. We will see below that these two effects compete; as the diffusion coefficient of the medium is increased, the excitation distribution will become more uniform in steady-state, counteracting the effects of spatial hole-burning.

Again, the normalization requirement can now be expressed as

$$B\boldsymbol{\rho} = \mathbf{N}, \quad (3.47)$$

where the matrix  $B$  and vector  $\mathbf{N}$  are likewise expanded over the spatial basis. Inserting Eq. (3.47) into Eq. (3.43) yields the generalized level population equation

$$\boldsymbol{\rho} = \left[ R + D\nabla^2 + B + \sum_j^{N_T} \frac{2|\theta_j|^2}{\hbar^2\gamma_{\perp,j}} \left( \sum_{\nu}^{N_L} \Gamma_{\nu,j} |\Psi_{\nu}|^2 \right) \Xi_j \right]^{-1} \mathbf{N}(x). \quad (3.48)$$

The solution now proceeds in the same way as in Sec. 3.3. Knowing the atomic level populations  $\boldsymbol{\rho}$ , we can use Eq. (3.41) to solve for the susceptibility, which is then inserted into the wave equation, Eq. (2.6). The problem thus reduces to a set of differential equations, one per lasing mode, coupled through the generalized level population equation, Eq. (3.48). The latter is now a much bigger matrix equation,  $MP \times MP$ , as opposed to  $M \times M$ , increasing the computational cost, but still keeping it within a manageable range, even for two-dimensional lasers, see Sec. 3.4.1.

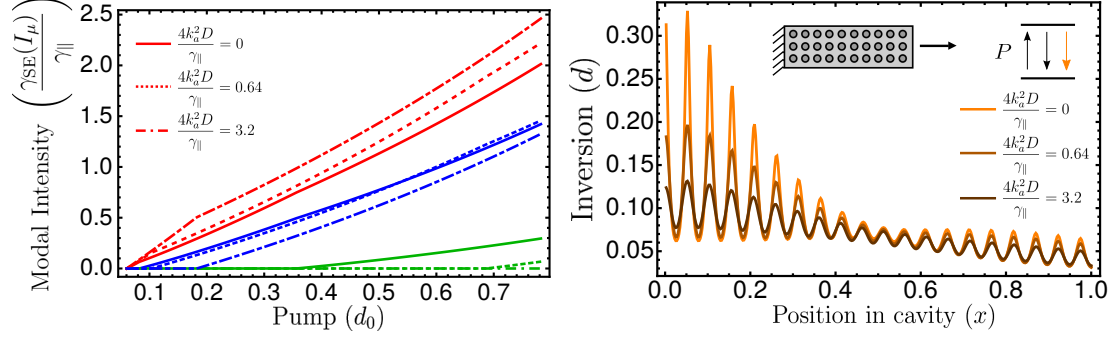


Figure 3.8: (Left panel) Plot of the modal intensities calculated using C-SALT as a function of pump strength for a dielectric slab cavity,  $n = 1.5$ , and a two level, single transition atomic gain medium, with  $\omega_a = 40$  and  $\gamma_{\perp} = 4$ , values again in units of  $c/L$ . Simulations for three different diffusion strengths are shown in solid, dashed, and dot-dashed lines. Different colors correspond to different lasing modes within each simulation. (Right panel) Plot of the inversion in the cavity as a function of position in the cavity at a pump strength of  $d_0 = 0.345$ . Darker colors indicate increasing values of the diffusion coefficient. Schematic shows a one-sided dielectric slab cavity containing a two level atomic medium subject to uniform pumping.

These two generalizations, Eqs. (3.40) and (3.48), along with their coupling to SALT, Eqs. (3.41) and (2.6), are the main results of this chapter. They extend the capabilities of SALT to cover many types of gain media, including newly-developed ones [137, 142]. C-SALT can thus be used as an efficient tool for the design and study of devices in which gain diffusion is present alongside spatial hole-burning, a regime which is challenging for traditional numerical methods to handle [139, 140, 146, 147].

### 3.4.1 Simulations of diffusive gain media

We now move to the case of lasers with multimode lasing and gain diffusion, for which FDTD is a very challenging computational effort, but which are relatively tractable using the C-SALT approach. In Fig. 3.8, we demonstrate how gain diffusion affects the transition from gain-clamped single-mode lasing (which can be described by the simplest form of laser theory [3]) to multimode lasing (which is possible as a result of spatial hole-burning). The left panel of Fig. 3.8 shows C-SALT simulations for a two level atomic medium with three different values for the diffusion coefficient. The solid lines show the modal intensities of the medium without diffusion, and dotted and dot-dashed lines of the same color show the evolution of the modal intensities as the diffusion coefficient is increased. We observe, as

expected, that increasing the diffusion coefficient postpones the transition from single-mode to multimode operation, by increasing the threshold of the second and higher-order lasing modes. In fact, for the largest diffusion coefficient the third lasing mode does not reach threshold within the pump values that were simulated. The right panel of Fig. 3.8 shows the inversion of the gain medium inside the cavity as a function of position within the cavity for a given pump value,  $d_0 = 0.345$ , a point at which all three simulations have exactly two lasing modes on. The faster the diffusion, the more uniform is the inversion in the presence of lasing. Darker colors indicate increasing values of the diffusion coefficient.

The results in Fig. 3.8 make intuitive sense: an increased diffusion coefficient spatially “smooths out” the population inversion of the first lasing mode; this supplies the first mode with more gain, acting against the effects of spatial hole-burning. Specifically, the right panel of Fig. 3.8 shows that increasing the diffusion coefficient flattens the inversion close to the cavity mirror, where the lasing modes spatially overlap. Near the end facet of the cavity, the gain is already being used fairly uniformly, so the effects of diffusion are substantially reduced. These results can also be understood quantitatively by writing down a steady-state, effective inversion equation for an atomic gain medium,  $d$ , which can be done as there is only a single lasing transition [98],

$$0 = \partial_t d = -\gamma_{\parallel}(d - d_0(x)) + D\nabla^2 d - \frac{4|\theta|^2}{\hbar^2\gamma_{\perp}} \sum_{\nu}^{N_L} \Gamma_{\nu}|E_{\nu}|^2 d, \quad (3.49)$$

where  $d_0(x)$  is the equilibrium value of the inversion density in the absence of both fields inside the cavity and diffusion. The final term on the right hand side can be identified as the rate of stimulated emission,

$$\gamma_{\text{SE}}(I) = \frac{4|\theta|^2}{\hbar^2\gamma_{\perp}} \sum_{\nu}^{N_L} \Gamma_{\nu}|E_{\nu}|^2, \quad (3.50)$$

which is spatially dependent and proportional to the intensity of the local electric field. Using the stationary population approximation, Eq. (3.49) can be solved for the inversion density, as

$$d(x) = \left[ 1 + \frac{\gamma_{\text{SE}}(I)}{\gamma_{\parallel}} - \frac{D}{\gamma_{\parallel}} \nabla^2 \right]^{-1} d_0(x). \quad (3.51)$$

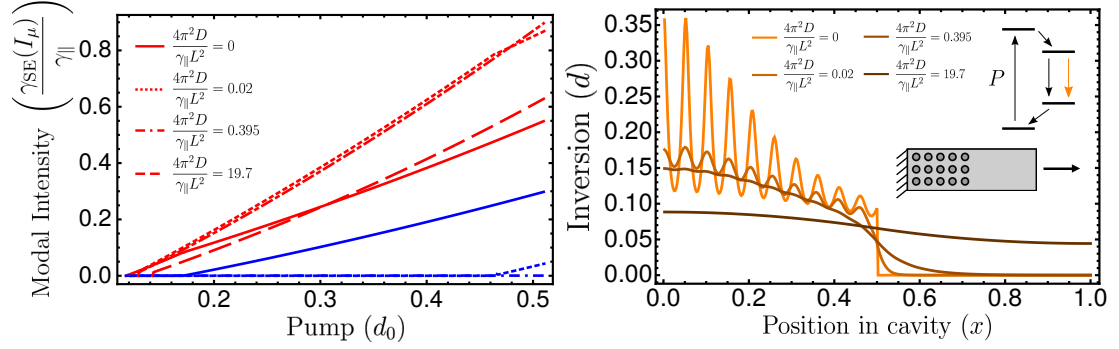


Figure 3.9: (Left panel) Plot of the modal intensities calculated using SALT as a function of pump strength for a partially pumped dielectric slab cavity,  $n = 1.5$ , containing a four level, single transition atomic gain medium. Simulations of four different values of diffusion are shown as solid, dotted, dot-dashed, and dashed lines. The first lasing mode to turn on in all of the simulations is shown in red, and the second lasing mode, which only turns on in two of the simulations, in blue. (Right panel) Plot of the inversion in the cavity as a function of position in the cavity at a pump strength of  $d_0 = 0.37$ . Darker colors indicate increasing values of the diffusion coefficient. Schematic shows a partially pumped one-sided dielectric slab cavity containing a four level atomic medium with a single lasing transition.

Thus, for diffusion to be germane to the system,

$$\frac{k_D^2 D}{\gamma_{\parallel}} \gtrsim 1 + \frac{\gamma_{SE}(I)}{\gamma_{\parallel}}, \quad (3.52)$$

where  $k_D$  is the wavevector associated with the scale of the inhomogeneity in the inversion. If the inversion is less than this, the gain atoms are unable to move very far before they either non-radiatively decay or undergo stimulated emission, preventing the diffusion from washing out the effects of the spatial inhomogeneity in the inversion. For spatial hole-burning, this variation in the inversion is on the order of the atomic transition wavelength,  $k_D = 2k_a$ , as the inversion oscillates twice as fast as the electric field [136]. This prediction is consistent with the numerical results shown in Fig. 3.8, where the onset of strong diffusion suppresses multimode operation and leads to gain clamped behavior.

For partially pumped cavities [126–130], there is, in addition to the scale associated with smoothing out spatial hole-burning, another relevant scale for measuring the strength of diffusion. This is the scale at which the diffusion begins to overcome the spatially inhomogeneous pumping, an inhomogeneity on the scale of the entire cavity length. Quantitatively, this can still be understood from Eq. (3.52), except that now  $k_D = 2\pi/L$ , where  $L$  is the

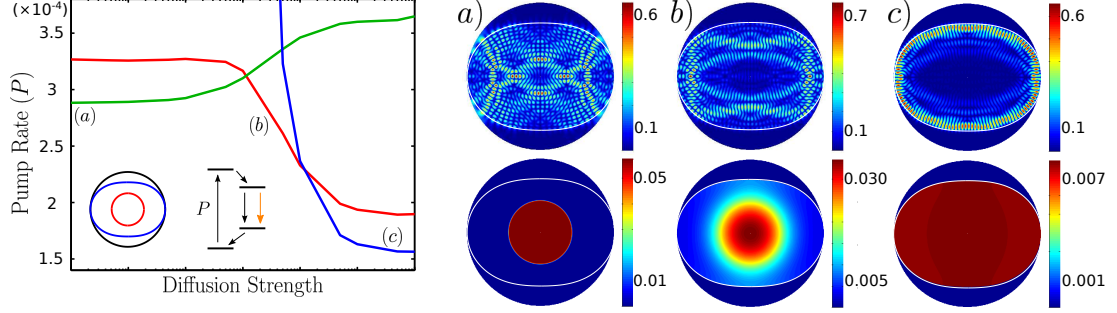


Figure 3.10: Plot of the non-interacting modal thresholds as a function of the diffusion coefficient in a quadrupole cavity with  $\epsilon = 0.16$ ,  $r_0 = 3.45\mu\text{m}$ ,  $k_a = 6.27\mu\text{m}^{-1}$ ,  $\gamma_{\perp} = .19\mu\text{m}^{-1}$ ,  $n = 3 + .004i$ . Only the three modes that become the threshold lasing mode for different values of the diffusion are plotted. Left schematic within the plot shows the boundary of the simulated region, black circle, boundary of the cavity, blue quadrupole, and applied pump profile, red circle. The right schematic within the plot depicts the four level gain medium that fills the entire quadrupole cavity. Markers in the plot correspond to the threshold lasing mode and corresponding inversion profile accounting for the effects of diffusion at their locations. The inversion profile is shown in a false color plot, with red corresponding to large inversion, and blue corresponding to small inversion. The white boundary in the plots denotes the cavity boundary.

length of the cavity, and we are assuming that the variation of the pumping is on the scale of the entire cavity. This leads to the criterion that when  $4\pi^2 D/L^2 > \gamma_{\parallel} + \gamma_{\text{SE}}(I)$  diffusion will strongly reduce the effects of non-uniform pumping by allowing the inversion to penetrate into the non-pumped regions.

Both types of diffusion-induced transitions are demonstrated in Fig. 3.9, which shows the results of C-SALT simulations of a four-level gain medium with a single transition, which is only pumped in half the cavity. A two-level medium would not be suitable for this test as it would have strong absorption in the unpumped region. As the diffusion coefficient is increased, the first transition from the spatial hole-burning regime to the spatially-averaged gain saturation regime is observed, as well as the effects of gain clamping which increases the second lasing threshold. In this regime, the inversion does not penetrate into the unpumped region. However, as the diffusion coefficient is further increased, the inverted atoms are able to penetrate further into the unpumped region. For this example, the effective spatial scale of the partial pumping is the length of the cavity,  $L$ , by choice. As expected, we observe this second transition when  $4\pi^2 D/L^2 \gamma_{\parallel} \sim 1 + \gamma_{\text{SE}}(I)/\gamma_{\parallel}$ . Once the first transition has occurred the gain is sufficiently clamped, even though it is not uniform over the entire cavity, and we

only find single mode lasing. If one intentionally pumps non-uniformly on a smaller scale than  $L$ , that would decrease the diffusion coefficient needed for the second transition until in the case of wavelength scale non-uniform pumping the two transitions would coincide roughly.

To demonstrate the scalability of C-SALT to multiple dimensions we ran 2D TM simulations of quadrupole-shaped dielectric cavities, whose boundary is defined by the equation  $r(\theta) = r_0(1 + \epsilon \cos(2\theta))$ , where  $\epsilon$  represents the degree of deformation from a circular cavity. Such cavities have been extensively studied in the context of wave chaos theory and experiments [60, 61, 97]. It was found that the spatial profile of the first lasing mode depends upon both the deformation and the pumping profile [60, 61, 97]. Here we show in Fig. 3.10 that for a quadrupole cavity with  $\epsilon = 0.16$  which is being partially pumped in the middle of the cavity, the spatial profile of the threshold lasing mode changes with the strength of the carrier diffusion in the system. When the diffusion strength is too weak to overcome the partial pumping of the cavity, the first threshold mode is found to have strong angular dependence in its far-field intensity output and heavily overlap the center of the cavity where the gain medium is inverted. As the diffusion coefficient is increased, the threshold lasing mode changes to become one that lives closer to the edge of the cavity, increasing its lifetime. Finally, when the gain becomes nearly uniform due to diffusion, we find that the threshold lasing mode is a whispering gallery mode.

### 3.5 Discussion of the stationary population approximation

In the derivation of the population equation given above, Eq. (3.40), we took as an assumption that the beating terms from the coupling of different mode amplitudes averaged to zero and thus could be neglected. In this section we will make explicit this approximation. Similar to the discussion for a two-level gain medium in Sec. 2.2, there are two criteria that go into the stationary population approximation: the populations do not acquire beating terms in the presence of multiple lasing modes, and that relaxation oscillations are not resonantly enhanced by being driven at the beat frequency. As previously discussed, for a two level medium, the former criterion requires that  $\gamma_{\parallel} \ll \Delta, \gamma_{\perp}$ , and the later requirement

that  $\omega_r \sim \sqrt{\kappa\gamma_{\parallel}} < \Delta$ . The main difficulty encountered when generalizing these equations in the presence of multiple transitions is the absence of an explicit formula for an effective  $\gamma_{\parallel}$  parameter entering these inequalities. However, the example of the N-level single transition case [98], for which we have such an explicit formula, strongly suggests if all of the  $\{\gamma_{lu}\}$  are small in the relevant sense, (where  $\{\gamma_{lu}\}$  is the set of non-radiative decay rates from the upper lasing level to the lower lasing level of each lasing transition) then the stationary population approximation will hold. Thus, since  $\kappa \leq \Delta$  (they are comparable for most of the lasers studied here), as long as  $\sqrt{\Delta} > \sqrt{\gamma_{lu}^j}, \forall j$ , we expect that the stationary population approximation will be satisfied. This is consistent with our FDTD simulation results.

In the limit of small violations of the stationary population approximation, it is possible to correct perturbatively for the effects of the beating populations within a generalized SALT framework. This calculation is discussed in Appendix E.

### 3.6 Free-carrier semiconductors in SALT

A natural extension of the discussion on atomic gain media with multiple transitions is to a treatment of bulk semiconductor gain media, in which there is a continuum of available transitions for the electrons between the conduction and valence bands. In doing so, we must also consider Pauli exclusion and Fermi-Dirac statistics. The polarization-Bloch equation for semiconductor media was originally derived by Lindberg and Koch, who took into account many-body effects [102],

$$(\hbar\omega - \Delta\varepsilon_q + i\hbar\gamma_q)\rho_{cv,q}(x, \omega) = (f_{c,q}(x) - f_{v,q}(x)) \left[ \theta_q E(x, \omega) + \frac{1}{V} \sum_{q'} V_s(q - q') \rho_{cv,q'}(x, \omega) \right], \quad (3.53)$$

in which  $\rho_{cv,q}$  is the off-diagonal density matrix element between the conduction and valence bands at electron momentum  $q$ ,  $\theta_q$  is the dipole matrix element for the transition at  $q$ ,  $\Delta\varepsilon_q$  is the re-normalized energy difference between the conduction and valence states,  $\gamma_q$  is the dephasing rate, and  $V_s$  is the Coulomb interaction. Note that the inversion term is the simplification of  $f_c(1 - f_v) - f_v(1 - f_c)$ , the probability that a conduction state is filled and the relevant valence state is open minus the probability that a valence state is filled and

the conduction state is open. The macroscopic polarization field in Maxwell's equations is then given by [103]

$$P(x, \omega) = \frac{1}{V} \sum_q \theta_q \rho_{cv,q}(x, \omega). \quad (3.54)$$

To proceed we will make the free-carrier approximation, setting  $V_s = 0$ , with full understanding that Coulomb repulsion is an important effect in semiconductor lasers, and thus that the results found here are just the first step towards a more complete theory. Doing so allows one to write down the free-carrier susceptibility,

$$\chi_g(r, \omega) = \int d^3q \frac{2}{(2\pi)^3} \theta_q^2 \frac{f_{c,q}(x; \phi, |E|) - f_{v,q}(x; \phi, |E|)}{\hbar\omega - \Delta\varepsilon_q + i\hbar\gamma_q}, \quad (3.55)$$

where the factor of two appearing in the numerator accounts for spin degeneracy. The factors of  $f_{c,q}$  and  $f_{v,q}$  are simply the occupation probabilities for finding an electron at momentum  $q$  in the conduction and valence bands respectively and depend both upon the applied electric potential,  $\phi$ , as well as the magnitude of the electric field within the cavity. The inversion equations, taking into account Fermi-Dirac statistics, take the form:

$$\partial_t d_q(x) = -\gamma_{\parallel,q}(d_q(x) - d_q^{(0)}) - \frac{2}{i\hbar} ((E\theta_q^* \rho_{cv,q})^* - c.c.) \quad (3.56)$$

$$d_q(x) = f_{c,q}(x) - f_{v,q}(x) \quad (3.57)$$

$$\begin{aligned} d_q^{(0)} &= f_{c,q}^{(0)} - f_{v,q}^{(0)} \\ &= \frac{1}{e^{\beta(\varepsilon_{c,q} - \mu - e\phi)} + 1} - \frac{1}{e^{\beta(\varepsilon_{v,q} - \mu + e\phi)} + 1}, \end{aligned} \quad (3.58)$$

where  $\gamma_{\parallel,q}$  is the non-radiative interband relaxation rate between the conduction and valence bands at momentum state  $q$ , and  $f_{c,q}^{(0)}$  is the Fermi function for the conduction band at momentum  $q$  in which we have introduced the electro-chemical potential  $\mu + e\phi$ . In this theory the applied voltage  $\phi$ , related to the injected current, will play the role of the pump. In writing such a simple inversion equation we are neglecting intraband transitions, which is why a population equation similar to Eq. (3.40) is not needed here.

Next, we expand  $E(x, t)$  and  $\rho_{cv,q}(x, t)$  as a summation of distinct lasing modes with different spatial profiles in the same manner as done previously in Eqs. (2.1) and (2.2).

Using the above equations, we again assume stationary inversion of all of the constituent transitions  $\partial_t d_q(x) = 0$ , assuming that the modal beating terms in the product  $E\rho_{cv,q}^*$  are negligible, so that we can solve for the susceptibility and insert it into Maxwell's wave equation, resulting in the Semi-SALT equations,

$$0 = [\nabla^2 + (\varepsilon_c + 4\pi\chi_g(x, \omega)) k_\mu^2] \Psi_\mu \quad (3.59)$$

$$\chi_g(x, \omega) = \int d^3q \frac{2}{(2\pi)^3} \theta_q^2 \frac{f_{c,q}^{(0)} - f_{v,q}^{(0)}}{\hbar\omega - \Delta\varepsilon_q + i\hbar\gamma_q} \left( \frac{1}{1 + \frac{4\theta_q^2}{\gamma_\parallel \hbar} \sum_\nu \Gamma_{\nu,q} |\Psi_\nu(x)|^2} \right) \quad (3.60)$$

where

$$\Gamma_{\nu,q} = \frac{\hbar\gamma_q}{(\hbar\omega_\nu - \Delta\varepsilon_q)^2 + \hbar^2\gamma_q^2} \quad (3.61)$$

is the Lorentzian linewidth.

To solve the Semi-SALT equations we will assume that we are modeling a direct band-gap semiconductor laser where the renormalized energy gap can be written as

$$\Delta\varepsilon_q = \frac{\hbar^2 q^2}{2m_r} + E_g \quad (3.62)$$

in which  $m_r$  is the reduced mass and  $E_g$  is the energy gap when  $q = 0$ . If we take both  $\gamma_q$  and  $g_q$  to be independent of  $q$ , we find that the integral defining the real part of  $\chi$  is divergent, as both the numerator and the denominator  $\propto q^4$ , and for large  $q$ ,  $d_q^{(0)} \rightarrow -1$ . This is a known problem [90], which stems from the fact that the Lorentzian line-shape of the dipole transition is too broad and that other many-body effects truncate the line-shape. However, within the assumptions already used in this treatment the integral can be regularized by incorporating the correct  $q$  dependence in to  $\theta_q$  [90],

$$\theta_q = \frac{\theta_0}{1 + \frac{\hbar^2 q^2}{2m_r} \frac{1}{E_g}} \quad (3.63)$$

in which

$$\theta_0 = \langle \lambda' | \hat{p} | \lambda \rangle \quad (3.64)$$

and where  $|\lambda\rangle$  represents a lattice periodic function,  $\hat{p}$  is the momentum operator, and as

such  $\theta_0$  has no further dependence upon  $q$ . Note that even when many-body effects are considered,  $\gamma_q$  is still relatively constant as a function of  $q$ .

Numerically solving the Semi-SALT equations is substantially more computationally demanding than the usual SALT [98], or C-SALT equations discussed above. The reason for this is two-fold. First, the electric susceptibility no longer depends linearly upon the pump variable. Instead the applied electric potential,  $\phi$ , appears in the Fermi-Dirac functions defining the equilibrium inversion of the semiconductor, yielding a nonlinear dependence in the susceptibility on the applied potential. This has the effect of making the lasing threshold problem non-linear in the pump variable and thus increasing the computational difficulty, both to find the first lasing threshold, and to find subsequent laser thresholds for additional modes. Second, the integral over  $q$  must be performed at each spatial location, another computationally expensive task.

### 3.6.1 Performing the Semi-SALT calculation

There are two main new difficulties that one encounters upon implementing Semi-SALT that are not seen in SALT computations using atomic gain media. The first is that the lasing threshold problem is no longer linear in the pump parameter. To find the non-interacting laser thresholds using the TCF basis [25] one must solve the equation,

$$\eta_n(\omega_\mu) = 4\pi \int \frac{2}{(2\pi)^3} d^3q \theta_q^2 \left( \frac{d_q^{(0)}}{\hbar\omega_\mu - \Delta\varepsilon_q + i\hbar\gamma_q} \right), \quad (3.65)$$

which cannot be reformulated as a linear eigenvalue problem. Here,  $\eta_n(\omega)$  is the eigenvalue being tracked across frequency space of the TCF basis equation for which we are attempting to determine where the threshold lasing state it corresponds to reaches threshold. Instead, to find all of the laser thresholds one must use both the real and imaginary parts of this equation to first solve for  $\phi_{thr}$  where  $\text{Re}[\eta(\omega)] = 4\pi\text{Re}[\chi_g(\omega, \phi_{thr})]$ , and then solve for the offset in the imaginary part of this equation,

$$\delta = \text{Im}[\eta(\omega)] - 4\pi\text{Im}[\chi(\omega, \phi_{thr})]. \quad (3.66)$$

By monitoring for when  $\delta$  changes sign as the frequency is swept through, the lasing threshold can be found.

The second main computational problem arises from attempting to directly solve the Semi-SALT equations, Eqs. (3.59) and (3.60), using a non-linear solver above threshold. Such an algorithm for finding the solution to the Semi-SALT equations requires evaluating the integrals over the electron momentum at every point in space for every guess at the lasing mode amplitudes and frequency until the non-linear solver converges, and is hopelessly inefficient. Instead, for each iteration of the Semi-SALT equations in the pump variable above threshold this difficulty can be sidestepped by performing a Taylor expansion on the electric susceptibility in terms of the variables solved for at each iteration above threshold,

$$\chi_g(\omega_{N+1}, \vec{a}_{N+1}) = \chi(\omega_N, \vec{a}_N) + \left. \frac{\partial \chi}{\partial \vec{a}} \right|_N \cdot (\vec{a}_{N+1} - \vec{a}_N) + \sum_{\nu} \left. \frac{\partial \chi}{\partial \omega_{\nu}} \right|_N (\omega_{\nu, N+1} - \omega_{\nu, N}) \quad (3.67)$$

where  $\chi(\omega_N, \vec{a}_N)$  is the self-consistent solution for the electric susceptibility for the applied electric potential  $\phi_N$ , and is a function of all of the different lasing frequencies present,  $\{\omega_{\mu}\}$  and the decomposition of the all of the lasing modes  $\{\Psi_{\mu}\}$ , where,

$$\Psi_{\mu}(x) = \vec{a}^{(\mu)} \cdot \vec{u}(x; \omega_{\mu}), \quad (3.68)$$

is the spatial decomposition of each lasing mode over the TCF basis at the correct frequency. Using this Taylor expansion of the susceptibility, now all of the spatially dependent integrals can be evaluated before invoking the non-linear solver, dramatically improving performance.

### 3.6.2 Semi-SALT results

Even under the limiting assumptions made, Semi-SALT is able to predict two features unique to semiconductor lasers, as seen in Fig. 3.11. Unlike the atomic gain media discussed above, the gain curve of a semiconductor gain media is asymmetric due to the continuum of transitions available above the energy gap. As such, we expect that the thresholds of lasing modes with frequencies above the energy gap will experience more gain and thus have lower thresholds, an effect clearly seen in the left panel of Fig. 3.11. The frequencies of

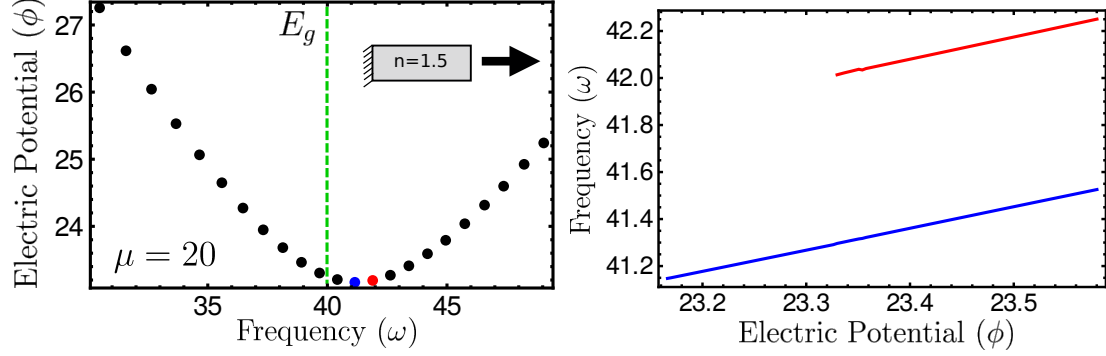


Figure 3.11: (Left panel) Plot of the lasing thresholds for each of the non-interacting modes in the cavity as a function of the applied electric potential,  $\phi$ , for a single sided, slab semiconductor laser. The energy gap at  $q = 0$  has been set to  $E_g = 40$ , and the chemical potential set at half that,  $\mu = 20$ . The non-interacting thresholds of the two modes studied in the right panel are given the same colors as appear in the right panel. (Right panel) Plot of the frequencies of the two lasing modes as a function of the applied electric potential. The frequency for the second lasing mode (red) is only shown after it reaches threshold.

semiconductor laser modes are also expected to shift away from the energy gap as the pump is increased due to Pauli blocking, additional electrons excited across the band gap from the increasing the applied electric potential must find higher energy states to transition to, yielding more energetic stimulated emission transitions. This effect is clearly predicted by Semi-SALT, as shown in the right panel of Fig. 3.11.

In general, quantitative computational study of semiconductor lasers is very challenging and is only feasible with supercomputers and specialized codes. We hope that incorporating the steady-state ansatz and the SIA into the electromagnetic part of the calculation, as is done in Semi-SALT, could eventually lead to more efficient computational approaches to parts of this problem.

### 3.7 Summary

In this chapter we have demonstrated how to expand SALT to treat realistic and complex gain media. Using the stationary population approximation, N-level atomic gain media with a single lasing transition can be renormalized to a two-level system, while gain media with multiple transitions can be treated using C-SALT. Furthermore, we have shown how to incorporate gain diffusion into the SALT formalism. Using a frequency domain solution

method is substantially more efficient computationally than incorporating diffusion into an FDTD algorithm because the effects of diffusion are numerically stiff, and thus require the use of very small time steps. Finally, we have given an initial treatment of semiconductor gain media in SALT. In the next chapter, we will show how to treat amplified signals simultaneously with any lasing modes within the laser cavity naturally using the SALT framework.

## Chapter 4

# Injected Signals

Laser action in the presence of an injected signal is an extremely important topic for research in both nonlinear dynamics and laser physics and for applications of lasers. Under certain conditions, a laser mode can be locked to the injection frequency, allowing for stabilization and modulation of a “slave” laser based on control by a “master” laser. This and related effects have been the topic of a large literature going back to the beginning of laser theory [115, 151–153] and certain features are now well-described in textbook treatments [2], where the basic paradigm is that of frequency locking of nonlinear oscillators as described by Adler [121] well before the invention of the laser.

From the mid-1970s onward [3], it was also appreciated that lasers with injected signals can exhibit complex dynamical behavior and even chaos based on the general principle of nonlinear dynamics that damped driven nonlinear systems with three or more independent time-varying fields generically have nontrivial dynamics over large regions of phase space [101, 154]. Since the basic laser equations involve three distinct and possibly complex functions (the electric field, the polarization, and the inversion amplitude) a self-oscillating laser without injection can exhibit this behavior [3], but in most lasers the time scales are such that the polarization field (Class B laser) or the polarization and inversion (Class A laser) can be adiabatically eliminated and treated as functions of the other variables, leaving only one or two independent field(s). Experiments have also been able to verify many of these effects [155–158].

Class B lasers are by far the most common type (they include semiconductor and most

other solid state lasers), and so injecting an additional signal can in many cases generate interesting dynamical states outside the locking region. Hence Class B lasers with an injected signal have been used extensively to study such states in the past 30 years. Deterministic chaos was first reported in Class B lasers with injected signals by Arecchi *et al.* [99], who introduced the Class A, B, and C categories based on the relative size of the decay rates of the electric field,  $\kappa$ , polarization,  $\gamma_{\perp}$ , and inversion of the gain medium,  $\gamma_{\parallel}$ . (Class C is the case in which all time constants are comparable, none of the fields can be adiabatically eliminated, and the laser in isolation can exhibit chaotic dynamics. These lasers are very rare and are not technologically important.) The goal of much of this earlier work has been to understand and categorize all of the different regimes of stability, bistability, and instability for injected class B lasers [99, 100, 156, 159–161]. These interesting dynamical effects arise because the injected signal beats against the existing, free-running laser output and drives the inversion to oscillate at this beat frequency. When this frequency coincides with other relevant dynamical scales in the laser, usually the frequency of the relaxation oscillations,  $\omega_r \sim \sqrt{\kappa\gamma_{\parallel}}$ , resonant driving occurs, leading to complex dynamics. In addition, for semiconductor lasers, there are dynamical scales associated with the dispersion of the gain medium [162], and to carrier dynamics, which enter the equations as well; these effects arise from the real part of the gain susceptibility at the lasing frequency and are quantified by the Henry  $\alpha$  factor [18, 19, 156, 162].

In the current work we develop a theory of injection locking of Class A and B lasers in a regime relevant particularly to microlasers, in which complex dynamical states do not arise, and for atomic like gain media for which the  $\alpha$  factor is typically negligible. The existence of such a regime does not seem to have been clearly identified in previous work on injection locking. In this regime the physical effect is primarily that of quenching of the free-running laser oscillation due to cross saturation. There have been some relatively recent works [163, 164] emphasizing locking through cross saturation as opposed to synchronization, but these models do not include spatial hole burning, which we find to play an important role, and the models also involve many more approximations than our method, which is essentially an exact solution of the problem in the relevant regime.

The approach here is a generalization of SALT. SALT keeps the full space dependence of

the electric field, polarization, and inversion and hence goes beyond the earlier treatments that led to the classifications A, B, and C, where these quantities were only functions of time. In this chapter, we retain this terminology to reference the hierarchy of time scales, but refer to the electric field, polarization, and inversion as fields. The accuracy of the generalized theory, injection-SALT, or I-SALT, is here confirmed by direct simulation of the relevant Maxwell-Bloch equations describing the laser with injected signal. In the limit where the laser is locked to the input signal we show that an approximate treatment of our theory reduces to an Adler type of steady-state solution, but that the behavior outside of the locking range is completely different than expected from the Adler description. Moreover, the Adler approximation is not very accurate for the phase difference between the locked input signal and the resulting amplified output. The only substantial approximation in I-SALT is the same as that for SALT, the neglect of the field beating terms in the multimode regime which can lead to complex dynamics and destabilize the multimode solution, which leads to the stationary inversion approximation (SIA). Thus, by its nature, SALT and its generalization to I-SALT, will not describe complex dynamical effects in injected lasers of the type mentioned above.

The SIA was discussed in relationship to SALT in Sec. 2.2, however, the important distinction in its application to I-SALT is that the inversion beat frequency is not  $\Delta$ , but the frequency difference between the injected signal  $\omega_{in}$  and the free-running signal  $\omega_1$  (we assume here only one free running mode and one injected signal for simplicity). For the generalization to I-SALT to work in the unlocked regime, where there are two beating signals, we must have  $\omega_{in} - \omega_1 > \omega_r$ . However, even if this is not the case, I-SALT will still describe quantitatively the locked regime and predict the unlocking threshold exactly.

However, as noted, there is an interesting regime in which such effects do not occur, and in which SALT and I-SALT will describe accurately the steady-state lasing or lasing with injection in either the locked or unlocked state. The theories will predict fully the classical fields, their frequencies, output power, emission pattern, etc., except properties due to quantum fluctuations, such as the linewidth. Moreover, recent extensions of SALT [123,131] have found exact linewidth formulas which are generalizations of Schawlow-Townes based on SALT solutions, and are discussed further in Ch. 6.

In the cases studied below, in which I-SALT describes both the locked and the unlocked behaviors, we find an effect in 1D Fabry-Pérot-type cavities: Instead of the free-running frequency being “pulled in” to the injected frequency, as in the standard Adler picture [2], we find that the lasing frequency is repelled from the injected signal frequency due to the effects of gain competition and spatial hole burning. In Oppo *et al.* frequency repulsion is also found in a certain limit, but it is due to the dynamical effects of relaxation oscillations which are absent for the cases we consider and thus is a distinct effect. Moreover, essentially all of the injection literature treats single-mode one-dimensional cavities. I-SALT naturally allows the description of multimode lasing with injection, leading to the possibility of a partially locked lasing state, in which one or more modes have been quenched by cross saturation, while other modes still lase, as we demonstrate below. Also, I-SALT provides a formulation for describing injection into a cavity with arbitrary two- or three-dimensional geometry; we apply the method to injection into a two-dimensional chaotic cavity laser below.

## 4.1 Derivation of I-SALT

As discussed above, we assume the existence of a steady state with stationary level populations, which in general requires that  $\gamma_{\parallel}, \omega_r \ll \delta\omega, \Delta, \gamma_{\perp}$ , where  $\delta\omega$  is the detuning of the injected signal from the free-running laser frequency and  $\omega_r, \Delta, \gamma_{\perp}$  are as previously defined. However, for a cavity with only a single operating mode, either injected or free-running, this inequality is not necessary, and the I-SALT solution is exact (in the RWA). In general, the multimode ansatz made by SALT in Eqs. (2.1) and (2.2) can be expanded to include the injected signals, such that the positive frequency components of the electric field and atomic polarization inside the cavity for a given pump value,  $d_0$ , take the form

$$\mathbf{E}^+(\mathbf{x}, t) = \sum_{\mu}^{N_L} \Psi_{\mu}(\mathbf{x}) e^{-i\omega_{\mu}t} + \sum_{\alpha}^{N_A} \Psi_{\alpha}(\mathbf{x}) e^{-i\omega_{\alpha}t}, \quad (4.1)$$

$$\mathbf{P}^+(\mathbf{x}, t) = \sum_{\mu}^{N_L} \mathbf{p}_{\mu}(\mathbf{x}) e^{-i\omega_{\mu}t} + \sum_{\alpha}^{N_A} \mathbf{p}_{\alpha}(\mathbf{x}) e^{-i\omega_{\alpha}t}, \quad (4.2)$$

where the  $N_L$  lasing modes,  $\Psi_\mu(\mathbf{x})$ , and associated polarization fields,  $\mathbf{p}_\mu(\mathbf{x})$ , have unknown spatial variation, and unknown frequencies,  $\omega_\mu$ , and there are  $N_A$  amplified signals injected into the cavity, at *given* frequencies,  $\omega_\alpha$ , and *given* incoming amplitudes,  $B_\alpha$ , but with unknown overall amplitude, spatial variation,  $\Psi_\alpha(\mathbf{x})$ , and polarization,  $\mathbf{p}_\alpha(\mathbf{x})$ , within the cavity. All of the unknown quantities are determined from the resulting I-SALT equations and their boundary conditions self-consistently. We now insert the multiperiodic ansatz of Eqs. (4.1) and (4.2) into the Maxwell-Bloch equations and apply the SIA to write

$$\mathbf{p}_\sigma(\mathbf{x}) = \frac{\boldsymbol{\theta}}{\hbar} \frac{d(\mathbf{x})}{\omega_\sigma - \omega_a + i\gamma_\perp} (\Psi_\sigma(\mathbf{x}) \cdot \boldsymbol{\theta}), \quad (4.3)$$

where  $\sigma$  is either a free-running or and injected mode. This allows for the elimination of the polarization and atomic inversion, leading to  $N_L + N_A$  coupled nonlinear wave equations, which can be written as three-dimensional vectorial equations, but which here we only consider in their scalar form, appropriate for the geometries analyzed in Sec. 4.3:

$$\left[ \nabla^2 + \left( \varepsilon_c(x) + \frac{\gamma_\perp d(x)}{\omega_\sigma - \omega_a + i\gamma_\perp} \right) k_\sigma^2 \right] \Psi_\sigma(x) = 0, \quad (4.4)$$

$$d(x) = \frac{d_0 F(x)}{1 + \sum_\mu^{N_L} \Gamma_\mu |\Psi_\mu(x)|^2 + \sum_\alpha^{N_A} \Gamma_\alpha |\Psi_\alpha(x)|^2}, \quad (4.5)$$

where  $\Gamma_\sigma \equiv \gamma_\perp^2 / [(\omega_\sigma - \omega_a)^2 + \gamma_\perp^2]$  is the gain curve and  $k_\sigma = \omega_\sigma/c$  is the wave vector. The electric field and inversion have also been scaled to natural units,  $E_c$  and  $d_c$ . The wave equations for lasing modes,  $\Psi_\mu(x)$ , are to be solved with purely outgoing boundary conditions, while those for amplified modes,  $\Psi_\alpha(x)$ , are to be solved with the boundary condition of fixed input amplitude  $B_\alpha$  at  $\omega_\alpha$ .

We solve these coupled equations by nonlinear iteration after expanding the solutions in a non-Hermitian basis set with the appropriate boundary conditions. For the lasing modes,  $\Psi_\mu$ , this set is the same TCF states used in SALT, Eqs. (2.13)-(2.15). The amplified modes,  $\Psi_\alpha$ , however, must be treated differently from the lasing modes since they have a fixed incoming signal amplitude and fixed frequency. To represent these modes we require terms with an incoming component in addition to the outgoing TCF expansion terms, which we do conveniently by solving the same TCF equation inside the cavity with a purely incoming

boundary condition,

$$\Psi_\alpha(x) = \sum_n a_n^{(\alpha)} u_n(x; \omega_\alpha) + \sum_m b_m^{(\alpha)} v_m(x; \omega_\alpha), \quad (4.6)$$

where the states  $v_m(x; \omega)$  and associated eigenvalues  $\beta_m$  are given by

$$[\nabla^2 + (\varepsilon_c(x) + \beta_m F(x)) k^2] v_m(x; \omega) = 0, \quad (4.7)$$

$$\partial_x v_m(x; \omega)|_{x=L} = -ik v_m(L; \omega), \quad (4.8)$$

$$v_m(0; \omega) = 0, \quad (4.9)$$

and thus represent states that are purely incoming.

In general, the incoming TCF states do not represent the biorthogonal partners of the outgoing TCF states. While the biorthogonal partner states, those which are used in coherent perfect absorption [165, 166] have an incoming boundary condition, they are also defined as having absorption in the cavity in the place of gain,

$$[\nabla^2 + (\varepsilon_c^*(x) + \tilde{\eta}_l F(x)) k^2] \tilde{u}_l(x; \omega) = 0, \quad (4.10)$$

where  $\tilde{\eta}_l$  is the eigenvalue of the coherently absorbed TCF state  $\tilde{u}_l$ , and  $\tilde{\eta}_l = \eta_l^*$ . For passive cavities without loss or gain,  $\varepsilon_c \in \mathbb{R}$ , and  $v_l = \tilde{u}_l$ , and these sets are biorthogonal partners, which is the case we will consider here.

The incoming and outgoing TCF states are not power orthogonal, but they do satisfy a self-orthogonality condition between themselves,

$$\frac{1}{L} \int_C dx F(x) u_n(x; \omega) u_m(x; \omega) = \delta_{nm}, \quad (4.11)$$

$$\frac{1}{L} \int_C dx F(x) v_n(x; \omega) v_m(x; \omega) = \delta_{nm}, \quad (4.12)$$

which can be derived from the definitions of the states and Green's theorem [97]. Either the incoming or the outgoing TCF states represent a complete basis for fields *within the cavity* at  $\omega_\alpha$ , but the incoming terms are needed to represent the input boundary condition.

Because they are purely incoming, they do not contribute directly to the emitted fields, but they correctly represent the full spatial hole-burning and gain competition effects of the amplified input.

For amplified modes, we can easily write the incoming boundary condition for a one-sided slab cavity of length  $L$  as

$$B_\alpha e^{-ik_\alpha L} = \sum_m b_m^{(\alpha)} v_m(L; \omega_\alpha), \quad (4.13)$$

where  $B_\alpha$  is the given incoming field amplitude at frequency  $\omega_\alpha$ . This single equation vastly under-determines the coefficients  $b_m^{(\alpha)}$  in the sum, so that the choice is based on convenience. This freedom arises from the overcompleteness of using both  $\{u_n\}$  and  $\{v_m\}$  to represent the internal fields. Hence, the coefficients  $a_n^{(\alpha)}$  depend strongly on the choice of the  $b_m^{(\alpha)}$ . A natural choice is to take only a single term,  $v_0(x; \omega_\alpha)$ , which corresponds to the outgoing TCF state for the nearest lasing mode. This is allowed for a cavity with a single input channel, as in the one-sided slab geometry we are considering here; in general, one needs a minimum of  $M$  independent incoming states to represent an arbitrary input for an  $M$ -channel cavity, and these can be chosen again to be similar in character to the nearest lasing mode in order to optimize the calculation.

Once a representation of the input field is chosen, one can insert Eq. (4.6) for the amplified modes and Eq. (2.8) for the lasing modes into the fundamental Eqs. (4.4) and (4.5) and use the self-orthogonality relations of the outgoing TCF states to find coupled nonlinear matrix equations for the coefficients  $a_n^{(\mu)}, a_n^{(\alpha)}$  which determine their solutions. For the lasing modes,  $\Psi_\mu$ , one finds

$$\eta_l a_l^{(\mu)} = \sum_n T_{ln}^{(\mu)} a_n^{(\mu)}, \quad (4.14)$$

$$T_{ln}^{(\mu)} = \frac{\gamma_\mu d_0}{L} \int_C dx \frac{F(x) u_l(x; \omega_\mu) u_n(x; \omega_\mu)}{1 + \sum_\sigma^{(N_L + N_A)} \Gamma_\sigma |\Psi_\sigma(x)|^2}, \quad (4.15)$$

where  $\gamma_\mu = \gamma_\perp / (\omega_\mu - \omega_a + i\gamma_\perp)$ . This is identical to the lasing equations of SALT except for the presence of the amplified mode intensities in the nonlinear hole burning denominator.

In a similar manner the coupled equations for the amplified modes can be determined,

and they take the form

$$\eta_l a_l^{(\alpha)} = \sum_n T_{ln}^{(\alpha)} a_n^{(\alpha)} + \sum_m \left( W_{lm}^{(\alpha)} + V_{lm}^{(\alpha)} \right) b_m^{(\alpha)}, \quad (4.16)$$

$$W_{lm}^{(\alpha)} = \frac{\gamma_\alpha d_0}{L} \int_C dx \frac{F(x) u_l(x; \omega_\alpha) v_m(x; \omega_\alpha)}{1 + \sum_\sigma^{(N_L + N_A)} \Gamma_\sigma |\Psi_\sigma(x)|^2}, \quad (4.17)$$

$$V_{lm}^{(\alpha)} = \frac{\beta_m}{L} \int_C dx F(x) u_l(x; \omega_\alpha) v_m(x; \omega_\alpha). \quad (4.18)$$

The result for the overlap integral can be simplified further through the use of the definitions of the incoming and outgoing TCF states and Green's theorem, starting with the definition of the incoming and outgoing TCF states and multiplying through by a member from the opposite set at the same frequency,

$$v_m \nabla^2 u_l = -v_m (\varepsilon_c(x) + \eta_l F(x)) k^2 u_l, \quad (4.19)$$

$$u_l \nabla^2 v_m = -u_l (\varepsilon_c(x) + \beta_m F(x)) k^2 v_m. \quad (4.20)$$

Next, by subtracting the two equations and integrating over the cavity,

$$\int_C v_m \nabla^2 u_l - u_l \nabla^2 v_m d^d x = k^2 (\beta_m - \eta_l) \int_C F(x) v_m u_l d^d x, \quad (4.21)$$

Green's theorem can be invoked to evaluate the integral on the left side over the boundary of the cavity,  $\partial C$ , as

$$\int_{\partial C} (v_m \nabla u_l - u_l \nabla v_m) \cdot \mathbf{n} da = k^2 (\beta_m - \eta_l) \int_C F(x) v_m u_l d^d x. \quad (4.22)$$

In general, the integral over the boundary can be evaluated using the incoming or outgoing boundary condition specified in the definition of the TCF states, and in a one-dimensional, single-sided cavity, the boundary integral is readily evaluated as

$$\begin{aligned} \int_{\partial C} (v_m \nabla u_l - u_l \nabla v_m) \cdot \mathbf{n} da &= \left[ v_m \frac{du_l}{dx} - u_l \frac{dv_m}{dx} \right]_{x=L}, \\ &= 2ik v_m(L) u_l(L). \end{aligned} \quad (4.23)$$

Which finally results in,

$$V_{lm}^{(\alpha)} = \frac{2i}{Lk_\alpha} \frac{\beta_m}{\beta_m - \eta_l} u_l(L; \omega_\alpha) v_m(L; \omega_\alpha). \quad (4.24)$$

As with any basis expansion method, this method of representing the original differential equations will require truncation of the sums at a finite number of TCFs,  $N$ , in the numerical implementation.

From this form of the overlap integral, it is simple to understand why the most numerically efficient choice of incoming TCF states to use,  $b_m^{(\alpha)} \neq 0$ , are those related to the outgoing states of the nearest lasing mode. In the case of a lossless cavity,  $\varepsilon_c(x) \in \mathbb{R}$ , the incoming and outgoing TCF states form a biorthogonal set, with  $\beta_m = \eta_m^*$  and  $v_m = u_m^*$ . Thus,  $V_{lm}$  is maximized when the difference between the incoming and outgoing TCF eigenvalues is minimized. This choice allows the outgoing states required by  $T_{ln}$  to also have significant overlap with the incoming states chosen, rather than needing to include additional outgoing states to properly compute the sum over overlap integrals.

The I-SALT equations for free-running modes, Eqs. (4.14) and (4.15), have a critical difference from the equations for amplified modes, Eqs. (4.16), (4.17), and (4.24): In the former, there is an undetermined global phase, whereas for the latter the phase is set by the injected signal,  $B_\alpha$ . For lasing modes the undetermined global phase is chosen by convention (gauge condition) [22, 25]. This leaves  $2N - 1$  expansion coefficients to fully determine the real and imaginary parts of  $a_n^{(\mu)}$ , and one additional equation which determines the unknown lasing frequency. It is this equation which determines the full intensity-dependent line-pulling effects on the lasing frequencies, and, in the case of I-SALT, frequency pulling or pushing due to the injected mode. In contrast, for the amplified mode the frequency and phase of the input signal is fixed externally and uniquely determines all other phases (there is no global phase invariance); thus, there are  $2N$  expansion coefficients (the real and imaginary parts of  $a_n^{(\alpha)}$ ) that must be found, and an equal number of conditions determining them.

Together Eqs. (4.14)-(4.17), and (4.24) define I-SALT. In the regime in which the SIA holds, they provide essentially exact solutions of the full coupled wave equations for amplifi-

cation and injection locking. The method is *ab initio*, as in SALT, with no prior assumptions about the number, spatial form or frequencies of the lasing modes. Lasing modes correspond to poles of the nonlinear scattering matrix on the real axis. Amplified inputs do not; they are simply additional scattered waves which also deplete the gain. If the input signal becomes too strong, and is sufficiently near in frequency to the lasing mode, then the lasing mode has insufficient gain and falls below threshold, leaving only the amplified signal output. The output is “locked” to the input frequency, but not by pulling the lasing mode over to  $\omega_\alpha$ , but rather by turning it off.

## 4.2 From I-SALT to Adler’s Model

In this section we show how I-SALT can recover an improved version of the traditional Adler equations in their steady-state form. Because our approach starts from the full laser equations we use as comparison Eqs. (58) and (59) from Spencer and Lamb [115], which has a similar starting point (i.e., starts with the full Maxwell equations and includes the spatial degrees of freedom and gain saturation explicitly). The Adler theory assumes only a single input channel with small amplitude and only, at most, a single free-running mode and a single amplified mode; we model the injected laser following Spencer and Lamb via a cavity with a perfect mirror at one end and a high-reflectivity mirror at the other. I-SALT is a steady-state theory and should only approach the Adler description in the locked regime; thus, we assume that only a single, highly amplified mode is present in the cavity. This allows us to approximate the field inside the cavity as only having two components, one incoming TCF and one outgoing TCF (instead of the full expansion in outgoing TCFs),

$$\Psi_{in}(x) = au(x; \omega_{in}) + bv(x; \omega_{in}), \quad (4.25)$$

with  $a \gg b$  and where  $\omega_{in}$  is the frequency of the incident signal. In a single-channel cavity the use of a single incoming TCF is always justified and in a high- $Q$  cavity the use of a single outgoing TCF is justified by the single pole approximation [25], as the amplified signal is close to a high- $Q$  cavity resonance and thus only a single outgoing TCF is needed

to describe the amplified mode in this limit. We can use Eqs. (2.13) and (4.7) to rewrite Eq. (4.4) as

$$\frac{\gamma_{\perp}d(x)}{\omega_{in} - \omega_a + i\gamma_{\perp}}\Psi_{in}(x) = a\eta_{in}u(x) + b\beta_{in}v(x), \quad (4.26)$$

$$d(x) = \frac{d_0}{1 + \Gamma_{in}|\Psi_{in}(x)|^2}. \quad (4.27)$$

By adding and subtracting  $b\eta_{in}v(x)$  from the right side of the equation and defining  $\Psi_{in}(x) \equiv a\psi(x)$ , we are able to write

$$\frac{\gamma_{\perp}d(x)}{\omega_{in} - \omega_a + i\gamma_{\perp}}a\psi(x) - a\eta_{in}\psi(x) = b(\beta_{in} - \eta_{in})v(x). \quad (4.28)$$

While Spencer and Lamb used a  $\delta$ -function index jump to represent the imperfect mirror, for convenience we take our cavity to have a uniform index with the index step at one end to vacuum, comprising the mirror; hence, the TCF states will be sine functions of a complex argument. Thus, in this section only, we choose to normalize our incoming and outgoing TCF states for convenience as  $(2/L) \int dx u(x)u(x) = 1$  and similarly  $(2/L) \int dx v(x)v(x) = 1$ . Integrating through with respect to the mode describing the resonance of the cavity,  $(2/L) \int dx u(x)$ , we define the gain saturation function as

$$f(I) = \frac{\omega_{in}d_0}{2\varepsilon_c} \left(\frac{2}{L}\right) \int dx \frac{u(x)\psi(x)}{1 + \Gamma_{in}I|\psi(x)|^2}, \quad (4.29)$$

where  $I \simeq |a|^2$  is a measure of the intensity of the field inside of the cavity, and has essentially the same meaning as the similar quantity introduced in Spencer and Lamb (in their case they use a sine of real argument and are able to evaluate the resulting integral analytically) [115]. Although  $f(I)$  is complex in general, for high- $Q$  cavities, it is essentially real to  $10^{-3}$ , and thus here we approximate it as such. Next, we note that up to corrections of order  $b/a$ ,  $(2/L) \int u(x)\psi(x)dx = 1$  as the field profile inside of the cavity is dominated by the outgoing portion. Finally, the overlap integral between the incoming and outgoing

TCF states can be evaluated by use of Eq. (4.24), resulting in

$$\frac{\gamma_{\perp} f(I)}{\omega_{in} - \omega_a + i\gamma_{\perp}} \left( \frac{2\varepsilon_c}{\omega_{in}} \right) a - \eta_{in} a = \frac{2ic}{\omega_{in}} \left( \frac{2}{L} \right) u(0) B_{in}, \quad (4.30)$$

where the mirrored side of the cavity has been placed at  $x = -L$  and the open edge of the cavity at  $x = 0$  and noting that the definition of the input signal amplitude, Eq. (4.13), can be used to simplify  $B_{in} = bv(0)$ . The outgoing TCF eigenvalue for a dielectric slab cavity can be expressed in terms of the input frequency and the cavity resonance, following Ge *et al.* [25],

$$\begin{aligned} \eta_{in} &= \varepsilon_c \left( \frac{(\omega_0 - i\frac{\gamma_c}{2})^2 - \omega_{in}^2}{\omega_{in}^2} \right) \\ &\simeq \varepsilon_c \left( \frac{2(\omega_0 - \omega_{in})}{\omega_{in}} - \frac{2i}{\omega_{in}} \left( \frac{\gamma_c}{2} \right) \right), \end{aligned} \quad (4.31)$$

where  $\omega_0$  is the frequency of the passive cavity resonance,  $\gamma_c$  is the photon decay rate through the end of the cavity, and  $\omega_0 \simeq \omega_{in}$ , as the resonance corresponds to the closest passive cavity resonance to the injected frequency, at most half a free spectral range away. Finally, we approximate  $(\omega_{in} - \omega_a)^2 \simeq 0$ , resulting in

$$(\xi - i) f(I) a - \left( \Delta - i\frac{\gamma_c}{2} \right) a = \frac{2ic}{L\varepsilon_c} u(0) B_{in}, \quad (4.32)$$

where  $\xi = (\omega_{in} - \omega_a)/\gamma_{\perp}$  and  $\Delta = \omega_0 - \omega_{in}$ . In high- $Q$  cavities with the normalization for the outgoing TCFs chosen in this section, it can be shown that  $u(0) \simeq 1$ . The cavity decay rate can also be related to the round trip time in the cavity and the reflection coefficient [2],

$$\gamma_c = \frac{-c}{2Ln} \ln R, \quad (4.33)$$

where  $n$  is the index of refraction of the passive cavity. Finally, to connect to the Spencer and Lamb version of the Adler theory, we formally expand the reflection coefficient for large index, approximating the coefficient,  $-\ln R \approx T \approx 4/n$ , resulting in

$$\gamma_c \approx \frac{2c}{L\varepsilon_c}. \quad (4.34)$$

Finally, writing  $B_{in} = |B_{in}|e^{i\phi}$  and separating real and imaginary components, we find

$$0 = \left( f(I) - \frac{\gamma_c}{2} \right) a - \gamma_c |B_{in}| \cos(\phi), \quad (4.35)$$

$$0 = \xi f(I) - \Delta - \gamma_c \frac{|B_{in}|}{a} \sin(\phi). \quad (4.36)$$

Noting that in the locked regime  $\omega = \omega_{in}$ , Eqs. (4.35) and (4.36) are identical to the steady-state Adler equations as presented in Eqs. (58) and (59) from Spencer and Lamb [115], except that our definition of  $f(I)$  includes the openness of the cavity through different boundary condition on the TCF state, leading to a sine function of complex argument, instead of the Dirichlet boundary condition assumed in [115].

Thus, in the correct limit, an improved version of the traditional theory can be recovered from I-SALT, in the locked regime. If we make the further usual assumption that  $\xi$  is small, we obtain exactly the same locking range as predicted by the standard theory (see next section). In the unlocked regime the Adler theory predicts a residual time dependence of the relative phase of input and free-running signal which cannot be derived from I-SALT; but full I-SALT shows that the frequency shifts predicted by the usual theory in the unlocked regime are not correct in general (next section).

### 4.3 Injection simulations

To test the results of I-SALT, we compare them to the exact numerical solutions from FDTD simulations of the Maxwell-Bloch equations for a simple one-dimensional asymmetric Fabry-Pérot cavity with an injected signal (schematics) under various conditions. The FDTD simulations performed here used the time-stepping method proposed by Bidégaray, updating the atomic polarization and inversion alongside the magnetic field and were run for a total time of  $T_{tot} \sim 100(1/\gamma_{||})$  to ensure convergence, as  $\gamma_{||}$  corresponds to the longest time scale in the system [148]. Similar simulations without the injected signal were previously used for quantitative tests of SALT [24, 98].

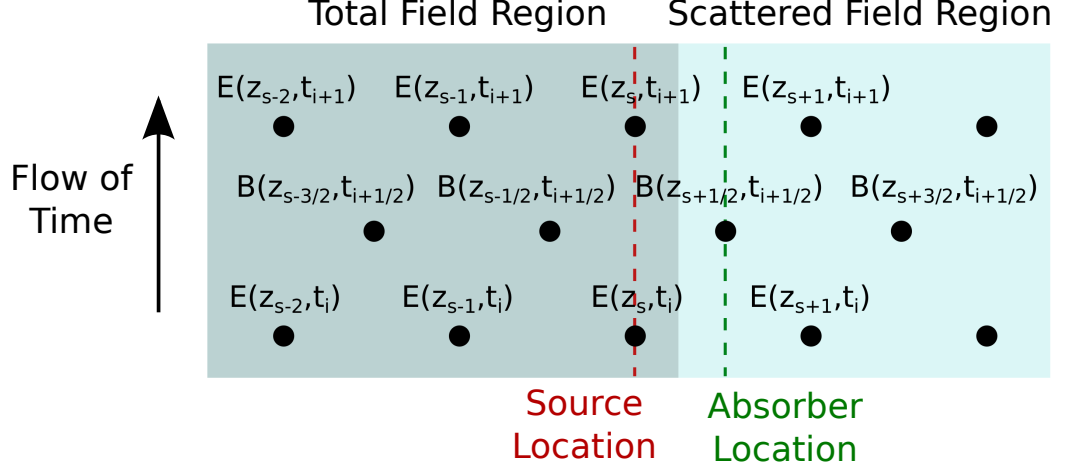


Figure 4.1: Schematic depicting the total field and scattering field regions for a FDTD algorithm. Field quantities in the total field region are a combination of fields from the source and any scattering events which might be taking place to the left of the diagram. Fields measured in the scattered field region are only those originally from leftward moving waves from the source that subsequently scattered off any interfaces.

#### 4.3.1 Injected signals in FDTD

Including an injected signal into the FDTD algorithm is a well understood problem in an arbitrary number of dimensions and is subsumed into the topic of total field, scattered field methods [167]. The basic challenge when including an incident signal is that the fields in an FDTD are always real, so if one were to add a source term at a single location,  $z_s$ , in the simulation domain such as

$$\frac{E(z_s, t_{i+1}) - E(z_s, t_i)}{\Delta t} = \frac{c^2}{\epsilon_c} \left( \frac{B(z_{s+\frac{1}{2}}, t_{i+\frac{1}{2}}) - B(z_{s-\frac{1}{2}}, t_{i+\frac{1}{2}})}{\Delta z} \right) + 2|B_{in}| \cos(\omega_{in} t_i + \phi_{in}), \quad (4.37)$$

the source will generate signal in both the incoming and outgoing directions. Thus, the incoming wave would enter the cavity and scatter back out, but this scattered signal, that we want to measure, would be combined with the outgoing signal coming directly from the source, making it difficult to disentangle the desired signal from the source' outgoing signal. In the above equation,  $|B_{in}|$  is still the amplitude of the incident signal as discussed in Sec. 4.1, and is not related to the magnetic field in any way.

The solution to this is to also include an absorbing term in the magnetic field update equation that perfectly absorbs this incident signal, resulting in fields beyond the absorbing

location to be only those from the scattering interaction,

$$\frac{E(z_s, t_{i+1}) - E(z_s, t_i)}{\Delta t} = \frac{c^2}{\varepsilon_c} \left( \frac{B(z_{s+\frac{1}{2}}, t_{i+\frac{1}{2}}) - B(z_{s-\frac{1}{2}}, t_{i+\frac{1}{2}})}{\Delta z} \right) + |B_{in}| \cos(\omega_{in} t_i + \phi_{in}), \quad (4.38)$$

$$\frac{B(z_{s+\frac{1}{2}}, t_{i+\frac{1}{2}}) - B(z_{s+\frac{1}{2}}, t_{i-\frac{1}{2}})}{\Delta t} = \left( \frac{E(z_{s+1}, t_i) - E(z_s, t_i)}{\Delta z} \right) + |B_{in}| \cos(\omega_{in} t_i + \phi_{in}), \quad (4.39)$$

as depicted in Fig. 4.1. As the source term is added at  $z_s$  in the electric field, when this is used to update the magnetic field at the absorbing location,  $z_{s+\frac{1}{2}}$ , it acquires a negative sign, and thus exactly cancels with the absorbing term. Furthermore, when the electric field is then updated with the magnetic field from the absorbing location, it keeps its positive sign, making the effective source in the leftward direction  $2|B_{in}| \cos(\omega_{in} t_i + \phi_{in})$ , which is the desired amplitude for representing a plane wave in the leftward direction when accounting for the factor of  $1/2$  in the definition of cosine. Another way to think of this is as adding a second source such that the two sources undergo complete destructive interference in the outgoing direction, resulting in perfect constructive interference in the incoming direction, creating a region in the simulation domain outside of both source locations where only waves scattered from the laser resonator will exist.

### 4.3.2 Locking transition

We first study the usual locking transition in Fig. 4.2 in which a single free-running mode eventually gives way to an injected mode. The simulations are done in a region of large detuning in which we expect good agreement with I-SALT. Indeed locking of the output signal to the input is found in the FDTD data in good quantitative agreement with I-SALT with no adjustable parameters. We note that the quantitative agreement seen between I-SALT and FDTD calculations is also a demonstration of the stability of the I-SALT solutions; any instabilities due to beating terms in the inversion would be present in the FDTD solutions, which do not rely on the SIA. A further analytical treatment of the stability of the I-SALT solutions is presented in Appendix F. The simulations in Fig. 4.2 are for

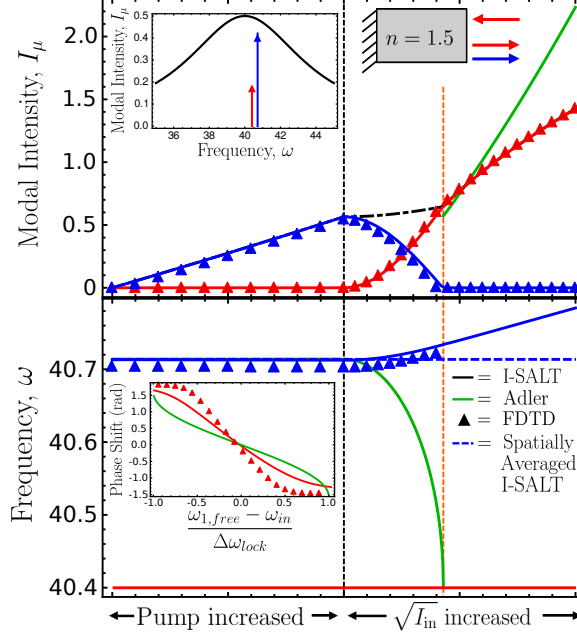


Figure 4.2: (Top) Simulations of single-mode injection locking in a one-sided dielectric slab cavity with  $n = 1.5$  (schematic) with a perfect mirror at one end and an index step to vacuum at the other. First, the pump is increased above the threshold for lasing at  $\omega_{1,free} = 40.714$ ,  $d_0 = 0.0603$  to  $d_0 = 0.08$ , and then held at a fixed value (vertical black line) while the input signal amplitude is ramped from  $B_{in} = 0$  until the free-running signal is quenched and the system “locks” (vertical orange line) to the injected frequency,  $\omega_{in} = 40.4$  at  $B_{in} = 0.176$ . Finally, the simulation is continued in the locked regime to  $B_{in} = 0.4$ . Solid lines are output intensities calculated from I-SALT; blue is lasing output, red is amplified output at signal frequency, dot-dashed black is total output. Triangles are the same quantities from FDTD for the same dielectric slab laser with  $\omega_a = 40$ , the width of the gain curve,  $\gamma_\perp = 4$ , and  $\gamma_\parallel = 0.001$ . The green curve in the locked regime is the prediction of our generalized Adler equations, (4.35) and (4.36). The top inset shows gain curve and  $\omega_{in}$  (red),  $\omega_1$  (blue). (Bottom) Frequency variation of the first lasing mode. Blue line is from I-SALT and blue triangles from FDTD. The green line shows the prediction of the Adler theory. The red line is the injected signal frequency. Again, the orange dashed line shows the locking threshold from I-SALT; frequencies beyond this point are taken as the real part of the location of the pole of the scattering matrix. Blue dashed lines showing negligible frequency shift are I-SALT calculation with uniform gain saturation and no spatial hole burning. The inset shows a plot of the phase shift between input and output signals of an injection-locked dielectric slab cavity at a fixed input intensity. I-SALT (red curve) and FDTD simulations (red triangles) are seen to have a better quantitative and qualitative agreement than the Adler prediction (green curve). For comparison with the Adler theory, the horizontal axis is plotted in terms of the free-running lasing frequency in the absence of an injected signal at threshold,  $\omega_{1,free}$ . Frequencies and rates are given in units of  $c/L$ , while the atomic inversion and modal intensities are given in SALT units of  $E_c$  and  $d_c$ .

large detuning, not the typical Adler regime; thus, for these parameters locking requires an input signal which is a significant fraction of the free-running output at that pump value,

$\sim 23\%$ . The total output intensity of the amplified mode when locking occurs is larger than the free-running signal also by  $\sim 18\%$  (in the Adler theory they are the same to a good approximation); however, this is not surprising due to the relatively large input intensity. Also, the independence of the spatial degrees of freedom of the amplified and free-running mode should allow the amplifier to extract more power from the gain medium. Consistent with this, in the unlocked region, when both free-running and amplified modes are emitting, the total output intensity is monotonically increasing, as indicated by the black dashed line in the figure. If we take the I-SALT version of the Adler equations in the locked regime and impose the condition that locking occurs when the amplified output is equal to the original free-running output, we can solve the nonlinear Eqs. (4.35) and (4.36) to predict the input amplitude at which the laser would lock. This transition line is very close to that found by I-SALT, slightly less by  $\sim 4.5\%$ . Above that point we can plot the Adler I-SALT predictions for the amplified mode intensity and find them to be in reasonable agreement with I-SALT and FDTD near the transition and in poor agreement far above it.

The difference between the locking behavior in this regime and in the usual Adler theory is strikingly illustrated by the frequency shift of the free-running mode prior to locking, which is qualitatively different from the Adler theory; the free-running frequency,  $\omega_1$ , is repelled from the input frequency (full blue line and data points), instead of being strongly attracted toward it (green line). This frequency repulsion can be explained by the combined effects of mode competition and spatial hole burning. As the incident signal is imposed and depletes the gain, the standing wave of the laser field shifts away from the frequency/wavelength of the incident standing wave in order to better extract energy from the regions of the cavity where the gain is not being saturated by the incident signal. To confirm this interpretation we replaced the *space-dependent* gain saturation denominator with its spatial average,

$$d_{ave}(x) = \frac{d_0}{1 + \sum_{\sigma}^{N_L+N_A} \frac{\Gamma_{\sigma}}{L} \int_C |\Psi_{\sigma}(x)|^2 dx}, \quad (4.40)$$

in place of Eq. (4.5), and noting that for this simulation the pump profile is uniform,  $F(x) = 1$ . Using this spatially averaged gain saturation, no movement of the lasing frequency is seen

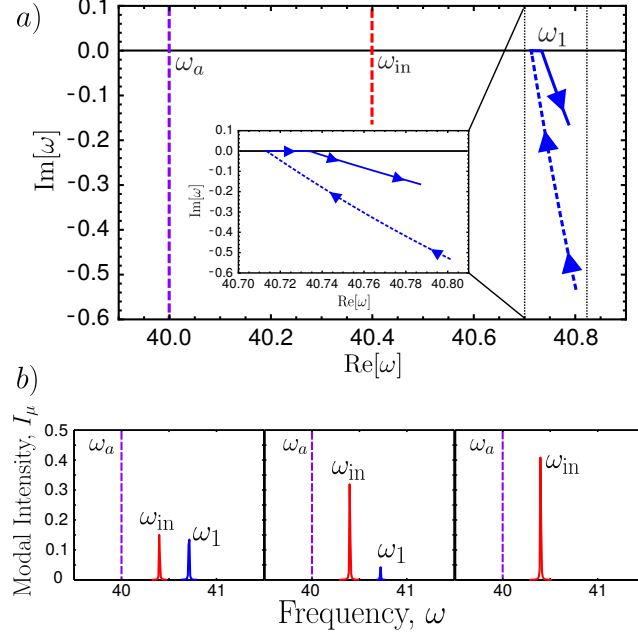


Figure 4.3: (a) Motion of the pole as described in the text corresponding to the free-running lasing mode in the locking scenario of Fig. 4.2. As the pump is increased below threshold the pole of the scattering matrix is pulled upwards towards the real axis and “in” towards  $\omega_a = 40$  (blue dashed line, recall there is no signal yet at  $\omega_{in} = 40.4$ ). Free-running lasing occurs when the pole reaches the real axis at  $\omega_{1,free} = 40.714$  and continues as the pump is increased further above threshold with negligible further frequency shift. Then the pump is fixed and the input signal is ramped, causing the pole (solid blue line) to move to higher frequency, away from the input frequency, and eventually off the real axis as the effects of gain saturation cause the lasing mode to go below threshold. The inset shows a magnification on the motion of the pole of the lasing mode inside the dotted box. (b) Frequency spectrum from FDTD simulations across the locking transition, showing no additional lines appearing, indicating that the effect is purely due to gain cross saturation. Frequencies and rates are given in units of  $c/L$ , while the atomic inversion and modal intensities are given in SALT units of  $E_c$  and  $d_c$ .

in Fig. 4.2(b) (dashed blue line). This provides strong evidence that the frequency pushing phenomenon observed here requires treating the full spatial dependence of the problem and can not be seen in previously developed spatially averaged injection theories [100, 159, 160].

Furthermore, as I-SALT and FDTD simulations both predict this same frequency repulsion and this solution is found to be stable, see Appendix F, the effect seen here is different from the frequency repulsion previously predicted in dynamical parameter regimes by Oppo *et al.*, where the SIA would not be appropriate and as a result more complex dynamical features are found [100]. The relatively weak repulsion found here is also distinct from that observed by Murakami *et al.* [168], which is a shift in the cavity resonance due

to the injected signal saturating the gain carriers in materials with large Henry  $\alpha$ -factors such as semiconductors where  $\alpha \sim 2 - 8$ . In contrast, for the Bloch gain medium used in Fig. 4.2,  $\alpha = 0.17$ . Additionally, the overall saturation of the gain medium is not changing significantly while this frequency repulsion is observed as the pump is held fixed while the injected signal is increased, thus keeping the total output intensity relatively constant, as is seen in Fig. 4.2(a) in the black dot-dashed line. For the effect predicted by Murakami *et al.* to be seen, a significant shift in the number of available gain carriers is needed, coupled to a large Henry  $\alpha$ -factor, and this effect would be seen in the spatially averaged I-SALT calculation if it were present [168].

As noted, the Adler theory describes locking driven by phase synchronization of the input and free-running fields. Since the threshold input intensity for locking decreases to zero as the input frequency,  $\omega_{in}$ , approaches the free-running frequency in the absence of an injected signal,  $\omega_{1,free}$ , the threshold condition can be expressed as a “locking range,” the frequency range  $\Delta\omega_{lock}$  over which the laser is locked for a given input intensity. In the Adler theory one finds

$$\Delta\omega_{lock} = \gamma_c \sqrt{\frac{|B_{in}|^2}{I_0}}, \quad (4.41)$$

where  $\gamma_c$  is the cavity decay rate,  $|B_{in}|^2$  is the intensity of the input signal, and  $I_0$  is the intensity of the free-running lasing signal in the absence of the input [2]. Within this locking range there is a fixed phase relationship between the input signal and the locked output which varies as

$$\Delta\phi = \arcsin \left[ \frac{\omega_{1,free} - \omega_{in}}{\Delta\omega_{lock}} \right]. \quad (4.42)$$

The same quantity can be calculated in I-SALT and is compared to the Adler prediction for the same slab cavity in the inset of Fig. 4.2(a). The phase shift variation found from I-SALT is substantially different from the Adler prediction and in good agreement with FDTD [see inset, Fig. 4.2(b)].

The fact that in this regime the locking transition is entirely due to gain cross saturation, with no contribution from beating or phase synchronization, is illustrated in Fig. 4.3(a). In the top panel we show the motion of the pole of the scattering matrix corresponding to

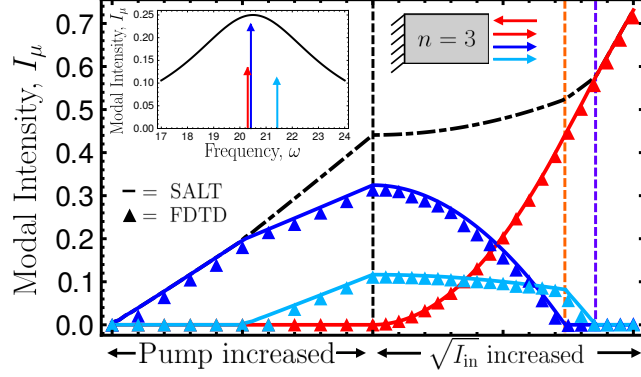


Figure 4.4: Partial locking transition as described in the text for a laser with two free-running modes and an injected signal (schematic) using a similar pumping and input ramping scheme as Fig. 4.2, starting at the first lasing threshold  $d_0 = 0.101$  and pumping until  $d_0 = 0.13$ , then increasing the input signal from  $B_{in} = 0$  to  $B_{in} = 0.4$ . Solid lines are output intensities calculated from I-SALT; blue and cyan lines are lasing output, the red line is amplified output at signal frequency,  $\omega_{in} = 20.3$ , the dot-dashed black line is total output. Triangles are the same quantities from FDTD for a similar dielectric slab laser with  $n = 3$ ,  $\omega_a = 20.5$ ,  $\gamma_{\perp} = 3$ ,  $\gamma_{\parallel} = 0.001$ . The inset shows the relationship of the three frequencies. As expected, the lasing mode nearest to the injected signal locks to the injected signal (orange line), then the more distant lasing mode locks (purple line). Frequencies and rates are given in units of  $c/L$ , while the atomic inversion and modal intensities are given in SALT units of  $E_c$  and  $d_c$ .

the lasing mode in Fig. 4.2 as the pump is increased and then fixed, and then the signal is injected and increased. The dashed blue line corresponds to the laser being below threshold; as the pole moves up towards the real axis its real frequency,  $\omega_1$ , decreases, pulled toward the center of the atomic line,  $\omega_a$ . When the pole reaches the real axis, corresponding to the free-running threshold,  $\omega_{1,free}$ , the gain balances loss and the mode lases. As the pump is further increased, the pole moves slightly further toward the center of the gain curve (not visible on this scale), but as soon as the pump is fixed and the injected signal is turned on at  $\omega_{in} < \omega_1$ , the behavior reverses. As the injected signal increases, the lasing frequency increases, shifting away from  $\omega_{in}$  (and  $\omega_a$ ). Eventually the injected mode saturates the gain enough to drive the lasing mode below threshold, and the pole leaves the real axis, although it continues to be repelled from  $\omega_{in}$ . This demonstrates that in the regime of stationary atomic populations the locking transition corresponds simply to driving the lasing mode below threshold due to the saturation of the gain medium from the injected mode.

A final important indication of the non-Adler nature of the transition is given in Fig.

4.3(b). In the Adler theory there are always strong four-wave mixing effects as the locking threshold is reached [2], and additional lines should appear in the frequency spectrum. In Fig. 4.3(b) we show the Fourier transforms of the FDTD data across the locking transition, which indicated a smooth transfer of intensity from the free-running line to the injected line with no additional frequencies appearing as the free-running line disappears.

### 4.3.3 partially locked states

Beyond yielding a correct and quantitative treatment of the locking transition of a single-mode laser in the relevant regime, as seen from the generality of Eqs. (4.14) and (4.24), I-SALT is able to treat simultaneously multimode lasing with multiple inputs. An interesting example is shown in Fig. 4.4. Here an asymmetric Fabry-Pérot slab laser similar to that in studied in Fig. 4.2 is pumped above the threshold for its *second* lasing mode (not to be confused with the instability threshold sometimes called the second lasing threshold [3]) and a signal is injected closer to the frequency of the first lasing mode. Because of its stronger interaction with the first mode (blue line), the signal is able to lock that mode, while the second mode (cyan line) remains active at a similar frequency to its free-running value, though shifted away from the injected frequency in the same manner as described before. As before, the solid lines (I-SALT) are in good agreement with the data points (FDTD). Thus, with relatively little additional computational effort, I-SALT predicts such “partially locked” states.

### 4.3.4 I-SALT and Adler I-SALT below threshold

The previous results assumed rather large detuning and hence relatively large injected signals to reach locking. To test our work in the more conventional regime of small detuning and small injected signals we consider injection near the free-running lasing frequency as a function of pump. Here we are near the center of the gain spectrum and will have much higher amplification. Since I-SALT is not reliable in the unlocked regime for detuning smaller than the relaxation oscillation frequency, we study only the behavior for pump values below the lasing threshold, when the cavity is functioning as a regenerative amplifier for the injected signal. Since there is only emission at the injected signal in this regime, we can also

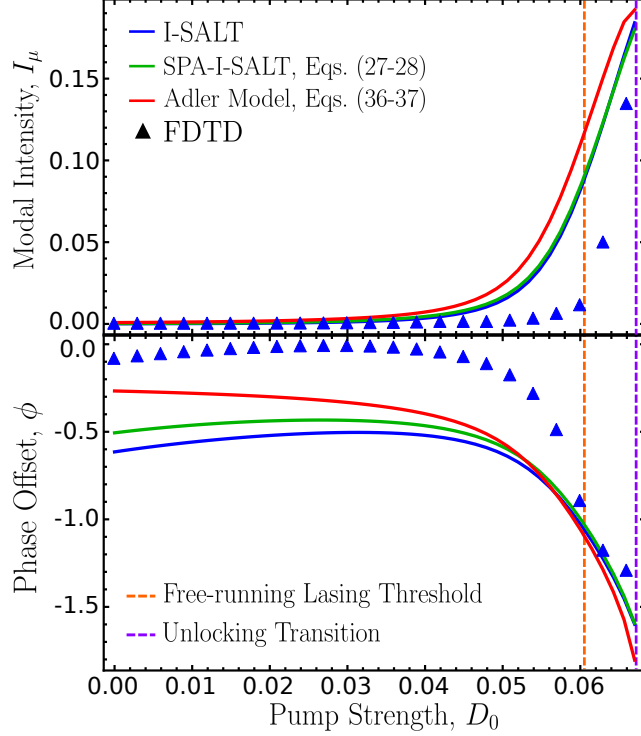


Figure 4.5: Comparison of the predictions of I-SALT (blue line), the SPA of I-SALT, given by Eqs. (4.26) and (4.27) (green line), the Adler model, as given by Eqs. (4.35) and (4.36) (red line), and FDTD (blue triangles) for both the output intensity (top) and the phase offset (bottom). The input intensity is negligible ( $|B_{in}|^2 = 10^{-4}$  in normalized SALT units) compared to the output, while the pump (gain) is increased from  $d_0 = 0$  to  $d_0 = 0.067$ , thus placing the simulations in the regime of validity for the Adler approximations. The vertical orange dashed line denotes the first lasing threshold in the absence of an incident signal, whereas the vertical purple dashed line shows where I-SALT predicts the unlocking transition to occur. Simulations are shown for a single-sided dielectric slab cavity with  $n = 1.5$ ,  $\omega_a = 40$ ,  $\omega_{in} = 40.7$ ,  $\omega_{1,free} = 40.714$ ,  $\gamma_{\perp} = 4$ , and  $\gamma_{\parallel} = 0.001$ . Frequencies and rates are given in units of  $c/L$ , while the atomic inversion and modal intensities are given in SALT units of  $E_c$  and  $d_c$ .

apply the Adler approximation to I-SALT. As shown in Fig. 4.5, even though I-SALT may not describe well the unlocked regime for this cavity, it provides a very accurate description of the amplifier, in good agreement with FDTD for both intensity and phase offset. We also find, as one might expect, that the Adler approximation to I-SALT (red curves) works almost as well. The dashed vertical lines in the figure show the lasing thresholds in the absence of the injected signal (orange) and in its presence (purple). In the presence of the injected signal, the first lasing threshold is synonymous with the unlocking transition, as this is when the cavity will begin to self-oscillate. Note that the injected signal pushes up

the lasing threshold significantly.

### 4.3.5 Injected Quadrupole Resonators

As noted in the Introduction, a strength of the SALT and I-SALT theories is that they can handle an arbitrary cavity geometry essentially exactly. Here we demonstrate the power of the method by simulating injected two-dimensional quadrupole resonators, below the first lasing threshold. The boundary of the quadrupole cavity is defined by

$$R(\phi) = R_0(1 + \epsilon \cos(2\phi)), \quad (4.43)$$

where  $\phi$  is the polar angle,  $R_0$  is the average radius, and  $\epsilon$  is the deformation parameter. Disk or cylinder resonators of this type have been of interest for some time [60, 61] because as a function of the deformation the ray dynamics in the cavity undergoes a transition to chaos, with an attendant change in the emission patterns from the laser modes. For thin disks in three dimensions, strictly speaking, one should treat the diffraction effects in the axial ( $z$ ) direction; for cylinders many wavelengths long one may treat them as infinite in the  $z$  direction and study the  $k_z = 0$  mode, which then reduces to this purely two-dimensional scalar problem for either the electric (TM) or the magnetic (TE) modes. It is slightly simpler to treat the TM case for which the electric field is continuous at the boundary and we will focus on that case here. Both SALT and I-SALT are capable of treating modes of arbitrary polarization [118]. In two dimensions, the boundary condition for the incoming and outgoing TCF states requires matching via continuity from the interior cavity solutions to exterior solutions consisting of a superposition of either incoming or outgoing Hankel functions. The detailed method for doing this has been previously described [23, 97], and for brevity we omit it here. As mentioned above, the injection profile must now be defined at the border of the entire two-dimensional cavity, which must then be matched to an expansion of the incoming TCF states along this boundary.

Unlike the simple injection boundary condition in a single dimension, Eq. (4.13), in two dimensions there is an infinite variety of injected fields at the boundary and we find that the choice of the injection profile plays a large role in determining the resulting amplified mode

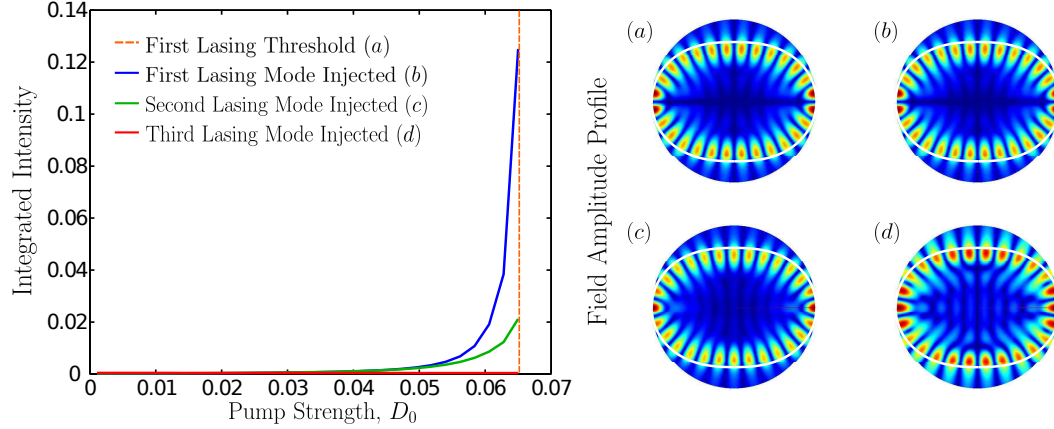


Figure 4.6: Simulations of a uniform index quadrupole cavity laser amplifier with  $n = 1.5$  (boundary indicated in white). The parameters chosen are  $R_0 = 1.72\mu m$ ,  $\lambda_a = 1\mu m$ ,  $\gamma_{\perp} = 0.03\mu m$ , and  $\epsilon = 0.16$ . The injected wavelength for all three simulations is the same as the that for the first free-running mode,  $\lambda_{in} = \lambda_1 = 0.989\mu m$ . The pump value was increased from  $D_0 = 0$  to the first free-running lasing threshold,  $d_0 = 0.065$ , vertical orange dashed line. The three solid curves show the amplifier output for three different injection conditions: blue, injection with the TCF corresponding to the first lasing mode; green, injection with the TCF corresponding to the second lasing mode; red, injection with the TCF corresponding to the third lasing mode. Lower plots show in color scale the normalized mode amplitude profiles: (a) The first free-running lasing mode at threshold. (b) The amplified mode with the first lasing mode's incoming TCF as input. (c) The amplified mode with the second lasing mode's incoming TCF as input. (d) The amplified mode with the third lasing mode's incoming TCF as input. The full disk shown in blue is the simulation region used; only TM modes were simulated. The atomic inversion and modal intensities are given in SALT units of  $E_c$  and  $d_c$ .

profile, as seen in Fig. 4.6. Here the cavity is injected with three different injection profiles, all at the first lasing mode's free-running frequency. The first lasing threshold in the absence of injection is shown as the orange dashed line and its corresponding mode profile is shown below. When the injected signal is given by the incoming TCF corresponding to the first lasing mode at threshold, the injected signal is amplified dramatically, and the resulting mode profile is nearly identical to that of the threshold lasing mode. However, when the injected signal, still at the same frequency, is chosen to be the incoming TCF corresponding to the second lasing mode, substantially less amplification occurs and the resulting mode profile is very similar to that of the second lasing mode at threshold, even though the difference in frequency between the first and second lasing modes is small compared with the linewidth of the atomic transition, and they have similar thresholds. Finally, when the incoming signal is represented by the incoming TCF state corresponding to the third lasing

mode, almost no amplification occurs, and the mode profile does not resemble the third lasing mode. Evidently, the injected mode profile plays a much stronger role in choosing the resulting amplified mode than the injected frequency does. Essentially, the injected profile is playing the role of a coherent pump or seed with a strong selectivity for a given resonance, so that we may think of it as interchanging the thresholds for, e.g., the first and second modes. This qualitative conclusion may have been difficult to guess in the absence of a quantitative theory.

## Chapter 5

# Designing an incoherent light source

As mentioned in the introduction, one of the defining characteristics of laser light is its coherence, due to its generation from stimulated, rather than spontaneous, emission. This coherence allows for laser beams to maintain their shape for long distances and is very useful for many applications, such as the detection of gravitational waves [169–171], which require measuring minute fluctuations in distance over hundreds of kilometers. However, this spatial coherence provides a major obstacle in using lasers for imaging techniques, as any uncontrolled scattering in the imaging system can lead to multipath interference, producing coherent artifacts in the resulting image, typically referred to as speckle. Thus, despite their lower power per mode, poorer collection efficiency, and reduced spectral control, many imaging applications continue to rely upon low spatial coherence light sources such as light emitting diodes (LEDs) instead of lasers. Some methods have already been developed to circumvent these problems, either using a raster-scan based method with a laser, or by reducing the spatial coherence of the emitted laser light with an intermediate device such as a spinning diffuser [172], colloidal solution [173], or microelectromechanical mirror [174]. However, all of these methods result in a dramatic increase in the measurement time, either by the requirement to individually measure every pixel in the image for the scanning methods, or to average over many speckle patterns in the latter, mitigating the

benefits of using a laser light source. Broadband sources such as superluminescent diodes and supercontinuum sources with low temporal coherence have also been used to suppress speckle in imaging systems [175]. Unfortunately, these sources still maintain high spatial coherence, producing speckle in the resulting image [176], and these sources cannot be readily adapted for narrowband illumination applications.

Different modes emitted by lasers typically generate uncorrelated speckle patterns and hence multimode emission reduces spatial coherence. Thus, recently, random lasers have been used as a source of effectively incoherent light, producing a sufficient number of laser modes so as to produce spatially incoherent light [177–179]. The underlying idea in these experiments is that the laser cavity can be optimized to produce an intermediate number of modes, without a definite phase relationship between them as occurs in mode-locked lasers, such that speckle can be suppressed while maintaining a much higher power per mode than an LED or thermal light source. Unfortunately, random lasers are difficult to fabricate and typically require optical pumping systems, which are large and expensive, reducing their attractiveness as components in commercial imaging systems. On chip arrays of VCSELs can provide upwards of 1000 simultaneous lasing modes, but require a relatively large footprint on the chip, and each individual VCSEL typically only lases in a single longitudinal mode, which is an impediment to developing such a device into a broadband source suitable, e.g. for optical coherence tomography (OCT) [180].

Broadly speaking, there are two requirements in designing a laser cavity suitable as an incoherent light source. First, there must be many modes with similar  $Q$ -factors, such that the device has the potential for many lasing modes, and second, the mode-competition between these modes needs to be minimized, so that all of these modes are able to reach threshold even in the presence of other modes. This is why random lasers in the diffusive regime are a good candidate for producing an effectively incoherent light source, they have many modes with similar  $Q$ -factors, whose spatial profiles are uniformly distributed throughout the cavity, which tends to minimize gain competition. For comparison, disk lasers are a poor choice for an incoherent light source, while disk cavities do support many high  $Q$  modes, these are all whispering gallery modes, localized at the edge of the cavity, which leads to large mode competition so that few of these modes ever reach threshold.

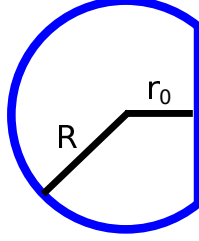


Figure 5.1: Schematic of a D-shaped cavity.

Here, we instead turn to chaotic cavity lasers, which refer to laser cavities whose ray dynamics are chaotic over much of the phase space [60, 181]. Neglecting out-coupling losses and considering the system as an ‘ideal billiard,’ the ray orbits for such a system cover much of the area of the cavity, indicating that the resulting spatial mode profiles are, on average, likely to be uniformly distributed across the cavity, leading to reduced mode competition, and no strongly preferred high  $Q$  modes as are seen in disk resonators. Note, a laser possessing a chaotic cavity is no more or less likely to demonstrate chaotic dynamics in its temporal behavior [101], despite their similar sounding names these two effects are completely unrelated. If the gain medium of the chaotic cavity laser satisfies  $\gamma_{\parallel} \ll \Delta, \gamma_{\perp}$ , then temporal chaos will not occur. In this chapter, we will focus on so called “D-shaped cavities,” consisting of a disk with radius  $R$ , with a section removed along a chord parameterized by  $r_0$ , as shown in Fig. 5.1. These cavities are known to support chaotic ray dynamics [182, 183], and a similar structure has already been used to improve the pumping efficiency of fiber amplifiers [184]. Furthermore, D-shaped cavities are much simpler to fabricate and can be electrically pumped, leading to a substantially simplified experimental setup when compared to a random laser.

Although D-shaped cavities are chaotic for any value of  $0 < r_0 < R$ , as  $r_0$  approaches either of these limits, the system approaches the non-chaotic limit, as both disks and semi-circles are not chaotic cavities, and thus we would expect to find lasing modes that are more spatially localized corresponding to the periodic orbits of these systems. As such, a reasonable guess for finding many spatially distributed modes is  $r_0 = .5R$ , where one would be unlikely to find any remnants of strongly preferred, spatially localized modes, leading to many modes with similar  $Q$  values. However, this only satisfies one of the criteria for

making an effectively incoherent light source, we also need to ensure that mode competition allows for all of these modes to reach threshold, as spatially delocalized modes still compete for gain with one another.

In this chapter we will use SALT to analyze the above threshold behavior of D-shaped cavities. In Sec. 5.1 we show exact SALT calculations demonstrating that the cavity with  $r_0 = .5R$  is indeed the correct choice for building an incoherent light source. In Sec. 5.2 we demonstrate that the single pole approximation can also be used to reach a similar conclusion, allowing such device design to be done without running the full, above threshold SALT calculation. Furthermore, we will also show in this section that COMSOL Multiphysics can be used in lieu of generating the TCF states for use in the single pole approximation of SALT (SPA-SALT). Finally, we will give a brief summary of the experimental results of D-shaped cavities fabricated by Brandon Redding from Hui Cao’s group at Yale University demonstrating that these cavities do produce spatially incoherent light suitable for a wide range of imaging applications [122].

## 5.1 D-shaped cavity design with SALT

To optimize the design of the D-shaped cavity, we simulated many such cavities with different values of  $r_0$  using SALT, as well as a circular cavity for comparison. For these two-dimensional, highly multimode simulations, the TCF lasing map Jacobian derived in Sec. 2.3.1 was an essential development, without which these simulations would have been prohibitively expensive to perform. As predicted, the D-shaped cavities demonstrate a substantially more uniform distribution of  $Q$ -factors, as can be seen in the left panel of Fig. 5.2, whereas the circular cavity boasts a small set of high- $Q$  modes. Results of the full SALT simulation can be seen in the right panel of Fig. 5.2, where the modal thresholds are plotted both for the non-interacting case (dashed lines), and with five modes lasing in each cavity (solid lines). Thus the difference between these two curves shows the effect of mode competition upon the lasing thresholds. As can be seen, the cavity with  $r_0 = .5R$  demonstrates both the most uniform distribution of  $Q$ -factors and the least amount of mode competition. Furthermore, the circular cavity can be seen to have modal thresholds similar to those of

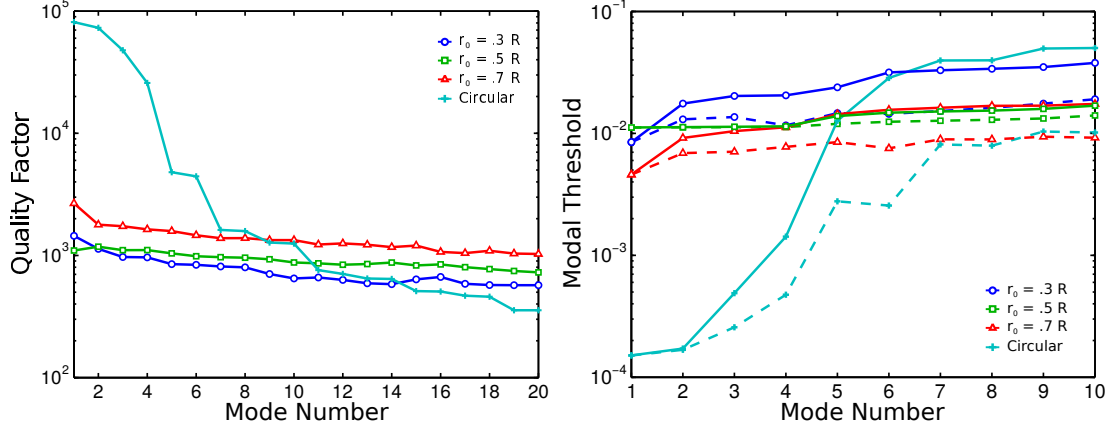


Figure 5.2: (Left panel) Semilog plot of the  $Q$ -factors for the first twenty modes for circular and D-shaped cavities with  $R = 5\mu\text{m}$ ,  $n = 3.5$ ,  $k_a = 1\mu\text{m}^{-1}$ , and  $\gamma_{\perp} = 0.03\mu\text{m}^{-1}$  in order of their modal thresholds as predicted by SALT. The circular cavity displays a few very high  $Q$  modes corresponding to whispering gallery modes, while the  $Q$  distributions for the D-shaped cavities are seen to be much more uniform, with no strongly preferred modes. (Right panel) Semilog plot of the threshold pump values,  $d_0$ , for the same set of circular and D-shaped cavities. Dashed lines show the non-interacting modal thresholds, while the solid lines show the thresholds calculated with five lasing modes active in the cavity. Thus, the first five values for the solid lines are exact, while the remaining values should be viewed as a lower bound, due to the increased gain saturation as the pump is further increased to reach subsequent modal thresholds.

the D-shaped cavities after the first few modes, and higher thresholds when considering mode competition.

The explanation for the benefits of the  $r_0 = .5R$  D-shaped cavity, as compared with the  $r_0 = .3R$  and  $r_0 = .7R$  can be seen in Fig. 5.3, which plots the spatial amplitude profiles of the first four lasing modes for each cavity. As can be seen, in the former case, the middle column of Fig. 5.3, the modes are uniformly distributed (with wavelength scale fluctuations) throughout the cavity, whereas the modes for the other two cavities appear to be near unstable periodic orbits, yielding relatively localized modes. Thus, for D-shaped cavities, the most chaotic cavity,  $r_0 = .5R$ , seems to not only have the most uniform  $Q$ -factor distribution, but also the least mode competition, making it an ideal candidate for making an effectively incoherent laser light source.

The information shown in Fig. 5.2 can also be summarized in terms of the normalized modal thresholds shown in Fig. 5.4. Here, the same information is shown, but the mode thresholds have been normalized to the first lasing threshold for each cavity. The effects of

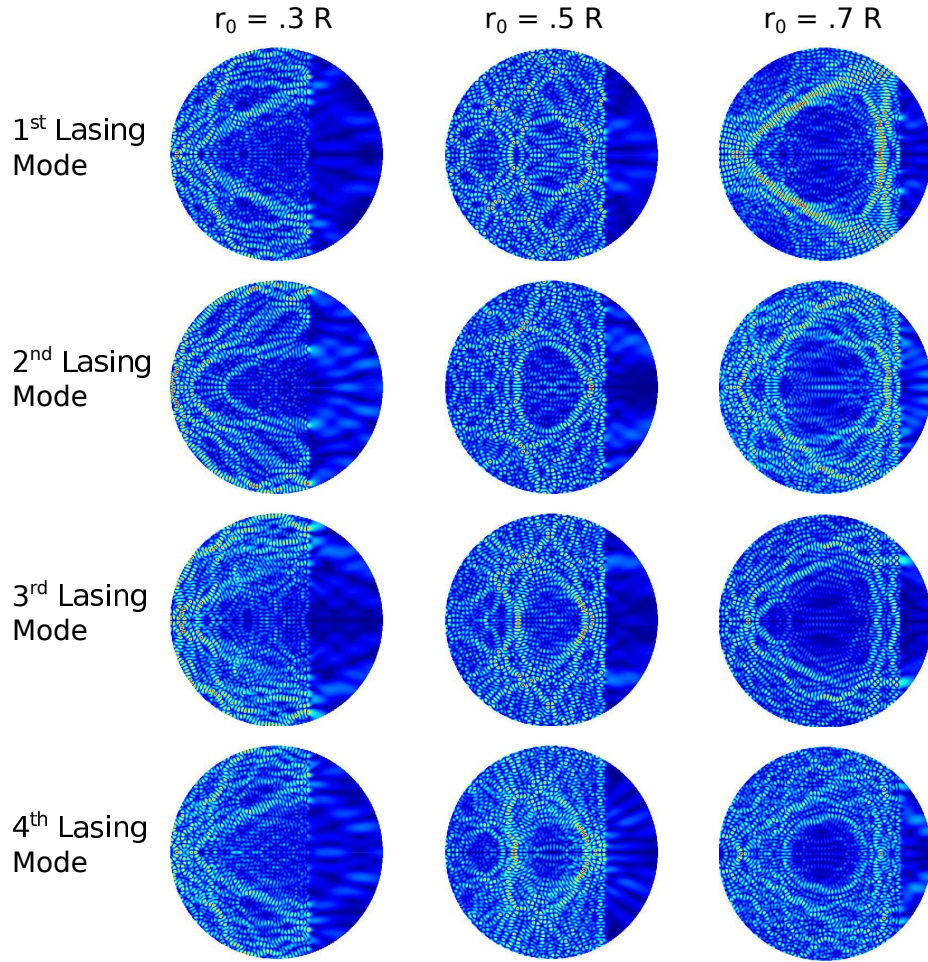


Figure 5.3: Spatial profile of the amplitude for the first four lasing modes at threshold for  $r_0 = .3R$ ,  $r_0 = .5R$ , and  $r_0 = .7R$ , shown in the first, second, and third columns respectively.

gain competition, again shown as the difference between the interacting SALT calculation (solid lines) and the non-interacting calculation (dashed-lines), are most pronounced in this representation. As noted above, the interacting modal thresholds are calculated with five active lasing modes, and thus the solid lines are exact for the first five lasing modes and should be considered as a lower bound for the remainder of the curve, as increasing the pump will lead to increased gain competition.

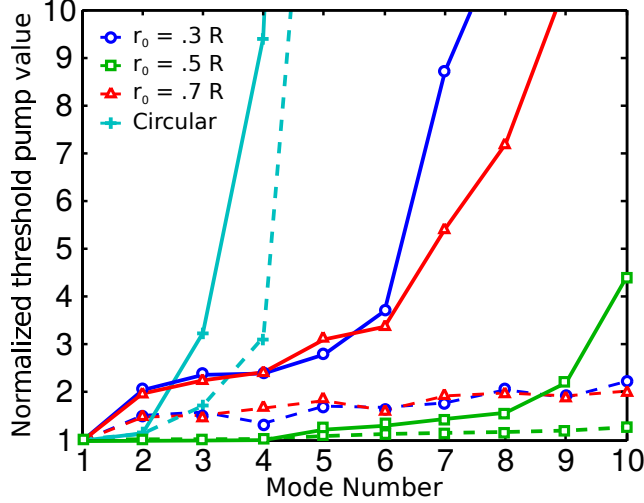


Figure 5.4: Plot of the normalized modal thresholds as predicted by SALT for circular and D-shaped cavities with  $R = 5\mu m$ ,  $n = 3.5$ ,  $k_a = 1\mu m^{-1}$ , and  $\gamma_{\perp} = 0.03\mu m^{-1}$ . Each curve has been normalized by the first lasing threshold for that laser cavity. Dashed lines denote non-interacting normalized modal thresholds while solid lines denote interacting modal thresholds when each system has five active lasing modes. Again, the solid lines are thus exact for the first five modes, while the remaining values represent a lower bound as increased competition will drive them higher as the pump is increased.

## 5.2 Using the single pole approximation

The full SALT calculations discussed in the previous section demonstrated unequivocally that the optimal D-shaped cavity design for an incoherent light source device was the maximally chaotic structure with  $r_0 = .5R$ . Unfortunately, these simulations were computationally expensive to perform, and thus might not be suitable for performing exploratory device design calculations over a wide array of structures. However, the relative  $Q$ -factors of these devices, at least  $Q \geq 10^3$ , make these structures ideal candidates for the single pole approximation, first worked out by Ge *et al.*, which allows for the effects of mode competition to be studied without the need for full SALT calculations to be made [25]. The essence of the single pole approximation is that the lasing mode frequency and spatial profile do not change much from their values at threshold, such that all that remains to be determined is the mode amplitude. The single pole approximation is valid for high  $Q$  cavities, where  $\gamma_c \ll \gamma_{\perp}$ , and thus corresponds to neglecting line pulling effects. The single pole approximation takes its name from the eigenvalue decomposition of the Green's function of the laser cavity, in which the Green's function is approximated as only having a contribution

from a single pole corresponding to the above threshold lasing mode.

Using the single pole approximation with SALT (SPA-SALT) allows for the rapid calculation of the above threshold properties of a laser system in terms of the mode overlap integrals,

$$\chi_{\mu\nu} = \int_C F(x) u_\mu^2(x) |u_\nu|^2 dx, \quad (5.1)$$

where  $u_\mu$  is the dominant TCF eigenstate corresponding to the  $\mu$ th lasing mode. While this integral is complex, for high- $Q$  systems in which the single pole approximation is valid,  $\chi_{\mu\nu}$  is essentially real, and thus  $\chi_{\mu\nu}$  is approximated to be real. Using these overlap integrals the interacting thresholds,  $d_{int}^{(\mu)}$ , can be calculated self-consistently as

$$d_{int}^{(\mu)} = d_0^{(\mu)} \left[ 1 + \sum_{\nu=1}^{N_L} A_{\mu\nu} (c_\nu d_{int}^{(\mu)} - b_\nu) \right], \quad (5.2)$$

where  $d_0^{(\mu)}$  is the non-interacting modal threshold for the  $\mu$ th lasing mode, the matrix  $A_{\mu\nu}$  is given by

$$A_{\mu\nu} = \frac{\gamma_\perp^2}{(\omega_\nu - \omega_a)^2 + \gamma_\perp^2} \chi_{\mu\nu}, \quad (5.3)$$

and the coefficients  $b_\mu$  and  $c_\mu$  are defined as

$$b_\mu = \sum_{\nu=1}^{N_L} (A^{-1})_{\mu\nu}, \quad (5.4)$$

$$c_\mu = \sum_{\nu=1}^{N_L} \frac{(A^{-1})_{\mu\nu}}{D_0^{(\nu)}}. \quad (5.5)$$

The effects of mode competition can be found using SPA-SALT through the ratio of the interacting and non-interacting modal thresholds by defining the mode competition parameter  $\lambda_\mu$  for the  $\mu$ th mode as,

$$d_{int}^{(\mu)} = \frac{d_0^{(\mu)}}{1 - \lambda_\mu}. \quad (5.6)$$

Thus,  $0 \leq \lambda \leq 1$ , where the lower bound is only reached at the first lasing threshold where there is no gain competition,  $\lambda_\mu = 0$ , and the upper bound is satisfied when mode clamping due to gain competition occurs, and no further lasing modes are able to turn on,  $\lambda_\mu = 1$ .

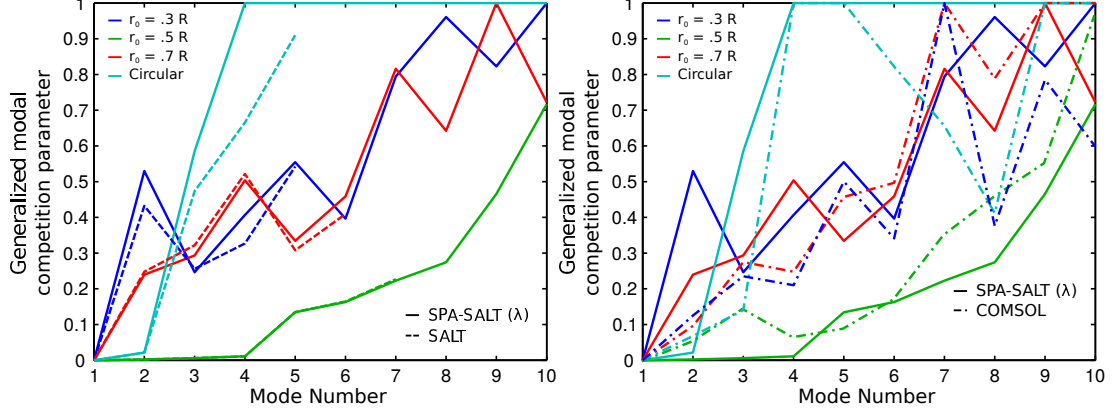


Figure 5.5: (Left panel) Comparison between SPA-SALT (solid lines) and full SALT (dashed lines) calculations for the D-shaped and circular cavities with  $R = 5\mu m$ ,  $n = 3.5$ ,  $k_a = 1\mu m^{-1}$ , and  $\gamma_{\perp} = 0.03\mu m^{-1}$ . Excellent agreement is seen between these two calculations, especially for the  $r_0 = .5R$  case, where the two curves are nearly indistinguishable. (Right panel) Solid lines again indicate the same SPA-SALT calculations shown in the left panel, and are plotted alongside SPA-SALT simulations performed using mode profiles calculated with COMSOL Multiphysics. Semi-quantitative agreement is seen, indicating that COMSOL Multiphysics can be easily expanded to give good above threshold predictions of lasers in the multimode regime.

One can solve for the generalized mode competition parameter by rewriting Eq. (5.2) as

$$\begin{aligned}
 d_{int}^{(\mu)} &= \frac{1 - \sum_{\nu=1}^{N_L} A_{\mu\nu} b_{\nu}}{1 - \sum_{\nu=1}^{N_L} A_{\mu\nu} c_{\nu} d_0^{(\mu)}} d_0^{(\mu)}, \\
 &= \frac{1}{1 - \frac{\sum_{\nu=1}^{N_L} A_{\mu\nu} (c_{\nu} d_0^{(\mu)} - b_{\nu})}{1 - \sum_{\nu=1}^{N_L} A_{\mu\nu} b_{\nu}}} d_0^{(\mu)}, \tag{5.7}
 \end{aligned}$$

which allows for the identification of the mode competition parameter as,

$$\lambda_{\mu} = \left[ 1 - \sum_{\nu=1}^{N_L} A_{\mu\nu} b_{\nu} \right]^{-1} \left( \sum_{\nu=1}^{N_L} A_{\mu\nu} (c_{\nu} d_0^{(\mu)} - b_{\nu}) \right). \tag{5.8}$$

Here, it is clear that while  $\lambda_{\mu}$  depends on the modal overlap parameters,  $\chi_{\mu\nu}$ , it is also dependent upon the  $Q$ -factors of the lasing modes, which enter through the non-interacting modal thresholds.

With the generalized mode competition parameter derived, we can compare it against the actual ratio of  $d_{int}^{(\mu)}/d_0^{(\mu)}$  which can be found from the full SALT calculation. The results of such a comparison can be seen for three different D-shaped cavities and a circular cavity

in the left panel of Fig. 5.5, where the SPA-SALT and SALT calculations are seen to be in close quantitative agreement even in the deep multimode regime. In fact, for the optimal D-shaped cavity with  $r_0 = .5R$ , the SPA-SALT and SALT calculations are almost identical. As SPA-SALT calculations are relatively cheap computationally to perform, this demonstrates that SPA-SALT using the TCF basis states is a viable tool for performing device design. Furthermore, the right panel of Fig. 5.5 shows semi-quantitative agreement between two different SPA-SALT calculations of the generalized mode competition parameter, the first calculated using the overlap integrals of TCF states (and is the same SPA-SALT data shown in the left panel), and the second calculated with overlap integrals using eigenstates generated by COMSOL Multiphysics. COMSOL Multiphysics is able to solve for the eigenfunctions and associated eigenvalues of dielectric structures by embedding those structures within a box, bounded on all four sides with an absorbing medium (usually a perfectly matched layer), so that only the resonances of the cavity in question are found. This feature directly calculates the spatial profile of these modes, as well as giving the frequencies,  $\omega_\mu$ , and  $Q$ -factors,  $Q_\mu = \omega_\mu/\gamma_{c,\mu}$ , for each potential mode. The spatial profile can be equated approximately to the TCF basis state for a uniform passive dielectric structure, while the TCF eigenvalue at the lasing frequency can be found by first finding the modal decay rates,  $\gamma_{c,\mu}$ , and then solving for

$$\eta_\mu(\omega_\mu) = \varepsilon_c \left( \frac{\left(\omega_\mu - \frac{i\gamma_{c,\mu}}{2}\right)^2}{\omega_\mu^2} - 1 \right), \quad (5.9)$$

where again we are assuming a uniform passive cavity dielectric function. Unlike building a full TCF basis which allows for one to solve for the eigenvalues as a function of the frequency everywhere,  $\eta(\omega)$ , COMSOL only solves for them at their resonance frequencies. However, this is exactly the limit where the single pole approximation is valid, as we are neglecting the effects of line pulling and mode competition leading to frequency shifts as seen in Ch. 4. Thus, the quantitative agreement seen in the left panel of Fig. 5.5 indicates that SPA-SALT can be used to perform device design calculations with reasonable accuracy, while the right panel demonstrates that the results found using SPA-SALT are robust

against different methods of calculating the threshold lasing modes and frequencies. Because COMSOL Multiphysics is a standard and widely available code (as opposed to the TCF codes at present), and the SPA-SALT equations are relatively simple, this provides a short-cut solution for using a SALT approach to treat strong modal interactions to reasonable accuracy.

### 5.3 Experimental results

In this section we will briefly discuss the experimental realization of the D-shaped cavity laser performed by Brandon Redding from Hui Cao’s group at Yale University [122]. Following the theoretical prediction in Sec. 5.1, D-shaped cavities were fabricated with the optimal multimode configuration,  $r_0 = .5R$ . These resonators, along with Fabry-Pérot cavities for comparison, were fabricated using standard photolithography and wet etching techniques on a commercial laser diode wafer containing a GaAs quantum well gain medium, suitable for electrical pumping.

To characterize the spatial coherence of the cavities, the output emission was collected using a 1-meter long, step-index multimode fiber and the speckle contrast was measured at the end of the fiber. The different lasing modes in the D-shaped cavities will excite different modes within the fiber, resulting in different speckle patterns at the fiber’s end. Assuming that these modes are undergoing independent oscillation, their speckle patterns are independent, causing them to add in intensity. The speckle contrast at the end of the fiber is given as  $C = \sigma_I / \langle I \rangle$ , where  $\sigma_I$  is the standard deviation of the intensity and  $\langle I \rangle$  is the average intensity. Thus, for mutually incoherent modes, the average intensity increases as additional modes participate, resulting in  $C = 1/\sqrt{N_L}$ , where  $N_L$  is the number of lasing modes present.

In Fig. 5.6(a-b) we show optical images of the speckle pattern at the output facet of the multimode fiber for the Fabry-Pérot and D-shaped cavities respectively. The Fabry-Pérot laser emission produced high spatial coherence, resulting in a speckle contrast of  $C = 0.58$ , indicating that the cavity was only producing  $\sim 3$  lasing modes. This is the result of mode competition within the cavity, which has the potential to support  $\sim 450$

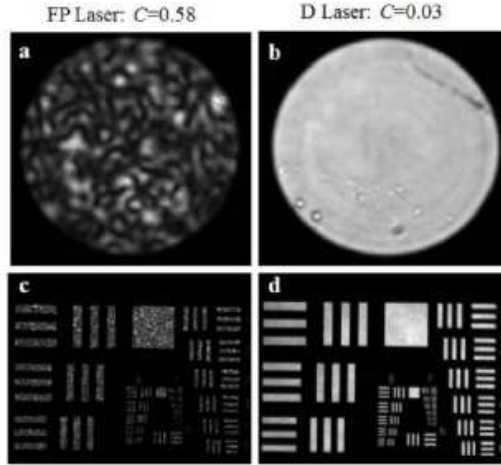


Figure 5.6: (a,b) Optical images of the speckle pattern at the end of a  $1m$  long multimode fiber by emission from a Fabry-Pérot laser (a) and D-shaped cavity laser (b). The Fabry-Pérot laser emission produced high contrast speckle ( $C = 0.58$ ), indicating that lasing was limited to  $\sim 3$  transverse modes, whereas the D cavity laser produced low contrast speckle ( $C = 0.03$ ), implying independent lasing in  $\sim 1000$  modes. (c,d) The emission from the end of the multimode fiber was used to illuminate an Air Force resolution test chart in transmission mode through an immobile ground glass diffuser. The high spatial coherence of the Fabry-Pérot laser produced a speckled image (c) whereas the low spatial coherence of the D laser emission gave a high quality image with low speckle contrast (d) [122].

transverse modes given its construction as a  $100\mu m$  wide ridge waveguide. The D-shaped cavity with  $R = 500\mu m$ , demonstrated a much lower speckle contrast,  $C = 0.03$ , suggesting that at  $\sim 1000$  lasing modes are simultaneously above threshold, indicating the suppression of gain competition in this cavity. Finally, both lasers were used to illuminate an Air Force resolution test chart in transmission operation through an immobile glass diffuser. As can be seen in Fig. 5.6(c-d), the Fabry-Pérot laser yields too much speckle to identify the test chart, while this speckle vanishes when the test chart is imaged using the D-shaped cavity laser. This provides a conclusive demonstration that the D-shaped cavity laser produces spatially incoherent emission suitable for many optical imaging techniques.

## Chapter 6

# The TCMT linewidth formula: a quantitative test

The most important property of laser physics not captured by semiclassical theories is the intrinsic laser linewidth due to spontaneous emission from the gain medium. Above the laser threshold, this causes an uncertainty in the phase of the emitted laser signal, leading to a broadening of the observed frequency. The magnitude of the signal’s linewidth depends upon the geometry of the laser cavity as well as the output power and was first calculated by Schawlow and Townes to be [31],

$$\delta\omega_{\text{ST}} = \frac{\hbar\omega_0\gamma_c^2}{2P} \quad (6.1)$$

where  $\omega_0$  is the central frequency of the emitted laser light,  $\gamma_c$  is the decay rate of the passive cavity resonance corresponding to the laser mode, and  $P$  is the output power. In subsequent decades, improved theoretical analyses allowed for the discovery of corrections to this formula, most of which tended to increase the linewidth. One correction, the Henry  $\alpha$  factor, arises from the coupling between intensity and phase fluctuations [18, 19]. A second correction arises from the incomplete inversion of the gain medium, and accounts for the number of inverted gain atoms (rather than the total) which are able to spontaneously emit [185]. The Petermann factor describes the increase in the linewidth due to the non-orthogonality of the lasing mode [17, 186–189]. Finally, the “bad-cavity” factor leads to

a reduction in the laser linewidth and only deviates from unity when the cavity decay rate is similar to the dephasing rate of the polarization of the gain medium [4, 185, 190–193]. This correction was originally attributed to the slowdown of phase diffusion due to atomic memory effects [4, 185, 190], and subsequently an alternative explanation was offered, attributing the effect to an increase in the cavity’s group refractive index caused by the frequency dispersion of the gain medium [191]. Recently however, it has been discovered that the Petermann correction, the bad-cavity factor, and the passive cavity mode decay rate are intertwined; they are all associated with the motion of, and distance between, the poles and zeros of the scattering matrix describing the laser cavity, and can only be disentangled in specific cases [131, 132].

Pick *et al.* have recently completed a general derivation of the intrinsic linewidth of the laser that incorporates all of these corrections into a single expression [123]. This formula is based on the temporal coupled mode theory (TCMT), and predicts the laser linewidth to be,

$$\delta\omega_{\text{TCMT}} = \frac{\hbar\omega_0 \omega_0^2 \int \text{Im}[\varepsilon(x, \omega_0)] |\psi_0(x)|^2 dx \int \text{Im}[\varepsilon(x, \omega_0)] \frac{N_2(x)}{d(x)} |\psi_0(x)|^2 dx}{2P \left| \int \psi_0^2(x) \left( \varepsilon(x, \omega_0) + \frac{\omega_0}{2} \frac{d\varepsilon}{d\omega} \Big|_{\omega_0} \right) dx \right|^2} (1 + \tilde{\alpha}^2), \quad (6.2)$$

where  $\varepsilon(x)$  is the total dielectric function of the passive cavity plus gain medium,  $N_2(x)$  and  $D(x)$  are the number of excited atoms and the atomic inversion respectively,  $\tilde{\alpha}$  is the generalized  $\alpha$  factor [123], and  $\psi_0(x)$  is the normalized spatial profile of the semiclassical lasing field inside of the cavity and can be calculated exactly using SALT, such that  $\int \psi_0^2 dx = 1$  [21, 23, 25]. This equation reduces to the separable corrections discussed above in the appropriate limits [123, 132], but in general reinforces the notion that the incomplete inversion, Petermann, and bad-cavity linewidth corrections cannot be considered independent from each other or the cavity decay rate. In this chapter, we test the predictions of the TCMT linewidth formula against the Schawlow-Townes linewidth formula, including the Petermann correction and incomplete inversion factor, by directly integrating the laser equations using the Finite Difference Time Domain (FDTD) method, including the quantum fluctuations using the method proposed by Drummond and Raymer [194], using the time-stepping method proposed by Bidégaray [148].

Many previous numerical studies of spontaneous emission in laser cavities have implemented the noise based on knowledge of the lasing mode structure [195–198]. However, these studies did not have access to the above threshold lasing mode profiles, which are similar to, but not exactly the same as, the passive cavity modes used in calculating the Petermann factor. Thus for our purposes here it would be unwise to make a particular spatial mode ansatz. Hoffman and Hess derived noisy semiconductor-Bloch lasing equations, but the analysis made the assumption that the gain carrier and photon number fluctuations were independent, an assumption which breaks down above the lasing threshold [199]. The effects of fluctuations in the electromagnetic fields due to thermal effects has been previously studied using the FDTD algorithm [200,201], and these effects are necessary when studying the noise properties of masers or other long wavelength lasers, but can be safely neglected at optical frequencies where the spontaneous emission events being considered here dominate the noise of the laser. The approach used in this manuscript is similar to that used by Andreasen *et al.*, both in the equations used and in the analysis method to obtain the signal’s linewidth; here though we will be interested in the above threshold linewidths, which have not been previously studied [202–204]. Unlike these previous studies however, we will be considering relatively simple and small laser cavities allowing us to achieve the spectral resolution necessary to resolve the narrow laser linewidths far above the lasing threshold.

The outline of the remainder of this chapter is as follows, first, in Sec. 6.1 we provide a derivation of the TCMT linewidth result. Next, in Sec. 6.2 we demonstrate the equivalence of the macroscopic picture of the TCMT linewidth formula with the microscopic picture used by Drummond and Raymer. In Sec. 6.3 we review the equations and numerical method used in the FDTD algorithm to simulate a noisy gain medium coupled to a laser cavity. Sec. 6.4 presents the methodologies for extracting a linewidth from the resultant noisy signal in both the frequency and time domains. The results of our study are given in Sec. 6.5, including the direct comparison between the Schawlow-Townes and TCMT linewidth predictions in a simple laser cavity, the increase in the linewidth in the first lasing mode as the second lasing mode nears threshold, and simulations for lasers with a large Henry  $\alpha$  factor.

## 6.1 Temporal coupled mode theory

In this section we will derive the TCMT linewidth result for a gain medium in the instantaneous response limit, where any fluctuations in the field are immediately incorporated into the polarization and inversion. This approximation is suitable for class A lasers, where both the inversion and polarization can be adiabatically eliminated [101]. Furthermore, Pick *et al.* have demonstrated that this result is identical to that found in the non-instantaneous model as well, appropriate for class B lasers [123]. As the dynamics of the gain medium are neglected, we begin with the noisy wave equation in the frequency domain,

$$[\nabla \times \nabla \times -\omega^2 \varepsilon(\omega, \mathbf{E})] \mathbf{E}(\mathbf{x}, \omega) = \mathbf{F}_S(\mathbf{x}, \omega), \quad (6.3)$$

where  $\varepsilon$  is the full dielectric function of the cavity and gain medium, and  $\mathbf{F}_S$  is a random noise source corresponding to the spontaneous emission from the gain medium. Here, we will focus on the single lasing mode linewidth and identify the semiclassical and quantum mechanical portions of the wave equation as

$$[\nabla \times \nabla \times -\omega^2 \varepsilon(\omega, \mathbf{E}_0)] \mathbf{E} = \omega^2 (\varepsilon(\omega, \mathbf{E}) - \varepsilon(\omega, \mathbf{E}_0)) \mathbf{E} + \mathbf{F}_S, \quad (6.4)$$

in which  $\varepsilon(\omega, \mathbf{E}_0)$  is the dielectric function of the cavity in the presence of the semiclassical lasing mode  $\mathbf{E}_0(\mathbf{x})$ . The left side of this equation represents the semiclassical lasing problem, while the right side represents the noise sources, direct spontaneous emission,  $\mathbf{F}_S$ , and the fluctuations in the saturation of the gain medium as a result of the spontaneous emission events. The Green's function for the semiclassical problem can be written as,

$$[\nabla \times \nabla \times -\omega^2 \varepsilon(\omega, \mathbf{E}_0)] \mathbf{G}(\mathbf{x}, \mathbf{x}'; \omega) = \delta(\mathbf{x} - \mathbf{x}'), \quad (6.5)$$

and can be solved for using the eigenvalue decomposition method as

$$\mathbf{G}(\mathbf{x}, \mathbf{x}'; \omega) = \sum_{n=1} \frac{\mathbf{E}_n(\mathbf{x}) \mathbf{E}_n^T(\mathbf{x}')}{\lambda_n(\omega) \int \mathbf{E}_n^2(\mathbf{x}) d\mathbf{x}}, \quad (6.6)$$

wherein  $\lambda_n$  is the eigenvalue of the  $n$ th spatial mode,  $\mathbf{E}_n$ . Note, the bounds of integration in Eq. (6.6) are over all of space, not just the cavity. In a cavity below threshold the modes of the cavity are similar to the TCF states, and above threshold they correspond to the lasing mode and interacting below-threshold modes of the cavity.

When a single lasing mode is active, the Green's function is dominated in the vicinity of that frequency by the contribution from the lasing mode, which has a pole on the real axis at that frequency. This allows us to expand the eigenvalue in the vicinity of the pole as

$$\lambda_0(\omega) = (\omega - \omega_0) \left. \frac{\partial \lambda_0}{\partial \omega} \right|_{\omega_0}. \quad (6.7)$$

The derivative of this eigenvalue can be found using the Hellmann-Feynman theorem by first identifying the semiclassical lasing operator as

$$\mathcal{L}_{\omega_0} = [\nabla \times \nabla \times -\omega_0^2 \varepsilon(\omega_0, \mathbf{E}_0)] \quad (6.8)$$

where the frequency perturbation term is expanded as

$$V(\omega) = \frac{\partial}{\partial \omega} [\omega^2 \varepsilon(\omega, \mathbf{E}_0)]_{\omega_0} (\omega - \omega_0). \quad (6.9)$$

Then, the derivative  $\partial \lambda_0 / \partial \omega$  can be evaluated from  $dV/d\omega$ , resulting in

$$\left. \frac{\partial \lambda_0}{\partial \omega} \right|_{\omega_0} = \frac{\int \mathbf{E}_0^2(\mathbf{x}) \frac{\partial}{\partial \omega} [\omega^2 \varepsilon(\omega, \mathbf{E}_0)]_{\omega_0} d\mathbf{x}}{\int \mathbf{E}_0^2 d\mathbf{x}}. \quad (6.10)$$

Thus, the Green's function for frequencies close to the lasing frequency can be approximated as

$$\mathbf{G}(\mathbf{x}, \mathbf{x}'; \omega) = \frac{\mathbf{E}_0(\mathbf{x}) \mathbf{E}_0^T(\mathbf{x}')}{(\omega - \omega_0) \int \frac{\partial}{\partial \omega} [\omega^2 \varepsilon(\omega, \mathbf{E}_0)]_{\omega_0} \mathbf{E}_0^2 d\mathbf{x}}. \quad (6.11)$$

With this result in hand, we can return to the original problem containing noise,

Eq. (6.4), and solve for the electric field for a single mode, as

$$\begin{aligned} \mathbf{E}(\mathbf{x}, \omega) &= \omega^2 \int \mathbf{G}(\mathbf{x}, \mathbf{x}'; \omega) (\varepsilon(\omega, \mathbf{E}) - \varepsilon(\omega, \mathbf{E}_0)) \mathbf{E}(\mathbf{x}', \omega) d\mathbf{x}' + \int \mathbf{G}(\mathbf{x}, \mathbf{x}'; \omega) \mathbf{F}_S(\mathbf{x}', \omega) d\mathbf{x}' \\ &= \frac{\mathbf{E}_0(\mathbf{x})}{\omega - \omega_0} \left[ \frac{\omega^2 \int_C \mathbf{E}_0(\mathbf{x}) \cdot \mathbf{E}(\mathbf{x}, \omega) (\varepsilon - \varepsilon_0) d\mathbf{x}}{\int_C \frac{\partial}{\partial \omega} [\omega^2 \varepsilon(\omega, \mathbf{E}_0)]_{\omega_0} \mathbf{E}_0^2 d\mathbf{x}} + \frac{\int_C \mathbf{E}_0(\mathbf{x}) \cdot \mathbf{F}_S(\mathbf{x}, \omega) d\mathbf{x}}{\int_C \frac{\partial}{\partial \omega} [\omega^2 \varepsilon(\omega, \mathbf{E}_0)]_{\omega_0} \mathbf{E}_0^2 d\mathbf{x}} \right], \end{aligned} \quad (6.12)$$

where in the numerator of the second line we have written  $\varepsilon_0 = \varepsilon(\omega, \mathbf{E}_0)$  as the dielectric function of the cavity saturated with the semiclassical lasing mode, and we have approximated the integrals over all of space as integrals strictly over the cavity, which is nearly exact [123, 132]. Next, we note that there is no explicit dependence upon the normalization of the spatial profile of the lasing mode, thus we can replace  $\mathbf{E}_0 \rightarrow \psi_0$ , where  $\psi_0$  is the normalized spatial profile of the lasing mode which can be calculated using SALT, such that  $\int \psi_0^2 d\mathbf{x} = 1$ . (The overall magnitude of the semiclassical solution still is needed in the evaluation of the spatial hole-burning in  $\varepsilon$ .) Finally, we expand the full electric field as  $\mathbf{E}(\mathbf{x}, \omega) = A(\omega) \psi_0(\mathbf{x})$ , resulting in,

$$(\omega - \omega_0) A(\omega) \psi_0 = \psi_0 \left[ \frac{\omega^2 \int_C \psi_0^2 (\varepsilon - \varepsilon_0) d\mathbf{x} A(\omega)}{\int_C \frac{\partial}{\partial \omega} [\omega^2 \varepsilon_0(\omega, \mathbf{E}_0)]_{\omega_0} \psi_0^2 d\mathbf{x}} + \frac{\int_C \psi_0 \cdot \mathbf{F}_S(\mathbf{x}, \omega) d\mathbf{x}}{\int_C \frac{\partial}{\partial \omega} [\omega^2 \varepsilon_0(\omega, \mathbf{E}_0)]_{\omega_0} \psi_0^2 d\mathbf{x}} \right]. \quad (6.13)$$

For a two-level gain medium the dielectric function is,

$$\varepsilon(\omega, \mathbf{E}) = \varepsilon_c + \frac{4\pi\theta^2}{\hbar} \frac{d_0}{\omega - \omega_a + i\gamma_{\perp}} \left( \frac{1}{1 + \frac{4\theta^2}{\hbar^2 \gamma_{\perp} \gamma_{\parallel}} \Gamma |A\psi_0(x)|^2} \right), \quad (6.14)$$

where  $\Gamma = \gamma_{\perp}^2 / ((\omega - \omega_a)^2 + \gamma_{\perp}^2)$  is the Lorentzian linewidth of the atomic transition. This allows for the difference in the instantaneous and steady-state dielectric functions to be written as,

$$\begin{aligned} \varepsilon - \varepsilon_0 &= \varepsilon(\omega, |A\psi|^2) - \varepsilon(\omega, |A_0\psi|^2), \\ &= \frac{4\pi\theta^2}{\hbar} \frac{d_0}{\omega - \omega_a + i\gamma_{\perp}} \left[ \frac{\frac{4\theta^2}{\hbar^2 \gamma_{\perp} \gamma_{\parallel}} \Gamma (|A_0\psi_0|^2 - |A\psi_0|^2)}{\left(1 + \frac{4\theta^2}{\hbar^2 \gamma_{\perp} \gamma_{\parallel}} \Gamma |A\psi_0|^2\right) \left(1 + \frac{4\theta^2}{\hbar^2 \gamma_{\perp} \gamma_{\parallel}} \Gamma |A_0\psi_0|^2\right)} \right]. \end{aligned} \quad (6.15)$$

As additional lasing transitions appear in the definition of the dielectric as the sum of their

susceptibilities, we can in general write that

$$\varepsilon - \varepsilon_0 = \frac{\partial \varepsilon}{\partial |A|^2} \Big|_{A=A_0} (|A|^2 - |A_0|^2), \quad (6.16)$$

which allows for us to rewrite Eq. 6.13 as,

$$(\omega - \omega_0)A(\omega)\psi_0 = \psi_0 \left[ \frac{\omega^2 \int_C \psi_0^2 \frac{\partial \varepsilon}{\partial |A|^2} \Big|_{A_0} d\mathbf{x} (|A|^2 - |A_0|^2) A(\omega)}{\int_C \frac{\partial}{\partial \omega} [\omega^2 \varepsilon_0(\omega, \mathbf{E}_0)]_{\omega_0} \psi_0^2 d\mathbf{x}} + \frac{\int_C \psi_0 \cdot \mathbf{F}_S(\mathbf{x}, \omega) d\mathbf{x}}{\int_C \frac{\partial}{\partial \omega} [\omega^2 \varepsilon_0(\omega, \mathbf{E}_0)]_{\omega_0} \psi_0^2 d\mathbf{x}} \right]. \quad (6.17)$$

This expression can be clearly identified as the Fourier transform of an evolution equation for the amplitude  $A(t) = a(t)e^{-i\omega_0 t}$ , which can be written in the generic form of

$$\partial_t a = C(a_0^2 - |a|^2)a + f(t), \quad (6.18)$$

where  $C$  is the dependence of the amplitude on the non-linear gain medium,

$$C = \frac{-i\omega_0^2 \int_C \psi_0^2 \frac{\partial \varepsilon}{\partial |a|^2} \Big|_{a_0} d\mathbf{x}}{\int_C \frac{\partial}{\partial \omega} [\omega^2 \varepsilon(\omega, \mathbf{E}_0)]_{\omega_0} \psi_0^2 d\mathbf{x}}, \quad (6.19)$$

and  $f(t)$  is the effective Langevin noise,

$$f(t) = \frac{\int_C \psi_0 \cdot \mathbf{F}_S(\mathbf{x}, \omega) d\mathbf{x}}{\int_C \frac{\partial}{\partial \omega} [\omega^2 \varepsilon(\omega, \mathbf{E}_0)]_{\omega_0} \psi_0^2 d\mathbf{x}}, \quad (6.20)$$

both of which can be identified from Eq. (6.13).

As mentioned before, the above threshold laser linewidth is given by the phase fluctuations in the amplitude of the electric field, which can be identified by defining

$$a(t) = (a_0 + \delta(t))e^{i\phi(t)}. \quad (6.21)$$

This allows for the linearization of Eq. (6.18) as

$$\partial_t \delta = -A\delta + \text{Re}[f(t)], \quad (6.22)$$

$$a_0 \partial_t \phi = -B\delta + \text{Im}[f(t)], \quad (6.23)$$

where the constants are given by  $A = 2a_0^2 \text{Re}[C]$  and  $B = 2a_0^2 \text{Im}[C]$ . By solving the former equation, Eq. (6.22), for  $\delta(t)$ , the latter, Eq. (6.23), can be used to solve for the phase correlations as

$$\langle (\phi(t) - \phi(0))^2 \rangle = \Delta\omega |t| = \frac{R}{2a_0^2} (1 + \tilde{\alpha}^2) |t|, \quad (6.24)$$

where  $\tilde{\alpha} = \text{Im}[C]/\text{Re}[C]$  is the generalized  $\alpha$ -factor and  $R$  is the diffusion coefficient of the Langevin force  $f(t)$ ,

$$\langle f(\omega) f^*(\omega) \rangle = R. \quad (6.25)$$

To evaluate the diffusion coefficient, we use the fluctuation dissipation theorem to calculate the noise associated with the polarization of the gain medium,  $\mathbf{P}_N$ ,

$$\langle \mathbf{P}_N(\mathbf{x}, \omega) \mathbf{P}_N^*(\mathbf{x}', \omega) \rangle = \hbar \text{Im}[\chi(\mathbf{x}, \mathbf{E}_0)] \coth\left(\frac{\hbar\omega\beta(\mathbf{x})}{2}\right) \delta(\mathbf{x} - \mathbf{x}'), \quad (6.26)$$

where  $\chi(\mathbf{x}, \mathbf{E}_0)$  is the electric susceptibility of the gain medium. The hyperbolic cotangent factor arises as a sum of a Bose-Einstein distribution and a factor of 1/2 from the quantum zero-point fluctuations, which is why the auto-correlation does not vanish in the zero temperature limit ( $\beta \rightarrow \infty$ ). However, it was shown by Henry and Kazarinov that the contributions from the zero-point fluctuations cancel in the linewidth formula [205], and as such it is convenient to explicitly subtract this contribution,

$$\langle \mathbf{P}_N(\mathbf{x}, \omega) \mathbf{P}_N^*(\mathbf{x}', \omega) \rangle = 2\hbar \text{Im}[\chi(\mathbf{x}, \mathbf{E}_0)] \left( \frac{1}{2} \coth\left(\frac{\hbar\omega\beta(\mathbf{x})}{2}\right) - \frac{1}{2} \right) \delta(\mathbf{x} - \mathbf{x}'). \quad (6.27)$$

The polarization can be related to the noise source as  $\mathbf{F}_S(\mathbf{x}, \omega) = -4\pi\omega^2 \mathbf{P}_N(\mathbf{x}, \omega)$ , resulting in

$$\langle \mathbf{F}_S(\mathbf{x}, \omega) \mathbf{F}_S^*(\mathbf{x}', \omega) \rangle = 8\pi\hbar\omega^4 \text{Im}[\varepsilon(\mathbf{x}, \mathbf{E}_0)] \left( \frac{1}{2} \coth\left(\frac{\hbar\omega\beta(\mathbf{x})}{2}\right) - \frac{1}{2} \right) \delta(\mathbf{x} - \mathbf{x}'), \quad (6.28)$$

noting that  $\text{Im}[\varepsilon] = 4\pi\text{Im}[\chi]$ . The diffusion coefficient, Eq. (6.20), can then be evaluated as

$$R = 8\pi\hbar\omega_0^4 \frac{\int_C |\psi_0|^2 \text{Im}[-\varepsilon(\mathbf{x}, \mathbf{E}_0)] \frac{N_2(\mathbf{x})}{d(\mathbf{x})} d\mathbf{x}}{\left| \int_C \frac{\partial}{\partial \omega} [\omega^2 \varepsilon(\omega, \mathbf{E}_0)]_{\omega_0} \psi_0^2 d\mathbf{x} \right|^2}, \quad (6.29)$$

where the effective inverse temperature has been identified as relating to the inversion of the atomic gain medium as [123, 185],

$$\frac{1}{2} \left[ \coth \left( \frac{\hbar\omega_0\beta(\mathbf{x})}{2} \right) - 1 \right] = -\frac{N_2(\mathbf{x})}{d(\mathbf{x})}, \quad (6.30)$$

with  $N_2$  being the spatially dependent number of atoms in the upper atomic state. By multiplying the top and bottom of Eq. (6.29) by  $a_0^2$ , we can identify the SALT lasing mode solution as  $\Psi_0(x) = a_0\psi_0(x)$ , resulting in the linewidth, Eq. (6.24), of

$$\Delta\omega = 4\pi\hbar\omega_0^4 \frac{\int_C |\Psi_0|^2 \text{Im}[-\varepsilon(\mathbf{x}, \mathbf{E}_0)] \frac{N_2(\mathbf{x})}{d(\mathbf{x})} d\mathbf{x}}{\left| \int_C \frac{\partial}{\partial \omega} [\omega^2 \varepsilon(\omega, \mathbf{E}_0)]_{\omega_0} \Psi_0^2 d\mathbf{x} \right|^2}. \quad (6.31)$$

The bad-cavity factor can be recognized in the denominator of this expression explicitly by partially evaluating the frequency derivative,

$$\frac{\partial}{\partial \omega} [\omega^2 \varepsilon(\omega, \mathbf{E}_0)]_{\omega_0} = 2\omega_0 \left[ \varepsilon + \frac{\omega_0}{2} \frac{\partial \varepsilon}{\partial \omega} \Big|_{\omega_0} \right]. \quad (6.32)$$

Finally, the time-averaged power can be calculated as [25, 112],

$$P = \frac{\omega_0}{2\pi} \int_C \text{Im}[-\varepsilon(\mathbf{x}, \omega_0)] |\Psi_0|^2 d\mathbf{x}, \quad (6.33)$$

which results in Eq. (6.31) yielding the TCMT linewidth, Eq. (6.2), which is repeated here,

$$\delta\omega_{\text{TCMT}} = \frac{\hbar\omega_0 \omega_0^2 \int \text{Im}[\varepsilon] |\Psi_0|^2 dx \int \text{Im}[\varepsilon] \frac{N_2}{d} |\Psi_0|^2 dx}{2P \left| \int \Psi_0^2 \left( \varepsilon + \frac{\omega_0}{2} \frac{d\varepsilon}{d\omega} \Big|_{\omega_0} \right) dx \right|^2} (1 + \tilde{\alpha}^2).$$

## 6.2 Microscopic and macroscopic noise equivalence

The derivation of the TCMT equation takes a macroscopic view, with many properties of the gain medium producing the spontaneous emission buried within the imaginary part of

the response of the medium used in the fluctuation dissipation theorem. However, many traditional theories of the noise in the gain media begin by treating the Langevin forces on the quantum operators of individual gain atoms and building up an understanding of the total noise this imparts upon the electric field, a decidedly microscopic view [3, 185, 194]. This section will demonstrate the equivalence of these two methods by deriving the total Langevin force on the polarization, Eq. (6.27, from the microscopic perspective. For a two-level atomic gain medium, the evolution equation for the off-diagonal matrix element of the  $\alpha$ th atom, including the Langevin force,  $\Gamma_{(\rho)}^{(\alpha)}(t)$ , is given by,

$$\partial_t \rho_{21}^{(\alpha)}(t) = -(\gamma_{\perp} + i\omega_a) \rho_{21}^{(\alpha)}(t) + \frac{id^{(\alpha)}}{\hbar} \boldsymbol{\theta} \cdot \mathbf{E}(\mathbf{x}^{(\alpha)}, t) + \Gamma_{(\rho)}^{(\alpha)}(t), \quad (6.34)$$

and the evolution of the inversion for that atom,  $d^{(\alpha)}$ , including the Langevin force,  $\Gamma_{(d)}^{(\alpha)}(t)$ , is given by

$$\partial_t d^{(\alpha)} = \gamma_{\parallel} (d_0^{(\alpha)} - d^{(\alpha)}) + \frac{2}{i\hbar} \boldsymbol{\theta} \cdot \mathbf{E}(\mathbf{x}^{(\alpha)}, t) (\rho_{21}^{(\alpha)*} - \rho_{21}^{(\alpha)}) + \Gamma_{(d)}^{(\alpha)}(t) \quad (6.35)$$

where  $d_0^{(\alpha)}$  is the inversion of the  $\alpha$ th atom in the absence of any electric field. Finally, the wave equation for the electric field can be written in this context by explicitly including the coupling between the field and each individual gain atom (see Eqs. (5.55) and (5.48) in Ref. [3]),

$$[\nabla \times \nabla \times -\omega_0^2 \varepsilon_c] \mathbf{E}(\mathbf{x}, \omega) = 4\pi\omega_0^2 \boldsymbol{\theta} \sum_{\alpha} \delta(\mathbf{x} - \mathbf{x}^{(\alpha)}) \rho_{21}^{(\alpha)}, \quad (6.36)$$

in which we have approximated that the electric field is oscillating at frequencies close to the semiclassical lasing frequency,  $\omega_0$ , and retained only the positive frequency components for both the electric field and atomic polarization. Our aim is to determine the form of the effective total Langevin force on the electric field by solving Eqs. (6.34) and (6.35) for the polarization and inversion, insert these expressions into the wave equation, and collect the resulting Langevin force terms.

To leading order,  $\rho_{21}$  will oscillate at the lasing frequency,  $\omega_0$ , and if we approximate

this as its only frequency component, we can solve for

$$\tilde{\rho}_{21}^{(\alpha)} = \frac{-d^{(\alpha)}}{\hbar(\omega_0 - \omega_a + i\gamma_{\perp})} \boldsymbol{\theta} \cdot \tilde{\mathbf{E}}(\mathbf{x}^{(\alpha)}, \omega) + \frac{ie^{i\omega_0 t}}{\omega_0 - \omega_a + i\gamma_{\perp}} \Gamma_{(\rho)}^{(\alpha)}, \quad (6.37)$$

where the electric field is assumed to be a constant over the volume of the atom at  $\mathbf{x}^{(\alpha)}$ . The fluctuation dissipation theorem states that the strength of the fluctuations is proportional to the strength of the dissipative terms. Thus, for the lasers of interest in this thesis, class A and B lasers,  $\gamma_{\parallel} \ll \gamma_{\perp}$ , so  $\Gamma_{(d)}^{(\alpha)}(t) \ll \Gamma_{(\rho)}^{(\alpha)}(t)$ , and we can safely ignore the fluctuations in the atomic inversion. Thus, we can insert Eq. (6.37) into Eq. (6.36),

$$[\nabla \times \nabla \times -\omega_0^2 \varepsilon_c] \mathbf{E}(\mathbf{x}, \omega) = 4\pi\omega_0^2 \boldsymbol{\theta} \sum_{\alpha} \delta(\mathbf{x} - \mathbf{x}^{(\alpha)}) \left[ \frac{-d^{(\alpha)}(\boldsymbol{\theta} \cdot \mathbf{E}(\mathbf{x}^{(\alpha)}, \omega))}{\hbar(\omega_0 - \omega_a + i\gamma_{\perp})} + \frac{ie^{i\omega_0 t}}{\omega_0 - \omega_a + i\gamma_{\perp}} \Gamma_{(\rho)}^{(\alpha)} \right]. \quad (6.38)$$

Equation (6.38) allows for the identification of the spontaneous noise in the polarization,  $\mathbf{P}_N$ , using Eq. (6.4) and noting that  $\mathbf{F}_S = -4\pi\omega^2 \mathbf{P}_N$ , as

$$\mathbf{P}_N(\mathbf{x}, \omega) = \sum_{\alpha} \delta(\mathbf{x} - \mathbf{x}^{(\alpha)}) \frac{i\boldsymbol{\theta} e^{i\omega_0 t}}{\omega_0 - \omega_a + i\gamma_{\perp}} \Gamma_{(\rho)}^{(\alpha)}(\omega). \quad (6.39)$$

We can now directly calculate the correlation function of the spontaneous noise in the polarization using the correlation of the atomic Langevin force [3],

$$\langle \Gamma^{(\alpha)}(t) \Gamma^{(\beta)\dagger}(t') \rangle = \left[ \gamma_{\perp} (1 + \langle d^{(\alpha)} \rangle) + \frac{\gamma_{\parallel}}{2} (d_0^{\alpha} - \langle d^{(\alpha)} \rangle) \right] \delta_{\alpha\beta} \delta(t - t'). \quad (6.40)$$

By assuming that the inversion is relatively stationary, we can identify the same frequency auto-correlation of the noise as [206]

$$\langle \Gamma^{(\alpha)}(\omega) \Gamma^{(\beta)\dagger}(\omega) \rangle = \gamma_{\perp} (1 + \langle d^{(\alpha)} \rangle) \delta_{\alpha\beta}, \quad (6.41)$$

in which we have again dropped the noise source proportional to  $\gamma_{\parallel}$ , to be consistent with the approximation neglecting fluctuations in the inversion made above. This allows us to

solve for

$$\langle \mathbf{P}_N^\dagger(\mathbf{x}, \omega) \mathbf{P}_N(\mathbf{x}', \omega) \rangle = \frac{2\theta^2 \gamma_\perp}{(\omega_0 - \omega_a)^2 + \gamma_\perp^2} N_2(\mathbf{x}) \delta(\mathbf{x} - \mathbf{x}'), \quad (6.42)$$

where the number of atoms in the upper lasing state,  $N_2(\mathbf{x})$  has been identified using,

$$N_2(\mathbf{x}) = \frac{1}{2} \sum_\alpha \delta(\mathbf{x} - \mathbf{x}^{(\alpha)}) (1 + \langle d^{(\alpha)} \rangle). \quad (6.43)$$

Upon substitution of the imaginary part of the electric susceptibility,

$$\text{Im}[\chi] = -\frac{\theta^2}{\hbar} \frac{\gamma_\perp d(\mathbf{x})}{(\omega - \omega_a)^2 + \gamma_\perp^2}, \quad (6.44)$$

and the definition of the temperature factor given in Eq. (6.30), Eq. (6.42) is identical to the macroscopic application of the fluctuation dissipation theorem, Eq. (6.27). With this, the derivation of the equivalence of the macroscopic application of the fluctuation dissipation theorem used in Eq. (6.27) and the microscopic application used in Eq. (6.40) is complete. Thus, all of the physical effects predicted in the TCMT theory should also be present in the microscopic model.

### 6.3 Noisy FDTD equations

The FDTD algorithm was introduced in Sec. 1.4.2 for studying the semiclassical Maxwell-Bloch equations independent of noise. The FDTD approach has only been used a few times previously to study noise [202–204], and never before for lasers far above the lasing threshold, as we do here. However, when including the spontaneous emission noise, care must be taken to simulate the appropriate atomic quantities consistent with the form of the Langevin noise term which has been introduced. As such, we will briefly review the simulated equations here. The Maxwell-Bloch equations for a two level atomic gain medium

in a one dimensional cavity can be written as

$$\frac{d}{dt}E_n = \frac{c^2}{\varepsilon_c} \left[ \frac{d}{dx}B_n + 4\pi \left( \frac{\theta}{V_s} \right) \frac{d}{dt} (J_n + J_n^*) \right], \quad (6.45)$$

$$\frac{d}{dt}B_n = \frac{d}{dx}E_n, \quad (6.46)$$

$$\frac{d}{dt}J_n = -(\gamma_{\perp} + i\omega_a)J_n + \frac{i\theta}{\hbar}E_n d_n + F_n^{(J)}, \quad (6.47)$$

$$\frac{d}{dt}d_n = -\gamma_{\parallel}(d_n - d_{0,n}) + \frac{2\theta}{i\hbar}E_n(J_n^* - J_n) + F_n^{(d)}, \quad (6.48)$$

where  $E_n$  and  $B_n$  are the electric and magnetic field densities at the spatial location  $x_n$  within the lasing cavity,  $V_s$  is the volume of the spatial location,  $J_n$  is the total atomic off-diagonal density matrix element (related to the polarization) with a positive frequency component, and  $d_n$  is the inversion of the  $N_s$  atoms at the spatial location  $x_n$ ,  $d_{0,n}$  is the inversion in the absence of an electric field, and plays the role of the pump in this theory, and  $F_n^{(J)}$  and  $F_n^{(d)}$  are the c-number values of the Langevin forces experienced by the atomic off-diagonal matrix element and inversion respectively. The choice of  $J_n$  for the total off-diagonal density matrix element is made for ease of comparison with Drummond and Raymer, who use  $J_n^-$  to denote the same quantity, which is given by,

$$J_n(x) = \sum_{\alpha} \rho_{21}^{(\alpha)} \delta(x - x^{(\alpha)}) = N_s \rho_{21}(x). \quad (6.49)$$

The c-number forms of the Langevin equations can be written as [194],

$$F_n^{(J)} = \xi_n^{(J)} \sqrt{-2i\theta E_n J_n} + \xi_n^{(P)} \sqrt{\gamma_P(d_n + N_s)} + \xi_n^{(N)} \sqrt{\gamma_{21,n} N_s}, \quad (6.50)$$

$$F_n^{(d)} = 2\xi_n^{(d)} \left[ \frac{\gamma_{\parallel}}{2} \left( N_s - \frac{d_{0,n}}{N_s} d_n \right) + i\theta (J_n E_n - J_n^* E_n) - 2\gamma_{21,n} \frac{J_n^* J_n}{N_s} \right]^{(1/2)} - 2 \left[ \xi_n^{(N)} J_n^* + \xi_n^{(N)*} J_n \right] \sqrt{\frac{\gamma_{21,n}}{N_s}}, \quad (6.51)$$

in which  $\gamma_{21}$  is the pumping rate from lower level  $|\varphi_l\rangle$  to the upper level  $|\varphi_u\rangle$  and is given by,

$$\gamma_{21,n} = \frac{\gamma_{\parallel}}{2} \left( 1 + \frac{d_{0,n}}{N_s} \right), \quad (6.52)$$

and  $\gamma_P = \gamma_\perp - \gamma_\parallel/2$  is the pure dephasing rate. In these equations the randomness is included through the stochastic variables  $\xi$ , which are complex except for  $\xi_n^{(d)} \in \mathbb{R}$ , and satisfy [194]

$$\langle \xi_n^{(i)}(t) \xi_m^{(j)}(t') \rangle = \delta(t - t') \delta_{nm} \delta_{ij}. \quad (6.53)$$

Many of the terms in Eqs. (6.50)-(6.51) arise from the different operator orderings which appear when reducing operator equations to c-number equations. However, for the present application the difference caused by resolving this ambiguity is minimal, as the addition or removal of a vacuum spontaneous emission event is negligible in the presence of the large number of gain atoms necessary for lasing to occur. Thus most of these terms can be neglected, a procedure that can also be checked *a posteriori* by calculating their relative size and noting that they are many orders of magnitude smaller than the terms retained here,

$$F_n^{(J)} = \xi_n^{(P)} \sqrt{\gamma_P(d_n + N_s)} + \xi_n^{(N)} \sqrt{\gamma_{21,n} N_s}, \quad (6.54)$$

$$F_n^{(d)} = 2\xi_n^{(d)} \sqrt{\frac{\gamma_\parallel}{2} \left( N_s - \frac{d_{0,n}}{N_s} d_n \right)}. \quad (6.55)$$

Finally, in accordance with the discussion in the previous section, the fluctuating force due to of the electric and magnetic fields have been dropped as they are tiny at optical frequencies.

The Maxwell-Bloch equations can then be discretized for use in the FDTD algorithm following the weak coupling method proposed by Bidégaray [148], evolving the atomic variables alongside the magnetic field in time, but at the same spatial locations as the electric field so as to avoid solving a non-linear equation. Furthermore, it is useful to separate the real and imaginary components of the atomic off-diagonal density matrix element,  $J_n = j_n^{(1)} + i j_n^{(2)}$ ,

resulting in

$$E_n(t_{i+1}) = E_n(t_i) + \frac{c^2 \Delta t}{\varepsilon_c} \left[ 8\pi \left( \frac{\theta}{V_s} \right) \left( \omega_a j_n^{(2)}(t_{i+\frac{1}{2}}) - \gamma_{\perp} j_n^{(1)}(t_{i+\frac{1}{2}}) \right) + \frac{B_{n+\frac{1}{2}}(t_{i+\frac{1}{2}}) - B_{n-\frac{1}{2}}(t_{i+\frac{1}{2}})}{\Delta x} \right], \quad (6.56)$$

$$B_{n+\frac{1}{2}}(t_{i+\frac{1}{2}}) = B_{n+\frac{1}{2}}(t_{i-\frac{1}{2}}) + \frac{\Delta t}{\Delta x} (E_{n+1}(t_i) - E_n(t_i)) \quad (6.57)$$

$$\mathbf{u}_n(t_{i+\frac{1}{2}}) = \left( \frac{1}{\Delta t} I - \frac{1}{2} M \right)^{-1} \left[ \mathbf{d}_n + \mathbf{f}_n + \left( \frac{1}{\Delta t} I + \frac{1}{2} M \right) \mathbf{u}_n(t_{i-\frac{1}{2}}) \right], \quad (6.58)$$

where  $\mathbf{u}_n = (d_n, j_n^{(1)}, j_n^{(2)})$  is the vector of the atomic variables,  $\mathbf{d}_n = (\gamma_{\parallel} d_{0,n}, 0, 0)$  is the pumping vector,  $I$  is the 3x3 identity matrix,  $M$  is a matrix which contains the coupling information between the atomic variables,

$$M = \begin{pmatrix} -\gamma_{\parallel} & 0 & -\frac{4\theta}{\hbar} E_n(t_i) \\ 0 & -\gamma_{\perp} & \omega_a \\ \frac{\theta}{\hbar} E_n(t_i) & -\omega_a & -\gamma_{\perp} \end{pmatrix}, \quad (6.59)$$

and  $\mathbf{f}_n$  is the Langevin force vector, whose elements are

$$f_{n,1} = 2\xi_n^{(1)} \sqrt{\frac{\gamma_{\parallel}}{2} (N_s - \frac{d_{0,n}}{N_s} d_n(t_{i-\frac{1}{2}}))}, \quad (6.60)$$

$$f_{n,2} = \frac{\xi_n^{(2)}}{\sqrt{2}} \sqrt{\gamma P(d_n(t_{i-\frac{1}{2}}) + N_s)} + \frac{\xi_n^{(3)}}{\sqrt{2}} \sqrt{\gamma_{21,n} N_s}, \quad (6.61)$$

$$f_{n,3} = \frac{\xi_n^{(4)}}{\sqrt{2}} \sqrt{\gamma P(d_n(t_{i-\frac{1}{2}}) + N_s)} + \frac{\xi_n^{(5)}}{\sqrt{2}} \sqrt{\gamma_{21,n} N_s}, \quad (6.62)$$

where we have renumbered the random variables  $\xi_n^{(i)}$ , which continue to satisfy Eq. (6.53), but are now real, rather than complex, and accumulated a factor of  $2^{-1/2}$  in this conversion process (except for  $\xi_n^{(1)}$ , which was real to begin with). Here we have used the final approximation that the Langevin force vector only depends upon the inversion at the previous time step, rather than the average of the previous and current time steps which would result in a non-linear equation [204]. This is justified for the simulations performed here because the inversion,  $d_n$ , is many orders of magnitude smaller than the total number of atoms,  $N_s$ , and thus these inversion dependent terms will have minimal impact upon the overall strength of

the noise. For the discretized Langevin forces, the stochastic variables  $\xi_n^{(k)}$  are chosen from a standard uniform distribution, and then renormalized to satisfy

$$\langle \xi_n^{(k)}(t_i) \xi_m^{(l)}(t_j) \rangle = \frac{1}{\Delta t} \delta_{ij} \delta_{nm} \delta_{kl}. \quad (6.63)$$

Equations 6.56-6.62 can now be readily evaluated numerically.

## 6.4 Numerical linewidth analysis

Broadly speaking there are two main ways of extracting a linewidth from a noisy signal, by either fitting a curve to the frequency domain data or calculating the cross-correlation of the time domain data [207]. Here we will use both methods, first calculating a linewidth from the spectral data and then confirming this linewidth by calculating  $\langle \phi(t') \phi(t) \rangle$ , where  $\phi(t)$  is the phase of the electric field.

### 6.4.1 frequency domain analysis

To analyze the spectrum of the electric field output from the cavity,  $E(\omega)$ , and find a linewidth, we will use the method proposed by Andreasen *et al.* [204], and fit the spectrum to a Lorentzian through the use of an error function. We assume that the noise is a Lorentzian,

$$L(\omega) = \left( \frac{2A}{\pi} \right) \frac{s^2}{(\omega - \omega_0)^2 + s^2} \quad (6.64)$$

where  $s$  is the half-width half-maximum of the noise,  $\delta\omega_{\text{FDTD}} = 2s$ . The Lorentz error function can then be defined as

$$L_{EF}(\omega) = \int_{\omega_0}^{\omega} L(\omega') d\omega' = \left( \frac{2As}{\pi} \right) \arctan \left( \frac{\omega - \omega_0}{s} \right). \quad (6.65)$$

As such, this integration can be carried out numerically directly upon  $E(\omega)$ , and then fit to Eq. (6.65). For all of the data shown in this paper the curve fitting is carried out using MATLAB. Performing this integration requires knowledge of the lasing frequency,  $\omega_0$ , which is known from the semiclassical SALT calculation. However, the presence of noise results

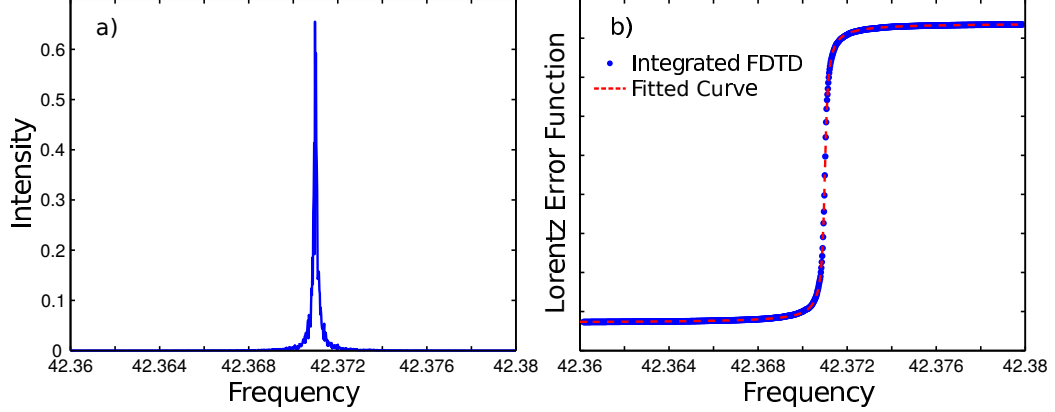


Figure 6.1: (a) Intensity spectrum of the output electric field of an  $n = 3$  dielectric slab cavity. The simulation parameters for the cavity are  $\gamma_{\perp} = .5$ ,  $\omega_a = 42.4$ ,  $\gamma_{\parallel} = .01$ ,  $\theta = 2 \times 10^{-9}$ ,  $N_A = 10^{10}$ , and the cavity is uniformly pumped at  $D_0 = 0.275$  which is close to 5 times the threshold lasing pump of  $D_{0,thr} = 0.0488$ . The rates quoted here are given in units of  $c/L$ , while the intensity is given in SALT units of  $4\theta^2/(\hbar^2\gamma_{\perp}\gamma_{\parallel})$ , and the number and inversion of gain atoms are given in the SALT units of  $4\pi\theta^2/(\hbar\gamma_{\perp})$ . (b) Plot of the fitted Lorentz error function (red line) and numerically integrated FDTD data (blue dots) of the simulation shown in (a). The spectral resolution for the simulated data in (a) and (b) is  $d\omega = 1.96 \times 10^{-5}$ . The analytic curve fit parameters are found using MATLAB's curve fitting algorithms.

in a slight shift of the semiclassical lasing frequency [18], which leads to a slightly shifted, both horizontally and vertically integrated spectrum, and as such it is useful to include two other unknown parameters in the Lorentz error function,

$$L'_{EF}(\omega) = \left(\frac{2As}{\pi}\right) \arctan\left(\frac{\omega - \omega_0 + d}{s}\right) + c, \quad (6.66)$$

where  $d$  plays the role of the horizontal offset and  $c$  is the vertical offset. Using this correction, the calculated linewidths are robust to the choice of  $\omega_0$  so long as the curve fitting algorithm converges.

An example of this process can be seen in Fig. 6.1, where the left panel shows the spectrum of the output electric field for a dielectric slab cavity which has been Fourier transformed and had multiple spectra been averaged together following Bartlett's method [207]. The right panel shows the Lorentz error function integral calculated numerically and fit against the analytic curve. The resulting linewidth predicted by this method is  $\delta\omega_{\text{FDTD}} = 2.22 \times 10^{-4}$ , which is around an order of magnitude larger than the resolution of

the resultant spectra,  $d\omega = 1.96 \times 10^{-5}$ , given in units of  $c/L$ .

#### 6.4.2 time domain confirmation

This calculation can be independently confirmed by calculating the autocorrelation of the output electric field as a function of time and expressing this as a function of the phase correlation, which is defined in terms of the linewidth of the signal. Writing the output electric field as

$$E(t) = C \cos(\omega t + \phi(t)), \quad (6.67)$$

we can similarly express the electric field at a later time using standard trigonometric identities,

$$E(t + \delta t) = C [\cos(\omega t + \phi(t)) \cos(\omega \delta t + \delta\phi(\delta t)) - \sin(\omega t + \phi(t)) \sin(\omega \delta t + \delta\phi(\delta t))], \quad (6.68)$$

where  $\delta\phi(\delta t) = \phi(t + \delta t) - \phi(t)$ . The autocorrelation of the electric field,  $R_{EE}(\delta t) = \langle E(t + \delta t)E(t) \rangle$ , can then be written as

$$R_{EE}(\delta t) = \langle E^2(t) \cos(\omega \delta t + \delta\phi(\delta t)) \rangle - \langle \frac{C^2}{2} \sin(2\omega t + 2\phi(t)) \sin(\omega \delta t + \delta\phi(\delta t)) \rangle, \quad (6.69)$$

where the double angle formula has been used in finding the second term on the right hand side. By assuming that the phase shift  $\delta\phi(\delta t)$  is uncorrelated with the phase  $\phi(t)$ , we can separate the correlations, note that the second term averages to zero, and again apply a trigonometric identity, resulting in

$$R_{EE}(\delta t) = \frac{C^2}{2} [\cos(\omega \delta t) \langle \cos(\delta\phi(\delta t)) \rangle - \sin(\omega \delta t) \langle \sin(\delta\phi(\delta t)) \rangle]. \quad (6.70)$$

This assumption that the phase shift,  $\delta\phi$  is uncorrelated with the instantaneous phase,  $\phi$ , is analogous to assuming that the phase of the gain medium is memory-less, and is also consistent with the earlier assumption that the bad-cavity factor is unity for the systems studied here. The second term in Eq. (6.70) averages to zero as well, as the phase shift is equally likely to be positive or negative. Finally, the cosine of the phase shift can be Taylor

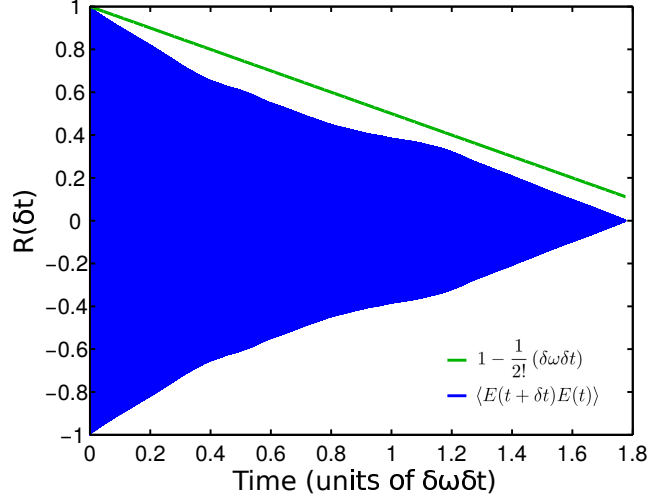


Figure 6.2: Plot of the autocorrelation of the electric field simulated numerically for the same parameter used in Fig. 6.1 (blue line) and the analytic prediction for the envelope of the autocorrelation given in the second factor in Eq. (6.72) (green line). The fast oscillations in the numerically simulated electric field are at the lasing frequency  $\omega_0$ , which is much faster than the other time scales in the problem, and leads to the densely packed curve shown in blue. Quantities are normalized, and plotted in units of  $\delta\omega\delta t$ .

expanded, and noting the definition of the linewidth,

$$\langle \delta\phi^2(\delta t) \rangle = \delta\omega\delta t, \quad (6.71)$$

the electric field autocorrelation can be written as

$$R_{EE}(\delta t) = \frac{C^2}{2} \cos(\omega\delta t) \left[ 1 - \frac{\delta\omega\delta t}{2} + O(\delta t^2) \right], \quad (6.72)$$

showing that in the presence of phase diffusion, the correlation should decrease linearly for small  $\delta t$ .

This trend can be observed in Fig. 6.2 for the same simulation as shown in Fig. 6.1, and demonstrates that for small  $\delta t$ , the decrease in the autocorrelation of the electric field is indeed linear. There are two oscillation scales present in the data of Fig. 6.2, the first of which is predicted theoretically in Eq. (6.72) and corresponds to the fast oscillations due to the frequency of the lasing signal. The second oscillation scale corresponds to the much longer frequency due to the beating between the lasing mode and the side-peaks generated by noise, which can be seen in Fig. 6.1, and is not included in the above derivation. However,

even given these difficulties, it is clear that the overall envelope of the autocorrelation does decay linearly for small  $\delta t$ , using the linewidth calculated for this same simulation in the previous section. This confirms that the linewidth analysis procedure given above is correct, and gives a reliable result for the linewidth of the simulated laser.

## 6.5 Linewidth comparison results

We first study the simple one-dimensional, single-sided dielectric slab cavity,  $n = 3$ , used in the previous two sections in Figs. 6.1 and 6.2 to compare the predictions of the TCMT linewidth, given in Eq. (6.2), with the corrected Schawlow-Townes linewidth [31],

$$\delta\omega_{\text{ST}}^{(\text{corr})} = \frac{\hbar\omega_0\gamma_c^2}{2P} \left( \frac{\bar{N}_2}{\bar{D}} \right) \left| \frac{\int |\phi_0(x)|^2 dx}{\int \phi_0^2(x) dx} \right|^2 \left| \frac{1}{1 + \frac{\omega_0}{2\varepsilon} \frac{\partial\varepsilon}{\partial\omega}|_{\omega_0}} \right|^2 (1 + \alpha^2), \quad (6.73)$$

where  $\phi_0(x)$  is the passive cavity resonance corresponding to the lasing mode, the spatial average of the inversion and occupation of the upper lasing state is denoted as  $\bar{D} = \int D(x)dx$ , the spatially averaged inversion is used to calculate the bad cavity factor, and  $\alpha$  is the Henry- $\alpha$  factor. The first term in parentheses of Eq. (6.73) corresponds to the cavity averaged incomplete inversion factor and the second corresponds to the Petermann factor [17, 132]. The quantities  $\psi_0(x)$ ,  $\phi_0(x)$ ,  $D(x)$ , and  $\varepsilon(x)$  are calculated using SALT, while the FDTD linewidths are extracted using the method described in Sec. 6.4.1, and run for enough time steps to average together at least six resulting spectra using Bartlett's method. The gain medium was chosen to yield a class A laser [101], with  $\delta\omega \ll \gamma_{\parallel} \ll \gamma_{\perp}$ , so no relaxation oscillation side-peaks are seen in the resulting spectra.

As can be seen in the left panel of Fig. 6.3, excellent quantitative agreement is seen between the TCMT prediction (green line) and the linewidths measured through direct integration of the noisy Maxwell-Bloch equations (magenta triangles), while both results differ from the corrected Schawlow-Townes theory (blue line). This discrepancy is shown to be more than a simple scaling factor in the right panel of Fig. 6.3, where the same data is plotted on a log-log scale, and it can be seen that the power law behavior of the linewidth with respect to the output power is different between the TCMT and corrected Schawlow-

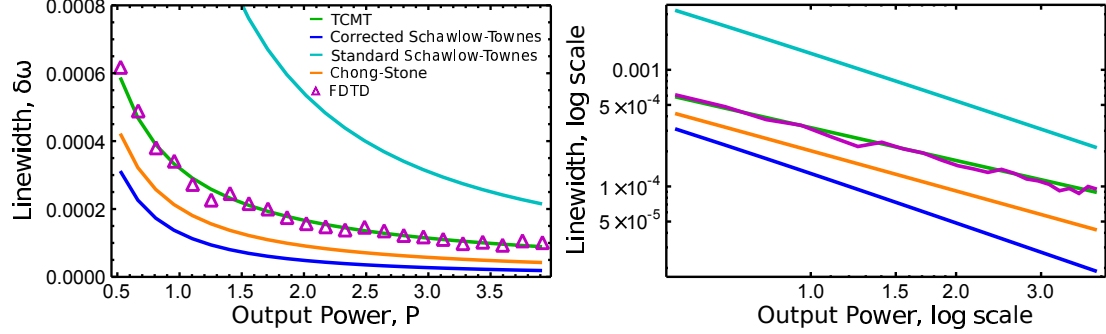


Figure 6.3: (Left panel) Plot showing the linewidth predictions given by the TCMT given in Eq. (6.2) (green), corrected Schawlow-Townes theory given in Eq. (6.73) (blue), corrected Schawlow-Townes theory calculated using the spatially averaged output power in Eq. (6.78) (cyan), integral form of the Chong-Stone linewidth formula given in Eq. (6.74) (orange), and FDTD simulations (magenta) for a uniformly pumped, dielectric slab cavity with  $n = 3$ ,  $\omega_a = 42.4$ ,  $\gamma_{\perp} = .5$ ,  $\gamma_{\parallel} = .01$ ,  $\theta = 2 \times 10^{-9}$ , and  $N_A = 10^{10}$ . Except where noted, all of the linewidth formulas are evaluated using the spatially dependent integral definition of the power given by Eq. (6.77). (Right panel) Plot of the same data shown on a log-log scale. The rates and frequency are given in units of  $c/L$ , the number of atoms in the cavity is given in terms of the SALT units of  $4\pi\theta^2/(\hbar\gamma_{\perp})$ , and the output power is given in the SALT units of  $4\theta^2/(\hbar^2\gamma_{\perp}\gamma_{\parallel})$ .

Townes linewidth predictions. To understand the source of this discrepancy, we also plot the Chong-Stone linewidth [131] calculated using its integral form [132],

$$\delta\omega_{\text{CS}} = \frac{\hbar\omega_0}{2P} \left( \frac{\bar{N}_2}{\bar{D}} \right) \frac{(\omega_0 \int \text{Im}[\varepsilon(x, \omega_0)] |\psi_0(x)|^2 dx)^2}{|\int \psi_0^2(x) (\varepsilon + \frac{\omega_0}{2} \frac{d\varepsilon}{d\omega}|_{\omega_0}) dx|^2} (1 + \alpha^2), \quad (6.74)$$

where we have neglected the vanishingly small boundary term. The Chong-Stone linewidth formula is derived through considering the behavior of the scattering matrix of the cavity, and thus is able to correctly account for effects stemming from the cavity: the proper cavity decay rate above threshold, the Petermann factor, and the bad-cavity correction. However, it does not provide an accurate treatment of the fluctuations in the gain medium, and is unable to account for the incomplete inversion factor and the Henry  $\alpha$  factor. For the dielectric slab cavity studied here, the detuning of the lasing mode from the atomic transition is very small, such that  $\alpha \ll 1$ . Thus, the fact that the TCMT and FDTD results also differ from the Chong-Stone prediction indicates that the largest source of discrepancy lies in the treatment of the incomplete inversion factor. The ratio of the TCMT and Chong-

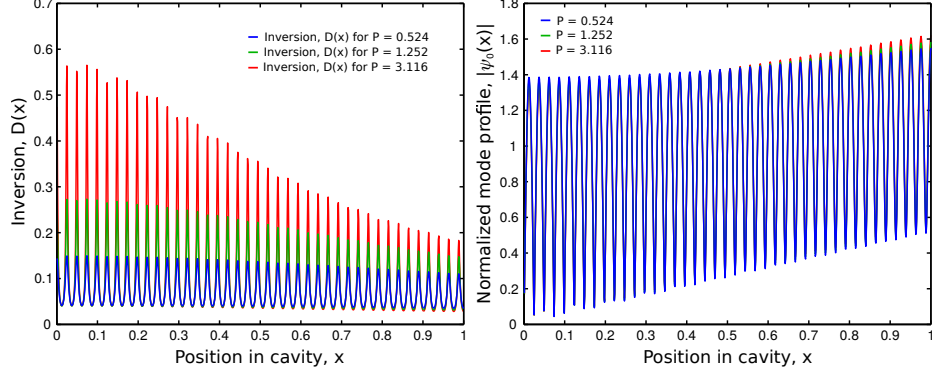


Figure 6.4: (Left panel) Plot of the steady-state inversion,  $D(x)$ , as a function of the location in the cavity for three different values of the output power,  $P = 0.524$  (blue),  $P = 1.252$  (green), and  $P = 3.116$  (red). These values correspond to the first, sixth, and eighteenth data points shown in Fig. 6.3. Strong spatial hole-burning is seen in the inversion due to the lasing mode. (Right panel) Plot of the normalized spatial profile of the lasing mode,  $|\psi_0(x)|$ , as a function of position in the cavity for the same three values of the output power shown in the left panel. The output power is given in dimensionless SALT units of  $4\theta^2/(\hbar^2\gamma_\perp\gamma_\parallel)$ .

Stone linewidth predictions in the limit that  $\tilde{\alpha} = \alpha = 0$  can be written as

$$\frac{\delta\omega_{\text{CS}}}{\delta\omega_{\text{TCMT}}} = \frac{\bar{N}_2 \int D(x)|\psi_0(x)|^2 dx}{\int N_2(x)|\psi_0(x)|^2 dx}. \quad (6.75)$$

However, for the two-level atomic gain media simulated here, the number of atoms in the excited atomic level is nearly constant  $N_2(x) \approx N_2$ , allowing for this ratio to be expressed as

$$\frac{\delta\omega_{\text{CS}}}{\delta\omega_{\text{TCMT}}} = \frac{\int D(x)|\psi_0(x)|^2 dx}{\int |\psi_0(x)|^2 dx \int D(x) dx}. \quad (6.76)$$

Note that the approximation of spatial invariance of the occupation of the upper lasing level does not hold when considering most gain media, with more than two levels, and is a result of the well known difficulty in pumping a two-level medium past the transparency point to achieve an inversion for lasing action to occur.

The linewidth prediction ratio expressed in Eq. (6.76) can be understood graphically from Fig. 6.4, where the left panel shows the steady-state inversion,  $D(x)$ , within the cavity for different values of the output power generated by the cavity, and the right panel shows the spatial dependence of the lasing mode profile,  $|\psi_0(x)|$ , for the same values of the output power. As the pump on the gain medium,  $D_0$ , is increased, the amplitude of the field within

the cavity increases, as does the output power. However, due to spatial hole-burning in the gain medium, the impact of the higher field intensity within the cavity is not felt uniformly in the inversion; thus the average inversion within the cavity still increases as the pump is ramped, mostly due to the positions near the mirror in the cavity where the electric field is very weak, while the weighted average of the inversion with the field intensity remains relatively constant, as the inversion where the field intensity is maximized stays relatively constant as the pump is increased. Thus, we expect to see the corrected Schawlow-Townes and Chong-Stone linewidth predictions decrease faster than  $1/P$ , as is observed in the right panel of Fig. 6.3, as both the output power,  $P$ , and spatially averaged inversion,  $\bar{D}$ , increase as the pump strength,  $D_0$ , is increased (see Eq. (6.74)), while the integral of the inversion weighted against the field intensity, used in the TCMT linewidth prediction, does not change as the pump is increased. Thus, there is a conspiracy between the lasing mode profile and the inversion to maintain the  $1/P$  dependence seen in the TCMT linewidth formula.

In the linewidth predictions discussed so far, we have taken for granted that we know how to correctly calculate the power that corresponds to the output power that would be observed experimentally. This can be calculated using Poynting's theorem in a dissipative media with losses as [112],

$$P = \frac{\omega_0}{2\pi} \int \text{Im}[-\varepsilon(x)] |E(x)|^2 dx, \quad (6.77)$$

where this equation is given in Gaussian units,  $E(x) = \sqrt{I}\psi_0(x)$  is the unnormalized lasing mode, and  $I$  is the mode intensity. Performing this calculation relies on spatially dependent quantities, which can be obtained using SALT. The quantitative agreement seen between the TCMT linewidth prediction and the FDTD simulations shown in Fig. 6.3 also provides independent confirmation that this is the correct formulation of the output power to use. However, prior to a spatial treatment of the properties of a laser, the output power was calculated using [4]

$$P_{\text{ST}} = \gamma_c \bar{n} \hbar \omega_0, \quad (6.78)$$

where  $\bar{n}$  is the average number of photons in the cavity. The linewidth prediction of the

corrected Schawlow-Townes theory using this spatially invariant power calculation (cyan line) can be seen in Fig. 6.3, where the data is still plotted against the output power that would be experimentally observed, Eq. (6.77). This also shows large disagreements with the FDTD simulation results. Thus we see that it is critical to use all of the spatial information in the fields  $E(x)$  and  $D(x)$  obtained from SALT in order to quantitatively predict the laser linewidth.

### 6.5.1 linewidth scaling relations

The overall intensity of the electric field enters directly into the linewidth formulas only through the output power, Eq. (6.77). SALT demonstrates that the electric field can be written in terms of dimensionless units, and thus the output power can also be written as,

$$P = \left( \frac{\hbar^2 \gamma_{\perp} \gamma_{\parallel}}{4\theta^2} \right) \frac{\omega_0}{2\pi} \int \text{Im}[-\varepsilon(x)] |E_{\text{SALT}}(x)|^2 dx, \quad (6.79)$$

where  $E_{\text{SALT}}(x)$  is the electric field of the lasing mode calculated in SALT units [25, 97]. This is how the dimension-full parameters stemming from the properties of the gain medium directly factor in to all of the linewidth formulas discussed here. In particular we can rewrite the TCMT linewidth in SALT units as,

$$\delta\omega_{\text{TCMT}} = \left( \frac{4\theta^2}{\hbar^2 \gamma_{\perp} \gamma_{\parallel}} \right) \frac{\hbar\omega_0}{2P_{\text{SALT}}} \frac{\omega_0^2 \int \text{Im}[\varepsilon] |\psi_0|^2 dx \int \text{Im}[\varepsilon] \frac{N_0}{D} |\psi_0|^2 dx}{\left| \int \psi_0^2 \left( \varepsilon + \frac{\omega_0}{2} \frac{d\varepsilon}{d\omega} \Big|_{\omega_0} \right) dx \right|^2} (1 + \tilde{\alpha}^2), \quad (6.80)$$

where  $P_{\text{SALT}}$  is the output power calculated using the electric field measured in SALT units.

As noted earlier, using SALT units and the stationary inversion approximation implies powerful scaling relations between lasing solutions at different gain medium parameter values, as discussed in Sec. 2.1. Similarly, Eq. (6.80) implies variable scaling relations for the linewidth. It clearly identifies the dependence of the intrinsic laser linewidth upon the properties of the gain medium,  $\theta$ ,  $\gamma_{\parallel}$ , and the main dependence upon  $\gamma_{\perp}$ . Thus it predicts that the linewidth should obey a set of scaling relations; e.g. keeping the ratio of  $\gamma_{\parallel}/\theta^2$  fixed should result in the same linewidth, and keeping the ratio  $\gamma_{\perp}\gamma_{\parallel}/\theta^2$  constant should result in only very modest changes in the linewidth (changing  $\gamma_{\perp}$  only changes the strength of the

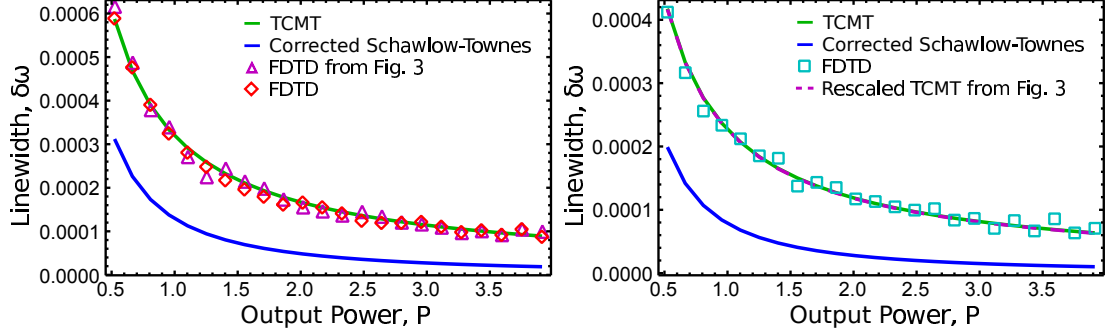


Figure 6.5: (Left panel) Plot showing the linewidth predictions given by the TCMT (green line), corrected Schawlow-Townes theory (blue line), and FDTD simulations (red diamonds and magenta triangles) for a uniformly pumped, dielectric slab cavity with  $n = 3$ ,  $\omega_a = 42.4$ ,  $\gamma_{\perp} = .5$ ,  $\gamma_{\parallel} = .04$ ,  $\theta = 4 \times 10^{-9}$ , and  $N_A = 10^{10}$ . The results of the new FDTD simulations are shown as red triangles, and are plotted alongside the FDTD results from Fig. 6.3, shown as magenta triangles. (Right panel) Plot showing the linewidth predictions given by the TCMT (green line), rescaled TCMT prediction from Fig. 6.3 (magenta dashed line), corrected Schawlow-Townes theory (blue line), and FDTD simulations (cyan squares) for a uniformly pumped, dielectric slab cavity with  $n = 3$ ,  $\omega_a = 42.4$ ,  $\gamma_{\perp} = .25$ ,  $\gamma_{\parallel} = .02$ ,  $\theta = 2 \times 10^{-9}$ , and  $N_A = 10^{10}$ . The rates and frequency are given in units of  $c/L$ , the number of atoms in the cavity is given in terms of the SALT units of  $4\pi\theta^2/(\hbar\gamma_{\perp})$ , and the output power is given in the SALT units of  $4\theta^2/(\hbar^2\gamma_{\perp}\gamma_{\parallel})$ .

bad cavity correction). These predictions are confirmed by FDTD simulations. In the left panel of Fig. 6.5, the ratio of  $\gamma_{\parallel}/\theta^2$  is equal to that of the simulations shown in Fig. 6.3, and the resulting FDTD linewidths (red diamonds, plotted alongside magenta triangles from Fig. 6.3) are seen to be identical. This serves as a validation of the FDTD simulations shown here, as both of these parameters enter into the equations in a non-trivial manner. In practice however, this scaling relationship is not yielding much new information, as the total relaxation rate of the inversion,  $\gamma_{\parallel}$ , can be written as a sum of contributions from spontaneous emission and non-radiative decay,

$$\gamma_{\parallel} = \gamma_{spon} + \gamma_{nr}, \quad (6.81)$$

in which the spontaneous decay rate can be written as [113],

$$\gamma_{spon} = \frac{4\alpha_{fs}\omega_a^3 n \theta^2}{3c^2}, \quad (6.82)$$

where  $\alpha_{fs}$  is the fine structure constant and  $\gamma_{spon}$  is seen to be exactly dependent upon

$\theta^2$ . Thus, in the limit of an atomic gain media without a non-radiative decay channel available from the upper level to the ground state, the ratio of  $\gamma_{\parallel}/\theta^2$  in the linewidth is not yielding any new information, as these two parameters are not independent. However, this analysis does verify the intuitive statement that the laser linewidth will be reduced if the non-radiative decay rate is substantially larger than the spontaneous emission decay rate, as the relative ratio of  $\theta^2/\gamma_{\parallel}$  that appears in Eq. (6.80) will be reduced.

In the right panel of Fig. 6.5, the ratio of  $\gamma_{\perp}\gamma_{\parallel}/\theta^2$  is held constant and equal to that of Fig. 6.3, and the observed laser linewidth is similar in magnitude. Furthermore, we can account for the shift in the bad cavity factor by noting that when  $\omega_a \approx \omega_0 \gg \gamma_{\perp}$ , we can express the bad cavity factor as

$$B = \frac{1}{\left| \int \psi_0^2(x) \left( \varepsilon + \frac{\omega_0}{2} \frac{d\varepsilon}{d\omega} \Big|_{\omega_0} \right) dx \right|} \approx \left| \frac{1}{1 + \frac{\gamma_c}{2\gamma_{\perp}}} \right|. \quad (6.83)$$

Using this, we can rescale the TCMT linewidth prediction by  $B_{new}^2/B_{old}^2$  calculated using the simple form on the right-hand side of Eq. (6.83) (magenta dashed line), and this is seen to exactly agree with the TCMT prediction for the new gain media parameters (green line) and quantitatively agree with the FDTD simulations (cyan squares).

## Chapter 7

# Conclusion

In this thesis we have demonstrated a number of important extensions and applications of the steady-state *ab initio* laser theory (SALT). We have shown that SALT can be generalized to treat gain media with an arbitrary number of atomic levels, transitions, and diffusion using C-SALT [98, 119], as well as naturally extended to treat injected signals resulting in amplified modes simultaneously as lasing modes using I-SALT [120]. We used SALT to successfully simulate the chaotic D-shaped cavities which were experimentally demonstrated to produce incoherent laser light [122]. Finally, we demonstrated how to use the SALT solutions to calculate the quantum noise spectrum of the above threshold laser, which resulted in a new theory that contained all previously known linewidth effects [123, 124]. In addition to the works presented in this thesis, we have been involved in other works relating to SALT. We have aided in the development of additional results using SALT, such as performing FDTD verification of the prediction of the laser turn-off as a function of increasing the pump due to the presence of an exceptional point [125], provided FDTD verification of interaction-induced mode switching in laser cavities [208], and assisted in developing numerically efficient methods of solving the SALT equations without the TCF basis [118]. Finally, we have also used SALT simulations to test predictions made by a new analytic statistical theory of random lasers [135].

To use SALT to treat realistic and complex gain media, we have developed two complementary approaches. In the case where the gain medium has only a single lasing transition, we have demonstrated that the gain medium in the stationary limit can be renormalized

to a two-level medium and demonstrated that SALT is more efficient numerically than FDTD [98]. In the more general scenario, where an atomic gain medium has multiple lasing transitions, we have derived complex-SALT (C-SALT), which solves the coupled equations corresponding to the lasing modes and atomic level populations [119]. Furthermore, unlike in the case of a single lasing transition, when multiple transitions are present there is not a natural choice of dimensionless units for the electric field and inversion of the medium. The structure of C-SALT has also been shown to be naturally extended to treat diffusive gain media, facilitating the solution of what is an extremely challenging problem using time-domain methods. Finally, we have also outlined a preliminary treatment of semiconductor gain media in the free-carrier limit who possess a continuum of available lasing transitions between the conduction and valence bands, and were able to numerically demonstrate shift in the lasing frequency due to Pauli-blocking.

We have also extended SALT to treat amplified modes alongside self-oscillating lasing modes by introducing the incoming-TCF basis [120]. This new theory of injection-SALT (I-SALT) is then shown to reduce to the previously known Adler theory of injection locked lasing in the steady-state scenario, but provides an entirely different physical picture of the phenomena. Rather than predicting that the injection-locking transition is dictated by phase synchronization, where we would observe the frequency of the lasing mode being pulled in to that of the injected mode, I-SALT predicts that the locking transition occurs through gain competition, wherein the injected mode eventually out competes the lasing mode for gain as its input intensity is increased, driving the lasing mode below threshold. Furthermore, we demonstrated that, in the steady-state regime, this picture of gain competition is correct through the use of FDTD simulations which agree with I-SALT simulations in showing that the frequency of the lasing mode shifts *away* from that of the injected frequency. Additionally, one of the most important conclusions to come from this work is a proper analysis of the validity of the stationary inversion approximation. The published version of this SALT paper was the first that gives a proper description of the analytic regimes of validity of SALT and connects the theory to previous work on chaotic dynamics in laser systems.

In this thesis we have also demonstrated the first example of using SALT in the multi-

mode regime as an experimental design tool [122]. The goal of this project was to design an incoherent light source with a greater efficiency and power per mode than that of traditional incoherent light sources such as thermal sources or light emitting diodes for use in optical imaging applications such as optical coherence tomography. To overcome the spatially coherent output of individual laser modes, our goal was to design a cavity that was able to operate in the multimode regime with many active lasing modes, with no fixed phase relationship between them, such that the effective output is spatially incoherent light. This requires two properties of the laser system, first the cavity must have a uniform distribution of quality factors for its modes, such that many modes have the potential to lase. Second, mode competition within the cavity must be reduced so that most of these modes are able to reach threshold. We predicted that these two criteria would be satisfied by chaotic cavity lasers, such as D-shaped cavities, where the mode profiles would be distributed throughout the cavity rather than localized like whispering gallery modes in circular cavities. To confirm this, the SALT solution algorithm first had to be optimized for the multimode regime, for which deriving the TCF lasing map Jacobian was necessary. SALT was then able to demonstrate that this hypothesis is correct, and that the maximally chaotic D-shaped cavity has both a uniform distribution of  $Q$ -factors and decreased mode competition due to its spatially delocalized modes. Furthermore, we were able to demonstrate that the single pole approximation in SALT (SPA-SALT) is accurate in the deep multimode regime for a variety of different cavities, and thus can also be used to aid in experimental device design. Finally, we also showed that the SPA-SALT calculation is robust to using different methods of calculating the eigenstates of the cavity, and that lasing mode profiles generated by COMSOL Multiphysics would also yield semi-quantitative agreement with SALT and SPA-SALT calculations made with the TCF basis.

Despite SALT being a semiclassical laser theory, we have also shown how to use SALT solutions to calculate the quantum limited laser linewidth using a temporal coupled mode theory [123]. This generalized linewidth is shown to contain all previously known corrections to the Schawlow-Townes linewidth, but demonstrates that many of these effects are intertwined, and can only be separated in specific limits. The macroscopic perspective taken by the TCMT analysis is also shown to be identical to the microscopic perspective, where each

individual gain atom is assumed to be coupled to a reservoir and fluctuates separately from the other atoms within the cavity. Using the c-number equations derived by Drummond and Raymer [194] for the Langevin forces on the atomic operators, we then simulated the quantum limited laser linewidth using a noisy-FDTD algorithm, demonstrating quantitative agreement with the TCMT prediction. This is the first such quantitative numerical test of above threshold laser linewidth physics to our knowledge.

Looking forward, there are still many phenomena that it would be beneficial to explore using SALT. First and foremost, it would be useful to have precise experimental tests of the predictions of SALT, particularly with respect to interacting modal thresholds due to gain competition. Along with this project it would be excellent to release an open source version of a SALT code such that other members of the scientific community can use SALT. This could either take the form of a full SALT solver, or possibly a SALT or SPA-SALT extension to COMSOL Multiphysics, building on an already well known tool in the community. In a similar vein, it would be useful to perform a full stability analysis of the SALT solutions, including the possibility for spatial or temporal fluctuations. Ideally, this would also yield a SALT based theory able to treat certain regimes of laser dynamics. It also might be possible to use a similar analytic method to treat mode locked lasing. Structures exhibiting long-range order without short-range order, such as Fibonacci lasers in one dimension or hyperuniform cavities in multiple dimensions, have yet to be studied using SALT, and might contain interesting properties. Finally, there might be an interesting application of using SALT to studying plasmonic lasers, whose optical cavities can be much smaller than the wavelength of the emitted light.

# Appendix A

## FDTD simulation algorithm

The fundamental concept behind the FDTD algorithm is to break up the wave equation into Faraday and Ampère's laws, which are first order differential equations in space and time and use a leap-frog method in time to systematically update the electric and magnetic fields. In one dimension, with a wave vector along the  $z$ -axis, the electric and magnetic fields satisfy the equations,

$$\partial_t E(z, t) = \frac{c^2}{\varepsilon_c} \partial_z B(z, t), \quad (\text{A.1})$$

$$\partial_t B(z, t) = \partial_z E(z, t), \quad (\text{A.2})$$

which can be rewritten using the FDTD algorithm as [167],

$$\frac{E(z_n, t_{i+1}) - E(z_n, t_i)}{\Delta t} = \frac{c^2}{\varepsilon_c} \left( \frac{B\left(z_{n+\frac{1}{2}}, t_{i+\frac{1}{2}}\right) - B\left(z_{n-\frac{1}{2}}, t_{i+\frac{1}{2}}\right)}{\Delta z} \right), \quad (\text{A.3})$$

$$\frac{B\left(z_{n+\frac{1}{2}}, t_{i+\frac{1}{2}}\right) - B\left(z_{n+\frac{1}{2}}, t_{i-\frac{1}{2}}\right)}{\Delta t} = \left( \frac{E(z_{n+1}, t_i) - E(z_n, t_i)}{\Delta z} \right), \quad (\text{A.4})$$

in which the electric field is being evaluated at integer time steps and locations,  $E(z_n, t_i)$ , and the magnetic field is evaluated at half-integer time steps and locations,  $B(z_{n+\frac{1}{2}}, t_{i+\frac{1}{2}})$ , with  $z_{n+1} - z_n = \Delta z$  and  $t_{i+1} - t_i = \Delta t$ . The effect of an absorbing medium in the cavity

can be included through a conductivity term, altering Eq. (A.1) to be,

$$\varepsilon_c \partial_t E(z, t) + \sigma E(z, t) = c^2 \partial_z B(z, t), \quad (\text{A.5})$$

where  $\sigma$  is the conductivity, and then discretized in the usual way. This can be used to simulate a frequency dependent absorbing medium as now the cavity dielectric is given by

$$\varepsilon_{full}(\omega) = \varepsilon_c + \frac{i\sigma}{\omega}. \quad (\text{A.6})$$

In practice, for the large frequencies of lasers relative to the splitting between different laser modes, a frequency independent absorption can be treated approximately by using  $\sigma$  defined at the atomic transition frequency.

The choice of how large to make the spatial step is determined by the resolution of the calculation, typically  $25\Delta z = \lambda$  is sufficient, where  $\lambda = \lambda_0/n$  is the wavelength of the wave in the laser cavity ( $\lambda_0$  is the wavelength in vacuum). The duration of the time step is then set with respect to the resolution,  $v_{max}\Delta t = S\Delta z$ , where  $S$  is called the Courant number [167], and  $v_{max}$  is the maximum speed of the light at any point in the cavity. As laser cavities are usually incident upon air,  $n = 1$ ,  $v_{max} = c$ . For choices of  $S > 1$ , the FDTD algorithm is unstable. For choices of  $S < 1$  the simulations will acquire dispersion due to the numerical discretization of the problem. However, for the simple one dimensional laser cavities that are simulated in this thesis, the ‘magic’ number of  $S = 1$  is used, where this numerical dispersion is exactly zero where  $n = 1$ . However, this still means that in higher index regions of the simulation, some amount of numerical error is expected, though for the simulations in this thesis, this error is seen to be negligible.

Another difficulty that arises when performing numerical analyses is appropriately truncating the simulated region. In one dimension, boundary conditions are straightforward. Mirrors are implemented by setting the electric field to zero at the pixel where the mirror exists,  $E(z_n, t_i) = 0$ . At the edge of the simulated region, to update one of the fields, one would need knowledge of the other field at location not part of the simulation. However, this is easily solved by noting that in free space for an outgoing plane wave, using the

‘magic’ time step,  $S = 1$ , all of field at the previous location and time step moves to the next location and time step,

$$B\left(z_{N+\frac{1}{2}}, t_{i+\frac{1}{2}}\right) = B\left(z_{N-\frac{1}{2}}, t_{i-\frac{1}{2}}\right) \quad (\text{A.7})$$

where  $N$  is the number of pixels used in the simulation, and location  $z_N$  is the last simulated location for the electric field. Thus, the equation for updating the electric field at  $z_N$  is well defined as the magnetic field is known at both locations half a pixel away. In more than one dimension, there is no analytic boundary condition and to simulate outgoing waves one needs a numerical solution. The usual method for this is implementing a perfectly matched layer (PML), which involves creating a medium at the boundary of the simulated region that is impedance-matched to free space so that there are no reflections when the incident wave enters the PML, but this medium has strong absorption, so that the subsequently reflected waves off of the hard (reflecting) boundary at the edge of the simulated region are exponentially suppressed [167].

To use the FDTD algorithm to simulate a laser, we apply it to the Maxwell-Bloch equations, Eqs. (1.8), (1.22), and (1.24). The most critical question encountered when discretizing these equations is where and when the atomic variables should be updated. These variables are coupled to the electric field, so it is most logical to simulate them at the same locations as the electric field. However, if we choose to update the atomic variables at the same time steps as the electric field, termed the “strongly coupled method,” we encounter the problem that we must then solve a non-linear system of equations at each spatial location, at each time step, which is extremely inefficient. Instead, in the FDTD simulations in this thesis we use the “weakly coupled method” developed by Bidégaray [148], which updates the atomic variables at the same time as the magnetic field, and using the known electric field from the previous half-time step, thereby decoupling the non-linear equations. As such, the FDTD update equations for the Maxwell-Bloch equations in one

dimension are,

$$E(z_n, t_{i+1}) = E(z_n, t_i) + \frac{c^2 \Delta t}{\varepsilon_c(z_n)} \left[ \frac{B(z_{n+\frac{1}{2}}, t_{i+\frac{1}{2}}) - B(z_{n-\frac{1}{2}}, t_{i+\frac{1}{2}})}{\Delta z} + 8\pi \left( \omega_a p^{(2)}(z_n, t_{i+\frac{1}{2}}) - \gamma_{\perp} p^{(1)}(z_n, t_{i+\frac{1}{2}}) \right) \right], \quad (\text{A.8})$$

$$B(z_{n+\frac{1}{2}}, t_{i+\frac{1}{2}}) = B(z_{n+\frac{1}{2}}, t_{i-\frac{1}{2}}) + \frac{\Delta t}{\Delta z} (E(z_{n+1}, t_i) - E(z_n, t_i)), \quad (\text{A.9})$$

$$\mathbf{u}(z_n, t_{i+\frac{1}{2}}) = \left( \frac{1}{\Delta t} I - \frac{1}{2} M \right)^{-1} \left[ \mathbf{d}(z_n) + \left( \frac{1}{\Delta t} I + \frac{1}{2} M \right) \mathbf{u}(z_n, t_{i-\frac{1}{2}}) \right], \quad (\text{A.10})$$

where  $\mathbf{u}(z_n) = (d(z_n), p^{(1)}(z_n), p^{(2)}(z_n))$  is the vector of the atomic variables in which the polarization has been written as  $P_g^+ = p^{(1)} + ip^{(2)}$ ,  $\mathbf{d}(z_n) = (\gamma_{\parallel} d_{0,n}, 0, 0)$  is the pumping vector,  $I$  is the 3x3 identity matrix, and  $M$  is a matrix which contains the coupling information between the atomic variables,

$$M = \begin{pmatrix} -\gamma_{\parallel} & 0 & -\frac{4}{\hbar} E(z_n, t_i) \\ 0 & -\gamma_{\perp} & \omega_a \\ \frac{\theta^2}{\hbar} E(z_n, t_i) & -\omega_a & -\gamma_{\perp} \end{pmatrix}. \quad (\text{A.11})$$

Given the brute-force nature of the FDTD algorithm, even though these equations contain all of the physics of lasers it is difficult to use them to understand the underlying physics of what occurs within a cavity. Another drawback of the FDTD method is that there is no test to confirm whether convergence has actually been achieved. In practice, one typically runs the algorithm for an order of magnitude or two longer than the largest time scale in the system,  $T_1 = 1/\gamma_{\parallel}$ , but this is no guarantee of the stability of the final solution.

## Appendix B

# Derivation of the TCF lasing map Jacobian

In this appendix we calculate the Jacobian for the TCF lasing map equation for expediting the numerical solution of the above threshold non-linear SALT equations, following Sec. 2.3.1. As a reminder, here we will use the superscripts  $R$  and  $I$  to denote real and imaginary parts of objects. The derivatives of the modified lasing map equation, Eq. (2.21), with respect to the magnitude of the mode are

$$\frac{\partial y_n^{R,\mu}}{\partial Z_\nu} = - \sum_m \frac{\partial T_{nm}^{R,\mu}}{\partial Z_\nu} \tilde{a}_m^{R,\mu} + \sum_m \frac{\partial T_{nm}^{I,\mu}}{\partial Z_\nu} \tilde{a}_m^{I,\mu}, \quad (\text{B.1})$$

$$\frac{\partial y_n^{I,\mu}}{\partial Z_\nu} = - \sum_m \frac{\partial T_{nm}^{I,\mu}}{\partial Z_\nu} \tilde{a}_m^{R,\mu} - \sum_m \frac{\partial T_{nm}^{R,\mu}}{\partial Z_\nu} \tilde{a}_m^{I,\mu}, \quad (\text{B.2})$$

$$\frac{\partial T_{nm}^{R,\mu}}{\partial Z_\nu} = - \int_C \frac{(u_n^{R,\mu} u_m^{R,\mu} - u_n^{I,\mu} u_m^{I,\mu}) F dx}{(1 + \sum_\sigma \Gamma_\sigma |\Psi_\sigma|^2)^2} \left( 2\Gamma_\nu Z_\nu \left| \sum_{k=1} \tilde{a}_k^\nu u_k^\nu \right|^2 \right), \quad (\text{B.3})$$

$$\frac{\partial T_{nm}^{I,\mu}}{\partial Z_\nu} = - \int_C \frac{(u_n^{R,\mu} u_m^{I,\mu} + u_n^{I,\mu} u_m^{R,\mu}) F dx}{(1 + \sum_\sigma \Gamma_\sigma |\Psi_\sigma|^2)^2} \left( 2\Gamma_\nu Z_\nu \left| \sum_{k=1} \tilde{a}_k^\nu u_k^\nu \right|^2 \right). \quad (\text{B.4})$$

The derivatives with respect to the frequency involve calculating terms such as  $\partial\eta/\partial\omega$  which are analytically very difficult to calculate. These terms are also important to the calculation, and neglecting them will often lead to large errors. This can be seen intuitively by the fact that  $\eta$  contains the information about the location of the passive cavity resonance, and there needs to be a cost associated with changing  $\omega$  to move closer to the center of the gain

curve. However, we can approximate these derivatives through linear interpolation in the same way that is normally done when the TCF eigenvalues and eigenvectors are desired for a wavevector inbetween two TCF library wavevector values. Thus we approximate

$$\frac{\partial \eta_n^\mu}{\partial \omega_\nu} = \frac{\Delta \eta_n^\mu}{\Delta \omega_\mu} \delta_{\nu\mu}, \quad (\text{B.5})$$

$$\frac{\partial u_n^\mu}{\partial \omega_\nu} = \frac{\Delta u_n^\mu}{\Delta \omega_\mu} \delta_{\nu\mu}. \quad (\text{B.6})$$

Following this, the derivatives with respect to  $\omega$  can be calculated as

$$\frac{\partial y_n^{R,\mu}}{\partial \omega_\nu} = \text{Re} \left[ \frac{\partial y_n^\mu}{\partial \omega_\nu} \right], \quad (\text{B.7})$$

$$\frac{\partial y_n^{I,\mu}}{\partial \omega_\nu} = \text{Im} \left[ \frac{\partial y_n^\mu}{\partial \omega_\nu} \right], \quad (\text{B.8})$$

in which,

$$\frac{\partial y_n^\mu}{\partial \omega_\nu} = \frac{\partial C_n^\mu}{\partial \omega_\mu} \tilde{a}_n^\mu \delta_{\mu\nu} - \sum_m \frac{\partial T_{nm}^\mu}{\partial \omega_\nu} \tilde{a}_m^\mu, \quad (\text{B.9})$$

$$\frac{\partial C_n^\mu}{\partial \omega_\mu} = \frac{\eta_n^\mu}{D_0 \gamma_\perp} + \frac{\omega_\mu - \omega_a + i\gamma_\perp}{D_0 \gamma_\perp} \frac{\Delta \eta_n^\mu}{\Delta \omega_\mu}, \quad (\text{B.10})$$

$$\begin{aligned} \frac{\partial T_{nm}^\mu}{\partial \omega_\nu} = & \int_C \frac{\left( \frac{\Delta u_n^\mu}{\Delta \omega_\mu} u_m^\mu + u_n^\mu \frac{\Delta u_m^\mu}{\Delta \omega_\mu} \right) F dx}{1 + \sum_\sigma \Gamma_\sigma |\Psi_\sigma(x)|^2} \delta_{\mu\nu} \\ & - \int_C \frac{(u_n^\mu u_m^\mu) F dx}{(1 + \sum_\sigma \Gamma_\sigma |\Psi_\sigma|^2)^2} \left( \frac{\partial \Gamma_\nu}{\partial \omega_\nu} |\Psi_\nu|^2 + \Gamma_\nu \Psi_\nu Z_\nu \sum_k \frac{\Delta u_k^{*,\nu}}{\Delta \omega_\nu} \tilde{a}_k^{*,\nu} \right. \\ & \left. + \Gamma_\nu \Psi_\nu^* Z_\nu \sum_k \frac{\Delta u_k^\nu}{\Delta \omega_\nu} \tilde{a}_k^\nu \right), \end{aligned} \quad (\text{B.11})$$

$$\frac{\partial \Gamma_\nu}{\partial \omega_\nu} = -2\Gamma_\nu \frac{\omega_\nu - \omega_a}{(\omega_\nu - \omega_a)^2 + \gamma_\perp^2}. \quad (\text{B.12})$$

Finally, the derivatives with respect to the normalized TCF projection coefficients are

$$\frac{\partial y_n^{R,\mu}}{\partial \tilde{a}_l^{R,\nu}} = C_n^{R,\mu} \delta_{nl} \delta_{\mu\nu} - T_{nl}^{R,\mu} \delta_{\mu\nu} - \sum_m \frac{\partial T_{nm}^{R,\mu}}{\partial \tilde{a}_l^{R,\nu}} \tilde{a}_m^{R,\mu} + \sum_m \frac{\partial T_{nm}^{I,\mu}}{\partial \tilde{a}_l^{R,\nu}} \tilde{a}_m^{I,\mu}, \quad (\text{B.13})$$

$$\frac{\partial y_n^{R,\mu}}{\partial \tilde{a}_l^{I,\nu}} = -C_n^{I,\mu} \delta_{nl} \delta_{\mu\nu} + T_{nl}^{I,\mu} \delta_{\mu\nu} - \sum_m \frac{\partial T_{nm}^{R,\mu}}{\partial \tilde{a}_l^{I,\nu}} \tilde{a}_m^{R,\mu} + \sum_m \frac{\partial T_{nm}^{I,\mu}}{\partial \tilde{a}_l^{I,\nu}} \tilde{a}_m^{I,\mu}, \quad (\text{B.14})$$

$$\frac{\partial y_n^{I,\mu}}{\partial \tilde{a}_l^{R,\nu}} = C_n^{I,\mu} \delta_{nl} \delta_{\mu\nu} - T_{nl}^{I,\mu} \delta_{\mu\nu} - \sum_m \frac{\partial T_{nm}^{R,\mu}}{\partial \tilde{a}_l^{R,\nu}} \tilde{a}_m^{I,\mu} - \sum_m \frac{\partial T_{nm}^{I,\mu}}{\partial \tilde{a}_l^{R,\nu}} \tilde{a}_m^{R,\mu}, \quad (\text{B.15})$$

$$\frac{\partial y_n^{I,\mu}}{\partial \tilde{a}_l^{I,\nu}} = C_n^{R,\mu} \delta_{nl} \delta_{\mu\nu} - T_{nl}^{R,\mu} \delta_{\mu\nu} - \sum_m \frac{\partial T_{nm}^{R,\mu}}{\partial \tilde{a}_l^{I,\nu}} \tilde{a}_m^{I,\mu} - \sum_m \frac{\partial T_{nm}^{I,\mu}}{\partial \tilde{a}_l^{I,\nu}} \tilde{a}_m^{R,\mu}, \quad (\text{B.16})$$

where,

$$\begin{aligned} \frac{\partial T_{nm}^{R,\mu}}{\partial \tilde{a}_l^{R,\nu}} = & - (2\Gamma_\nu Z_\nu^2) \int_C \frac{(u_n^{R,\mu} u_m^{R,\mu} - u_n^{I,\mu} u_m^{I,\mu}) F}{(1 + \sum_\sigma \Gamma_\sigma |\Psi_\sigma|^2)^2} \\ & \times \left[ \left( \sum_k \tilde{a}_k^{R,\nu} u_k^{R,\nu} - \tilde{a}_k^{I,\nu} u_k^{I,\nu} \right) u_l^{R,\nu} + \left( \sum_k \tilde{a}_k^{R,\nu} u_k^{I,\nu} + \tilde{a}_k^{I,\nu} u_k^{R,\nu} \right) u_l^{I,\nu} \right] dx, \end{aligned} \quad (\text{B.17})$$

$$\begin{aligned} \frac{\partial T_{nm}^{R,\mu}}{\partial \tilde{a}_l^{I,\nu}} = & - (2\Gamma_\nu Z_\nu^2) \int_C \frac{(u_n^{R,\mu} u_m^{R,\mu} - u_n^{I,\mu} u_m^{I,\mu}) F}{(1 + \sum_\sigma \Gamma_\sigma |\Psi_\sigma|^2)^2} \\ & \times \left[ \left( \sum_k \tilde{a}_k^{R,\nu} u_k^{I,\nu} + \tilde{a}_k^{I,\nu} u_k^{R,\nu} \right) u_l^{R,\nu} - \left( \sum_k \tilde{a}_k^{R,\nu} u_k^{R,\nu} - \tilde{a}_k^{I,\nu} u_k^{I,\nu} \right) u_l^{I,\nu} \right] dx, \end{aligned} \quad (\text{B.18})$$

$$\begin{aligned} \frac{\partial T_{nm}^{I,\mu}}{\partial \tilde{a}_l^{R,\nu}} = & - (2\Gamma_\nu Z_\nu^2) \int_C \frac{(u_n^{R,\mu} u_m^{I,\mu} + u_n^{I,\mu} u_m^{R,\mu}) F}{(1 + \sum_\sigma \Gamma_\sigma |\Psi_\sigma|^2)^2} \\ & \times \left[ \left( \sum_k \tilde{a}_k^{R,\nu} u_k^{R,\nu} - \tilde{a}_k^{I,\nu} u_k^{I,\nu} \right) u_l^{R,\nu} + \left( \sum_k \tilde{a}_k^{R,\nu} u_k^{I,\nu} + \tilde{a}_k^{I,\nu} u_k^{R,\nu} \right) u_l^{I,\nu} \right] dx, \end{aligned} \quad (\text{B.19})$$

$$\begin{aligned} \frac{\partial T_{nm}^{I,\mu}}{\partial \tilde{a}_l^{I,\nu}} = & - (2\Gamma_\nu Z_\nu^2) \int_C \frac{(u_n^{R,\mu} u_m^{I,\mu} + u_n^{I,\mu} u_m^{R,\mu}) F}{(1 + \sum_\sigma \Gamma_\sigma |\Psi_\sigma|^2)^2} \\ & \times \left[ \left( \sum_k \tilde{a}_k^{R,\nu} u_k^{I,\nu} + \tilde{a}_k^{I,\nu} u_k^{R,\nu} \right) u_l^{R,\nu} - \left( \sum_k \tilde{a}_k^{R,\nu} u_k^{R,\nu} - \tilde{a}_k^{I,\nu} u_k^{I,\nu} \right) u_l^{I,\nu} \right] dx. \end{aligned} \quad (\text{B.20})$$

With these, the Jacobian matrix is fully specified, however, the above formalism does not make clear the most efficient implementation of these equations numerically. Intuitively, we need to evaluate each matrix element,  $(n, l)$  separately, where  $n$  and  $l$  specify members of the TCF basis. However, the sums over  $m$  and  $k$  can be contracted into single objects, alleviating the need to have an additional, computationally expensive nested loop. Furthermore, it is then possible to evaluate the entire matrix of  $\partial y^{R,\mu} / \partial a^{R,\nu}$  through the use of

matrix multiplication. For example, if we define,

$$d^{1,\nu} = Z_\nu \left( \sum_k \tilde{a}_k^{R,\nu} u_k^{R,\nu} - \tilde{a}_k^{I,\nu} u_k^{I,\nu} \right), \quad (\text{B.21})$$

$$d^{2,\nu} = Z_\nu \left( \sum_k \tilde{a}_k^{R,\nu} u_k^{I,\nu} + \tilde{a}_k^{I,\nu} u_k^{R,\nu} \right), \quad (\text{B.22})$$

$$\phi^{RR,\mu} = \sum_m a_m^{R,\mu} u_m^{R,\mu}, \quad (\text{B.23})$$

$$\phi^{RI,\mu} = \sum_m a_m^{R,\mu} u_m^{I,\mu}, \quad (\text{B.24})$$

$$\phi^{IR,\mu} = \sum_m a_m^{I,\mu} u_m^{R,\mu}, \quad (\text{B.25})$$

$$\phi^{II,\mu} = \sum_m a_m^{I,\mu} u_m^{I,\mu}, \quad (\text{B.26})$$

then the whole collection of derivatives with respect to the TCF expansion coefficients can be written as

$$\frac{\partial y_n^{R,\mu}}{\partial \tilde{a}_l^{R,\nu}} = C_n^{R,\mu} \delta_{nl} \delta_{\mu\nu} - T_{nl}^{R,\mu} \delta_{\mu\nu} - \frac{\partial \tilde{T}_n^{R,\mu}}{\partial \tilde{a}_l^{R,\nu}} + \frac{\partial \tilde{T}_n^{I,\mu}}{\partial \tilde{a}_l^{R,\nu}}, \quad (\text{B.27})$$

$$\begin{aligned} \frac{\partial \tilde{T}_n^{R,\mu}}{\partial \tilde{a}_l^{R,\nu}} = & - (2\Gamma_\nu Z_\nu) \left[ \int_C \frac{u_n^{R,\mu} u_l^{R,\nu} \phi^{RR,\mu} d^{1,\nu} F}{(1 + \sum_\sigma \Gamma_\sigma |\Psi_\sigma|^2)^2} dx - \int_C \frac{u_n^{I,\mu} u_l^{R,\nu} \phi^{RI,\mu} d^{1,\nu} F}{(1 + \sum_\sigma \Gamma_\sigma |\Psi_\sigma|^2)^2} dx \right. \\ & \left. + \int_C \frac{u_n^{R,\mu} u_l^{I,\nu} \phi^{RR,\mu} d^{2,\nu} F}{(1 + \sum_\sigma \Gamma_\sigma |\Psi_\sigma|^2)^2} dx - \int_C \frac{u_n^{I,\mu} u_l^{I,\nu} \phi^{RI,\mu} d^{2,\nu} F}{(1 + \sum_\sigma \Gamma_\sigma |\Psi_\sigma|^2)^2} dx \right], \quad (\text{B.28}) \end{aligned}$$

where we have refrained from rewriting all of the terms in this new format, but the pattern is apparent. Written in this way, it becomes clear how to efficiently implement these equations numerically using matrix multiplication, and only requiring nested loops over the number of lasing modes,  $\mu$  and  $\nu$ .

## Appendix C

# N-level FDTD simulation constants

In this appendix we list the parameters used in each of the FDTD simulations described in Sec. 3.2.2. These constants are matrices, with  $\gamma_{ij}$  denoting the decay rate from  $|\varphi_j\rangle$  to  $|\varphi_i\rangle$ . These values are given in their dimensionless form, i.e.  $\gamma_{\text{meas}} = \gamma_{\text{real}}L/c$ . Unlisted entries are zero. We also note that throughout this section  $|\varphi_0\rangle$  denotes the ground state, so these matrices are 0 indexed.

For the four-level simulations in Fig. 3.2,

$$\gamma_{4lv, \text{ Fig. 3.2}} = \begin{pmatrix} \cdot & 0.8 & \cdot & \cdot \\ \cdot & \cdot & 5 \times 10^{-4} & \cdot \\ \cdot & \cdot & \cdot & 0.8 \\ \cdot & \cdot & \cdot & \cdot \end{pmatrix}. \quad (\text{C.1})$$

The dipole matrix element is  $g = 2.3 \cdot 10^{-12} \text{m}^{3/2}$ , and the number of gain atoms is  $n = 5 \cdot 10^{23} \text{m}^{-3}$ . The pump  $\mathcal{P}$  was varied between  $3 \cdot 10^{-6}$  and  $3 \cdot 10^{-5}$ .

Thus, for an optical wavelength of  $\lambda = 628 \text{nm}$ , the requirement in Fig. 3.2 that  $n_0 kL = 60$  means that  $L = 4 \mu\text{m}$ . Using this length, the decay rates can be converted to their unit-full values as  $\gamma_{\perp} = 3 \cdot 10^{14} \text{s}^{-1}$ ,  $\gamma_{23} = \gamma_{01} = 6 \cdot 10^{13} \text{s}^{-1}$ ,  $\gamma_{12} = 3.75 \cdot 10^{10} \text{s}^{-1}$ , and the pump at threshold is  $\mathcal{P} = 3 \cdot 10^8 \text{s}^{-1}$ . Similarly, the dipole matrix element also acquires units of inverse

time, and can be expressed as  $\theta^2/\hbar = 3.98 \cdot 10^{-9} \text{m}^3/\text{s}$ , which corresponds to a coupling constant in the classical oscillating dipole picture of  $\sigma = 10^{-4} \text{C}^2/\text{kg}$ . These constants can be seen to be similar to those used in other studies of optical microcavities [117,137].

For the six-level simulations in Fig. 3.2,

$$\gamma_{6\text{lv, Fig. 3.2}} = \begin{pmatrix} \cdot & 0.8 & 10^{-5} & 10^{-5} & 10^{-5} & 10^{-5} \\ \cdot & \cdot & 0.8 & 10^{-5} & 10^{-5} & 10^{-4} \\ \cdot & \cdot & \cdot & 5 \times 10^{-5} & 10^{-5} & 10^{-5} \\ \cdot & \cdot & \cdot & \cdot & 0.8 & 10^{-5} \\ \cdot & \cdot & \cdot & \cdot & \cdot & 0.8 \\ \cdot & \cdot & \cdot & \cdot & \cdot & \cdot \end{pmatrix}. \quad (\text{C.2})$$

Furthermore,  $\gamma_{15} = 10^{-4}$ , and the lasing transition is between levels  $|\varphi_3\rangle$  and  $|\varphi_1\rangle$  (where the ground state is again  $|\varphi_0\rangle$  and the states are numbered in order of increasing energy).

For the four-level simulations in Fig. 3.4,

$$\gamma_{4\text{lv, Fig. 3.4}} = \begin{pmatrix} \cdot & 0.8 & \cdot & \cdot \\ \cdot & \cdot & 5 \times 10^{-2} & \cdot \\ \cdot & \cdot & \cdot & 0.8 \\ \cdot & \cdot & \cdot & \cdot \end{pmatrix}. \quad (\text{C.3})$$

For the six-level simulations in Fig. 3.4,

$$\gamma_{6\text{lv, Fig. 3.4}} = \begin{pmatrix} \cdot & 0.8 & 10^{-5} & 10^{-5} & 10^{-5} & 10^{-5} \\ \cdot & \cdot & 0.8 & 10^{-5} & 10^{-5} & 10^{-4} \\ \cdot & \cdot & \cdot & 5 \times 10^{-5} & 10^{-5} & 10^{-5} \\ \cdot & \cdot & \cdot & \cdot & 0.8 & 10^{-5} \\ \cdot & \cdot & \cdot & \cdot & \cdot & 0.8 \\ \cdot & \cdot & \cdot & \cdot & \cdot & \cdot \end{pmatrix}. \quad (\text{C.4})$$

The four-level simulations of the random cavity in Fig. 3.5 used the same parameters as the four-level simulations in Fig. 3.2.

# Appendix D

## Matrix definitions

The rate matrix,  $R(x)$ , is an  $M \times M$  matrix where  $M$  is the number of atomic levels, and can be spatially dependent when partial pumping is applied to the cavity. In Eq. (3.37),  $R$  can be calculated explicitly as

$$R_{nn}(x) = - \sum_m \gamma_{mn}(x) \quad (\text{D.1})$$

$$R_{nm}(x) = \gamma_{nm}(x), \quad (n \neq m) \quad (\text{D.2})$$

where in most cases the non-radiative decay rates  $\gamma_{nm}$  are a property of the atomic medium, and hence are not spatially dependent. The coupling matrices  $\Xi_j$  also have size  $M \times M$  in Eq. (3.37), and are defined as

$$\Xi_{uu}^{(j)} = \Xi_{ll}^{(j)} = -1 \quad (\text{D.3})$$

$$\Xi_{ul}^{(j)} = \Xi_{lu}^{(j)} = 1 \quad (\text{D.4})$$

where the indices  $u$  and  $l$  refer to the upper and lower lasing levels of the constituent polarization  $j$  respectively.

In Eqs. (3.43) and (3.48), these matrices have size  $PM \times PM$  where  $P$  is the number of discretized spatial points in the cavity and  $M$  is the number of atomic levels. The definitions of these matrices are then adjusted to be zero everywhere except at the location  $x \in P$ , and have only a potentially non-zero block of size  $M \times M$  at this location in the matrix.

## Appendix E

# Treatment of beating populations

We will now investigate the breakdown of the stationary population approximation when the beat frequencies are picked up in the atomic population dynamics. Following Ge *et al.* [24], we assume that there are only two lasing modes in the cavity and will only be concerned with the lowest frequency components such as  $\omega_1 - \omega_2$ , neglecting the other side band terms that are generated such as  $2\omega_1 - \omega_2$  as these will oscillate much faster. We first calculate corrections to the atomic population densities defining

$$\rho(x, t) = \rho_s(x) + (\rho_b(x, t) + c.c.), \quad (\text{E.1})$$

where the subscript  $b$  denotes the portion of the population density beating at the difference frequency, and  $s$  denotes the steady state component. Using this to rewrite Eq. (3.42) and separating out the time dependent portions we find

$$\mathbf{0} = D\nabla^2 \rho_s(x) + R\rho_s(x) + \sum_{j=1} \frac{1}{i\hbar} (\Psi_1 p_{1,j}^* + \Psi_2 p_{2,j}^* - c.c.) \boldsymbol{\xi}_j, \quad (\text{E.2})$$

$$\partial_t \rho_b(x, t) = D\nabla^2 \rho_b(x, t) + R\rho_b(x, t) + \sum_{j=1} \frac{1}{i\hbar} (\Psi_1 p_{2,j}^* - \Psi_2^* p_{1,j}) e^{-i(\omega_1 - \omega_2)t} \boldsymbol{\xi}_j, \quad (\text{E.3})$$

where  $\boldsymbol{\xi}_j$  is the vector form of the elements  $\xi_{n,j}$ .

As we are neglecting higher order beating frequencies, there two contributions to each atomic polarization for the first mode,  $p_{1,j}$ , the first from the electric field oscillating at  $\omega_1$  coupled to the stationary population terms and a second from the electric field oscillating

at  $\omega_2$  coupled to the beating polarization at frequency  $\omega_1 - \omega_2$ .

$$p_{1,j} = \frac{g_j^2 \gamma_{1,j}}{\hbar} (\Psi_1 d_{j,s} + \Psi_2 d_{j,\Delta}), \quad (\text{E.4})$$

where  $d_{j,s}$  and  $d_{j,\Delta}$  are the stationary and beating inversions associated with lasing transition  $j$  and

$$\gamma_{\mu,j} = \frac{1}{\omega_\mu - \omega_{a,j} + i\gamma_{\perp,j}}, \quad (\text{E.5})$$

in which the time dependence has been separated from the beating population densities,  $\rho_b = \rho_\Delta e^{-i(\omega_1 - \omega_2)t}$ . To leading order the polarization of the  $j$ th transition can be written as

$$p_{\mu,j}^{(0)} = \frac{g_j^2 \gamma_{\mu,j}}{\hbar} \Psi_\mu d_{j,s}, \quad (\text{E.6})$$

and this is inserted into Eq. (E.3) to obtain

$$\rho_\Delta = \frac{1}{-i(\omega_1 - \omega_2)} (D\nabla^2 + R) \rho_\Delta + \sum_j \frac{g_j^2}{\hbar^2} \left( \frac{\gamma_{2,j}^* - \gamma_{1,j}}{\omega_1 - \omega_2} \right) \Psi_1 \Psi_2^* \Xi_j \rho_s, \quad (\text{E.7})$$

which can be inverted to find  $\rho_\Delta$ ,

$$\rho_\Delta = M(\omega_1, \omega_2) \Psi_1 \Psi_2^* \rho_s, \quad (\text{E.8})$$

where the matrix  $M(\omega_1, \omega_2) = M(\omega_2, \omega_1)^*$  contains all the information about the diffusion rates, decay rates, and field frequencies. Using this, we are able to write down the first correction to the atomic polarizations,

$$p_{1,j}^{(1)} = \frac{g_j^2 \gamma_{\mu,j}}{\hbar} \Psi_1 (1 + M(\omega_1, \omega_2) |\Psi_2|^2) d_{j,s}. \quad (\text{E.9})$$

Finally, this can be inserted into Eq. (E.2) to calculate the corrections to the steady state population densities. However, it is difficult to glean any analytic insight from these equations as there is no obvious choice of parameters to compare, with multiple atomic polarization relaxation rates and interlevel decay rates. Fortunately, as mentioned above, the beating population densities are negligible in the parameter regimes studied here, namely

when the upper lasing levels of the atomic transitions are metastable and have decay rates much less than the atomic polarization decay rates and the free spectral range.

## Appendix F

# Stability Analysis

The excellent agreement found between I-SALT and FDTD simulations in Sec. 4.3 is a good indication that the solutions of I-SALT are stable in time. To confirm this fact, we now perform a stability analysis of the I-SALT solutions under two simplifying assumptions. First, we continue to make the assumption from SALT that the beating terms of the form  $\exp[-i(\omega_\sigma - \omega_\nu)t]$  time average to zero, where  $\omega_\sigma$  and  $\omega_\nu$  are the frequencies of lasing or amplified modes in the system. Second, we only consider spatially uniform perturbations to the lasing and amplified modes. To address instabilities originating from the beating terms in the inversion equation that are neglected in I-SALT, a different analysis can be performed which is nearly identical to that presented by Ge *et al.* in which the magnitude of the beating the atomic inversion can be calculated [24]. To treat the more general problem of spatially dependent perturbations, a more detailed analysis is being performed by Rotter and Krimer [209]. However, in all previous treatments of stability for injected systems of which we are aware, the slowly varying envelope approximation (SVEA) is invoked, eliminating the spatial degrees of freedom for those treatments as well.

Starting from the Maxwell-Bloch equations, we again insert a modal decomposition of the electric field and polarization, where the amplitudes have been decomposed into their

steady-state values,  $\bar{E}, \bar{P}$ , and the time-dependent perturbations,  $\delta E, \delta P$ ,

$$E^+ = \sum_{\sigma} (\bar{E}_{\sigma} + \delta E_{\sigma}(t)) \Psi_{\sigma}(x) e^{-i\omega_{\sigma} t}, \quad (\text{F.1})$$

$$P^+ = \sum_{\sigma} (\bar{P}_{\sigma} + \delta P_{\sigma}(t)) p_{\sigma}(x) e^{-i\omega_{\sigma} t}. \quad (\text{F.2})$$

The inversion can also be decomposed in a similar manner, but with only the slowly varying part and no ‘‘carrier frequency’’,

$$d(x, t) = (\bar{d} + \delta d(t)) \Delta(x). \quad (\text{F.3})$$

These expansions are then inserted back into the Maxwell-Bloch equations in which we are assuming the cavity dielectric is a constant, the steady-state behavior is removed, and second derivatives of the perturbations are assumed to be much smaller than the other terms, to find

$$4\pi \left( -\omega_{\sigma}^2 \delta P_{\sigma} - 2i\omega_{\sigma} \delta \dot{P}_{\sigma} \right) p_{\sigma}(x) = \delta E_{\sigma} (\nabla^2 + \varepsilon_c \omega_{\sigma}^2) \Psi_{\sigma}(x) + 2i\varepsilon_c \omega_{\sigma} \delta \dot{E}_{\sigma} \Psi_{\sigma}(x), \quad (\text{F.4})$$

$$\delta \dot{P}_{\sigma} p_{\sigma}(x) = (i\omega_{\sigma} - i\omega_a - \gamma_{\perp}) \delta P_{\sigma} p_{\sigma}(x) + \frac{\gamma_{\perp}}{4\pi i} (\delta d E_{\sigma} + d \delta E_{\sigma}) \Delta(x) \Psi_{\sigma}(x), \quad (\text{F.5})$$

$$\delta \dot{d} \Delta(x) = -\gamma_{\parallel} \delta d \Delta(x) + 2\pi i \gamma_{\parallel} \left( \sum_{\sigma} (\bar{E}_{\sigma} \delta P_{\sigma}^* + \bar{P}_{\sigma}^* \delta E_{\sigma}) \Psi_{\sigma}(x) p_{\sigma}^*(x) - c.c. \right). \quad (\text{F.6})$$

The linearized stability equations, Eqs. (F.4)-(F.6), can be further simplified through the use of the known steady-state solutions,

$$-4\pi \omega_{\sigma}^2 \bar{P}_{\sigma} p_{\sigma}(x) = \bar{E}_{\sigma} (\nabla^2 + \varepsilon_c \omega_{\sigma}^2) \Psi_{\sigma}(x), \quad (\text{F.7})$$

$$\bar{P}_{\sigma} p_{\sigma}(x) = \frac{\gamma_{\sigma}}{4\pi} \bar{d} \bar{E}_{\sigma} \Delta(x) \Psi_{\sigma}(x), \quad (\text{F.8})$$

$$0 = \gamma_{\parallel} (d_0 - \bar{d} \Delta(x)) + 2\pi \gamma_{\parallel} i (\bar{E}_{\sigma} \bar{P}_{\sigma}^* \Psi_{\sigma}(x) p_{\sigma}^*(x) - c.c.), \quad (\text{F.9})$$

which allows for the removal of the spatial profiles of the modes. As such, the evolution of the perturbation of the polarization, Eq. (F.5), can be rewritten by dividing through by

$\bar{P}_\sigma p_\sigma(x)$  and using the steady-state solution, Eq. (F.8), to find

$$\frac{\delta \dot{P}_\sigma}{\bar{P}_\sigma} = \frac{i\gamma_\perp}{\gamma_\sigma} \left( \frac{\delta P_\sigma}{\bar{P}_\sigma} - \frac{\delta E_\sigma}{\bar{E}_\sigma} - \frac{\delta d}{\bar{d}} \right). \quad (\text{F.10})$$

To simplify the perturbations in the wave equation, Eq. (F.4), one can first evaluate the derivative of the spatial mode profile through the use of the steady-state solution of the wave equation, Eq. (F.7). Next, Eq. (F.8) is used to rewrite the remaining spatial dependence in terms of the inversion, and finally we integrate both sides with respect to  $1/V \int_C d^d x$ , resulting in

$$\frac{-2i\varepsilon_c}{\gamma_\sigma \langle \bar{d}\Delta(x) \rangle} \left( \frac{\delta \dot{E}_\sigma}{\bar{E}_\sigma} \right) - 2i \left( \frac{\delta \dot{P}_\sigma}{\bar{P}_\sigma} \right) = \omega_\sigma \left( \frac{\delta P_\sigma}{\bar{P}_\sigma} - \frac{\delta E_\sigma}{\bar{E}_\sigma} \right), \quad (\text{F.11})$$

where

$$\langle \bar{d}\Delta(x) \rangle = \frac{1}{V} \bar{d} \int_C \Delta(x) d^d x \quad (\text{F.12})$$

is the spatial average of the inversion. As we are not considering spatially dependent perturbations, only global changes in the amplitudes of the fields in the problem, treating the spatial variation of the inversion would violate our previous assumptions. It should be noted that this spatial average could also be performed at the outset in Eqs. (F.4)-(F.6) without changing any of these results.

Finally, the evolution of the perturbation in the inversion, Eq. (F.6), can be rewritten using the steady state of the polarization, Eq. (F.8), and its complex conjugate, and again integrating over the cavity, to find

$$\frac{\delta \dot{d}}{\bar{d}} = -\gamma_\parallel \frac{\delta d}{\bar{d}} + \left( \frac{i\gamma_\parallel}{2} \right) \sum_\sigma \langle |\bar{E}_\sigma \Psi_\sigma(x)|^2 \rangle \left[ \gamma_\sigma^* \left( \frac{\delta P_\sigma^*}{\bar{P}_\sigma^*} + \frac{\delta E_\sigma}{\bar{E}_\sigma} \right) - c.c. \right], \quad (\text{F.13})$$

where

$$\langle |\bar{E}_\sigma \Psi_\sigma(x)|^2 \rangle = \frac{1}{V} \int_C |\bar{E}_\sigma \Psi_\sigma(x)|^2 d^d x \quad (\text{F.14})$$

is the spatial average of the lasing mode profile.

The evolution equations for the perturbations, Eqs. (F.10), (F.11), and (F.13), collectively comprise  $4(N_L + N_A) + 1$  independent equations, four equations per mode for the real and imaginary portions of Eqs. (F.10) and (F.11), and a single real equation for the

	$D_0 = 0.075, B_{in} = 0$	$D_0 = 0.08, B_{in} = 0.10$
$\lambda_1$	$-4.60878 + 0.70576i$	$-4.61428 + 0.71661i$
$\lambda_2$	$-4.60878 - 0.70576i$	$-4.61428 - 0.71661i$
$\lambda_3$	$-0.00088$	$-0.00084$
$\lambda_4$	$-0.00012$	$-0.00016$
$\lambda_5$	$0$	$0$
$\lambda_6$		$-4.60483 + 0.34413i$
$\lambda_7$		$-4.60483 - 0.34413i$
$\lambda_8$		$0$
$\lambda_9$		$0$

Table F.1: Stability eigenvalues for the cavity shown in Fig. 4.2 at two different locations of pump and injection strength. The first column shows the eigenvalues right before the injected mode is turned on, with only a single lasing mode active in the cavity. The second column shows the eigenvalues when both the lasing mode and amplified mode are present in the cavity and have nearly the same output intensity. In both cases, the I-SALT solution is found to be stable, though in the second case, an extra marginal eigenvalue is found.

perturbation to the atomic inversion, Eq. (F.13), which couples all of the active modes together. The last step, which is standard in a stability analysis calculation, is to assume solutions of these equations in the form

$$\delta E_\sigma, \delta P_\sigma, \delta d \propto e^{\lambda t} \quad (\text{F.15})$$

and ensure that all of the solutions are decaying,  $\text{Re}[\lambda] < 0$ . However, in the case of a lasing mode there is an undetermined global phase of the mode; thus, for every lasing mode in the calculation we expect a single marginal eigenvalue,  $\text{Re}[\lambda] = 0$ , corresponding to the lack of a restoring force for the phase of the lasing mode. We also expect a single marginal eigenvalue for each amplified mode as well. This is a reflection of the fact that the amplitude perturbation of an injected mode being considered here is affecting both the incoming and the outgoing portions of the mode equally,

$$\delta E_\alpha(t) \Psi_\alpha(x) = \delta E_\alpha(t) \left( \sum_n a_n^{(\alpha)} u_n(x; \omega_\alpha) + \sum_m b_m^{(\alpha)} v_m(x; \omega_\alpha) \right), \quad (\text{F.16})$$

and thus has the ability to change the global phase of both the incoming and the outgoing components of the mode. However, it must alter both portions by the same phase shift, thus leaving the relative phase difference between the incident and the outgoing components

fixed, as is expected.

The results for this spatially averaged stability analysis for the simulations shown in Fig. 4.2 can be seen in Table F.1. The first column shows the eigenvalues for the cavity when only a single lasing mode is active, right before the pump is fixed and the incident mode is turned on, and the I-SALT solution is found to be stable. As expected, we find four decaying eigenvalues and a single marginal eigenvalue. The second column shows the eigenvalues for the cavity when both the lasing and the amplified modes are present in the cavity at nearly the location where their output intensities are equal. Again, the I-SALT solution found is stable, with only decaying or marginal eigenvalues found; however, an extra marginal eigenvalue is found, which was not anticipated. The analysis of why there is an extra marginal eigenvalue is left for the future, more complete stability analysis of the SALT and I-SALT solutions.

# Bibliography

- [1] P. J. Wisoff, M. W. Bowers, G. V. Erbert, D. F. Browning, and D. R. Jedlovec. NIF injection laser system. In M. A. Lane and C. R. Wuest, editors, *Optical Engineering at the Lawrence Livermore National Laboratory II: The National Ignition Facility*, volume 5341 of *Society of Photo-Optical Instrumentation Engineers (SPIE) Conference Series*, pages 146–155, May 2004.
- [2] A. E. Siegman. *Lasers*. University Science Books, Mill Valley - California, 1986.
- [3] H. Haken. *Light: Laser Dynamics*, volume 2. North-Holland Phys. Publishing, New York, 1985.
- [4] H. Haken. *Laser theory*. Springer-Verlag, 1984.
- [5] M. Sargent, M. O. Scully, and W. E. Lamb. *Laser physics*. Addison-Wesley Pub. Co., Advanced Book Program, 1974.
- [6] R. G. Gould. The laser, light amplification by stimulated emission of radiation. In P. A. Franken and R. H. Sands, editors, *The Ann Arbor Conference on Optical Pumping, the University of Michigan, 15 June through 18*, page 128. 1959.
- [7] V. DeGiorgio and M. O. Scully. Analogy between the laser threshold region and a second-order phase transition. *Phys. Rev. A*, 2(4):1170–1177, October 1970.
- [8] J. C. Goldstein, M. O. Scully, and P. A. Lee. Laser-phase transition analogy: II. *Physics Letters A*, 35(5):317–319, June 1971.

- [9] J. F. Scott, M. Sargent III, and C. D. Cantrell. Laser-phase transition analogy: Application to first-order transitions. *Optics Communications*, 15(1):13–16, September 1975.
- [10] H. Haken. Generalized ginzburg-landau equations for phase transition-like phenomena in lasers, nonlinear optics, hydrodynamics and chemical reactions. *Zeitschrift fr Physik B Condensed Matter*, 21(1):105–114, March 1975.
- [11] A. Einstein. Zur Quantentheorie der Strahlung. *Physikalische Zeitschrift*, 18:121–128, 1917.
- [12] J. P. Gordon, H. J. Zeiger, and C. H. Townes. The MaserNew type of microwave amplifier, frequency standard, and spectrometer. *Phys. Rev.*, 99(4):1264–1274, August 1955.
- [13] N. G. Basov and A. M. Prokhorov. *JETP*, 28, 1955.
- [14] T. H. Maiman. Stimulated optical radiation in ruby. *Nature*, 187(4736):493–494, August 1960.
- [15] A. Javan, W. R. Bennett, and D. R. Herriott. Population inversion and continuous optical maser oscillation in a gas discharge containing a he-ne mixture. *Phys. Rev. Lett.*, 6(3):106–110, February 1961.
- [16] R. W. Boyd. *Nonlinear Optics*. Academic Press, New York, 2008.
- [17] K. Petermann. Calculated spontaneous emission factor for double-heterostructure injection-lasers with gain-induced waveguiding. *IEEE J. Quantum Electron.*, 15(7):566–570, 1979.
- [18] C. Henry. Theory of the linewidth of semiconductor-lasers. *IEEE J. Quantum Electron.*, 18(2):259–264, 1982.
- [19] C. Henry. Theory of spontaneous emission noise in open resonators and its application to lasers and optical amplifiers. *J. Lightwave Technol.*, 4(3):288–297, March 1986.
- [20] A. Yariv. *Quantum Electronics*. Wiley, New York, 3 edition edition, January 1989.

- [21] H. E. Türeci, A. D. Stone, and B. Collier. Self-consistent multimode lasing theory for complex or random lasing media. *Phys. Rev. A*, 74:043822, 2006.
- [22] H. E. Türeci, A. D. Stone, and L. Ge. Theory of the spatial structure of nonlinear lasing modes. *Phys. Rev. A*, 76:013813, 2007.
- [23] H. E. Türeci, L. Ge, S. Rotter, and A. D. Stone. Strong interactions in multimode random lasers. *Science*, 320:643–646, 2008.
- [24] L. Ge, R. J. Tandy, A. D. Stone, and H. E. Türeci. Quantitative verification of ab initio self-consistent laser theory. *Opt. Express*, 16:16895–16902, 2008.
- [25] L. Ge, Y. D. Chong, and A. D. Stone. Steady-state ab initio laser theory: generalizations and analytic results. *Phys. Rev. A*, 82:063824, 2010.
- [26] A. J. DeMaria, D. A. Stetser, and W. H. Glenn Jr. Ultrashort light pulses. *Science*, 156(3782):1557–1568, June 1967.
- [27] S. L. Shapiro and D. H. Auston. *Ultrashort light pulses: picosecond techniques and applications*. Springer-Verlag, 1984.
- [28] P. Siffalovic, M. Drescher, M. Spieweck, T. Wiesenthal, Y. C. Lim, R. Weidner, A. Elizarov, and U. Heinzmann. Laser-based apparatus for extended ultraviolet femtosecond time-resolved photoemission spectroscopy. *Rev. Sci. Instrum.*, 72(1):30–35, January 2001.
- [29] J. D. Koralek, J. F. Douglas, N. C. Plumb, Z. Sun, A. V. Fedorov, M. M. Murnane, H. C. Kapteyn, S. T. Cundiff, Y. Aiura, K. Oka, H. Eisaki, and D. S. Dessau. Laser based angle-resolved photoemission, the sudden approximation, and quasiparticle-like spectral peaks in  $\text{Bi}_2\text{Sr}_2\text{CaCu}_2\text{O}_{8+\delta}$ . *Phys. Rev. Lett.*, 96(1):017005, January 2006.
- [30] J. D. Koralek, J. F. Douglas, N. C. Plumb, J. D. Griffith, S. T. Cundiff, H. C. Kapteyn, M. M. Murnane, and D. S. Dessau. Experimental setup for low-energy laser-based angle resolved photoemission spectroscopy. *Rev. Sci. Instrum.*, 78(5):053905, May 2007.

- [31] A. L. Schawlow and C. H. Townes. Infrared and optical masers. *Phys. Rev.*, 112(6):1940–1949, December 1958.
- [32] H. Soda, K.-i. Iga, C. Kitahara, and Y. Suematsu. GaInAsP/InP surface emitting injection lasers. *Japanese Journal of Applied Physics*, 18(12):2329, December 1979.
- [33] J. K. Guenter, R. A. Hawthorne, D. N. Granville, M. K. HibbsBrenner, and R. A. Morgan. *Reliability of proton-implanted VCSELs for data communications*, volume 2683. Spie - Int Soc Optical Engineering, Bellingham, 1996.
- [34] F. Koyama. Recent advances of VCSEL photonics. *J. Lightwave Technol.*, 24(12):4502–4513, December 2006.
- [35] A. Levi, R. Slusher, S. McCall, T. Tanbun-Ek, D. Coblentz, and S. Pearton. Room temperature operation of microdisc lasers with submilliamp threshold current. *Electronics Letters*, 28(11):1010–1012, May 1992.
- [36] S. L. McCall, A. F. J. Levi, R. E. Slusher, S. J. Pearton, and R. A. Logan. Whispering-gallery mode microdisk lasers. *Appl. Phys. Lett.*, 60(3):289–291, January 1992.
- [37] L. Collot, V. Lefvre-Seguin, M. Brune, J. M. Raimond, and S. Haroche. Very high-q whispering-gallery mode resonances observed on fused silica microspheres. *EPL (Europhysics Letters)*, 23(5):327, August 1993.
- [38] J. C. Knight, G. Cheung, F. Jacques, and T. A. Birks. Phase-matched excitation of whispering-gallery-mode resonances by a fiber taper. *Opt. Lett.*, 22(15):1129, August 1997.
- [39] D. K. Armani, T. J. Kippenberg, S. M. Spillane, and K. J. Vahala. Ultra-high-q toroid microcavity on a chip. *Nature*, 421(6926):925–928, February 2003.
- [40] E. Yablonovitch. Inhibited Spontaneous Emission in Solid-State Physics and Electronics. *Phys. Rev. Lett.*, 58(20):2059–2062, May 1987.

- [41] O. Painter, R. K. Lee, A. Scherer, A. Yariv, J. D. O'Brien, P. D. Dapkus, and I. Kim. Two-Dimensional Photonic Band-Gap Defect Mode Laser. *Science*, 284(5421):1819–1821, June 1999.
- [42] M. Meier, A. Mekis, A. Dodabalapur, A. Timko, R. E. Slusher, J. D. Joannopoulos, and O. Nalamasu. Laser action from two-dimensional distributed feedback in photonic crystals. *Appl. Phys. Lett.*, 74(1):7–9, January 1999.
- [43] M. Imada, S. Noda, A. Chutinan, T. Tokuda, M. Murata, and G. Sasaki. Coherent two-dimensional lasing action in surface-emitting laser with triangular-lattice photonic crystal structure. *Appl. Phys. Lett.*, 75(3):316–318, July 1999.
- [44] S. Noda, M. Yokoyama, M. Imada, A. Chutinan, and M. Mochizuki. Polarization Mode Control of Two-Dimensional Photonic Crystal Laser by Unit Cell Structure Design. *Science*, 293(5532):1123–1125, August 2001.
- [45] S. Noda. Seeking the Ultimate Nanolaser. *Science*, 314(5797):260–261, October 2006.
- [46] Y. Kurosaka, S. Iwahashi, Y. Liang, K. Sakai, E. Miyai, W. Kunishi, D. Ohnishi, and S. Noda. On-chip beam-steering photonic-crystal lasers. *Nat. Photonics*, 4(7):447–450, July 2010.
- [47] S. Noda. Photonic crystal lasersultimate nanolasers and broad-area coherent lasers [Invited]. *J. Opt. Soc. Am. B*, 27(11):B1, November 2010.
- [48] N. M. Lawandy, R. M. Balachandran, A. S. L. Gomes, and E. Sauvain. Laser action in strongly scattering media. *Nature*, 368(6470):436–438, March 1994.
- [49] P. Pradhan and N. Kumar. Localization of light in coherently amplifying random media. *Phys. Rev. B*, 50(13):9644–9647, October 1994.
- [50] H. Cao. Review on the latest developments in random lasers with coherent feedback. *J. Phys. A*, 38:10497–10535, 2005.

- [51] X. Huang, W. O. Charles, and C. Gmachl. Temperature-insensitive long-wavelength ( $\lambda \approx 14\mu\text{m}$ ) quantum cascade lasers with low threshold. *Optics Express*, 19(9):8297, April 2011.
- [52] H. W. Dinges, H. Burkhard, R. Lsch, H. Nickel, and W. Schlapp. Refractive indices of InAlAs and InGaAs/InP from 250 to 1900 nm determined by spectroscopic ellipsometry. *Applied Surface Science*, 54:477–481, January 1992.
- [53] X. Huang, Y. Chiu, W. O. Charles, and C. Gmachl. Ridge-width dependence of the threshold of long wavelength ( $\lambda \approx 14\mu\text{m}$ ) quantum cascade lasers with sloped and vertical sidewalls. *Opt. Express*, 20(3):2539, January 2012.
- [54] R. K. Chang and A. J. Campillo. *Optical Processes in Microcavities*. World Scientific Pub Co Inc, Singapore ; New Jersey, June 1996.
- [55] D. Rafizadeh, J. P. Zhang, S. C. Hagness, A. Taflove, K. A. Stair, S. T. Ho, and R. C. Tiberio. Waveguide-coupled AlGaAs / GaAs microcavity ring and disk resonators with high finesse and 21.6-nm free spectral range. *Opt. Lett.*, 22(16):1244, August 1997.
- [56] F. Vollmer, D. Braun, A. Libchaber, M. Khoshsim, I. Teraoka, and S. Arnold. Protein detection by optical shift of a resonant microcavity. *Applied Physics Letters*, 80(21):4057–4059, May 2002.
- [57] M. Hossein-Zadeh and K. J. Vahala. Fiber-taper coupling to whispering-gallery modes of fluidic resonators embedded in a liquid medium. *Optics Express*, 14(22):10800, 2006.
- [58] J. Hu, N. Carlie, N.-N. Feng, L. Petit, A. Agarwal, K. Richardson, and L. Kimerling. Planar waveguide-coupled, high-index-contrast, high-q resonators in chalcogenide glass for sensing. *Opt. Lett.*, 33(21):2500, November 2008.
- [59] L. Ge, O. Malik, and H. E. Türeci. Output power enhancement in microlasers by selective pumping. in submission.
- [60] J. U. Nöckel and A. D. Stone. Ray and wave chaos in asymmetric resonant optical cavities. *Nature*, 385:45–47, 1997.

- [61] C. Gmachl, F. Capasso, E. E. Narimanov, J. U. Nöckel, A. D. Stone, J. Faist, D. L. Sivco, and A. Y. Cho. High-power directional emission from microlasers with chaotic resonators. *Science*, 280:1556–1564, 1998.
- [62] S. Lacey, H. Wang, D. H. Foster, and J. U. Nöckel. Directional tunneling escape from nearly spherical optical resonators. *Phys. Rev. Lett.*, 91(3):033902, July 2003.
- [63] H. G. L. Schwefel, N. B. Rex, H. E. Türeci, R. K. Chang, A. D. Stone, T. Ben-Messaoud, and J. Zyss. Dramatic shape sensitivity of directional emission patterns from similarly deformed cylindrical polymer lasers. *Journal of the Optical Society of America B*, 21(5):923, 2004.
- [64] C. Yan, Q. J. Wang, L. Diehl, M. Hentschel, J. Wiersig, N. Yu, C. Pflgl, F. Capasso, M. A. Belkin, T. Edamura, M. Yamanishi, and H. Kan. Directional emission and universal far-field behavior from semiconductor lasers with limaçon-shaped microcavity. *Applied Physics Letters*, 94(25):251101, June 2009.
- [65] H. Cao, Y. G. Zhao, S. T. Ho, E. W. Seelig, Q. H. Wang, and R. P. H. Chang. Random laser action in semiconductor powder. *Phys. Rev. Lett.*, 82(11):2278–2281, March 1999.
- [66] H. Cao, J. Y. Xu, E. W. Seelig, and R. P. H. Chang. Microlaser made of disordered media. *Applied Physics Letters*, 76(21):2997–2999, May 2000.
- [67] R. C. Polson, A. Chipouline, and Z. V. Vardeny. Random lasing in  $\pi$ -conjugated films and infiltrated opals. *Advanced Materials*, 13(10):760–764, May 2001.
- [68] M. Bahoura and M. A. Noginov. Determination of the transport mean free path in a solid-state random laser. *Journal of the Optical Society of America B*, 20(11):2389, 2003.
- [69] K. L. van der Molen, R. W. Tjerkstra, A. P. Mosk, and A. Lagendijk. Spatial extent of random laser modes. *Phys. Rev. Lett.*, 98(14):143901, April 2007.
- [70] D. S. Wiersma and S. Cavaleri. Light emission: A temperature-tunable random laser. *Nature*, 414(6865):708–709, December 2001.

- [71] X. Wu, W. Fang, A. Yamilov, A. A. Chabanov, A. A. Asatryan, L. C. Botten, and H. Cao. Random lasing in weakly scattering systems. *Phys. Rev. A*, 74(5):053812, November 2006.
- [72] S. Johnson. Localization of light. *Physics Today*, 44(5):32, May 1991.
- [73] W. R. Bennett, Jr. Gaseous optical masers. *Applied Optics*, 1(S1):24, January 1962.
- [74] T. H. Maiman. Optical and microwave-optical experiments in ruby. *Phys. Rev. Lett.*, 4(11):564–566, June 1960.
- [75] C. K. N. Patel. Interpretation of CO<sub>2</sub> optical maser experiments. *Phys. Rev. Lett.*, 12(21):588–590, May 1964.
- [76] P. Sorokin and J. Lankard. Stimulated emission observed from an organic dye chloroaluminum phthalocyanine. *IBM J. of Res. and Dev.*, 10(2):162–&, 1966.
- [77] P. Sorokin, W. Culver, E. Hammond, and J. Lankard. End-pumped stimulated emission from a thiocarbocyanine dye. *Ibm J. of Res. and Dev.*, 10(5):401–&, 1966.
- [78] F. P. Schäfer, W. Schmidt, and J. Volze. Organic dye solution laser. *Appl. Phys. Lett.*, 9(8):306–309, October 1966.
- [79] M. L. Spaeth and D. P. Bortfeld. Stimulated emission from polymethine dyes. *Appl. Phys. Lett.*, 9(5):179–181, September 1966.
- [80] F. P. Schäfer, W. Schmidt, and K. Marth. New dye lasers covering the visible spectrum. *Phys. Lett. A*, 24(5):280–281, February 1967.
- [81] B. B. McFarland. Laser second-harmonic-induced stimulated emission of organic dyes. *Appl. Phys. Lett.*, 10(7):208–209, April 1967.
- [82] B. H. Soffer and B. B. McFarland. Continuously tunable, narrow-band organic dye lasers. *Appl. Phys. Lett.*, 10(10):266–267, May 1967.
- [83] O. G. Peterson, S. A. Tuccio, and B. B. Snavely. Cw operation of an organic dye solution laser. *Appl. Phys. Lett.*, 17(6):245–247, September 1970.

- [84] R. Bornemann, U. Lemmer, and E. Thiel. Continuous-wave solid-state dye laser. *Opt. Lett.*, 31(11):1669, 2006.
- [85] H. Kroemer. A proposed class of hetero-junction injection lasers. *Proc. IEEE*, 51(12):1782–1783, December 1963.
- [86] R. Dingle, W. Wiegmann, and C. H. Henry. Quantum states of confined carriers in very thin  $\text{Al}_x\text{Ga}_{1-x}\text{As}$ -GaAs- $\text{Al}_x\text{Ga}_{1-x}\text{As}$  heterostructures. *Phys. Rev. Lett.*, 33(14):827–830, September 1974.
- [87] D. L. Huffaker, G. Park, Z. Zou, O. B. Shchekin, and D. G. Deppe.  $1.3\mu\text{m}$  room-temperature GaAs-based quantum-dot laser. *Appl. Phys. Lett.*, 73(18):2564–2566, November 1998.
- [88] T. Newell, D. Bossert, A. Stintz, B. Fuchs, K. Malloy, and L. Lester. Gain and linewidth enhancement factor in InAs quantum-dot laser diodes. *IEEE Photonic. Tech. L.*, 11(12):1527–1529, December 1999.
- [89] L. Lester, A. Stintz, H. Li, T. Newell, E. A. Pease, B. Fuchs, and K. Malloy. Optical characteristics of  $1.24 - \mu\text{m}$  InAs quantum-dot laser diodes. *IEEE Photonic. Tech. L.*, 11(8):931–933, August 1999.
- [90] W. W. Chow and S. W. Koch. *Semiconductor-Laser Fundamentals: Physics of the Gain Materials*. Springer, New York, 1999.
- [91] Kazarino, Rf and R. Suris. Possibility of amplification of electromagnetic waves in a semiconductor with a superlattice. *Sov. Phys. Semicond.*, 5(4):707–&, 1971.
- [92] J. Faist, F. Capasso, D. L. Sivco, C. Sirtori, A. L. Hutchinson, and A. Y. Cho. Quantum cascade laser. *Science*, 264:553–556, 1994.
- [93] M. Razeghi. High-performance InP-Based mid-IR quantum cascade lasers. *IEEE J. Sel. Top. Quant.*, 15(3):941–951, May 2009.
- [94] H. Fu and H. Haken. Semiclassical dye-laser equations and the unidirectional single frequency operation. *Phys. Rev. A*, 36:4802–4816, 1987.

- [95] H. Fu and H. Haken. Semiclassical theory of dye lasers: the single-frequency and multifrequency steady states of operation. *J. Opt. Soc. Am. B*, 5:899–908, 1988.
- [96] Y. I. Khanin. *Principles of Laser Dynamics*. Elsevier, Amsterdam, 1995.
- [97] L. Ge. *Steady-state Ab Initio Laser Theory and its Applications in Random and Complex Media*. PhD thesis, Yale University, 2010.
- [98] A. Cerjan, Y. D. Chong, L. Ge, and A. D. Stone. Steady-state ab initio laser theory for n-level lasers. *Opt. Express*, 20:474–488, 2012.
- [99] F. T. Arecchi, G. L. Lippi, G. P. Puccioni, and J. R. Tredicce. Deterministic chaos in laser with injected signal. *Opt. Commun.*, 51:308–314, 1984.
- [100] G. L. Oppo, A. Politi, G. L. Lippi, and F. T. Arecchi. Frequency pushing in lasers with injected signal. *Phys. Rev. A*, 34:4000–4007, 1986.
- [101] J. Ohtsubo. *Semiconductor Lasers: Stability, Instability, and Chaos*. Springer, New York, 2007.
- [102] M. Lindberg and S. W. Koch. Effective bloch equations for semiconductors. *Phys. Rev. B*, 38:3342–3350, 1988.
- [103] H. Haug and S. W. Koch. Semiconductor laser theory with many-body effects. *Phys. Rev. A*, 39:1887–1898, 1989.
- [104] C. Z. Ning, R. A. Indik, and J. V. Moloney. Effective bloch equations for semiconductor lasers and amplifiers. *IEEE J. of Quantum Electron.*, 33:1543–1550, 1997.
- [105] R. N. Hall, G. E. Fenner, J. D. Kingsley, T. J. Soltys, and R. O. Carlson. Coherent light emission from gaas junctions. *Phys. Rev. Lett.*, 9(9):366–368, November 1962.
- [106] M. I. Nathan, W. P. Dumke, G. Burns, F. H. D. Jr, and G. Lasher. Stimulated emission of radiation from gaas p-n junctions. *Appl. Phys. Lett.*, 1(3):62–64, November 1962.
- [107] N. Holonyak and S. F. Bevacqua. Coherent visible light emission from  $\text{gaas}_{1-x}\text{px}$  junctions. *Appl. Phys. Lett.*, 1(4):82–83, December 1962.

- [108] R. Glauber and M. Lewenstein. Quantum optics of dielectric media. *Phys. Rev. A*, 43(1):467–491, January 1991.
- [109] G. Hackenbroich, C. Viviescas, and F. Haake. Field quantization for chaotic resonators with overlapping modes. *Phys. Rev. Lett.*, 89(8):083902, August 2002.
- [110] C. Viviescas and G. Hackenbroich. Field quantization for open optical cavities. *Phys. Rev. A*, 67(1):013805, January 2003.
- [111] G. Hackenbroich, C. Viviescas, and F. Haake. Quantum statistics of overlapping modes in open resonators. *Phys. Rev. A*, 68(6):063805, December 2003.
- [112] J. D. Jackson. *Classical Electrodynamics*. Wiley, New York, 3rd edition, August 1998.
- [113] R. Shankar. *Principles of Quantum Mechanics*. Springer, New York, 2nd edition, December 2013.
- [114] M. Lax, W. H. Louisell, and W. B. McKnight. From Maxwell to paraxial wave optics. *Phys. Rev. A*, 11(4):1365–1370, April 1975.
- [115] M. B. Spencer and W. E. Lamb. Laser with a transmitting window. *Phys. Rev. A*, 5:884–892, 1972.
- [116] K. S. Yee. Numerical solution of the initial boundary value problems involving maxwell’s equations in isotropic media. *IEEE Trans. Antennas Propag.*, 14:302–307, 1966.
- [117] A. S. Nagra and R. A. York. Fdtd analysis of wave propagation in nonlinear absorbing and gain media. *IEEE Trans. Antennas Propag.*, 46:334–340, 1998.
- [118] S. Esterhazy, D. Liu, M. Liertzer, A. Cerjan, L. Ge, K. G. Makris, A. D. Stone, J. M. Melenk, S. G. Johnson, and S. Rotter. Scalable numerical approach for the steady-state ab initio laser theory. *Phys. Rev. A*, 90:023816, Aug 2014.
- [119] A. Cerjan, Y. D. Chong, and A. D. Stone. Steady-state ab initio laser theory for complex gain media. *Opt. Express*, 23:6455–6477, 2015.

- [120] A. Cerjan and A. D. Stone. Steady-state *ab initio* theory of lasers with injected signals. *Phys. Rev. A*, 90:013840, Jul 2014.
- [121] R. Adler. A study of locking phenomena in oscillators. *Proc. IRE*, 34:351–356, 1946.
- [122] B. Redding, A. Cerjan, X. Huang, M. L. Lee, A. D. Stone, M. A. Choma, and H. Cao. Low spatial coherence electrically pumped semiconductor laser for speckle-free full-field imaging. *Proc. Natl. Acad. Sci. USA*, 112(5):1304–1309, February 2015.
- [123] A. Pick, A. Cerjan, D. Liu, A. Rodriguez, A. D. Stone, Y. D. Chong, and S. Johnson. Ab-initio multimode linewidth theory for arbitrary inhomogeneous laser cavities. arXiv: 1502.07268. in submission.
- [124] A. Cerjan, A. Pick, Y. D. Chong, A. W. Rodriguez, S. G. Johnson, and A. D. Stone. Quantitative verification of general theories of the intrinsic laser linewidth. in preparation.
- [125] M. Liertzer, L. Ge, A. Cerjan, A. D. Stone, H. E. Türeci, and S. Rotter. Pump-induced exceptional points in lasers. *Phys. Rev. Lett.*, 108:173901, 2012.
- [126] J. Andreasen and H. Cao. Creation of new lasing modes with spatially nonuniform gain. *Opt. Lett.*, 34(22):3586, November 2009.
- [127] J. Andreasen, C. Vanneste, L. Ge, and H. Cao. Effects of spatially nonuniform gain on lasing modes in weakly scattering random systems. *Phys. Rev. A*, 81(4):043818, April 2010.
- [128] L. Ge, Y. D. Chong, S. Rotter, H. E. Tuereci, and A. D. Stone. Unconventional modes in lasers with spatially varying gain and loss. *Phys. Rev. A*, 84(2):023820, August 2011.
- [129] N. Bachelard, J. Andreasen, S. Gigan, and P. Sebbah. Taming random lasers through active spatial control of the pump. *Phys. Rev. Lett.*, 109(3):033903, July 2012.

- [130] T. Hisch, M. Liertzer, D. Pogany, F. Mintert, and S. Rotter. Pump-controlled directional light emission from random lasers. *Phys. Rev. Lett.*, 111(2):023902, July 2013.
- [131] Y. D. Chong and A. D. Stone. General linewidth formula for steady-state multimode lasing in arbitrary cavities. *Phys. Rev. Lett.*, 109:063902, 2012.
- [132] J. C. Pillay, Y. Natsume, A. D. Stone, and Y. D. Chong. Generalized subSchawlow-Townes laser linewidths via material dispersion. *Phys. Rev. A*, 89(3):033840, March 2014.
- [133] A. Sommerfeld. *Partial Differential Equations in Physics*. Academic Press, New York, February 1949.
- [134] H. Fu and H. Haken. Multifrequency operations in a short-cavity standing-wave laser. *Phys. Rev. A*, 43:2446–2454, 1991.
- [135] A. Goetschy, A. Cerjan, and A. D. Stone. Analytic statistical theory of random lasers in the non-linear regime. in preparation.
- [136] A. Gordon, C. Y. Wang, L. Diehl, F. X. Kärtner, A. Belyanin, D. Bour, S. Corzine, G. Höfler, H. C. Liu, H. Schneider, T. Maier, M. Troccoli, J. Faist, and F. Capasso. Multimode regimes in quantum cascade lasers: From coherent instabilities to spatial hole burning. *Phys. Rev. A*, 77:053804, 2008.
- [137] S. Chua, Y. D. Chong, A. D. Stone, M. Soljačić, and J. Bravo-Abad. Low-threshold lasing action in photonic crystal slabs enabled by fano resonances. *Opt. Express*, 19:1539–1562, 2011.
- [138] Y. Huang and S. Ho. Computational model of solid-state, molecular, or atomic media for fdtd simulation based on a multi-level multi-electron system governed by pauli exclusion and fermi-dirac thermalization with application to semiconductor photonics. *Opt. Express*, 14:3569–3587, 2006.

- [139] K. Böhringer and O. Hess. A full-time-domain approach to spatio-temporal dynamics of semiconductor lasers. i. theoretical formulation. *Prog. Quantum Electron.*, 32(5-6):159–246, 2008.
- [140] K. Böhringer and O. Hess. A full time-domain approach to spatio-temporal dynamics of semiconductor lasers. II. spatio-temporal dynamics. *Prog. Quantum Electron.*, 32(5-6):247–307, 2008.
- [141] C. Sirtori, A. Tredicucci, F. Capasso, J. Faist, D. L. Sivco, A. L. Hutchinson, and A. Y. Cho. Dual-wavelength emission from optically cascaded intersubband transitions. *Opt. Lett.*, 23:463–465, 1998.
- [142] X. Huang, J. L. Zhang, V. Tokranov, S. Oktyabrsky, and C. F. Gmachl. Same-wavelength cascaded-transition quantum cascade laser. *Appl. Phys. Lett.*, 103:051113, 2013.
- [143] P. Mandel, C. Etrich, and K. Otsuka. Laser rate-equations with phase-sensitive interactions. *IEEE J. Quantum Electron.*, 29(3):836–843, March 1993.
- [144] P. Khandokhin, I. Koryukin, Y. Khanin, and P. Mandel. Influence of carrier diffusion on the dynamics of a 2-mode laser. *IEEE J. Quantum Electron.*, 31(4):647–652, April 1995.
- [145] M. Homar, J. V. Moloney, and M. S. Miguel. Traveling wave model of a multimode fabry-perot laser in free running and external cavity configurations. *IEEE J. Quantum Electron.*, 32(3):553–566, March 1996.
- [146] M. Jungo, D. Erni, and W. Baechthold. Alternative formulation of carrier transport in spatially-dependent laser rate equations. *Opt. Quantum Electron.*, 36:881–891, 2004.
- [147] W. H. P. Pernice, F. P. Payne, and D. F. G. Gallagher. A finite-difference time-domain method for the simulation of gain materials with carrier diffusion in photonic crystals. *J. Lightw. Technol.*, 25:2306–2314, 2007.
- [148] B. Bidégaray. Time discretizations for maxwell-bloch equations. *Numer. Meth. Partial Differential Equations*, 19:284–300, 2003.

- [149] X. Jiang and C. M. Soukoulis. Time dependent theory for random lasers. *Phys. Rev. Lett.*, 85:70–73, 2000.
- [150] X. Jiang, S. Feng, C. M. Soukoulis, J. Zi, J. D. Joannopoulos, and H. Cao. Coupling, competition, and stability of modes in random lasers. *Phys. Rev. B*, 69:104202, 2004.
- [151] R. Pantell. Laser oscillator with an external signal. *Proc. Inst. Electr. Eng.*, 53(5):474–&, 1965.
- [152] C. L. Tang and H. Statz. Phase-locking of laser oscillators by injected signal. *J. Appl. Phys.*, 38:323–324, 1967.
- [153] R. Boikova and E. Fradkin. Laser subject to an external signal. *Opt. Spectrosc. (USSR)*, 22(5):452–&, 1967.
- [154] S. Wieczorek, B. Krauskopf, T. B. Simpson, and D. Lenstra. The dynamical complexity of optically injected semiconductor lasers. *Phys. Rep.*, 416:1–128, 2005.
- [155] F. Mogensen, G. Jacobsen, and H. Olesen. Light-intensity pulsations in an injection locked semiconductor-laser. *Opt. Quantum Electron.*, 16(2):183–186, 1984.
- [156] F. Mogensen, H. Olesen, and G. Jacobsen. Locking conditions and stability properties for a semiconductor laser with external light injection. *IEEE J. Quantum Electron.*, 21:784–793, 1985.
- [157] T. B. Simpson. Mapping the nonlinear dynamics of a distributed feedback semiconductor laser subject to external optical injection. *Opt. Commun.*, 215(1-3):135–151, January 2003.
- [158] S. Valling, T. Fordell, and A. M. Lindberg. Experimental and numerical intensity time series of an optically injected solid state laser. *Opt. Commun.*, 254(4-6):282–289, October 2005.
- [159] H. G. Solari and G. L. Oppo. Laser with injected signal - perturbation of an invariant circle. *Opt. Commun.*, 111:173–190, 1994.

- [160] M. G. Zimmermann, M. A. Natiello, and H. G. Solari. Global bifurcations in a laser with injected signal: Beyond adler’s approximation. *Chaos*, 11:500–513, 2001.
- [161] B. Kelleher, S. P. Hegarty, and G. Huyet. Optically injected lasers: The transition from class b to class a lasers. *Phys. Rev. E*, 86:066206, 2012.
- [162] R. Lang. Injection locking properties of a semiconductor laser. *IEEE J. Quantum Electron.*, 18:976–983, 1982.
- [163] P. Even, K. A. Ameer, and G. M. Stéphan. Modeling of an injected gas laser. *Phys. Rev. A*, 55:1441–1453, 1997.
- [164] E. G. Lariontsev, I. Zolotoverkh, P. Besnard, and G. M. Stéphan. Injection locking properties of a microchip laser. *Eur. Phys. J. D*, 5:107–117, 1999.
- [165] Y. D. Chong, L. Ge, H. Cao, and A. D. Stone. Coherent perfect absorbers: Time-reversed lasers. *Phys. Rev. Lett.*, 105(5):053901, July 2010.
- [166] W. Wan, Y. Chong, L. Ge, H. Noh, A. D. Stone, and H. Cao. Time-reversed lasing and interferometric control of absorption. *Science*, 331(6019):889–892, February 2011.
- [167] A. Taflove and S. C. Hagness. *Computational Electrodynamics: The Finite-Difference Time-Domain Method*. Artech House, Incorporated, January 2005.
- [168] A. Murakami, K. Kawashima, and K. Atsuki. Cavity resonance shift and bandwidth enhancement in semiconductor lasers with strong light injection. *IEEE J. Quantum Electron.*, 39:1196–1204, 2003.
- [169] The LIGO Scientific Collaboration. Detector description and performance for the first coincidence observations between LIGO and GEO. *Nucl. Instrum. Meth. A*, 517(13):154–179, January 2004.
- [170] The LIGO Scientific Collaboration. A gravitational wave observatory operating beyond the quantum shot-noise limit. *Nat. Phys.*, 7(12):962–965, December 2011.
- [171] eLISA Collaboration. Low-frequency gravitational-wave science with eLISA/NGO. *Classical Quant. Grav.*, 29(12):124016, June 2012. arXiv: 1202.0839.

- [172] S. Lowenthal and D. Joyeux. Speckle removal by a slowly moving diffuser associated with a motionless diffuser. *J. Opt. Soc. Am.*, 61(7):847, July 1971.
- [173] B. Redding, G. Allen, E. R. Dufresne, and H. Cao. Low-loss high-speed speckle reduction using a colloidal dispersion. *Appl. Optics*, 52(6):1168–1172, February 2013.
- [174] M. N. Akram, Z. Tong, G. Ouyang, X. Chen, and V. Kartashov. Laser speckle reduction due to spatial and angular diversity introduced by fast scanning micromirror. *Appl. Optics*, 49(17):3297–3304, June 2010.
- [175] A.-H. Dhalla, J. V. Migacz, and J. A. Izatt. Crosstalk rejection in parallel optical coherence tomography using spatially incoherent illumination with partially coherent sources. *Opt. Lett.*, 35(13):2305–2307, July 2010.
- [176] B. Redding, M. A. Choma, and H. Cao. Speckle-free laser imaging using random laser illumination. *Nat. Photonics*, 6(6):355–359, June 2012.
- [177] B. Redding, M. A. Choma, and H. Cao. Spatial coherence of random laser emission. *Opt. Lett.*, 36(17):3404–3406, September 2011.
- [178] M. Nixon, B. Redding, A. A. Friesem, H. Cao, and N. Davidson. Efficient method for controlling the spatial coherence of a laser. *Opt. Lett.*, 38(19):3858–3861, October 2013.
- [179] B. H. Hokr, J. N. Bixler, G. D. Noojin, R. J. Thomas, B. A. Rockwell, V. V. Yakovlev, and M. O. Scully. Single-shot stand-off chemical identification of powders using random raman lasing. *Proc. Natl. Acad. Sci. USA*, 111(34):12320–12324, August 2014.
- [180] J.-F. Seurin, G. Xu, V. Khalfin, A. Miglo, J. D. Wynn, P. Pradhan, C. L. Ghosh, and L. A. D’Asaro. Progress in high-power high-efficiency VCSEL arrays. *P. Soc. Photo-opt. Ins.*, 7229:722903, 2009.
- [181] H. E. Türeci, H. G. L. Schwefel, P. Jacquod, and A. D. Stone. Modes of wave-chaotic dielectric resonators. In E. Wolf, editor, *Prog. Optics*, volume 47, pages 75–137. Elsevier Science Bv, Amsterdam, 2005.

- [182] L. Bunimovich. Ergodic properties of nowhere dispersing billiards. *Commun. Math. Phys.*, 65(3):295–312, 1979.
- [183] S. Ree and L. Reichl. Classical and quantum chaos in a circular billiard with a straight cut. *Phys. Rev. E*, 60(2):1607–1615, August 1999.
- [184] V. Doya, O. Legrand, and F. Mortessagne. Optimized absorption in a chaotic double-clad fiber amplifier. *Opt. Lett.*, 26(12):872–874, June 2001.
- [185] M. Lax. Quantum noise v: Phase noise in a homogeneously broadened maser. In P. L. Kelley, B. Lax, and P. E. Tannenwald, editors, *Physics of Quantum Electronics*, New York, 1966. McGraw-Hill.
- [186] H. Haus and S. Kawakami. On the excess spontaneous emission factor in gain-guided laser-amplifiers. *IEEE J. Quantum Electron.*, 21(1):63–69, 1985.
- [187] A. Siegman. Excess spontaneous emission in non-hermitian optical-systems .2. laser-oscillators. *Phys. Rev. A*, 39(3):1264–1268, February 1989.
- [188] W. Hamel and J. Woerdman. Nonorthogonality of the longitudinal eigenmodes of a laser. *Phys. Rev. A*, 40(5):2785–2787, September 1989.
- [189] W. Hamel and J. Woerdman. Observation of enhanced fundamental linewidth of a laser due to nonorthogonality of its longitudinal eigenmodes. *Phys. Rev. Lett.*, 64(13):1506–1509, March 1990.
- [190] M. Kolobov, L. Davidovich, E. Giacobino, and C. Fabre. Role of pumping statistics and dynamics of atomic polarization in quantum fluctuations of laser sources. *Phys. Rev. A*, 47(2):1431–1446, February 1993.
- [191] S. Kuppens, M. van Exter, and J. Woerdman. Quantum-limited linewidth of a bad-cavity laser. *Phys. Rev. Lett.*, 72(24):3815–3818, June 1994.
- [192] M. van Exter, S. Kuppens, and J. Woerdman. Theory for the linewidth of a bad-cavity laser. *Phys. Rev. A*, 51(1):809–816, January 1995.

- [193] S. Kuppens, M. van Exter, M. Vanduin, and J. Woerdman. Evidence of nonuniform phase-diffusion in a bad-cavity laser. *IEEE J. Quantum Electron.*, 31(7):1237–1241, July 1995.
- [194] P. Drummond and M. Raymer. Quantum-theory of propagation of nonclassical radiation in a near-resonant medium. *Phys. Rev. A*, 44(3):2072–2085, August 1991.
- [195] D. Marcuse. Computer-simulation of laser photon fluctuations - theory of single-cavity laser. *IEEE J. Quantum Electron.*, 20(10):1139–1148, 1984.
- [196] D. Marcuse. Computer-simulation of laser photon fluctuations - single-cavity laser results. *IEEE J. Quantum Electron.*, 20(10):1148–1155, 1984.
- [197] G. Gray and R. Roy. Noise in nearly-single-mode semiconductor-lasers. *Phys. Rev. A*, 40(5):2452–2462, September 1989.
- [198] M. Kira, F. Jahnke, W. Hoyer, and S. W. Koch. Quantum theory of spontaneous emission and coherent effects in semiconductor microstructures. *Prog. Quantum Electron.*, 23(6):189–279, 1999.
- [199] H. F. Hofmann and O. Hess. Quantum maxwell-bloch equations for spatially inhomogeneous semiconductor lasers. *Phys. Rev. A*, 59(3):2342–2358, March 1999.
- [200] J. Andreasen, H. Cao, A. Taflove, P. Kumar, and C.-q. Cao. Finite-difference time-domain simulation of thermal noise in open cavities. *Phys. Rev. A*, 77(2):023810, February 2008.
- [201] A. W. Rodriguez, A. P. McCauley, J. D. Joannopoulos, and S. G. Johnson. Casimir forces in the time domain: Theory. *Phys. Rev. A*, 80(1):012115, July 2009.
- [202] J. Andreasen and H. Cao. Finite-difference time-domain formulation of stochastic noise in macroscopic atomic systems. *J. Lightwave Technol.*, 27(20):4530–4535, October 2009.
- [203] J. Andreasen and H. Cao. Numerical study of amplified spontaneous emission and lasing in random media. *Phys. Rev. A*, 82(6):063835, December 2010.

- [204] J. Andreasen. *Numerical Studies of Lasing and Electromagnetic Fluctuations in Open Complex Systems*. PhD thesis, Northwestern University, 2009.
- [205] C. H. Henry and R. F. Kazarinov. Quantum noise in photonics. *Rev. Mod. Phys.*, 68(3):801–853, July 1996.
- [206] L. D. Landau and E. M. Lifshitz. *Statistical Physics, Part 1: Volume 5*. Butterworth-Heinemann, Oxford, 3 edition, January 1980.
- [207] J. G. Proakis and D. G. Manolakis. *Digital signal processing*. Pearson Prentice Hall, 2007.
- [208] L. Ge, D. Liu, S. G. Johnson, S. Rotter, H. Cao, A. Cerjan, A. D. Stone, and H. E. Türeci. Interaction-induced mode switching in lasers and other nonlinear media. in preparation.
- [209] D. Krimer and S. Rotter. private communication.